Electronic properties in heterostructures under external fields

John Alexander Gil Corrales

Submitted to the University of Antioquia in fulfillment of the Physics PhD requirements program

Advisor:
PhD Álvaro Morales Aramburo
Co-Advisor:
PhD Carlos Alberto Duque Echeverri

Research group:
Condensed Matter-UdeA

University of Antioquia
Faculty of Exact and Natural Sciences, Institute of Physics
Medellín, Colombia
2022

Publications

[1] L. Pulgar-Velásquez, J. Sierra-Ortega, J. A. Vinasco, D. Laroze, A. Radu, E. Kasapoglu, R. L. Restrepo, J. A. Gil-Corrales, A. L. Morales, C. A. Duque, *Shallow-donor impurity states with excitonic contribution in GaAs/AlGaAs and CdTe/CdSe truncated conical quantum dots under applied magnetic field.* Nanomaterials (**Q1** in scimago), **11**, 2832 (2021).

[2] J. A. Gil-Corrales, J. A. Vinasco, A. Radu, R. L. Restrepo, A. L. Morales, M. E. Mora-Ramos, C. A. Duque, *Self-Consistent Schrödinger-Poisson Study of Electronic Properties of GaAs Quantum Well Wires with Various Cross-Sectional Shapes.* Nanomaterials (**Q1** in scimago), **11**, 1219 (2021).

[3] J. A. Gil-Corrales, J. A. Vinasco, M. E. Mora-Ramos, A. L. Morales, C. A. Duque, *Study of Electronic and Transport Properties in Double Barrier Resonant Tunneling Systems.* submitted to the journal: Phys. Scr. (**Q3** in scimago) on July 28, 2021.

[4] H. Dakhlaoui, J. A. Gil-Corrales, A. L. Morales, E. Kasapoglu, A. Radu, R. L. Restrepo, V. Tulupenko, Juan A. Vinasco, M. E. Mora-Ramos, Carlos Duque, *Theoretical Study of Electronic and Optical Properties in Doped Quantum Structures with Razavy Confining Potential: Effects of External Fields.* Accepted for publication: J. Comput. Electron. (**Q3** in scimago) on January 13, 2022.

[5] J. A. Gil-Corrales, A. L. Morales, C. A. Duque, *Electronic transport properties in GaAs/AlGaAs and InSe/InP finite superlattices under the effect of nonresonant intense laser field and considering geometric modifications.* submitted to the journal: Superlattices Microstruct. (**Q2** in scimago) on October 11, 2021.

Events Participation

[1] *Electronic transport: fundamental concepts and main applications*, Jueves de la Ciencia, Bibioteca Pública Piloto, speaker, January (2022).

[2] *Study of electronic and transport properties in double barrier resonant tunneling systems*, XV Workshop on Physics of Condensed and Molecular Matter, Science Research Center, Autonomous University of the State of Morelos, speaker, July (2021).

[3] *Self-Consistent Schrödinger-Poisson Study of Electronic Properties of GaAs Quantum Well Wires with Various Cross-Sectional Shapes*, First Postgraduate Symposium, University of Antioquia, speaker, July (2021).

[4] The Student Chapter SMMater-UAZ, Mexican Society of Materials, assistant, May (2021).

[5] *International School on Plasmonics, Magnetoplasmonics and Applications-ISPMA 2019*, District University and Central University, assistant, May (2019).

Abstract

In this thesis the electronic properties in various confinement geometries are analyzed for the study of systems such as quantum wells, quantum wires, and quantum dots based on materials such as GaAs, AlGaAs, InTe, among others. In the study carried out, the response of these systems to the action of external fields such as electric, magnetic and intense non-resonant laser fields is investigated. In addition to the study of the electronic properties in these systems, in the particular work related to 3D confinement, the hole states and with these, the excitonic contribution, and the modification of the properties by means of the inclusion of an impurity along the axis of symmetry of the system were studied. In the 2D confinement system, the electronic properties in quantum wires with various cross-sectional shapes were analyzed by means of a self-consistent Schrödinger-Poisson coupling, the emergence of Friedel-like oscillations in the electron density profile at low temperatures should be highlighted. Regarding one-dimensional systems, the electronic and optical response of a Razavy-like quantum well was analyzed with the inclusion of a doped delta layer, as well as the application of external magnetic and electric fields. Similarly, a finite semiconductor superlattice connected to two metal contacts was analyzed for the study of electron tunneling current, as well as the application of an external laser field for various geometric shapes. Finally, the electronic transport properties were studied again by means of the self-consistent method in double-barrier tunneling systems with doping in the outer layers, these properties were calculated by means of the Landauer-Büttiker formalism and compared with experimental results of a resonant tunneling diode based on InGaAs/AlAs.

The first part of the thesis corresponds to the theory and obtaining the equations used in this research, starting with the Landauer-Büttiker theory of electronic transport, continuing with a brief development of linear susceptibility, a section dedicated to the development of the self-consistent method, then we get the Hamiltonian for systems subjected to external electric and magnetic fields, as well as the action of an intense non-resonant laser field, and finally a brief description of the finite element method. In all the calculations, the effective mass approximation has been used and the differential equations involved have been calculated using the finite element method. The main details of each chapter are:

Chapter 3: Using the effective mass approximation in a parabolic two-band model, the effects of the geometrical parameters, on the electron and hole states, in two truncated conical quantum dots: (i) GaAs-(Ga,Al)As in the presence of a shallow donor impurity and under an applied magnetic field and (ii) CdSe–CdTe core–shell type-II quantum dot is studied. The interaction of the electron and hole states is calculated in a first-order perturbative approximation. This study shows that the magnetic field and donor impurities are relevant factors in the optoelectronic properties of conical quantum dots.

Chapter 4: In this chapter, the problem of determining the electron states in semiconductor quantum wires in a self-consistent way is revisited. For that purpose, it is numerically solved the 2D system of coupled Schrödinger and Poisson equations within the envelope function and effective mass approximations. The calculation method uses the finite-element approach. Circle, square, triangle and pentagon geometries are considered for the wire cross-sectional shape. The features of self-consistent band profiles and confined electron state spectra are discussed. Particular attention is paid to elucidate the origin of Friedel-like oscillations in the density of carriers at low temperatures.

Chapter 5: In this chapter, we review an out-of-equilibrium double-barrier resonant tunneling diode system (DBRTD), including the effect of donor density and external potentials in a self-consistent way. The calculation method uses the finite-element approach, as well as the Landauer formalism. Quasi-stationary states, transmission probability, current density, and conductance are discussed considering variations in the donor density and the width of the central well. Finally, a comparison of the simulation with an experimental double barrier system based on InGaAs with AlAs barriers reported in the literature has been obtained.

Chapter 6: In this chapter, the energy states of confined electrons in doped quantum structures with Razavy-like confining potentials are studied. The theoretical investigation is performed within the effective mass and parabolic band approximations, including the influence of externally applied electric and magnetic fields. We analyze the case of a Razavy quantum well and determine its conduction subband spectrum, focusing on the lowest energy levels and their probability densities. These properties have been numerically determined by

self-consistently solving the coupled system of Schrödinger, Poisson, and charge neutrality equations. Doping is introduced via an on-center δ-like layer. In order to evaluate the associated total (linear plus nonlinear) optical absorption coefficient, we have calculated the corresponding diagonal and off-diagonal electric dipole matrix elements, the main energy separation, and the occupancy ratio which are the main factors governing the variation of this optical response. As an extension of the self-consistent method to a two-dimensional problem, the energy states of a quantum wire system of circular cross section, with internal doping and Razavy potential have been calculated. The response of eigenvalues, self-consistent potentials and electron densities is studied with the variation of δ-doping layer width and of the donor density. Finally, the origin of Friedel-like oscillations, that arise in the density profile, generated by the occupation of internal and surface electronic states has been explained.

Chapter 7: In this chapter, a finite periodic superlattice is studied, analyzing the probability of electronic transmission for two types of semiconductor materials, GaAs/AlGaAs and InSe/InP. The changes in the maxima of the quasistationary states for both materials are discussed, making variations in the number of periods of the superlattice and its shape by means of geometric parameters. The effect of a nonresonant intense laser field has been included to analyze the changes in the electronic transport properties.

Contents

List of symbols

Abbreviations

Abbreviation	**Name**
QD	Quantum dot
QW	Quantum well
QWs	Quantum wires
RTD	Resonant tunneling diode
NDR	Negative differential resistance
$TOAC$	Total optical absorption coefficient
FEM	Finite element method
SLs	Superlattices
ILF	Intense laser field

1. Introduction

In the last fifty years, experimental developments have evolved significantly, mainly in techniques for the growth of semiconductor heterostructures [1–4], which has allowed the possibility of creating devices based on low-dimensional systems such as quantum wells, quantum wires or quantum dots [5–7]. Nowdays, it is possible to generate and characterize structures, more complex forms, of various materials that make it possible to implement them in devices for fields such as microelectronics, medicine, engineering, telecommunications, etc [8–11].

In the same way, the theoretical models increasingly take into account more variables in the problems to get closer to the experimental results in a more meaningful way, which leads to much more complex differential equations that in many cases can be addressed through the implementation of numerical methods such as the finite element method (FEM) through softwares such as COMSOL Multiphysics [12–15] that are increasingly popular in different fields of applied physics. Through this and other numerical techniques, impurity problems in low-dimensional heterostructures have been addressed and in more recent works the response of these systems to the action of an intense non-resonant laser field has been analyzed, finding interesting results regarding the modification of electronic and optical properties [16, 17].

In the field of electronic transport, due to the need of having devices that can work at frequencies of the order of Tera Hertz, we work from a theoretical point of view in the characterization of the properties through the Landauer formalism combined with Green's function methods and the Schrödinger equation to reproduce current-voltage curves that are measured experimentally [18, 19]. As examples of these are resonant tunneling devices such as diodes that, depending

on certain geometric characteristics or materials, can present regions of negative differential resistance that are useful in applications to electronics [20, 21].

Three-dimensional confinement systems like quantum dots can be formed by joining two or more materials of different gap, this leads to discrete energy levels. The importance of this type of systems is the strong dependence of these energy levels on the shape, size, composition or the application of external fields. A consequence of this is the direct modification of the semiconductor properties such as optical, mechanical, electrical, among others. In the last thirty years, quantum wires of various geometric shapes have been extensively studied [22–25], in particular cylindrical systems [26] since under certain conditions they can modify the electronic confinement regime, for this reason they are sometimes referred to as quantum-well wires. In recent years, experimental techniques have allowed the synthesis of conical-shaped structures [27], it has been shown that these structures have interesting physical properties that can be attractive for modern technological applications and can be considered as potential candidates for the development of devices to nanometric scale [28, 29], one of these properties is the quality of the system to behave like a quantum wire, a quantum well or a quantum dot depending on geometric characteristics [30]. For approximately fifteen years, works related to the characterization of conical and cylindrical quantum wires from the point of view of light absorption or response to magnetic fields have emerged [31, 32]. An incentive to study QDs mainly based on materials such as CdSe and CdTe are their possibilities for potential applications in spintronic devices and memory systems [33].

In this way, the electron, shallow-donor impurity, and heavy-hole exciton states for two kinds of conical QDs are studied: *i*), shallow-donor impurity states in truncated conical shaped GaAs-(Ga,Al)As QDs, which can be modeled through a Coulomb interaction, in the simple model of a hydrogenic atom and considering the effects of an externally applied magnetic field. *ii*) CdSe-CdTe core/shell QDs without magnetic field and impurity effects. Once the wavefunctions and energies for electron and hole are available, in the presence or absence of impurity, the correlation between both carriers is calculated using the Coulomb

integral together with a first-order perturbative model. The calculations for different donor impurity positions along the symmetry-axis, considering the effects of the magnetic field and the side of the structure (i) are carried out. Finally, the overlap integral is reported, information that is key to understanding the behavior of the binding energies for each configuration (i and ii).

Another type of low-dimensional structures are the quantum wires (QWs), which are systems with strong two-dimensional localization of charge carriers, leaving a single spatial direction for their displacement. This feature leads to the quantization of the energy levels for the motion along the cross-section of the structure. The beginnings of research on this type of structures date back to the 1980s [37–42], currently there is a considerable number of experimental and theoretical reports in the literature [43–46].

When considering an internal donor density of QWs, it is convenient to solve the problem by means of a self-consistent method (SC). This method is very useful to determine the spectrum of electron in low-dimensional semiconductor nanostructures when many-body contributions on the energy band profile are taken into account. In this way, it is possible to mention initial works by Laux and coworkers [47, 48]. In the Laux work, the electron states in narrow gate-induced channels in a one-dimensional Si conduction channel are self-consistently determined solutions. In the second one, the electron states were calculated by solving the Schrödinger-Poisson (SP) system of equations in a split-gate quasi-one-dimensional GaAs/AlGaAs heterostructure.

At this same time, that is, in the decade of the 80s, M. Razavy used double potential wells in the quantum theory of molecules to describe the motion of a particle in the presence of two force fields [49]. These types of potentials are known today as Razavy potentials [50, 51], and are used as a model to describe the coupling of two molecules or quantum dots [52–55]. Effects of intense laser field and position dependent effective mass in Razavy-like quantum wells were investigated in Ref. [56].

In the year 2000 Trellakis *et al.* [57] discusses the computational issues in the SC simulation of the electronic features of QWs. The authors discuss the numerical solution for the coupled SP equation system and developed an iteration procedure based on the predictor-corrector method for convergence of the iteration. The coupled SP equations, have been solved by Proetto for a GaAs quantum wire with cylindrical symmetry within the Hartree approximation [58]. In this work, the potential profile and electronic structure dependence on the wire radius and surface states concentration were discussed. In 2019 Popescu *et al.* [59] used the finite element method to calculate the energies and probability densities for an electron confined in a two-dimensional quantum dots, the shape of this system was a regular polygon where the number of sides has varied from three (triangle) to infinity (circle). They found that for very large systems, the shape may not be as important as the size is.

In this work, the effect of the QW cross-section shape by considering the circle, square, triangle, and pentagon geometries are studied. By using the effective mass approximation, we study an electron confined in an infinite GaAs QW and infinite confinement potential added to an electrostatic potential at the boundary caused by the fact of having the system with exposed borders. The energy levels in each of the structures with different cross-sections as a function of the transversal area, the doping donor density, and the temperature are reported. The oscillations that appear in electron density at low temperatures and the contribution percentage made by each of the confined electron states to such oscillations are discussed.

On the other hand, motivated by Razavy's work of 1980, we investigate the effects of the concentration of an on-center thin doping layer and of externally applied electric and magnetic fields on the total optical absorption coefficient in Razavy-like GaAs quantum structures. In a first development we develop the one-dimensional problem of a GaAs δ-doped quantum well having a Razavy-type confinement potential. For this system, the confined electronic states are calculated, as well as the self-consistent potentials, with a special care taken on determining the Fermi level position, affected by the both temperature and ioni-

zed impurity distribution. The second problem dealt with is a two-dimensional system corresponding to a GaAs quantum wire with circular cross section and exposed borders, with an additional δ-type doping and an inner Razavy-like potential. The problem for the electron energy states in this case is also solved in a self-consistent way, taking into account a fundamental difference: In this case the Fermi level is no longer modified by the density of donors because the system has exposed borders. So, a "Fermi Level Pinning" is presented which keeps it fixed.

Regarding one-dimensional confinement systems, Resonant Tunneling Diodes (RTDs) should be highlighted, these are semiconductor devices that consist of a system of two or more potential barriers that allow the transport of electrons only for certain states known as resonant states. The operating mechanism is fundamentally based on the tunneling effect of quantum mechanics. This type of system is characterized by developing one or more negative differential resistance (NDR) zones that are the central particularity of RTDs that permit a various application.

From the experimental point of view, these devices are developed in very thin layers, enabling them for applications even in the terahertz range [60–62]. The first investigations in this field were carried out around the 1950s from the theoretical point of view, later, after the development of experimental epitaxial growth techniques, between 1970 and 1980, there was an increase in the production of experimental work [63–68]. Of course, since that time the experimental techniques have been becoming more sophisticated, to mention some of the current work in this area, the following references are included [69–73]. The resonant tunneling effect is not only possible in double barrier systems, this feature is also present in multi-barrier systems or superlattices (SLs), in 2020 Mehmet Bati studied the effects of an intense laser field on the properties of resonant tunneling in a double-well structure parabolic reverse triple barrier system implementing the method of finite differences combined with the Green function formalism to calculate the transmission functions, obtaining as a conclusion that the increment of the well width causes the incident electron waves

to be localized. Consequently, the transmittance decreases, and the resonant peak becomes small or disappear [74].

At present, the SLs of semiconductor materials continue to be studied either to understand excitations in the system or to analyze the response under external fields. In works such as that from Komatsu *et al.* [75], the authors analyzed the intensity of exciton photoluminescence in the presence of an external magnetic field in a GaAs SL. In this type of material, the study of structural properties is of great importance since it is possible to tune electronic properties that lead to the optical response of the system. In 2004, Jeong *et al.* [76] studied these properties in a GaAs/AlGaAs SL layer on InAs quantum dots by means of photoluminescence, photoreflectance spectroscopy, and transmission electron microscopy. Their results showed that the wavelength of the quantum dots was effectively tailored by the high potential barriers. The effect of the interface on the modulation-doped of the SL-type heterostructures can considerably modify the electronic properties in n-doped and p-doped systems. This effect was studied by Bezerra *et al.* [77], finding that the presence of graded interfaces modifies the carrier confinement inside of the GaAs quantum well. When the semiconductor system is subjected to the action of external magnetic fields, it is possible to modify the properties of electronic transport, in particular, the current-voltage curves, or to generate the appearance of Magnetoresistance oscillations [78, 79].

In this work, we analyze the effect of charge redistribution and electron density in the system out of equilibrium to obtain in this way the profile at the bottom of the self-consistent conduction band, first, for a double barrier system. This profile act as an input parameter for the potential term in the Schrödinger equation considering open boundary conditions, this equation as well as the Poisson equation are solved to obtain a set of quasi-stationary states and probabilities of electronic transmission in the system, finally with these transmission functions the Landauer formalism is implemented for the calculation of the density current and conductance. In this first study we report the self-consistent potentials, quasi-stationary electronic states, tunneling currents, and conduc-

tances for different widths of the central well and different donor densities, then a comparison is made between theoretical results of this procedure with recently reported experimental results. In a second work, the transport properties of a finite periodic lattice are studied. We are particularly interested in studying the tunneling current considering geometric variations of the heterostructure for two different combinations of the semiconductor materials, GaAs/AlGaAs and InSe/InP. The current due to the tunneling of electrons from the emitter to the collector, generated by a potential difference between the terminals of the device, is calculated. The power due to the diffusion of charge carriers and the effects of a nonresonant intense laser field (ILF) on the conduction band profile and, therefore, on the conduction current are also studied.

In most of the studied systems, obtaining an analytical solution for the Schrödinger equation is practically impossible, and in fact the possibility of obtaining analytical solutions in systems of interest is very limited. This fact makes it necessary to implement of numerical methods for the solution of differential equations involved in the description of the properties of semiconductor systems. Some of these methods can be variational, perturbative, finite differences, finite elements, diagonalization, among others. Particularly, the results presented in this work are obtained through the implementation of the finite element method (FEM) that has proven to be very effective in obtaining the solution to the differential equations that arise in the analysis of electronic properties in structural problems, deformations, impurities, transport, among others [80–82]. In all the problems, the effective mass approximation for electrons has been used [83, 84], considering for the wave function, the boundary conditions imposed according to the Bendaniel duke theory [85].

The thesis order is as follows: the next chapter is devoted to the theoretical framework. Chapter 3 contains an study of the shallow-donor impurity states with excitonic contribution in GaAs/AlGaAs and CdTe/CdSe truncated conical quantum dots under applied magnetic field. Chapter 4 is an study of the electronic properties of GaAs Quantum Well-Wires using the self-consistent Schrödinger-Poisson method. Chapter 5 contains the study of electronic and

transport properties in double barrier resonant tunneling systems. Chapter 6 shows results for the electro-transport properties in GaAs/AlGaAs and InSe/InP finite superlattices under the effect of nonresonant intense laser field. Finally, general conclusions are included.

1.1. General objective

Calculate and analyze the electronic, optical and transport properties in low dimensional systems under the action of external fields.

1.1.1. Specific objectives

- To studying the effects of the geometrical parameters on the electron and hole states in two truncated conical core-shell quantum dots based on GaAs-(Ga,Al)As and CdSe-CdTe, in the presence of a shallow-donor impurity and under an applied magnetic field.

- Analyze the problem of the electron states, electron density in semiconductor quantum wires of different cross section (circle, triangle, square and pentagon) in a self-consistent way.

- Calculate the Quasi-stationary states, transmission probability, current density, and conductance in a Double Barrier Resonant Tunneling System considering geometric and donor density variations.

- Analyze a Razavy quantum well and determine its conduction subband spectrum and the optical absorption coefficient, including the effect of a doped delta layer and under the application of an external electric and magnetic field.

- Calculate the energy states of quantum wire system of circular cross section, with internal doping and Razavy potential and explain the origin of the oscillations in the electron density profile at low temperatures.

- To study the changes in the electronic transmission probability and the current-voltage characteristics in a finite superlattice of GaAs/AlGaAs and InSe/InP, considering geometric changes and the application of a nonresonant intense laser field.

References

[1] G. jaliel, R. K. Puddy, R. Sanchez, A. N. Jordan, B. Sothmann, I. Farrer, J. P. Griffiths, D. A. Ritchie, and C. G. Smith, *Experimental Realization of a Quantum Dot Energy Harvester*, Phys. Rev. Lett. **123**, 117701 (2019).

[2] J. R. I. Lee, R. W. Meulenberg, K. M. Hanif, H. Mattoussi, J. E. Klepeis, L. J. Terminello, and T. van Buuren, *Experimental Observation of Quantum Confinement in the Conduction Band of CdSe Quantum Dots*, Phys. Rev. Lett. **98**, 146803 (2007).

[3] S. Raymond, K. Hinzer, S. Fafard, and J. L. Merz, *Experimental determination of Auger capture coefficients in self-assembled quantum dots*, Phys. Rev. B **61**, R16331(R) (2000).

[4] N. Sircar and D. Bougeard, *Experimental investigation of the optical spin-selection rules in bulk Si and Ge/Si quantum dots*, Phys. Rev. B **89**, 041301(R) (2014).

[5] T. Hidouri, S. Nasr, and F. Saidi, *Experimental and theoretical study of novel BGaAs/GaAs single quantum well for photonic applications*, Vacuum **173**, 109182 (2020).

[6] A. Yumak, S. Goumri-Said, W. Khan, K. Boubaker, P. Petkova, *Doping-induced stability in vanadium-doped ZnO quantum well wires (QWW): Combination of DFT calculations within experimental measurements*, Solid State Sci. **57**, 33-37(2016).

[7] N. V. Agrinskaya, V. A. Berezovets, V. I. Kozub, *Temperature-dependent disorder and magnetic field driven disorder: Experimental observations for doped GaAs/AlGaAs quantum well structures*, Solid State Commun. **225**, 56-60(2016).

[8] E. Biolatti, I. D'Amico, P. Zanardi, and F. Rossi, *Electro-optical properties of semiconductor quantum dots: Application to quantum information processing*, Phys. Rev. B **65**, 075306 (2002).

[9] H. Hashiba, V. Antonov, L. Kulik, A. Tzalenchuk, P. Kleinschmid, S. Giblin, and S. Komiyama, *Isolated quantum dot in application to terahertz photon counting*, Phys. Rev. B **73**, 081310(R) (2006).

[10] S. De Rinaldis, I. D'Amico, E. Biolatti, R. Rinaldi, R. Cingolani, and F. Rossi, *Intrinsic exciton-exciton coupling in GaN-based quantum dots: Application to solid-state quantum computing*, Phys. Rev. B **65**, 081309(R) (2002).

[11] L. Schneebeli, T. Feldtmann, M. Kira, S. W. Koch, and N. Peyghambarian, *Zeno-logic applications of semiconductor quantum dots*, Phys. Rev. A **81**, 053852 (2010).

[12] A. Flores-Pacheco, R. López-Delgado, M. E. Álvarez-Ramos, *Determination of power conversion efficiency of CdTe QDs luminescent solar concentrators by analytic model and COMSOL photogeneration model*, Optik **248**, 168024 (2021).

[13] COMSOL *Multiphysics, v. 5.4*; COMSOL AB: Stockholm, Sweden, 2020.

[14] COMSOL *Multiphysics Reference Guide*; COMSOL: Stockholm, Sweden, 2012.

[15] COMSOL *Multiphysics Users Guide*; COMSOL: Stockholm, Sweden, 2012.

[16] E. Kasapoglu, S. Sakiroglu, H. Sari, I. Sökmen, and C. A. Duque, *Morse quantum well modulated by nonresonant intense laser field: Binding energy and optical absorption related to shallow donor impurities*, Optik **181**, 432-439 (2019).

[17] A. Radu, N. Eseanu, and A. Spandonide, *Tuning a conventional quantum well laser by nonresonant laser field dressing of the active layer*, Phys. Lett. A **378**, 3308-3314 (2014).

[18] H. Ness, L. K. Dash, and R. W. Godby, *Generalization and applicability of the Landauer formula for nonequilibrium current in the presence of interactions*, Phys. Rev. B **82**, 085426 (2010).

[19] M. Ashhadi and S. A. Ketabi, *Electronic transport properties through ZGNR/BNAM/ZGNR*, Phys. E: Low-Dimens. Syst. Nanostructures **46**, 250-253(2012).

[20] M. S. Krishna and S. Singh, *Disconnected N-doped zigzag ZnO nanoribbon for potential Negative Differential Resistance (NDR) applications*, Microelectronics J. **115**, 105204(2021).

[21] Jung-Hui Tsai, *High-performance AlInAs/GaInAs δ-doped HEMT with negative differential resistance switch for logic application*, Solid State Electron. **48**, 81-85 (2004).

[22] M. Cristea, E. C. Niculescu, C. R. Truşcă, *Optical non-linearities associated to hydrogenic impurities in InAs/GaAs self-assembled quantum dots under applied electric fields*. Philos. Mag. **97**, 3343-3360 (2017).

[23] E. C. Niculescu, C. Stan, M. Cristea, C. Truscă, *Magnetic-field dependence of the impurity states in a dome-shaped quantum dot*. Chem. Phys. **493**, 32-41 (2017).

[24] W. Zhou, J. J. Coleman, *Semiconductor quantum dots*. Curr. Opin. Solid St. M. **20**, 352-360 (2016).

[25] S. V. Gaponenko, H. V. Demir, *Applied Nanophotonics*, Cambridge University Press, Cambridge, p. 433 (2019).

[26] I. Mal, D. P. Samajdar, A. J. Peter, *Theoretical studies on band structure and optical gain of GaInAsN/GaAs/GaAs cylindrical quantum dot*. Superlattice Microst. **119**, 103-113 (2018).

[27] H.-M. Lin, Y.-L. Chen, J. Yang, Y.-C. Liu, K.-M. Yin, J.-J. Kai, F.-R. Chen, L.-C. Chen, Y.-F. Chen, C.-C. Chen, C.-C. *Synthesis and characterization of core-shell GaP@GaN and GaN@GaP nanowires*. Nano Lett. **3**, 537-541 (2003).

[28] S. Heedt, W. Prost, J. Schubert, D. Grützmacher, T. Schäpers, *Ballistic transport and exchange interaction in InAs nanowire quantum point contacts*. Nano Lett. **16**, 3116-3123 (2016).

[29] J. Tatebayashi, S. Kako, J. Ho, Y. Ota, S. Iwamoto, Y. Arakawa, *Room-temperature lasing in a single nanowire with quantum dots*. Nat. Photonics **9**, 501-505 (2015).

[30] A. Medvid, P. Onufrijevs, A. Mychko, *Properties of nanocones formed on a surface of semiconductors by laser radiation: quantum confinement effect of electrons, phonons, and excitons*. Nanoscale Res. Lett. **6**, 582 (2011).

[31] S. L. Diedenhofen, O.T.A. Janssen, G. Grzela, E.P.A.M. Bakkers, J. Gómez Rivas, *Strong geometrical dependence of the absorption of light in arrays of semiconductor nanowires*. ACS Nano **5**, 2316-2323 (2011).

[32] D. B. Hayrapetyan, E. M. Kazaryan, H. A. Sarkisyan, *Magneto-absorption in conical quantum dot ensemble: possible applications for QD LED*. Opt. Commun. **371**, 138-143 (2016).

[33] P. Kumar, *Semiconductor (CdSe and CdTe)quantum dot: synthesis, properties and applications*. Mater. Today-Proc. (2021).

[34] Y. Wang, J. Wang, H. Guo, *Magnetoconductance of a stadium-shaped quantum dot: a finite-element-method approach*. Phys. Rev. B **49**, 1928-1934 (1994).

[35] G. Jurczak, P. Dłużewski, *Finite element modelling of threading dislocation effect on polar GaN/AlN quantum dot*. Physica E **95**, 11-15 (2018).

[36] W.-M. Zhou, C.-Y. Wang, Y.-H. Chen, Z.-G. Wang, *Finite element analysis of stress and strain distributions in InAs/GaAs quantum dots*. Chinese Phys. **15**, 1315-1319 (2006).

[37] V. K. Arora, *Quantum size effect in thin-wire transport*. Phys. Rev. B **23**, 5611-5612 (1981).

[38] G. W. Bryant, *Hydrogenic impurity states in quantum-well wires.* Phys. Rev. B **29**, 6632-6639 (1984).

[39] S. Luryi, and F. Capasso, *Resonant tunneling of two-dimensional electrons through a quantum wire: A negative transconductance device.* Appl. Phys. Lett. **47**, 1347-1349 (1985); Erratum in **48**, 1693 (1986).

[40] K. B. Wong, M. Jaros, J. P. Hagon, *Confined electron states in GaAs-$Ga_{1-x}Al_xAs$ quantum wires.* Phys. Rev. B **35**, 2463-2466 (1987).

[41] D. S. Citrin, and Y. -C. Chang, *Valence-subband structures of $GaAs/Al_xGa_{1-x}As$ quantum wires: The effect of split-off bands.* Phys. Rev. B **40**, 5507-5514 (1989).

[42] T. Yamauchi, and Y. Arakawa, Y. *Tight binding analysis of GaAsAlGaAs quantum wire structures.* Superlattices Microstruct. **10**, 83-87 (1991).

[43] H. Kes, S. E. Okan, and S. Aktas, *The excitons in infinite potential centered multilayered coaxial quantum wire and the magnetic field effects on their properties.* Superlattices Microstruct. **139**, 106421 (2020).

[44] F. V. Boström, A. Tsintzis, M. Hell, and M. Leijnse, *Band structure and end states in InAs/GaSb core-shell-shell nanowires.* Phys. Rev. B **102**, 195434 (2020).

[45] R. Méndez-Camacho, R. Casta neda-Priego, and E. Cruz-Hernández, *Many-electron redistribution in n-doped semiconductor nanostructures under external electric field by using a center-of-mass approach.* Phys. Rev. B **102**, 035403 (2020).

[46] B. D. Woods, S. D. Sarma, and T. D. Stanescu, *Subband occupation in semiconductor-superconductor nanowires.* Phys. Rev. B **101**, 045405 (2020).

[47] S. E. Laux, and F. Stern, *Electron states in narrow gate-induced channels in Si.* Appl. Phys. Lett. **49**, 91-93 (1986).

[48] S. E. Laux, D. J. Frank, and F. Stern, *Quasi-one-dimensional electron states in a split-gate GaAs/AlGaAs heterostructure.* Surf. Sci. **196**, 101-106 (1988).

[49] M. Razavy, *An exactly soluble Schrödinger equation with a bistable potential*, Am. J. Phys. **48**, 285 (1980).

[50] M. Baradaran and H. Panahi, *Exact Solutions of a Class of Double-Well Potentials: Algebraic Bethe Ansatz*, Adv. High Energy Phys. **2017**, 8429863 (2017).

[51] H. Karayer, D. Demirhan, K. G. Atman, *Analytical exact solutions for the Razavy type potential*, Math Meth Appl Sci. **93**, 9185-9194 (2020).

[52] J. Feist, J. Galego, and F. J. García-Vidal, *Polaritonic Chemistry with Organic Molecules*, ACS Photonics **5**, 205–216 (2018).

[53] Y. E. Panfil, D. Shamalia, J. Cui, S. Koley, and U. Banin, *Electronic coupling in colloidal quantum dot molecules; the case of CdSe/CdS core/shell homodimers*, J. Chem. Phys. **151**, 224501 (2019).

[54] Z. Han, G. Czap, C. Xu, Chi-lun Chiang, D. Yuan, R. Wu, and W. Ho, *Probing Intermolecular Coupled Vibrations between Two Molecules*, Phys. Rev. Lett. **118**, 036801 (2017).

[55] X. Li, A. Mandal, and P. Huo, *Cavity frequency-dependent theory for vibrational polariton chemistry*, Nat. Commun. **12**, 1315 (2021).

[56] E. Kasapoglu, H. Sari, I. Sökmen, J. A. Vinasco, D. Laroze, and C. A. Duque, *Effects of intense laser field and position dependent effective mass in Razavy quantum wells and quantum dots*, Physica E **126**, 114461 (12pp) (2021).

[57] A. Trellakis, and U. Ravaioli, *Computational issues in the simulation of semiconductor quantum wires.* Comput. Method. Appl. Mech. Eng. **181**, 437-449 (2000).

[58] C. R. Proetto, *Self-consistent electronic structure of a cylindrical quantum wire.* Phys. Rev. B **45**, 11911 (1992).

[59] I. Popescu, M. Hristache, S.-S. Ciobanu, M. G. Barseghyan, J. A. Vinasco, A. L. Morales, A. Radu, and C. A. Duque, *Size or shape-what matters most at the nanoscale?* Comput. Mater. Sci. **165**, 13-22 (2019).

[60] E. R. Brown, J. R. Söderström, C. D. Parker, L. J. Mahoney, K. M. Molvar, and T. C. McGill, *Oscillations up to 712 GHz in InAs/AlSb resonant-tunneling diodes*, Appl. Phys. Lett. **58**, 2291-2293 (1991).

[61] T. Miyamoto, A. Yamaguchi, and T. Mukai, *Terahertz imaging system with resonant tunneling diodes*, Jpn. J. Appl. Phys. **55**, 032201 (6pp) (2016).

[62] M. Bezhko, S. Suzuki, and M. Asada, *Frequency increase in resonant-tunneling diode cavity-type terahertz oscillator by simulation-based structure optimization*, Jpn. J. Appl. Phys. **59**, 032004 (6pp) (2020).

[63] A. M. Andrews, H. W. Korb, N. Holonyak, C. B. Duke, and G. G. Kleiman, *Tunnel mechanisms and junction characterization in III-V tunnel diodes*, Phys. Rev. B **5**, 2273-2295 (1972).

[64] A. M. Andrews, H. W. Korb, N. Holonyak, C. B. Duke, and G. G. Kleiman, *Photosensitive impurity-assisted tunneling in Au-Ge-doped $Ga_{1-x}Al_xAs$ p-n diodes*, Phys. Rev. B **5**, 4191-4194 (1972).

[65] W. R. Frensley, *Transient response of a tunneling device obtained from the Wigner function*, Phys. Rev. Lett. **57**, 2853-2856 (1986).

[66] V. J. Goldman, D. C. Tsui, and J. E. Cunningham, *Observation of intrinsic bistability in resonant-tunneling structures*, Phys. Rev. Lett. **58**, 1256-1259 (1987).

[67] H. Yoshimura, J. N. Schulman, and H. Sakaki, *Charge accumulation in a double-barrier resonant-tunneling structure studied by photoluminescence and photoluminescence-excitation spectroscopy*, Phys. Rev. Lett. **64**, 2422-2425 (1990).

[68] M. Rahman and J. H. Davies, *Theory of intrinsic bistability in a resonant tunneling diode*, Semicond. Sci. Tech. **5**, 168-176 (1990).

[69] A. Belkadi, A. Weerakkody, and G. Moddel, *Demonstration of resonant tunneling effects in metal-double-insulator-metal (MI^2M) diodes*, Nat. Commun. **12**, 2925 (6pp) (2021).

[70] H. Qian, S. Li, S.-W. Hsu, C.-F. Chen, F. Tian, A. R. Tao, and Z. Liu, *Highly-efficient electrically-driven localized surface plasmon source enabled by resonant inelastic electron tunneling*, Nat. Commun. **12**, 3111 (7pp) (2021).

[71] H. Althib, *Effect of quantum barrier width and quantum resonant tunneling through InGaN/GaN parabolic quantum well-LED structure on LED efficiency*, Results Phys. **22**, 103943 (9pp) (2021).

[72] I. Ortega-Piwonka, O. Piro, J. Figueiredo, B. Romeira, and J. Javaloyes, *Bursting and excitability in neuromorphic resonant tunneling diodes*, Phys. Rev. Appl. **15**, 034017 (14pp) (2021).

[73] J. Encomendero, V. Protasenko, F. Rana, D. Jena, and H. G. Xing, *Fighting broken symmetry with doping: toward polar resonant tunneling diodes with symmetric characteristics*, Phys. Rev. Appl. **13**, 034048 (10pp) (2020).

[74] M. Bati, *The effects of the intense laser field on the resonant tunneling properties of the symmetric triple inverse parabolic barrier double-well structure*, Physica B **594**, 412314 (9pp) (2020).

[75] T. Komatsu, E. Kawahata, T. Karasawa, I. Akai, V. F. Aguekian, M. Nakayama, K. Uchida, and N. Miura, *Dynamical process of excitons under magnetic fields in GaAs/AlGaAs superlattices*, J. Lumin. **66**, 468-472 (1995).

[76] Y. Jeong, H. Choi, Y. Park, S. Hwang, J. -J. Yoon, J. Lee, J. -Y. Leem, and M. Jeon, *Structural and optical properties of GaAs/AlGaAs superlattice layer on InAs quantum dots*, J. Cryst. Growth **273**, 129-135 (2004).

[77] M. G. Bezerra, J. A. K. Freire, V. N. Freire, G. A. Farias, F. M. S. Lima, A. L. A. Fonseca, and O. A. C. Nunes, *Interface effects in modulation-doped GaAs/AlGaAs single quantum wells and superlattices*, Microelectron. J **36**, 359-361 (2005).

[78] L. Smrcka, P. Vaseka, P. Svoboda, N. A. Goncharuk, O. Pacherova, Y. Krupko, Y. Sheikin, and W. Wegscheider, *Magnetoresistance oscillations in*

GaAs/AlGaAs superlattices subject to in-plane magnetic fields, Physica E **34**, 632-635 (2006).

[79] Y. A. Mityagin, V. N. Murzin, and M. P. Telenkov, *Resonant tunneling in weakly coupled GaAs/AlGaAs superlattices in a transverse magnetic field: A probe of electronic distribution function*, Physica E **32**, 297-300 (2006).

[80] Y. Wang, J. Wang, and H. Guo, *Magnetoconductance of a stadium-shaped quantum dot: a finite-element-method approach.* Phys. Rev. B **49**, 1928-1934 (1994).

[81] G. Jurczak, and P. Dłużewski, *Finite element modelling of threading dislocation effect on polar GaN/AlN quantum dot.* Physica E **95**, *95*, 11-15 (2018).

[82] W. -M. Zhou, C. -Y. Wang, Y. -G. Chen, and Z. -G. Wang, *Finite element analysis of stress and strain distributions in InAs/GaAs quantum dots.* Chinese Phys. **15**, 1315-1319 (2006).

[83] W. Kohn, *Effective Mass Theory in Solids from a Many-Particle Standpoint*, Phys. Rev. **205**, 2 (1957).

[84] M. A. Green, *Intrinsic concentration, effective densities of states, and effective mass in silicon*, J. Appl. Phys. **67**, 2944 (1990).

[85] D. J. Bendaniel and C. B. Duke, *Space-Charge Effects on Electron Tunneling*, Phys. Rev. B **152**, 2 (1966).

2. General theoretical framework

2.1. Electronic transport in semiconductor systems

This section briefly demonstrates the equation for the tunneling current, better known as the Landauer formula [1, 2]. This equation is not only valid for semiconductor systems, it is also widely used for the calculation of transport properties through molecular systems [3, 4].

The starting point is the eigenvalue Schrödinger equation,

$$\hat{H}\ |\Psi\rangle = E\ |\Psi\rangle\,, \tag{2-1}$$

where $\hat{H}$ is the complete Hamiltonian of the system that accounts for the contacts through an operator $\hat{H}_L$ for the left contact and $\hat{H}_R$ for the right contact, the dispersion region or central region is characterized by the term $\hat{H}_C$, see Fig. **2-1**, E is the system energy and $|\Psi\rangle$ the wave function that has $|\Psi_i\rangle$ components with $i = [L, R, C]$ for each of the regions. With these considerations, the Eq. (2-1) can be written as,

$$\begin{bmatrix} \hat{H}_L & \hat{V}_{LC} & 0 \\ \hat{V}_{LC}^{\dagger} & \hat{H}_C & \hat{V}_{CR}^{\dagger} \\ 0 & \hat{V}_{CR} & \hat{H}_R \end{bmatrix} \begin{bmatrix} |\Psi_L\rangle \\ |\Psi_C\rangle \\ |\Psi_R\rangle \end{bmatrix} = E \begin{bmatrix} |\Psi_L\rangle \\ |\Psi_C\rangle \\ |\Psi_R\rangle \end{bmatrix}, \tag{2-2}$$

where the terms $\hat{V}_{LC}$ and $\hat{V}_{CR}$ represent the interaction between the left and right contract with the central region respectively. The Green's function of the

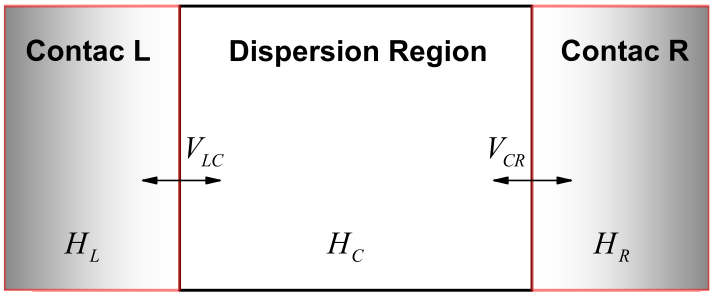

Figure 2-1.: System scheme characterized by the dispersion zone ($\hat{H}_C$) connected with each of the contacts on the left and right ($\hat{H}_L$ and $\hat{H}_R$).

system is defined as the function (operator) $\hat{G}$ which,

$$\left(E - \hat{H}\right) \hat{G} \equiv \hat{I}, \tag{2-3}$$

where $\hat{I}$ is the identity matrix. From Eqs. (2-2) and (2-3), we can write the complete Hamiltonian of the system in terms of the Green's matrix:

$$\begin{aligned}
&\begin{bmatrix} E - \hat{H}_L & -\hat{V}_{LC} & 0 \\ -\hat{V}_{LC}^{\dagger} & E - \hat{H}_C & -\hat{V}_{CR}^{\dagger} \\ 0 & -\hat{V}_{CR} & E - \hat{H}_R \end{bmatrix} \hat{G} = \hat{I}, \\
&\begin{bmatrix} E - \hat{H}_L & -\hat{V}_{LC} & 0 \\ -\hat{V}_{LC}^{\dagger} & E - \hat{H}_C & -\hat{V}_{CR}^{\dagger} \\ 0 & -\hat{V}_{CR} & E - \hat{H}_R \end{bmatrix} \begin{bmatrix} \hat{G}_L & \hat{G}_{LC} & \hat{G}_{LR} \\ \hat{G}_{CL} & \hat{G}_C & \hat{G}_{CR} \\ \hat{G}_{RL} & \hat{G}_{RC} & \hat{G}_R \end{bmatrix} = \begin{bmatrix} I & 0 & 0 \\ 0 & I & 0 \\ 0 & 0 & I \end{bmatrix},
\end{aligned} \tag{2-4}$$

doing the multiplication of the two matrices on the left, subsequently, extracting only the equations corresponding to the product with the second column of

matrix $\hat{G}$:

$$\begin{aligned}
&\left(E-\hat{H}_L\right)\hat{G}_{LC}-\hat{V}_{LC}\hat{G}_C=0,\\
&-\hat{V}_{LC}^{\dagger}\hat{G}_{LC}+\left(E-\hat{H}_C\right)\hat{G}_C-\hat{V}_{CR}^{\dagger}\hat{G}_{RC}=I,\\
&-\hat{V}_{CR}\hat{G}_C+\left(E-\hat{H}_R\right)\hat{G}_{RC}=0,
\end{aligned} \tag{2-5}$$

from the first equation in (2-5):

$$\begin{aligned}
&\left(E-\hat{H}_L\right)\hat{G}_{LC}=\hat{V}_{LC}\hat{G}_C,\\
&\hat{G}_{LC}=\left(E-\hat{H}_L\right)^{-1}\hat{V}_{LC}\hat{G}_C,\\
&\hat{G}_{LC}=\hat{G}_L\hat{V}_{LC}\hat{G}_C,
\end{aligned} \tag{2-6}$$

where the Green function associated with each contact had already been defined as:

$$\hat{G}_{L(R)}=\left(E-\hat{H}_{L(R)}\right)^{-1}, \tag{2-7}$$

Similarly, from the last of the equations in (2-5),

$$\begin{aligned}
&\left(E-\hat{H}_R\right)\hat{G}_{RC}=\hat{V}_{CR}\hat{G}_C,\\
&\hat{G}_{RC}=\hat{G}_R\hat{V}_{CR}\hat{G}_C.
\end{aligned} \tag{2-8}$$

Replacing (2-6) and (2-8) in the equation of the middle of (2-5),

$$\begin{aligned}
&-\hat{V}_{LC}^{\dagger}\hat{G}_L\hat{V}_{LC}\hat{G}_C+\left(E-\hat{H}_C\right)\hat{G}_C-\hat{V}_{CR}^{\dagger}\hat{G}_R\hat{V}_{CR}\hat{G}_C=I,\\
&\left(-\hat{V}_{LC}^{\dagger}\hat{G}_L\hat{V}_{LC}+\left(E-\hat{H}_C\right)-\hat{V}_{CR}^{\dagger}\hat{G}_R\hat{V}_{CR}\right)\hat{G}_C=I,
\end{aligned} \tag{2-9}$$

the terms $\hat{V}_{LC}^{\dagger}\hat{G}_L\hat{V}_{LC}\equiv\widehat{\Sigma}_L$ and $\hat{V}_{CR}^{\dagger}\hat{G}_R\hat{V}_{CR}\equiv\widehat{\Sigma}_R$ are known as the self-energies of the system,

$$\left(\hat{\Sigma}_L+\left(E-\hat{H}_C\right)-\hat{\Sigma}_R\right)\hat{G}_C=I, \tag{2-10}$$

where we obtain the Green's function associated with the central region

$$\hat{G}_C = \left(E - \hat{H}_C - \hat{\Sigma}_L - \hat{\Sigma}_R\right)^{-1}. \tag{2-11}$$

This equation indicates that the effect of the contacts on the device is to add the self-energies to the device Hamiltonian since when we calculate the Green's function on the device we just calculate the Green's function for the effective Hamiltonian $\hat{H}_{effective} = \hat{H}_C + \hat{\Sigma_L} + \hat{\Sigma}_R$.

Non-equilibrium system

When the system is non-equilibrium, electrons can pass through the central region due to the difference between the Fermi functions in both contacts, these inputs will enter as plane waves (incident waves). Therefore, we want to find the solutions corresponding to these incoming waves.

Consider contact L isolated from the other contacts and the device. At a certain energy we have a wavefunction corresponding to an incoming wave that is totally reflected at the end of the contact. We will denote this wavefunction with $|\psi_{L,n}\rangle$, where L is the contact name and n is a quantum number associated to several modes in the contacts.

For connecting the contacts to the device we can calculate the total wavefunction caused by the incoming wave in contact L (the incident electron acts as a disturbance in the central region). We note that a wavefunction has the form $|\psi_{L,n}\rangle + \left|\psi^R\right\rangle$ where $|\psi_{L,n}\rangle$ is the totally reflected wave and $\left|\psi^R\right\rangle$ is the retarded

response of the system. With them, the Schrödinger equation gives,

$$
\begin{aligned}
&\hat{H}\left(|\psi_{L,n}\rangle + \left|\psi^R\right\rangle\right) = E\left(|\psi_{L,n}\rangle + \left|\psi^R\right\rangle\right), \\
&\left(\hat{H}_L + \hat{H}_R + \hat{H}_C + \hat{V}_{LC} + \hat{V}_{LC}^\dagger + \hat{V}_{CR}^\dagger + \hat{V}_{CR}\right)\left(|\psi_{L,n}\rangle + \left|\psi^R\right\rangle\right) = \\
&E\left(|\psi_{L,n}\rangle + \left|\psi^R\right\rangle\right), \\
&\Big(\hat{H}_L|\psi_{L,n}\rangle + \hat{H}_R|\psi_{L,n}\rangle + \hat{H}_C|\psi_{L,n}\rangle + \hat{V}_{LC}|\psi_{L,n}\rangle + \hat{V}_{LC}^\dagger|\psi_{L,n}\rangle + \\
&\hat{V}_{CR}^\dagger|\psi_{L,n}\rangle + \hat{V}_{CR}|\psi_{L,n}\rangle\Big) + \hat{H}\left|\psi^R\right\rangle = E\left(|\psi_{L,n}\rangle + \left|\psi^R\right\rangle\right), \\
&\left(E|\psi_{L,n}\rangle + \hat{V}_{LC}^\dagger|\psi_{L,n}\rangle\right) + \hat{H}\left|\psi^R\right\rangle = E|\psi_{L,n}\rangle + E\left|\psi^R\right\rangle, \\
&E|\psi_{L,n}\rangle + \hat{V}_{LC}^\dagger|\psi_{L,n}\rangle + \hat{H}\left|\psi^R\right\rangle - E|\psi_{L,n}\rangle = E\left|\psi^R\right\rangle, \\
&\hat{H}\left|\psi^R\right\rangle = E\left|\psi^R\right\rangle - \hat{V}_{LC}^\dagger|\psi_{L,n}\rangle,
\end{aligned}
\tag{2-12}
$$

We see that $\left|\psi^R\right\rangle$ is the response of the system to a perturbation of $\hat{V}_{LC}^\dagger|\psi_{L,n}\rangle$. On the other hand, the last equation can be written in the form,

$$\left(E - \hat{H}\right)\left|\psi^R\right\rangle = \hat{V}_{LC}^\dagger|\psi_{L,n}\rangle, \tag{2-13}$$

from (2-3) we to see that,

$$\left(E - \hat{H}\right) = \hat{G}^{-1}, \tag{2-14}$$

replacing Eq. 2-14 in 2-13,

$$\hat{G}^{-1}\left|\psi^R\right\rangle = \hat{V}_{LC}^\dagger|\psi_{L,n}\rangle, \tag{2-15}$$

from this equation it is finally obtained,

$$\left|\psi^R\right\rangle = \hat{G}\hat{V}_{LC}^\dagger|\psi_{L,n}\rangle. \tag{2-16}$$

The Eq. (2-16) is a scattering state generated by the incident electron, using all possible incoming waves from each contact $|\psi_{L,n}\rangle$.

Secondly, the device wavefunction $|\psi_C\rangle$ in given by

$$|\psi_C\rangle = \hat{G}_C \hat{V}_{LC}^{\dagger} |\psi_{L,n}\rangle \,, \tag{2-17}$$

It is not difficult to show that the wavefunction in the R contact is given by,

$$\begin{aligned} |\phi_R\rangle &= \hat{G}_R(z)\hat{V}_{CR} |\phi_C\rangle = \hat{G}_R(z)\hat{V}_{CR}\hat{G}_C\hat{V}_{LC}^{\dagger} |\psi_{L,n}\rangle \,, \\ |\phi_R\rangle &= \hat{G}_R(z)\hat{V}_{CR}\hat{G}_C\hat{V}_{LC}^{\dagger} |\psi_{L,n}\rangle \,. \end{aligned} \tag{2-18}$$

Similarly, the wavefunction in the L contact is given by,

$$\begin{aligned} |\phi_L\rangle &= |\psi_{L,n}\rangle + \hat{G}_L(z)\hat{V}_{LC}\hat{G}_C\hat{V}_{LC}^{\dagger} |\psi_{L,n}\rangle \,, \\ |\phi_L\rangle &= \left(1 + \hat{G}_L(z)\hat{V}_{LC}\hat{G}_C\hat{V}_{LC}^{\dagger}\right) |\psi_{L,n}\rangle \,. \end{aligned} \tag{2-19}$$

Through the wave functions (2-17 - 2-19), in terms of the incident perturbation $|\psi_{L,n}\rangle$, it is possible to calculate the complete set solutions for the Schrödinger equation both in the contact regions L and R as well as in the central scattering region and analyze how the electrons that enter with a given energy can modify the properties of the system.

When calculating the electronic current through the system, it is necessary to know the charge density in each reservoir. For the system out of equilibrium, this quantity is different in each one. The starting point is to write the density matrix of the system,

$$\rho = \sum_k f(E_k, E_F) \, |\psi_k\rangle \langle\psi_k| \,, \tag{2-20}$$

The electronic occupation of the reservoirs can be measured by means of the Fermi-Dirac function in terms of the Fermi $E_{F,L(R)}$ level in each reservoir at a fixed temperature T,

$$f(E_k, E_{F,L}) = \frac{1}{1 + e^{(E_k - E_{F,L})/k_B T}}, \tag{2-21}$$

The sum in (2-20) runs over all occupied states given by (2-21).
The wavefunction on the device (Eq. (2-17)) generated by an incoming wave in contact L in a k mode is

$$|\psi_{C,k}\rangle = \hat{G}_C \hat{V}_{LC}^{\dagger} |\psi_{L,k}\rangle \,, \tag{2-22}$$

Adding over all states of contact L:

$$\rho_{C,L} = \int_{-\infty}^{\infty} \sum_k f(E, E_{F,L}) \, |\psi_{d,k}\rangle \, \langle\psi_{d,k}| \, \delta(E - E_k) dE, \tag{2-23}$$

by using (2-22) in 2-23,

$$\begin{aligned} \rho_{C,L} &= \int_{-\infty}^{\infty} \sum_k f\left(E, E_{F,L}\right) \hat{G}_C \hat{V}_{LC}^{\dagger} \, |\psi_{L,k}\rangle \, \langle\psi_{L,k}| \, \hat{V}_{LC} \hat{G}_C^{\dagger} \delta\left(E - E_k\right) dE, \\ \rho_{C,L} &= \int_{-\infty}^{\infty} f\left(E, E_{F,L}\right) \hat{G}_C \hat{V}_{LC}^{\dagger} \left(\sum_k \delta\left(E - E_k\right) |\psi_{L,k}\rangle \, \langle\psi_{L,k}| \right) \hat{V}_{LC} \hat{G}_C^{\dagger} dE, \end{aligned} \tag{2-24}$$

the term in parentheses is known as the spectral function and by definition, it is given by

$$\hat{D}(E) \equiv i(\hat{G}^{+} - \hat{G}^{-})/2\pi = \sum_k \delta\left(E - E_k\right) |\psi_{L,k}\rangle \, \langle\psi_{L,k}| \,, \tag{2-25}$$

where $\hat{G}^{+}$ and $\hat{G}^{-}$ are the leading and lagging Green's functions respectively. Taking into account the above, we get

$$\rho_{C,L} = \int_{-\infty}^{\infty} f(E, E_{F,L}) \hat{G}_C \hat{V}_{LC}^{\dagger} \hat{D}(E) \hat{V}_{LC} \hat{G}_C^{\dagger} dE, \tag{2-26}$$

it is possible to rewrite the integrand considering:

$$\begin{aligned}\hat{V}_{LC}^{\dagger}\hat{D}(E)\hat{V}_{LC} &= \hat{V}_{LC}^{\dagger}\left(i\frac{\hat{G}^{+}-\hat{G}^{-}}{2\pi}\right)\hat{V}_{LC} = \\ &= \frac{i}{2\pi}\left(\hat{V}_{LC}^{\dagger}\hat{G}^{+}\hat{V}_{LC}-\hat{V}_{LC}^{\dagger}\hat{G}^{-}\hat{V}_{LC}\right) = \frac{i}{2\pi}\left(\hat{\Sigma}_{L}^{+}-\hat{\Sigma}_{L}^{-}\right) \equiv \frac{1}{2\pi}\hat{\Gamma}_{L}\end{aligned} \tag{2-27}$$

The term $\hat{\Gamma}_L$ that appears in the last equality is a definition in terms of the selfenergies and corresponds to the coupling potential between the dispersion region with the contact of the region L. Replacing this result in (2-26),

$$\rho_{C,L} = \frac{1}{2\pi}\int_{-\infty}^{\infty} f(E,E_{F,L})\hat{G}_C\hat{\Gamma}_L\hat{G}_C^{\dagger}dE. \tag{2-28}$$

Similarly, an expression is obtained for the charge density associated with the R contact,

$$\rho_{C,R} = \frac{1}{2\pi}\int_{-\infty}^{\infty} f(E,E_{F,R})\hat{G}_C\hat{\Gamma}_R\hat{G}_C^{\dagger}dE. \tag{2-29}$$

The total charge density is a sum over the two contacts L and R, adding a factor of 2 by spin degeneration,

$$\begin{aligned}&\rho = 2\left(\rho_{C,L}+\rho_{C,R}\right),\\ &\rho = \frac{2}{2\pi}\left[\int_{-\infty}^{\infty} f\left(E,E_{F,L}\right)\hat{G}_C\hat{\Gamma}_L\hat{G}_C^{\dagger}dE + \int_{-\infty}^{\infty} f\left(E,E_{F,R}\right)\hat{G}_C\hat{\Gamma}_R\hat{G}_C^{\dagger}dE\right],\\ &\rho = \frac{1}{\pi}\int_{-\infty}^{\infty}\left[f\left(E,E_{F,L}\right)\hat{G}_C\hat{\Gamma}_L\hat{G}_C^{\dagger} + f\left(E,E_{F,R}\right)\hat{G}_C\hat{\Gamma}_R\hat{G}_C^{\dagger}\right]dE.\end{aligned} \tag{2-30}$$

Probability Current

Already at this point, it is possible to calculate the tunneling current that is generated by the electron population difference in both reservoirs, to derive

an expression of the current, let's use the temporal conservation of the total probability density in the complete system,

$$0 = \frac{\partial \sum_j |\psi_j|^2}{\partial t} = \sum_j \frac{\partial \langle\psi|j\rangle \langle j|\psi\rangle}{\partial t} = \sum_j \left(\frac{\partial \langle\psi|j\rangle}{\partial t} \langle j|\psi\rangle + \langle\psi|j\rangle \frac{\partial \langle j|\psi\rangle}{\partial t} \right), \tag{2-31}$$

by using the Schrödinger equation:

$$\begin{aligned} i\hbar \frac{\partial |\psi\rangle}{\partial t} &= \widehat{H}|\psi\rangle, \\ \langle j| i\hbar \frac{\partial |\psi\rangle}{\partial t} &= \langle j|\widehat{H}|\psi\rangle, \\ i\hbar \frac{\partial \langle j \mid \psi\rangle}{\partial t} &= \langle j|\widehat{H}|\psi\rangle, \\ \frac{\partial \langle j \mid \psi\rangle}{\partial t} &= -\frac{i}{\hbar} \langle j|\widehat{H}|\psi\rangle, \end{aligned} \tag{2-32}$$

and

$$\begin{aligned} -i\hbar \frac{\partial \langle\psi|}{\partial t} &= \langle\psi|\widehat{H}, \\ -i\hbar \frac{\partial \langle\psi|}{\partial t} |j\rangle &= \langle\psi|\hat{H}|j\rangle, \\ -i\hbar \frac{\partial \langle\psi \mid j\rangle}{\partial t} &= \langle\psi|\widehat{H}|j\rangle, \\ \frac{\partial \langle\psi \mid j\rangle}{\partial t} &= \frac{i}{\hbar} \langle\psi|\widehat{H}|j\rangle, \end{aligned} \tag{2-33}$$

replacing Eqs. (2-32) and (2-33) in (2-31), we get,

$$\begin{aligned} 0 &= \sum_j \left(\frac{i}{\hbar} \langle \psi | \hat{H} | j \rangle \langle j \mid \psi \rangle - \langle \psi \mid j \rangle \frac{i}{\hbar} \langle j | \hat{H} | \psi \rangle \right), \\ 0 &= \frac{i}{\hbar} \sum_j (\langle \psi | \hat{H} | j \rangle \langle j \mid \psi \rangle - \langle \psi \mid j \rangle \langle j | \hat{H} | \psi \rangle), \\ 0 &= \frac{i}{\hbar} \left(\langle \psi | \hat{H} \left[\sum_j |j\rangle \langle j \mid \psi \rangle \right] - \left[\sum_j \langle \psi \mid j \rangle \langle j | \right] \hat{H} | \psi \rangle \right), \end{aligned} \tag{2-34}$$

on the other hand, we see that:

$$|\psi_C\rangle = \left(\sum_j |j\rangle \langle j| \right) |\psi_C\rangle = \sum_j |j\rangle \langle j|\psi_C\rangle = \sum_j |j\rangle \psi_j = \sum_j |j\rangle \langle j|\psi\rangle , \tag{2-35}$$

$$\langle \psi_C| = \langle \psi_C| \left(\sum_j |j\rangle \langle j| \right) = \sum_j \langle \psi_C|j\rangle |j\rangle = \sum_j \psi_j^* |j\rangle = \sum_j \langle \psi|j\rangle |j\rangle . \tag{2-36}$$

Using these results in Eq. (2-34),

$$0 = \frac{i}{\hbar} \Big(\langle \psi | \hat{H} | \psi_C \rangle - \langle \psi_C | \hat{H} | \psi \rangle \Big) , \tag{2-37}$$

expanding $\hat{H}$,

$$0 = \frac{i}{\hbar} \Big(\langle \psi | \Big(\hat{H}_C + \hat{V}_{LC} + \hat{V}_{CR} \Big) | \psi_C \rangle - \langle \psi_C | \Big(\hat{H}_C + \hat{V}_{LC}^\dagger + \hat{V}_{CR}^\dagger \Big) | \psi \rangle \Big) , \tag{2-38}$$

$$
\begin{aligned}
0 &= \frac{i}{\hbar}\Big(\langle\psi|\hat{H}_C|\psi_C\rangle + \langle\psi|\hat{V}_{LC}|\psi_C\rangle + \langle\psi|\hat{V}_{CR}|\psi_C\rangle - \langle\psi_C|\hat{H}_C|\psi\rangle - \langle\psi_C|\hat{V}_{LC}^{\dagger}|\psi\rangle - \\
&\quad \langle\psi_C|\hat{V}_{CR}^{\dagger}|\psi\rangle \Big), \\
0 &= \frac{i}{\hbar}\Big(E_C\langle\psi|\psi_C\rangle + \langle\psi|\hat{V}_{LC}|\psi_C\rangle + \langle\psi|\hat{V}_{CR}|\psi_C\rangle - E_C\langle\psi_C|\psi\rangle - \langle\psi_C|\hat{V}_{LC}^{\dagger}|\psi\rangle - \\
&\quad \langle\psi_C|\hat{V}_{CR}^{\dagger}|\psi\rangle \Big), \\
0 &= \frac{i}{\hbar}\Big(\langle\psi|\hat{V}_{LC}|\psi_C\rangle + \langle\psi|\hat{V}_{CR}|\psi_C\rangle - \langle\psi_C|\hat{V}_{LC}^{\dagger}|\psi\rangle - \langle\psi_C|\hat{V}_{CR}^{\dagger}|\psi\rangle \Big), \\
0 &= \frac{i}{\hbar}\Big\{ \langle\psi_L|\hat{V}_{LC}|\psi_C\rangle - \langle\psi_C|\hat{V}_{LC}^{\dagger}|\psi_L\rangle\Big\} + \frac{i}{\hbar}\Big\{ \langle\psi_R|\hat{V}_{CR}|\psi_C\rangle - \langle\psi_C|\hat{V}_{CR}^{\dagger}|\psi_R\rangle\Big\}.
\end{aligned}
\tag{2-39}
$$

The term in the first bracket correspond to the incoming probability current into the device from contact L and the second bracket from contact R.
For an arbitrary contact k, the electric current is given by the product between the electron charge $-e$ and the probability current:

$$
i_k = -\frac{i\,e}{\hbar}\Big\{ \langle\psi_k|\hat{V}_{Ck}|\psi_C\rangle - \langle\psi_C|\hat{V}_{Ck}^{\dagger}|\psi_k\rangle\Big\}. \tag{2-40}
$$

i_k is positive for a current from the contacts into the device.
To calculate the total tunneling current through the device we need to put all the contributions together in the wavefunction of the device and the contacts ($|\psi_L\rangle, |\psi_C\rangle, |\psi_R\rangle$) given by Eqs. (2-17 - 2-19)

$$
\begin{aligned}
i_{L\to R} &- \frac{i\,e}{\hbar}\Big\{ \langle\psi_R|\hat{V}_{CR}|\psi_C\rangle - \langle\psi_C|\hat{V}_{CR}^{\dagger}|\psi_R\rangle\Big\}, \\
i_{L\to R} &= -\frac{i\,e}{\hbar}\Big\{ \langle\psi_R|\hat{V}_{CR}\hat{G}_C\hat{V}_{LC}^{\dagger}|\psi_{L,n}\rangle - \langle\psi_{L,n}|\hat{V}_{LC}\hat{G}_C^{\dagger}\hat{V}_{CR}^{\dagger}|\psi_R\rangle\Big\}, \\
i_{L\to R} &= -\frac{i\,e}{\hbar}\langle\psi_{L,n}|\hat{V}_{LC}\hat{G}_C^{\dagger}\hat{V}_{CR}^{\dagger}\Big\{\hat{G}_R^{\dagger} - \hat{G}_R\Big\}\hat{V}_{CR}\hat{G}_C\hat{V}_{LC}^{\dagger}|\psi_{L,n}\rangle,
\end{aligned}
\tag{2-41}
$$

On the other hand, from Eq. (2-27),

$$
\begin{aligned}
\hat{\Gamma}_R &= i\left[\hat{\Sigma}_R^+ - \hat{\Sigma}_R^-\right], \\
\hat{\Gamma}_R &= i\left[\hat{V}_{CR}^\dagger \hat{G}_R^\dagger \hat{V}_{CR} - \hat{V}_{CR}^\dagger \hat{G}_R^- \hat{V}_{CR}\right], \\
\hat{\Gamma}_R &= i\hat{V}_{CR}^\dagger \left[\hat{\mathrm{G}}_R^\dagger - \hat{\mathrm{G}}_R^-\right] \hat{V}_{CR}, \\
-i\hat{\Gamma}_R &= \hat{V}_{CR}^\dagger \left[\hat{\mathrm{G}}_R^\dagger - \hat{\mathrm{G}}_R^-\right] \hat{V}_{CR}, \\
-i\hat{\Gamma}_R &= \hat{V}_{CR}^\dagger \left[\hat{\mathrm{G}}_R^\dagger - \left[\hat{\mathrm{G}}_R^\dagger\right]^\dagger\right] \hat{V}_{CR}, \\
-i\hat{\Gamma}_R &= \hat{V}_{CR}^\dagger \left[\hat{G}_R - \left[\hat{G}_R\right]^\dagger\right] \hat{V}_{CR}, \\
i\hat{\Gamma}_R &= \hat{V}_{CR}^\dagger \left[\hat{G}_R^\dagger - \hat{G}_R\right] \hat{V}_{CR},
\end{aligned}
\tag{2-42}
$$

Replacing these result in the expression for $i_{L\to R}$, we get,

$$
\begin{aligned}
i_{L\to R} &= -\frac{i\,e}{\hbar} \langle \psi_{L,n} | \hat{V}_{LC} \hat{G}_C^\dagger \left\{ i\hat{\Gamma}_R \right\} \hat{G}_C \hat{V}_{LC}^\dagger | \psi_{L,n} \rangle \,, \\
i_{L\to R} &= \frac{e}{\hbar} \langle \psi_{L,n} | \hat{V}_{LC} \hat{G}_C^\dagger \hat{\Gamma}_R \hat{G}_C \hat{V}_{LC}^\dagger | \psi_{L,n} \rangle \,.
\end{aligned}
\tag{2-43}
$$

This equation correspond to the current into the device from an electron incident ($|\psi_{L,n}\rangle$) of one energy (E) and one mode n in contact L through the coupling defined by $\hat{V}_{CR}$. Adding over the n modes and considering that the electrons enter through the reservoir L,

$$
i_{L\to R}(E) = \frac{2e}{\hbar} f(E, E_{F,L}) \sum_n \delta(E - E_n) \langle \psi_{L,n} | \hat{V}_{LC} \hat{G}_C^\dagger \hat{\Gamma}_R \hat{G}_C \hat{V}_{LC}^\dagger | \psi_{L,n} \rangle \,,
$$

(2 is for spin), adding up all the possible energies of the incident wave E,

$$
\begin{aligned}
I_{L\to R} &= \frac{2e}{\hbar}\int_{-\infty}^{\infty} f\left(E,E_{F,L}\right)\sum_n \delta\left(E-E_n\right)\,\langle\psi_{L,n}|\hat{V}_{LC}\hat{G}_C^{\dagger}\hat{\Gamma}_R\hat{G}_C\hat{V}_{LC}^{\dagger}|\psi_{L,n}\rangle\,dE,\\
&= \frac{2e}{\hbar}\int_{-\infty}^{\infty} f\left(E,E_{F,L}\right)\sum_n \delta\left(E-E_n\right)\,\langle\psi_{L,n}|\hat{V}_{LC}\hat{I}\hat{G}_C^{\dagger}\hat{\Gamma}_R\hat{G}_C\hat{V}_{LC}^{\dagger}|\psi_{L,n}\rangle\,dE,\\
&= \frac{2e}{\hbar}\int_{-\infty}^{\infty} f\left(E,E_{F,L}\right)\sum_n \delta\left(E-E_n\right)\\
&\langle\psi_{L,n}|\hat{V}_{LC}\left(\sum_m |m\rangle\langle m|\right)\hat{G}_C^{\dagger}\hat{\Gamma}_R\hat{G}_C\hat{V}_{LC}^{\dagger}|\psi_{L,n}\rangle\,dE,\\
&= \frac{2e}{\hbar}\int_{-\infty}^{\infty} f\left(E,E_{F,L}\right)\sum_{n,m} \delta\left(E-E_n\right)\,\langle\psi_{L,n}|\hat{V}_{LC}\,|m\rangle\langle m|\,\hat{G}_C^{\dagger}\hat{\Gamma}_R\hat{G}_C\hat{V}_{LC}^{\dagger}|\psi_{L,n}\rangle\,dE,\\
&= \frac{2e}{\hbar}\int_{-\infty}^{\infty} f\left(E,E_{F,L}\right)\sum_{n,m} \delta\left(E-E_n\right)\,\langle m|\hat{G}_C^{\dagger}\hat{\Gamma}_R\hat{G}_C\hat{V}_{LC}^{\dagger}|\psi_{L,n}\rangle\,\langle\psi_{L,n}|\hat{V}_{LC}|m\rangle\,dE,\\
&= \frac{2e}{\hbar}\int_{-\infty}^{\infty} f\left(E,E_{F,L}\right)\sum_{n,m} \langle m|\hat{G}_C^{\dagger}\hat{\Gamma}_R\hat{G}_C\hat{V}_{LC}^{\dagger}\delta\left(E-E_n\right)|\psi_{L,n}\rangle\,\langle\psi_{L,n}|\hat{V}_{LC}|m\rangle\,dE,\\
&= \frac{2e}{\hbar}\int_{-\infty}^{\infty} f\left(E,E_{F,L}\right)\\
&\sum_{n,m}\langle m|\hat{G}_C^{\dagger}\hat{\Gamma}_R\hat{G}_C\hat{V}_{LC}^{\dagger}\left\{\delta\left(E-E_n\right)|\psi_{L,n}\rangle\,\langle\psi_{L,n}|\right\}\hat{V}_{LC}|m\rangle\,dE,\\
&= \frac{2e}{\hbar}\int_{-\infty}^{\infty} f\left(E,E_{F,L}\right)\\
&\sum_{m}\langle m|\hat{G}_C^{\dagger}\hat{\Gamma}_R\hat{G}_C\hat{V}_{LC}^{\dagger}\left\{\sum_n \delta\left(E-E_n\right)|\psi_{L,n}\rangle\,\langle\psi_{L,n}|\right\}\hat{V}_{LC}|m\rangle\,dE,
\end{aligned}
\tag{2-44}
$$

by using Eq. (2-25),

$$\begin{aligned}
I_{L\to R} &= \frac{2e}{\hbar}\int_{-\infty}^{\infty} f\left(E,E_{F,L}\right)\sum_{m}\langle m|\hat{G}_C^{\dagger}\hat{\Gamma}_R\hat{G}_C\left(\frac{1}{2\pi}\hat{\Gamma}_L\right)|m\rangle\, dE,\\
I_{L\to R} &= \frac{2e}{\hbar}\frac{1}{2\pi}\int_{-\infty}^{\infty} f\left(E,E_{F,L}\right)\sum_{m}\langle m|\hat{G}_C^{\dagger}\hat{\Gamma}_R\hat{G}_C\hat{\Gamma}_L|m\rangle\, dE,\\
I_{L\to R} &= \frac{e}{\pi\hbar}\int_{-\infty}^{\infty} f\left(E,E_{F,L}\right)\sum_{m}\langle m|\hat{G}_C^{\dagger}\hat{\Gamma}_R\hat{G}_C\hat{\Gamma}_L|m\rangle\, dE,\\
I_{L\to R} &= \frac{e}{\pi\hbar}\int_{-\infty}^{\infty} f\left(E,E_{F,L}\right)\mathrm{Tr}\left(\hat{G}_C^{\dagger}\hat{\Gamma}_R\hat{G}_C\hat{\Gamma}_L\right)dE,
\end{aligned} \tag{2-45}$$

to get the total current through the device the current is given by,

$$I = I_{L\to R} - I_{R\to L}, \tag{2-46}$$

$$I = \frac{e}{\pi\hbar}\int_{-\infty}^{\infty}\left\{f\left(E,E_{F,L}\right) - f\left(E,E_{F,R}\right)\right\}\mathrm{Tr}\left(\hat{G}_C^{\dagger}\hat{\Gamma}_R\hat{G}_C\hat{\Gamma}_L\right)dE. \tag{2-47}$$

The transmission in the system can be calculated by means of the Green's functions according to the relation known as the Fischer-Lee relationship [5],

$$\mathcal{T}(E) = \mathrm{Tr}\left(\hat{G}_C^{\dagger}\hat{\Gamma}_R\hat{G}_C\hat{\Gamma}_L\right). \tag{2-48}$$

From the above, an expression for the electronic tunneling current is finally obtained in terms of the difference in electronic population in both reservoirs and the probability transmission through the system,

$$I = \frac{e}{\pi\hbar}\int_{-\infty}^{\infty}\left\{f\left(E,E_{F,L}\right) - f\left(E,E_{F,R}\right)\right\}\mathcal{T}(E)dE. \tag{2-49}$$

The Eq. (2-49) is known as the Landauer formula for tunneling current and is necessary to calculate transport properties through semiconductor structures or molecular systems.

2.2. Optical absorption theory

Consider a two-level system with $|a\rangle$ and $|b\rangle$ corresponding to the low and high level, respectively in a monochromatic electromagnetic radiation presence of frequency ω (classic field), which is a coupling field with these states. The most common approach to tackle the problem of interaction of radiation with matter is that of the density matrix, whose time evolution is governed by the Liouville-Von Neumann equation [6] (including dissipation terms):

$$\frac{\partial \rho}{\partial t} = \frac{1}{i\hbar}\left[H_0 - ME(t), \rho\right] - \frac{1}{2}\left[\gamma(\rho - \rho^{(0)}) + (\rho - \rho^{(0)})\gamma\right], \tag{2-50}$$

where ρ is the density matrix, H_0 is unperturbed Hamiltonian of the system, i.e. without the resonant electromagnetic radiation, M is a dipole operator, $E(t)$ the electric field with frequency ω, $\rho^{(0)}$ is the density matrix for the unperturbed system, and γ is the phenomenological term that accounts for the dissipations in the system presented by the presence of impurities or electron-phonon and electron-electron interactions. γ can be considered as a diagonal matrix and its elements γ_{mm} correspond to the inverse of relaxation time for the $|m\rangle$ state.
The Hamiltonian H_0 has the eigenvalues E_a and E_b corresponding to the levels $|a\rangle$ and $|b\rangle$, respectively.
The electric field can be expressed as:

$$E(t) = Re\left(E_0\, e^{-i\omega t}\right) = \frac{1}{2}E_0\, e^{-i\omega t} + \frac{1}{2}E_0\, e^{i\omega t} = \widetilde{E}\, e^{-i\omega t} + \widetilde{E}\, e^{i\omega t}, \tag{2-51}$$

where E_0 denotes the amplitude of the field. The only nonzero matrix elements for the γ operator are:

$$\langle b|\gamma|b\rangle = \frac{1}{\tau_b} \quad \text{and} \quad \langle a|\gamma|a\rangle = \frac{1}{\tau_a}, \tag{2-52}$$

where τ_a and τ_b are the relaxation times for the states $|a\rangle$ and $|b\rangle$, respectively. One way to calculate the density matrix is by means of a perturbative method, expanding it in a power serie as:

$$\rho = \sum_n \rho^{(n)}, \tag{2-53}$$

the density matrix for zero order $\rho^{(0)}$ has only diagonal elements because the electronic population is located in each of the states and there are no interaction effects between them. The notations used for the n-order density matrix elements are: $\rho_{aa}^{(n)} = \langle a|\rho^{(n)}|a\rangle$, $\rho_{ab}^{(n)} = \langle a|\,\rho^{(n)}\,|b\rangle$, $\rho_{ba}^{(n)} = \langle b|\,\rho^{(n)}\,|a\rangle$, and $\rho_{bb}^{(n)} = \langle b|\rho^{(n)}|b\rangle$. Thus, ρ has the symmetric property $\rho_{ab}(t) = \rho_{ba}^{*}(t)$.
By expanding the commutator from Eq. (2-50):

$$\begin{aligned}\frac{\partial\rho}{\partial t} = \frac{1}{i\hbar}\left[(H_0 - ME(t))\rho - \rho(H_0 - ME(t))\right] \\ - \frac{1}{2}\left[\gamma(\rho - \rho^{(0)}) + (\rho - \rho^{(0)})\gamma\right],\end{aligned} \tag{2-54}$$

by substituting (2-53) into Eq. (2-54):

$$\begin{aligned}\sum_n \frac{\partial\rho^{(n)}}{\partial t} = \frac{1}{i\hbar}\left[(H_0 - ME(t))\sum_n \rho^{(n)} - \sum_n \rho^{(n)}(H_0 - ME(t))\right] \\ - \frac{1}{2}\left[\gamma\left(\sum_n \rho^{(n)} - \rho^{(0)}\right) + \left(\sum_n \rho^{(n)} - \rho^{(0)}\right)\gamma\right],\end{aligned} \tag{2-55}$$

and taking into account that

$$\sum_n \rho^{(n)} - \rho^{(0)} = \left(\rho^{(0)} + \rho^{(1)} + \rho^{(2)} + ...\right) - \rho^{(0)} = \rho^{(1)} + \rho^{(2)} + \rho^{(3)} + ... = \sum_n \rho^{(n+1)}, \tag{2-56}$$

this expression is substituted into Eq. (2-55)

$$\begin{aligned}\sum_n \frac{\partial\rho^{(n)}}{\partial t} = \frac{1}{i\hbar}\left[(H_0 - ME(t))\sum_n \rho^{(n)} - \sum_n \rho^{(n)}(H_0 - ME(t))\right] \\ - \frac{1}{2}\left[\gamma\sum_n \rho^{(n+1)} + \sum_n \rho^{(n+1)}\gamma\right].\end{aligned} \tag{2-57}$$

For the calculation of the first order absorption, it is sufficient to calculate the matrix element ρ_{ba}. Applying the states $\langle b|$ and $|a\rangle$ on the left and right in the

last equation, we obtain

$$\left\langle b\middle|\sum_n \frac{\partial\rho^{(n)}}{\partial t}\middle|a\right\rangle = \frac{1}{i\hbar}\left\langle b\middle|\sum_n \Big((H_0 - ME(t))\,\rho^{(n)} - \rho^{(n)}(H_0 - ME(t))\Big)\middle|a\right\rangle - \frac{1}{2}\left\langle b\middle|\gamma\sum_n \rho^{(n+1)} + \sum_n \rho^{(n+1)}\gamma\middle|a\right\rangle, \tag{2-58}$$

by using the distributing property:

$$\sum_n \frac{\partial}{\partial t}\left\langle b\middle|\rho^{(n)}\middle|a\right\rangle = \frac{1}{i\hbar}\sum_n\Bigg(\Big(\Big\langle b\Big|H_0\rho^{(n)}\Big|a\Big\rangle - \Big\langle b\Big|ME(t)\rho^{(n)}\Big|a\Big\rangle\Big) - \Big(\Big\langle b\Big|\rho^{(n)}H_0\Big|a\Big\rangle - \Big\langle b\Big|\rho^{(n)}ME(t)\Big|a\Big\rangle\Big)\Bigg) - \frac{1}{2}\Bigg(\sum_n\Big\langle b\Big|\gamma\rho^{(n+1)}\Big|a\Big\rangle + \sum_n\Big\langle b\Big|\rho^{(n+1)}\gamma\Big|a\Big\rangle\Bigg), \tag{2-59}$$

by using the completeness relation $|a\rangle\langle a| + |b\rangle\langle b| = \widehat{1}$ and substituting the corresponding energy values

$$\sum_n \frac{\partial}{\partial t}\left\langle b\middle|\rho^{(n)}\middle|a\right\rangle = \frac{1}{i\hbar}\sum_n\Bigg(\Big(E_b\rho_{ba}^{(n)} - \Big\langle b\Big|M(|a\rangle\langle a| + |b\rangle\langle b|)\rho^{(n)}\Big|a\Big\rangle E(t)\Big) - \Big(\rho_{ba}^{(n)}E_a - \Big\langle b\Big|\rho^{(n)}(|a\rangle\langle a| + |b\rangle\langle b|)M\Big|a\Big\rangle E(t)\Big)\Bigg) - \frac{1}{2}\Bigg(\sum_n\Big\langle b\Big|\gamma(|a\rangle\langle a| + |b\rangle\langle b|)\rho^{(n+1)}\Big|a\Big\rangle + \sum_n\Big\langle b\Big|\rho^{(n+1)}(|a\rangle\langle a| + |b\rangle\langle b|)\gamma\Big|a\Big\rangle\Bigg), \tag{2-60}$$

by distributing terms

$$\begin{aligned}\sum_n \frac{\partial \rho_{ba}^{(n)}}{\partial t} = \frac{1}{i\hbar}\sum_n \Bigg(& E_b \rho_{ba}^{(n)} - \left[\langle b|M|a\rangle \left\langle a\middle|\rho^{(n)}\middle|a\right\rangle + \langle b|M|b\rangle \left\langle b\middle|\rho^{(n)}\middle|a\right\rangle\right] E(t) \\ & - \left(\rho_{ba}^{(n)} E_a - \left[\left\langle b\middle|\rho^{(n)}\middle|a\right\rangle \langle a|M|a\rangle + \left\langle b\middle|\rho^{(n)}\middle|b\right\rangle \langle b|M|a\rangle\right] E(t)\right)\Bigg) \\ & - \frac{1}{2}\Bigg(\sum_n \left[\langle b|\gamma|a\rangle \left\langle a\middle|\rho^{(n+1)}\middle|a\right\rangle + \langle b|\gamma|b\rangle \left\langle b\middle|\rho^{(n+1)}\middle|a\right\rangle\right] \\ & + \sum_n \left[\left\langle b\middle|\rho^{(n+1)}\middle|a\right\rangle \langle a|\gamma|a\rangle + \left\langle b\middle|\rho^{(n+1)}\middle|b\right\rangle \langle b|\gamma|a\rangle\right]\Bigg),\end{aligned} \tag{2-61}$$

and taking into account that the matrix γ has only diagonal elements and by defining the matrix element of M as $M_{nm} \equiv \langle n|M|m\rangle$

$$\begin{aligned}\sum_n \frac{\partial \rho_{ba}^{(n)}}{\partial t} = \frac{1}{i\hbar}\sum_n \Bigg(& E_b \rho_{ba}^{(n)} - \left[M_{ba}\rho_{aa}^{(n)} + M_{bb}\rho_{ba}^{(n)}\right] E(t) \\ & - \left(\rho_{ba}^{(n)} E_a - \left[\rho_{ba}^{(n)} M_{aa} + \rho_{bb}^{(n)} M_{ba}\right] E(t)\right)\Bigg) \\ & - \frac{1}{2}\left(\sum_n \gamma_{bb}\rho_{ba}^{(n+1)} + \sum_n \rho_{ba}^{(n+1)}\gamma_{aa}\right),\end{aligned} \tag{2-62}$$

rewriting terms $E_{ba} = E_b - E_a$, $\Gamma_{ab} = \Gamma_{ba} = \frac{1}{2}\left(\frac{1}{\tau_a} + \frac{1}{\tau_b}\right)$, and reordering

$$\begin{aligned}\sum_n \frac{\partial \rho_{ba}^{(n)}}{\partial t} = \frac{1}{i\hbar}\sum_n \Bigg(& E_{ba}\rho_{ba}^{(n)} - \left(\rho_{aa}^{(n)} - \rho_{bb}^{(n)}\right) M_{ba} E(t) \\ & - \left(M_{bb} - M_{aa}\right)\rho_{ba}^{(n)} E(t)\Bigg) - \sum_n \Gamma_{ab}\rho_{ba}^{(n+1)},\end{aligned} \tag{2-63}$$

since the unperturbed density matrix only has diagonal elements, i.e. $\rho_{ba}^{(0)} = \rho_{ab}^{(0)} = 0$ which implies $\sum_n \rho_{ba}^{(n)} = \sum_n \rho_{ba}^{(n+1)}$, using this result in the last equa-

tion,

$$\sum_n \frac{\partial \rho_{ba}^{(n+1)}}{\partial t} = \frac{1}{i\hbar}\sum_n \Bigg(E_{ba}\rho_{ba}^{(n+1)} - \left(\rho_{aa}^{(n)} - \rho_{bb}^{(n)}\right) M_{ba}E(t) - \left(M_{bb} - M_{aa}\right)\rho_{ba}^{(n)}E(t)\Bigg) - \sum_n \Gamma_{ab}\rho_{ba}^{(n+1)}, \tag{2-64}$$

extracting the nth term from this equation, it is possible to write a recurrence relation:

$$\frac{\partial \rho_{ba}^{(n+1)}}{\partial t} = \left(\frac{1}{i\hbar}E_{ba} - \Gamma_{ab}\right)\rho_{ba}^{(n+1)} - \frac{1}{i\hbar}\left(\rho_{aa}^{(n)} - \rho_{bb}^{(n)}\right) M_{ba}E(t) - \frac{1}{i\hbar}\left(M_{bb} - M_{aa}\right)E(t)\rho_{ba}^{(n)}, \tag{2-65}$$

Expanding the density matrix elements as proportional terms of $e^{\pm i\omega t}$, it is possible to obtain the solutions for this equation by equaling both sides. Taking into account that there will be two equalities, one of them for the exponent sign $(+)$ and the another one for $(-)$. Under steady state conditions, the n-order perturbative term is:

$$\rho^{(n)}(t) = \tilde{\rho}^{(n)}(\omega)\, e^{-i\omega t} + \tilde{\rho}^{(n)}(-\omega)\, e^{i\omega t}, \tag{2-66}$$

which is valid for n odd.
Taking $n = 0$ in Eq. (2-65)

$$\frac{\partial \rho_{ba}^{(1)}}{\partial t} = \left(\frac{1}{i\hbar}E_{ba} - \Gamma_{ab}\right)\rho_{ba}^{(1)} - \frac{1}{i\hbar}\left(\rho_{aa}^{(0)} - \rho_{bb}^{(0)}\right) M_{ba}E(t). \tag{2-67}$$

Let $n = 1$ in Eq. (2-66) for the coupling $b-a$ and by substituting it in conjunction with Eq. (2-51) into Eq. (2-67)

$$\begin{aligned}&\frac{\partial}{\partial t}\left(\tilde{\rho}_{ba}^{(1)}(\omega)\, e^{-i\omega t} + \tilde{\rho}_{ba}^{(1)}(-\omega)\, e^{i\omega t}\right) \\ &= \left(\frac{1}{i\hbar}E_{ba} - \Gamma_{ab}\right)\left(\tilde{\rho}_{ba}^{(1)}(\omega)\, e^{-i\omega t} + \tilde{\rho}_{ba}^{(1)}(-\omega)\, e^{i\omega t}\right) \\ &\quad - \frac{1}{i\hbar}\left(\rho_{aa}^{(n)} - \rho_{bb}^{(n)}\right) M_{ba}\left(\widetilde{E}\, e^{-i\omega t} + \widetilde{E}\, e^{i\omega t}\right),\end{aligned} \tag{2-68}$$

evaluating the derivative and grouping the terms with negative and positive power,

$$\begin{aligned}
&-i\omega\tilde{\rho}_{ba}^{(1)}(\omega)\,e^{-i\omega t} + i\omega\tilde{\rho}_{ba}^{(1)}(-\omega)\,e^{i\omega t} \\
&= \left[\left(\frac{1}{i\hbar}E_{ba} - \Gamma_{ab}\right)\tilde{\rho}_{ba}^{(1)}(\omega) - \frac{1}{i\hbar}\left(\rho_{aa}^{(0)} - \rho_{bb}^{(0)}\right)M_{ba}\widetilde{E}\right]\,e^{-i\omega t} \\
&\quad + \left[\left(\frac{1}{i\hbar}E_{ba} - \Gamma_{ab}\right)\tilde{\rho}_{ba}^{(1)}(-\omega) - \frac{1}{i\hbar}\left(\rho_{aa}^{(0)} - \rho_{bb}^{(0)}\right)M_{ba}\widetilde{E}\right]\,e^{i\omega t},
\end{aligned} \tag{2-69}$$

equaling terms for the negative power and solving for $\rho_{ba}^{(1)}(\omega)$

$$\tilde{\rho}_{ba}^{(1)}(\omega) = \frac{\left(\rho_{aa}^{(0)} - \rho_{bb}^{(0)}\right)M_{ba}\widetilde{E}}{E_{ba} - \hbar\omega - i\hbar\Gamma_{ab}}, \tag{2-70}$$

where ρ_0 are the state occupations in equilibrium, and depend on the Fermi level of the system by means of the Fermi-Dirac distribution function,

$$\rho_{aa}^{(0)} = \frac{1}{1 + e^{\beta\,(E_a - E_f)}} \quad \text{and} \quad \rho_{bb}^{(0)} = \frac{1}{1 + e^{\beta\,(E_b - E_f)}}, \tag{2-71}$$

where E_f is the Fermi level of the system and $\beta = 1/k_B T$ is the Boltzmann factor, with T the temperature, and k_B the Boltzmann constant.
Remembering the relationship between the electronic polarization $P(t)$ and the susceptibility χ [7]:

$$P(t) = \varepsilon_0\chi(\omega)\widetilde{E}\,e^{-i\omega t} + \varepsilon_0\chi(-\omega)\widetilde{E}\,e^{i\omega t} = \frac{1}{V}Tr(\rho\,M), \tag{2-72}$$

where V is the volume, ε_0 is the vacuum permittivity. The absorption coefficient $\alpha(\omega)$ is related to χ by

$$\alpha(\omega) = \omega\sqrt{\frac{\mu}{\varepsilon_R}}\,\mathrm{Im}\left(\varepsilon_0\chi(\omega)\right), \tag{2-73}$$

where μ is the permeability of the system, ε_R is the real part of the permittivity and $\chi(\omega)$ is the Fourier component of $\chi(t)$. The electronic polarization can be expressed as

$$P(t) = \frac{1}{V}\left[\langle a|\rho M|a\rangle + \langle b|\rho M|b\rangle\right], \tag{2-74}$$

where we can include the completeness relation:

$$P(t) = \frac{1}{V}\left[\langle a|\rho\left(|a\rangle\langle a| + |b\rangle\langle b|\right)M|a\rangle + \langle b|\rho\left(|b\rangle\langle a| + |b\rangle\langle b|\right)M|b\rangle\right], \tag{2-75}$$

by using distribute property

$$\begin{aligned} P(t) = \frac{1}{V}\big[&\langle a|\rho|a\rangle\langle a|M|a\rangle + \langle a|\rho|b\rangle\langle b|M|a\rangle \\ &+ \langle b|\rho|a\rangle\langle a|M|b\rangle + \langle b|\rho|b\rangle\langle b|M|b\rangle\big], \end{aligned} \tag{2-76}$$

we can write this electronic polarization by using matrix notation and the definitions of ρ given by Eqs. (2-53) and (2-66)

$$P(t) = \frac{1}{V}\sum\left[\tilde{\rho}_{aa}^{(n)}(\omega)M_{aa} + \tilde{\rho}_{ab}^{(n)}(\omega)M_{ba} + \tilde{\rho}_{ba}^{(n)}(\omega)M_{ab} + \tilde{\rho}_{bb}^{(n)}(\omega)M_{bb}\right]e^{-i\omega t}, \tag{2-77}$$

neglecting the terms outside of resonant transition $a-b$ and by using Eq. (2-72):

$$\varepsilon_0\chi^{(1)}(\omega)\widetilde{E} = \frac{1}{V}\left(\tilde{\rho}_{ba}^{(1)}(\omega)M_{ab}\right), \tag{2-78}$$

by substituting Eq. (2-70) into Eq. (2-78). It follows that

$$\varepsilon_0\chi^{(1)}(\omega)\widetilde{E} = \frac{1}{V}\frac{\left(\rho_{aa}^{(0)} - \rho_{bb}^{(0)}\right)M_{ba}\widetilde{E}}{E_{ba} - \hbar\omega - i\hbar\Gamma_{ab}}M_{ab}, \tag{2-79}$$

deleting $\widetilde{E}$ and multiplying numerator and denominator by $E_{ba} - \hbar\omega + i\hbar\Gamma_{ab}$ in order to eliminate the imaginary number in denominator

$$\varepsilon_0\chi^{(1)}(\omega) = \frac{1}{V}\frac{\left(\rho_{aa}^{(0)} - \rho_{bb}^{(0)}\right)|M_{ab}|^2}{(E_{ba} - \hbar\omega - i\hbar\Gamma_{ab})}\frac{(E_{ba} - \hbar\omega + i\hbar\Gamma_{ab})}{(E_{ba} - \hbar\omega + i\hbar\Gamma_{ab})}, \tag{2-80}$$

this equation takes the form,

$$\begin{aligned} &\varepsilon_0\chi^{(1)}(\omega) \\ &= \frac{1}{V}\left(\rho_{aa}^{(0)} - \rho_{bb}^{(0)}\right)|M_{ab}|^2\left(\frac{E_{ba} - \hbar\omega}{(E_{ba} - \hbar\omega)^2 + (\hbar\Gamma_{ab})^2} + i\frac{\hbar\Gamma_{ab}}{(E_{ba} - \hbar\omega)^2 + (\hbar\Gamma_{ab})^2}\right). \end{aligned}$$

(2-81)

Hence, by substituting the imaginary part of this expression into Eq. (2-73), the absorption coefficient is finally obtained in linear order [6, 8]:

$$\alpha^{(1)}(\omega) = \omega \sqrt{\frac{\mu}{\varepsilon_R}} \frac{|M_{ab}|^2 \left(\rho_{aa}^{(0)} - \rho_{bb}^{(0)}\right) \hbar\Gamma_{ab}}{V\left((E_{ba} - \hbar\omega)^2 + (\hbar\Gamma_{ab})^2\right)}. \tag{2-82}$$

2.3. Self-Consistent method

Currently there are several self-consistent methods to solve the Schrödinger equation coupled with the Poisson equation to model charge diffusion problems due to donor and acceptor effects included in semiconductor structures. This section briefly describes one of these methods for solving a quantum well [9] and includes the corresponding Fortran code in appendix B. The Fig. **2-2** shows the conduction band corresponding to a well of width $2L$ and depth ΔE_c, the shaded regions correspond to doped regions of n-type with density N_d. The entire system contains a small unintentional acceptor doping N_a. The term ΔE_d corresponds to the donor levels, in the low temperature limit $T = 0$ K, the Fermi level E_F is the highest populated level, clearly this level is characterized by the donor density N_d, in this case it is defined as $E_D = E_F$. From the above it is clear that the distance between the bottom of the conduction band and the Fermi level is given by ΔE_d. The Fig. **2-3** shows the self-consistent potential corresponding to the bottom of the conduction band in black, electron density is shown in red. Note how the profile of the bottom of the conduction band no longer has a square profile, this is modified by the effect of the diffusion of the charge carriers towards the interior of the well, as seen in the figure, the electron density $n(x)$ presents an accumulation region in the interior region of the well and decreases in the barrier regions. The charge density is given by

$$\rho(x) = \begin{cases} -e\, n(x), & x \leq -(D_d + D_s + L) \\ e\,(N_d - N_a - n(x)), & -(D_d + D_s + L) < x \leq -(D_s + L) \\ -e\,(N_a + n(x)), & -(D_s + L) < x \leq (D_s + L) \\ e\,(N_d - N_a - n(x)), & (D_s + L) < x \leq (D_d + D_s + L) \\ -e\, n(x), & x > (D_d + D_s + L) \end{cases} \tag{2-83}$$

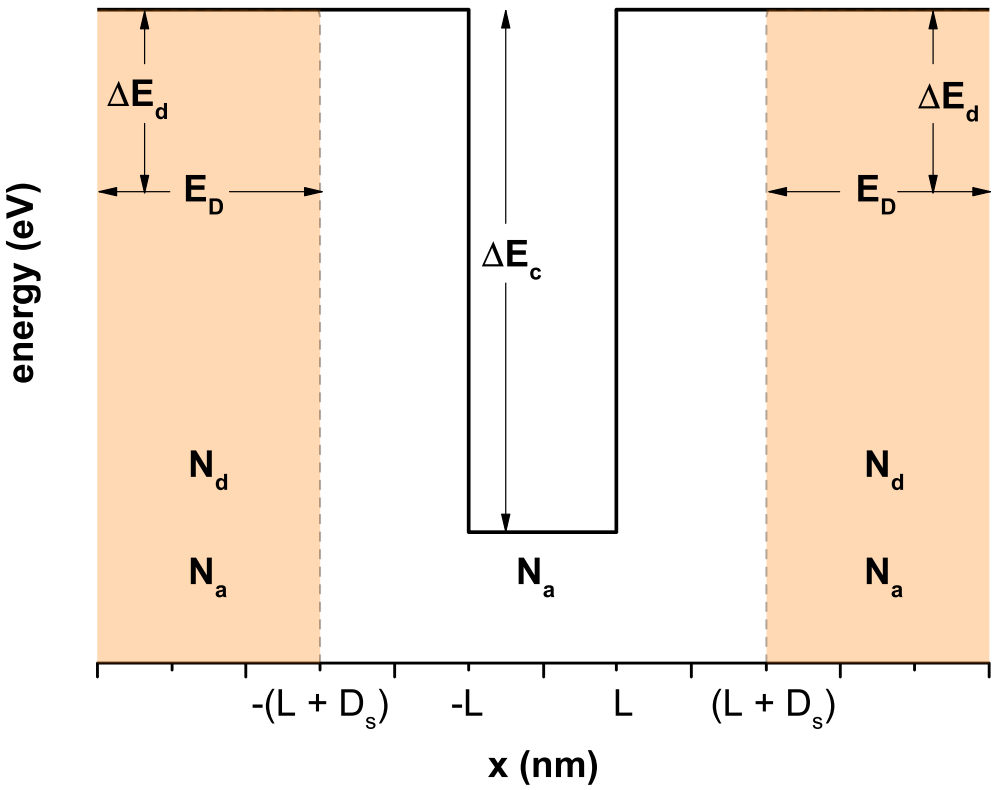

Figure 2-2.: Conduction band corresponding to a well of width $2L$ and depth ΔE_c, the shaded regions correspond to doped regions of n-type with density N_d. The entire system contains a small unintentional acceptor doping N_a.

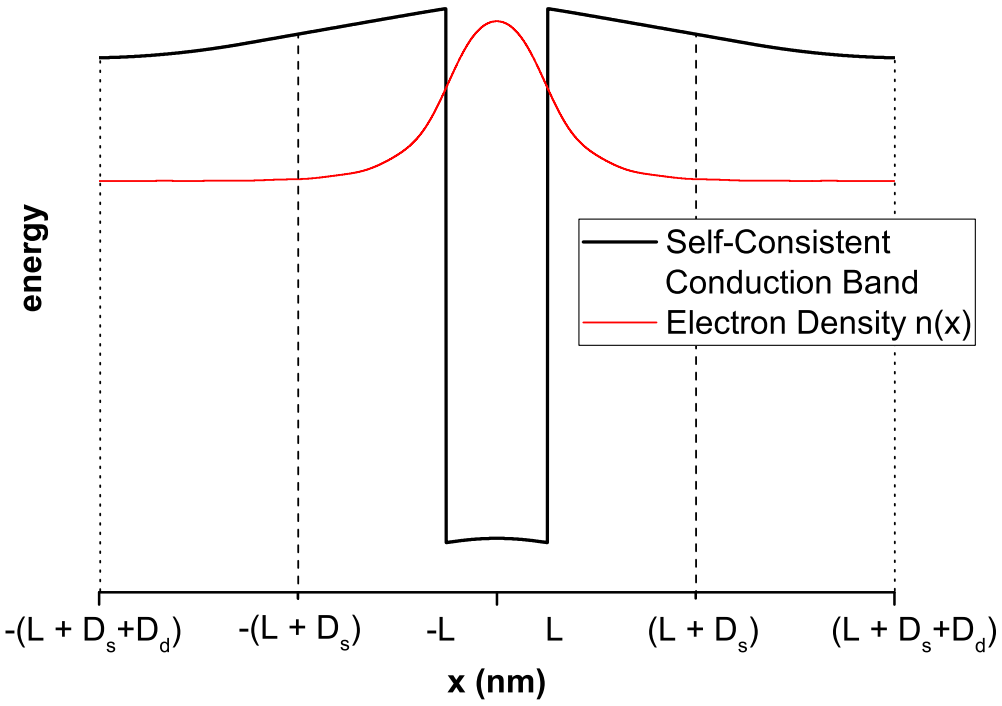

Figure 2-3.: Self-consistent potential corresponding to the bottom of the conduction band in black, electron density is shown in red.

in this equation e correspond to the electron charge. The Hartree potential is obtained from the Poisson equation,

$$\epsilon_0 \epsilon \frac{d^2\,\phi(x)}{dx^2} = \rho(x), \tag{2-84}$$

where, ϵ_0 and ϵ, are the vacuum and the relative dielectric constants, respectively. From this last equation we obtain the Coulomb electronic potential as $U_c(x) = e\,\phi$. At this point it is possible to introduce an exchange correlation term,

$$U_{xc}(x) = -\alpha\,(n(x))^{1/3}, \tag{2-85}$$

where, $\alpha = 0.0783\,e^2/\epsilon_0\epsilon$ for an GaAs well with $Al_{0.3}Ga_{0.7}As$ barriers [10]. In equation 2-85, the image charge effect has been ignored, considering two materials whose dielectric constant does not differ greatly. If we define $U_{bo}(x)$ as the band offset potential due to the energy difference between the well material and the barrier material in the conduction band band, then, it is possible to write an expression for the total potential:

$$U(x) = U_{bo}(x) + U_c(x) + U_{xc}(x), \tag{2-86}$$

this potential energy term must enter the Schrödinger equation to calculate the eigenvalues and eigenfunctions inside the well,

$$-\frac{\hbar^2}{2m^*}\,\frac{d^2\,\psi_i(x)}{dx^2} + U(x)\psi_i(x) = E_i\,\psi_i(x), \tag{2-87}$$

where E_i is the electron energy associated with the i-th state $\psi_i(x)$. Note that in Eq. 2-87 the effective mass approximation has been used as m^*. It should be noted that in the research results presented in the following chapters for materials such as GaAs/AlGaAs, CdTe/CdSe, etc. this approximation for the effective mass is not applied and instead of Eq. 2-87, a more general expression must be used to consider position-dependent effective masses. In this section, this approach is sufficient since the objective is to guide the operation of the self-consistent method. This last equation must be solved strictly applying BenDaniel-Duke boundary conditions, however, if the wave function penetration in barrier regions is small, it is possible to assume a single effective mass

through the system as the mass of the well material. Shifting the highest populated level to zero energy $E_F = 0$ and considering the low temperature limit $T = 0$ K, the electron density takes the form,

$$n(x) = -\sum_i \beta E_i \, |\psi_i(x)|^2, \tag{2-88}$$

where $\beta = m^*/\pi\hbar^2$. The sum in Eq. 2-88 must go over occupied states, that is, up to the Fermi level of the system. Taking into account that the Fermi level must coincide with the level of donors $E_F = E_D \equiv 0$, then, in the bulk of the system it must be fulfilled that,

$$U(x \to \pm\infty) = \Delta E_d, \tag{2-89}$$

This condition is a consequence of the fact that the electron density in these bulk regions tends asymptotically to zero. The Eqs. 2-83 - 2-89 must be solved in a self-consistent way according to the following algorithm:
(1) First, solve the Eq. 2-87 considering an initial potential that could contain only the band offset term $U_{old}(x) \equiv U_{bo}(x)$, in this first step we obtain a first set of eigenvalues and eigenfunctions $\{E_i, \, \psi_i(x)\}$.
(2) Calculate an expression for the electron density from Eq. 2-88 using the set of eigenvalues and eigenfunctions found in step (1).
(3) Calculate the exchange correlation potential $U_{xc}(x)$ by using the electron density obtained from the previous step by means of Eq. 2-85.
(4) The charge conservation equation implies that,

$$D_d = \frac{N_s + 2N_a(L + D_s)}{2(N_d - N_a)}, \tag{2-90}$$

with,

$$N_s = \int_{-\infty}^{+\infty} n(x)\, dx. \tag{2-91}$$

(5) With the calculation of D_d from Eq. 2-90, it is now possible to calculate the charge density $\rho(x)$ by means of 2-83.
(6) Next, the electron density found in the previous step is replaced in Eq. 2-84 to obtain the Hartree potential $\phi(x)$ at first approximation, considering

the boundary conditions $\phi(x \to \pm\infty) = 0$ and $d\phi(x)/dx|(x \to \pm\infty) \to 0$ (similarly, it must be fulfilled that $U_{xc}(x \to \pm\infty) = 0$).
(7) According to Eq. 2-86, we can write an expression for the new potential $U_{new}(x) = 95\,\% U_{bo}(x) + 5\,\% U^{old}(x)$ (It is important to introduce the old potential in small proportion to improve the numerical convergence of the self-consistent problem, in this case a 5 % has been used).
(8) If it is true that: $|U_{old}(x) - U_{new}(x)| < \varepsilon$ for $\varepsilon << 1$, stops the program and self-consistency has been obtained. If this condition is not met, the potential $U_{new}(x)$ must be replaced again in equation 2-87, to start the cycle again until reaching self-consistency. Appendix B includes a Fortran code that reproduces this self-consistent scheme for a GaAs well with $Al_{0.3}Ga_{0.7}As$ barriers.

2.4. External magnetic and electric fields

Consider a one-dimensional system (like a quantum well, for example) grown along the z axis, subjected to the action of a static magnetic field directed along y and an electric field directed at z. The magnetic field is clearly perpendicular to the growth direction of the structure. Let us consider explicitly $\overrightarrow{B} = B\,\widehat{j}$, in this way, the magnetic vector potential has the form $\overrightarrow{A} = B\,z\,\widehat{i}$ (within the Landau gauge), where B is the intensity of the magnetic field. On the other hand, the potential associated with the electric field is given by $-eFz$, where F is the intensity of the electric field and e is the charge of the electron. Taking the above into account, the Schrödinger equation takes the form [11]:

$$\left[\frac{1}{2m^*}\left(\widehat{\overrightarrow{p}} + e\overrightarrow{A}\right)^2 - eFz + V(z)\right]\psi(z) = E\,\psi(z), \tag{2-92}$$

where $V(z)$ is the geometrical confinement potential, m^* is the electron effective mass, and E is the electron energy along the growth direction. To get a more common expression, firstly, the quadratic term in Eq. (2-92) is expanded:

$$\begin{aligned}&\frac{1}{2m^*}\left(\widehat{\overrightarrow{p}} + e\overrightarrow{A}\right)\cdot\left[\left(\widehat{\overrightarrow{p}} + e\overrightarrow{A}\right)\psi(z)\right]\\ &= \frac{1}{2m^*}\left[\widehat{p}^2 + e\,\widehat{\overrightarrow{p}}\cdot\overrightarrow{A} + e\overrightarrow{A}\cdot\widehat{\overrightarrow{p}} + e^2A^2\right]\psi(z),\end{aligned} \tag{2-93}$$

by using $\widehat{\overrightarrow{p}} = -i\hbar\nabla$ and substituting (2-93) into Eq. (2-92)

$$\frac{1}{2m^*}\Big[-\hbar^2\nabla^2 - ie\hbar\nabla\cdot\overrightarrow{A} - ie\hbar\overrightarrow{A}\cdot\nabla + e^2A^2 - eFz + V(z)\Big]\psi(z) = E\,\psi(z). \quad (2\text{-}94)$$

Let's see that the cross terms are canceled

$$\begin{aligned}
\nabla\cdot\Big(\overrightarrow{A}\psi(z)\Big) &= \left(\frac{\partial}{\partial x}\widehat{i} + \frac{\partial}{\partial y}\widehat{j} + \frac{\partial}{\partial z}\widehat{k}\right)\cdot\Big[Bz\,\widehat{i}\,\psi(z)\Big] \\
&= Bz\frac{\partial\psi(z)}{\partial x} \\
&= 0 \\
&= Bz\,\widehat{i}\cdot\frac{\partial\psi(z)}{\partial x}\widehat{i} \\
&= Bz\,\widehat{i}\cdot\left(\frac{\partial\psi(z)}{\partial x}\widehat{i} + \frac{\partial\psi(z)}{\partial y}\widehat{j} + \frac{\partial\psi(z)}{\partial z}\widehat{k}\right) \\
&= Bz\,\widehat{i}\cdot\left(\frac{\partial}{\partial x}\widehat{i} + \frac{\partial}{\partial y}\widehat{j} + \frac{\partial}{\partial z}\widehat{k}\right)\,\psi(z) \\
&= \overrightarrow{A}\cdot\nabla\psi(z),
\end{aligned} \quad (2\text{-}95)$$

by using this result in Eq. (2-94)

$$\Big[\frac{1}{2m^*}\,\big(-\hbar^2\nabla^2 + e^2A^2\big) - eFz + V(z)\Big]\psi(z) = E\,\psi(z). \quad (2\text{-}96)$$

replacing $\overrightarrow{A}$ in terms of the magnitude of the magnetic field,

$$\Big[\frac{1}{2m^*}\,\big(-\hbar^2\nabla^2 + e^2B^2z^2\big) - eFz + V(z)\Big]\psi(z) = E\,\psi(z). \quad (2\text{-}97)$$

finally writing the gradient explicitly in the direction of growth of the structure,

$$\Big[-\frac{\hbar^2}{2m^*}\frac{\partial^2}{\partial z^2} + \frac{e^2B^2}{2m^*}\,z^2 - eFz + V(z)\Big]\psi(z) = E\,\psi(z). \quad (2\text{-}98)$$

This equation is used to solve one-dimensional structures subjected to the action of static electric and magnetic fields in the directions indicated in the Landau gauge [12].

States with Momentum in x, y, z and Position-Dependent Mass
Starting from the three-dimensional Schrödinger equation,

$$\hat{\mathcal{H}}\,\psi(\vec{r}) = E\,\psi(\vec{r}), \tag{2-99}$$

the dependence of the effective mass with the position, modifies only the kinetic term,

$$\vec{\nabla}\cdot\left(\frac{-\hbar^2}{2m^*(\bar{r})}\vec{\nabla}\right) = -i\hbar\vec{\nabla}\cdot\left(\frac{-i\hbar\vec{\nabla}}{2m^*(\vec{r})}\right) = \hat{\vec{p}}\cdot\left(\frac{\hat{\vec{p}}}{2m^*(\vec{r})}\right), \tag{2-100}$$

in this last equation the definition of the three-dimensional momentum operator has been used again. By including the magnetic field, a correction to the momentum term proportional to the magnetic vector potential is generated, in this way the Eq. (2-100) takes the form,

$$(\hat{\vec{p}} + e\vec{A})\cdot\left(\frac{\hat{\vec{p}} + e\vec{A}}{2m^*(\vec{r})}\right), \tag{2-101}$$

considering a magnetic field of the form $\vec{B} = B\hat{\jmath}$, then the magnetic vector potential is given by $\vec{A} = Bz\hat{\imath}$ (considering again the Landau Gauge). Taking this in mind, let us expand the operator given by Eq.(2-101) operating on the wave function,

$$\begin{aligned}
&(\hat{\vec{p}} + e\vec{A})\cdot\left(\frac{\hat{\vec{p}} + e\vec{A}}{2m^*(\vec{r})}\right)\psi(\vec{r}) = \\
&\left[\hat{\vec{p}}\cdot\left(\frac{\vec{p}}{2m^*(\vec{r})}\right) + e\hat{\vec{p}}\cdot\left(\frac{\vec{A}}{2m^*(\vec{r})}\right) + e\vec{A}\cdot\frac{\hat{\vec{p}}}{2m^*(\vec{r})} + \frac{e^2A^2}{2m^*(\vec{r})}\right]\psi(\vec{r}) = \\
&\left[-i\hbar\vec{\nabla}\cdot\left(\frac{-i\hbar\vec{\nabla}}{2m^*(\vec{r})}\right) - ie\hbar\vec{\nabla}\cdot\left(\frac{\vec{A}}{2m^*\,(\vec{r})}\right) + e\vec{A}\cdot\frac{(-i\hbar\vec{\nabla})}{2m^*\,(\vec{r})} + \frac{e^2A^2}{2m^*(\vec{r})}\right]\psi(\vec{r}) = \\
&\left[-\hbar^2\vec{\nabla}\cdot\left(\frac{\vec{\nabla}}{2m^*(\vec{r})}\right) - \frac{ie\hbar\vec{\nabla}}{2}\cdot\left(\frac{\vec{A}}{m^*(\vec{r})}\right) - \frac{ie\hbar}{2}\frac{\vec{A}\cdot\vec{\nabla}}{m^*(\vec{r})} + \frac{e^2A^2}{2m^*\,(\vec{r})}\right]\psi(\vec{r}).
\end{aligned} \tag{2-102}$$

Let's consider the second term in Eq. (2-102):

$$\begin{aligned}\frac{ie\hbar}{2}\vec{\nabla}\cdot\left(\frac{\vec{A}\psi(\vec{r})}{m^*(\vec{r})}\right) &= \frac{ie\hbar}{2}\vec{\nabla}\cdot\left(\frac{Bz\,\psi(\vec{r})\hat{\imath}}{m^*(\vec{r})}\right) = \frac{ie\hbar}{2}\frac{\partial}{\partial x}\left(\frac{Bz\,\psi(\vec{r})}{m^*(\vec{r})}\right) \\ &= \frac{ie\hbar Bz}{2}\frac{\partial}{\partial x}\left(\frac{\psi(\vec{r})}{m^*(\vec{r})}\right) = \frac{ie\hbar Bz}{2m^*(\vec{r})}\frac{\partial\psi(\vec{r})}{\partial x} - \frac{ie\hbar Bz\,\psi(\vec{r})}{2m^{*2}(\vec{r})}\frac{\partial m^*(\vec{r})}{\partial x}.\end{aligned} \tag{2-103}$$

On the other hand, the third term in Eq.(2-102) takes the form:

$$\begin{aligned}\frac{ie\hbar}{2}\frac{\vec{A}}{m^*(\vec{r})}\cdot\vec{\nabla}\psi(\vec{r}) = \frac{ie\hbar}{2}\frac{Bz\hat{\imath}}{m^*(\vec{r})}\cdot\vec{\nabla}\psi(\vec{r}) &= \frac{ie\hbar Bz}{2m^*(\vec{r})}\frac{\partial\psi(\vec{r})}{\partial x} \\ &= \frac{ie\hbar}{2}\vec{\nabla}\cdot\left(\frac{\vec{A}\psi(\vec{r})}{m^*(\vec{r})}\right) + \frac{ie\hbar Bz\,\psi(\vec{r})}{2m^{*2}(\vec{r})}\frac{\partial m^*(\vec{r})}{\partial x},\end{aligned} \tag{2-104}$$

from this last relation is found,

$$\begin{aligned}&\frac{ie\hbar}{2}\vec{\nabla}\cdot\left(\frac{\vec{A}\psi(\vec{r})}{m^*(\vec{r})}\right) + \frac{ie\hbar}{2}\frac{\vec{A}}{m^*(\vec{r})}\cdot\vec{\nabla}\psi(\vec{r}) \\ &\qquad = \frac{ie\hbar Bz}{m^*(\vec{r})}\frac{\partial\psi(\vec{r})}{\partial x} - \frac{ie\hbar Bz\,\psi(\vec{r})}{2m^{*2}(\vec{r})}\frac{\partial m^*(\vec{r})}{\partial x}.\end{aligned} \tag{2-105}$$

From Eq. (2-104) it can be seen that the equality of the crossed terms in Eq. (2-102) is presented only in the case in which the effective mass takes a constant value. Replacing the Eq.(2-105) in the Eq.(2-102) and rewriting the magnetic vector potential,:

$$\left[-\hbar^2\vec{\nabla}\cdot\left(\frac{\vec{\nabla}}{2m^*(\vec{r})}\right) - \frac{ie\hbar Bz}{m^*(\vec{r})}\frac{\partial}{\partial x} + \frac{ie\hbar Bz}{2m^{*2}(\vec{r})}\frac{\partial m^*(\vec{r})}{\partial x} + \frac{e^2B^2z^2}{2m^*(\vec{r})}\right]\psi(\vec{r}). \tag{2-106}$$

Remembering that this expression corresponds to the kinetic term of an electron in a uniform magnetic field, we can write the complete Schrödinger equation introducing the simultaneous action of an electric field in the form $\vec{F} = F\hat{k}$,

with which we obtain,

$$\left[-\hbar^2\vec{\nabla}\cdot\left(\frac{\vec{\nabla}}{2m^*(\vec{r})}\right)-\frac{ie\hbar Bz}{m^*(\vec{r})}\frac{\partial}{\partial x}+\frac{ie\hbar Bz}{2m^{*2}(\vec{r})}\frac{\partial m^*(\vec{r})}{\partial x}+\frac{e^2B^2z^2}{2m^*(\vec{r})}-eFz+V(\vec{r})\right]\psi(\vec{r})=E\,\psi(\vec{r}). \tag{2-107}$$

This equation includes the effect of states with momentum in x, y, z in addition to considering the position-dependent effective mass for an electron in a simultaneous electric and magnetic field confined in a $V(\vec{r})$ potential.

2.5. Non-resonant laser effect

In this section we will find an explicit form for the interaction potential of an intense non-resonant laser field with a heterostructure. let's start by analyze the interaction between a confined electron and a laser beam considered as an ideal monochromatic, plane wave described by the magnetic vector potential $\overrightarrow{A}(\overrightarrow{r},t)=\overrightarrow{A_0}\exp\left[i(\overrightarrow{k}\cdot\overrightarrow{r}-\omega t)\right]$. The laser field can be taken from a semi-classical point of view, and for development the Coulomb gauge will be used. The above means that $\nabla\cdot\overrightarrow{A}(\overrightarrow{r},t)=0$ and $\phi=0$, where $\overrightarrow{A}$ and ϕ are the vector and scalar potentials respectively. With these considerations, the time dependent Schrödinger equation is given by:

$$i\hbar\frac{\partial}{\partial t}\Psi_L(\overrightarrow{r},t)=\frac{1}{2m^*}\left(\widehat{p}-e\overrightarrow{A}(\overrightarrow{r},t)\right)^2\Psi_L(\overrightarrow{r},t)+V(\overrightarrow{r})\Psi_L(\overrightarrow{r},t), \tag{2-108}$$

the subscript in Ψ_L indicates that the equation is in the laboratory frame.
By expanding the first term on the right side of the Hamiltonian,

$$\begin{aligned}i\hbar\frac{\partial}{\partial t}\Psi_L(\overrightarrow{r},t)=&\left[\frac{1}{2m^*}\left[\widehat{p}^2-e\,\widehat{p}\cdot\overrightarrow{A}(\overrightarrow{r},t)-e\overrightarrow{A}(\overrightarrow{r},t)\cdot\widehat{p}+e^2\overrightarrow{A}^2(\overrightarrow{r},t)\right]\right.\\&\left.+V(\overrightarrow{r})\right]\Psi_L(\overrightarrow{r},t)\\=&\left[\frac{1}{2m^*}\widehat{p}^2-\frac{e}{2m^*}\left[\widehat{p}\cdot\overrightarrow{A}(\overrightarrow{r},t)+\overrightarrow{A}(\overrightarrow{r},t)\cdot\widehat{p}\right]+\frac{e^2}{2m^*}\overrightarrow{A}^2(\overrightarrow{r},t)\right.\\&\left.+V(\overrightarrow{r})\right]\Psi_L(\overrightarrow{r},t).\end{aligned}$$

(2-109)

The product $\widehat{p}\cdot\overrightarrow{A}(\overrightarrow{r},t)$ commutes due to the Coulomb gauge. At this point it is possible to apply the dipole approximation for the magnetic vector potential, to neglect its dependence on the $\overrightarrow{r}$ coordinate. The above implies that $\overrightarrow{A}(\overrightarrow{r},t)\approx\overrightarrow{A}(t)$. Secondly using the momentum operator representation in coordinates, $\widehat{p}=-i\hbar\nabla$, the Schrödinger equation takes the form,

$$i\hbar\frac{\partial}{\partial t}\Psi_L(\overrightarrow{r},t)=\left[-\frac{\hbar^2}{2m^*}\nabla^2+\frac{i\hbar e}{m^*}\overrightarrow{A}(t)\cdot\nabla+\frac{e^2}{2m^*}\overrightarrow{A}^2(t)+V(\overrightarrow{r})\right]\Psi_L(\overrightarrow{r},t), \tag{2-110}$$

This equation can be simplified according to the work of Kramers-Henneberger [13, 14] who proposed a transformation to the previous expression for transfer the time dependence from the kinetic to potential term [15], that is why this transformation is largely known as the laser-dressing of the potential. This transformation can be subdivided into two transformations U_1 and U_2 [16], by the first one the $\overrightarrow{A}^2(t)$ term being reduced and by the second one, the $\overrightarrow{A}(t)$ term being eliminated.
The transformations U_1 and U_2 are defined as

$$U_1=e^{-\frac{ie^2}{2m^*\hbar}\int^t\overrightarrow{A}^2(t')dt'}, \tag{2-111}$$

and

$$U_2=e^{-\frac{i}{\hbar}\overrightarrow{\alpha}(t)\cdot\widehat{p}}\ \text{with}\ \overrightarrow{\alpha}(t)=-\frac{e}{m^*}\int^t\overrightarrow{A}(t')dt'. \tag{2-112}$$

applying the transformation U_1 to the wave function in the laboratory frame, a new wave function in the velocity frame is obtained,

$$\Psi_v(\overrightarrow{r},t)=U_1^\dagger\Psi_L(\overrightarrow{r},t). \tag{2-113}$$

By applying the $U_1^\dagger$ transformation in Eq. (2-110), one will obtain

$$\begin{aligned}&i\hbar U_1^\dagger\frac{\partial}{\partial t}[U_1\Psi_v(\overrightarrow{r},t)]=\\&U_1^\dagger\left[-\frac{\hbar^2}{2m^*}\nabla^2+\frac{i\hbar e}{m^*}\overrightarrow{A}(t)\cdot\nabla+\frac{e^2}{2m^*}\overrightarrow{A}^2(t)+V(\overrightarrow{r})\right]U_1\Psi_v(\overrightarrow{r},t).\end{aligned} \tag{2-114}$$

On the right side, the U_1 operator only acts on the terms $\overrightarrow{A}^2$ and $\overrightarrow{A}$ since they are the only terms that depend on t like U_1. Expanding the derivative on the left side of the equation we have

$$\begin{aligned} &U_1^\dagger \frac{e^2}{2m^*}\overrightarrow{A}^2(t)U_1\Psi_v(\overrightarrow{r},t) + i\hbar\frac{\partial}{\partial t}\Psi_v(\overrightarrow{r},t) = \\ &U_1^\dagger\left[-\frac{\hbar^2}{2m^*}\nabla^2 + \frac{i\hbar e}{m^*}\overrightarrow{A}(t)\cdot\nabla + \frac{e^2}{2m^*}\overrightarrow{A}^2(t) + V(\overrightarrow{r})\right]U_1\Psi_v(\overrightarrow{r},t). \end{aligned} \tag{2-115}$$

Simplifying, an independent equation of the quadratic term $\overrightarrow{A}^2$ is obtained. In this way, the Schrödinger equation takes the form,

$$i\hbar\frac{\partial}{\partial t}\Psi_v(\overrightarrow{r},t) = \left[-\frac{\hbar^2}{2m^*}\nabla^2 + \frac{i\hbar e}{m^*}\overrightarrow{A}(t)\cdot\nabla + V(\overrightarrow{r})\right]\Psi_v(\overrightarrow{r},t). \tag{2-116}$$

The objective now is to eliminate the term $\overrightarrow{A}\cdot\nabla$ by means of the second transformation U_2 that this can be rewritten as $U_2 = e^{\frac{e}{m^*}\int^t \overrightarrow{A}(t')dt'\cdot\nabla}$. The wave function can be modified by this operator as, $\Psi_N(\overrightarrow{r},t) = U_2^\dagger\Psi_v(\overrightarrow{r},t)$. Through a similar procedure to the previous one, by applying this transformation to Eq. (2-116) it is possible to eliminate the term $\frac{i\hbar e}{m^*}\overrightarrow{A}\cdot\nabla$, to obtain after a simplification

$$i\hbar\frac{\partial}{\partial t}\Psi_N(\overrightarrow{r},t) = U_2^\dagger\left[-\frac{\hbar^2}{2m^*}\nabla^2 + V(\overrightarrow{r})\right]U_2\Psi_N(\overrightarrow{r},t). \tag{2-117}$$

At this point, it is necessary to explicitly calculate the term $U_2^\dagger V(\overrightarrow{r})U_2$ since the momentum operator is not affected by the transformation. To do this, let's use the Campbell-Baker-Hausdorff identity $e^{\widehat{A}}\widehat{B}e^{-\widehat{A}} = \widehat{B} + [\widehat{A},\widehat{B}] + [\widehat{A},[\widehat{A},\widehat{B}]]/2! + \cdots$,

$$\begin{aligned} U_2^\dagger V(\overrightarrow{r})U_2 &= e^{\frac{i}{\hbar}\overrightarrow{\alpha}(t)\cdot\widehat{p}}V(\overrightarrow{r})e^{-\frac{i}{\hbar}\overrightarrow{\alpha}(t)\cdot\widehat{p}} \\ &= V(\overrightarrow{r}) + [\overrightarrow{\alpha}(t)\cdot\nabla]V(\overrightarrow{r}) + \frac{1}{2!}[\overrightarrow{\alpha}(t)\cdot\nabla]^2V(\overrightarrow{r}) + \cdots \\ &= V[\overrightarrow{r} + \overrightarrow{\alpha}(t)]. \end{aligned} \tag{2-118}$$

This means that the only time dependence of the Schrödinger equation, through Kramers-Henneberger transformation, is through the potential term V. Note

that U_2 operator generates a translation given by $\overrightarrow{\alpha}(t)$. Of the above, the Schrödinger equation takes the form

$$i\hbar\frac{\partial}{\partial t}\Psi_N(\overrightarrow{r},t)=\left[-\frac{\hbar^2}{2m^*}\nabla^2+V[\overrightarrow{r}+\overrightarrow{\alpha}(t)]\right]\Psi_N(\overrightarrow{r},t). \tag{2-119}$$

The shape of the new potential (commonly called laser-dressed potential) is a consequence of the laser effect.
It is convenient to find an explicit form for $\overrightarrow{\alpha}(t)$, for this, let's calculate the second derivative with respect to the time of $\overrightarrow{\alpha}(t)$, we have $\ddot{\overrightarrow{\alpha}}(t)=\frac{e}{m^*}\overrightarrow{E}(t)$, where $\overrightarrow{E}(t)$ is an electric field. Hence, $\overrightarrow{\alpha}(t)$ is interpreted as the classical displacement of the electron under the electric field $\overrightarrow{E}(t)$. In the case of a steady laser field, i.e. $\overrightarrow{E}(t)=E_0\sin(\omega t)\,\widehat{x}$ (E_0 is the amplitude of the electric field, ω is the angular frequency of the laser, and $\widehat{x}$ represents the propagation direction of the field), later $\overrightarrow{\alpha}(t)=\frac{eE_0}{m^*\omega^2}\sin(\omega t)\,\widehat{x}$. This can be rewritten as $\overrightarrow{\alpha}(t)=\alpha_0\sin(\omega t)\,\widehat{x}$, where $\alpha_0=\frac{eE_0}{m^*\omega^2}$ represents the oscillation amplitude of the electron under the laser field (called the laser-dressing parameter).
The Floquet theory provides a solution for the Eq. (2-119) [14, 17]:

$$\Psi_N(\overrightarrow{r},t)=e^{-\frac{E_N}{\hbar}t}\sum_n\Psi_n^N(\overrightarrow{r})e^{-in\omega t}, \tag{2-120}$$

where E_N is the Floquet quasi-energy. By expanding the potential V in Fourier series,

$$V[\overrightarrow{r}+\overrightarrow{\alpha}(t)]=\sum_{n=-\infty}^{\infty}V_n(\alpha_0;\overrightarrow{r})e^{-in\omega t}, \tag{2-121}$$

$$\text{with }\ V_n(\alpha_0;\overrightarrow{r})=\frac{i^n}{\pi}\int_{-1}^{1}V(\overrightarrow{r}+\alpha_0 u\,\widehat{x})T_n(u)(1-u^2)^{-1/2}du \tag{2-122}$$

where $T_n(u)$ are the Chebyshev polynomials.
Considering a high frequency laser field (compared with the transition frequencies characteristic to the system), it is enough to consider the lowest order in (2-122)

$$V_0(\alpha_0,\overrightarrow{r})=\frac{1}{\pi}\int_{-1}^{1}\frac{V(\overrightarrow{r}+\alpha_0 u\widehat{e})}{\sqrt{1-u^2}}du. \tag{2-123}$$

By making a trigonometric substitution $u = \sin(\omega t)$, the laser-dressed potential can be written as:

$$V_0(\alpha_0, \overrightarrow{r}) = \frac{\omega}{2\pi} \int_0^{2\pi/\omega} V(\overrightarrow{r} + \alpha_0 \sin(\omega t)\, \widehat{e}) dt. \tag{2-124}$$

Finally, the time dependent Schrödinger equation will have the form

$$i\hbar \frac{\partial}{\partial t} \Psi(\overrightarrow{r}) = \left[-\frac{\hbar^2}{2m^*} \nabla^2 + V_0(\alpha_0, \overrightarrow{r}) \right] \Psi(\overrightarrow{r}), \tag{2-125}$$

Note that this equation only depends on $\overrightarrow{r}$ since $V_0(\alpha_0, \overrightarrow{r})$ corresponds to the average of the oscillating potential function:

$$V_0(\alpha_0, \overrightarrow{r}) = \frac{1}{T} \int_0^T V(\overrightarrow{r} + \overrightarrow{\alpha}(t)) dt. \tag{2-126}$$

Equations (2-125) and (2-126) must be solved to take into account the effect of an intense non-resonant laser field on electrons confined in a structure.

2.6. Finite elements method

The Finite Element Method (FEM) is a numerical method for solving in general non-trivial partial differential equations applied to systems with complex geometry [18]. It is a method widely used in fields such as physical sciences and engineering and is applicable to problems from 1 to 3 dimensions. The objective of the method is to generate a discretization of the geometric system by means of a mesh that completely fills the domain of smaller subsystems called finite elements, these elements can be of different shapes, depending on the dimension of the geometry in which the differential equations are being solved, these elements can be line segments, rectangles, tetrahedral, etc. The objective of the FEM is to convert a problem of a partial differential equation into a problem of a system of algebraic equations. Fig. **2-4** shows a mesh diagram of a one-dimensional system (upper figure), where the finite elements correspond to line segments, a two-dimensional system (lower left figure) where the finite elements are triangles, and a three-dimensional system (lower right figure) where the finite elements correspond to tetrahedron. The diagrams are obtained from

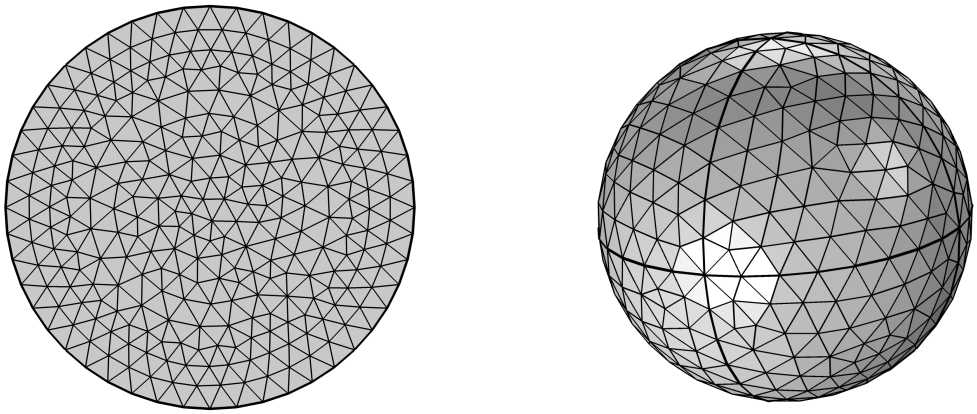

Figure 2-4.: Different mesh for a 1D, 2D and 3D problem respectively, the diagrams are obtained from the COMSOL multiphysics Software [19, 20].

the COMSOL multiphysics Software [19, 20].

Brief method description in the weak formulation
Consider the boundary conditions problem:

$$\nabla \cdot [f(\overrightarrow{r})\nabla]\, u(\overrightarrow{r}) + g(\overrightarrow{r})u(\overrightarrow{r}) = \lambda\, u(\overrightarrow{r}), \tag{2-127}$$

In this equation λ is an coordinate independent parameter of $\overrightarrow{r}$, note that the time independent Schrödinger equation is a particular case of 2-127. The last equation can be rewritten as,

$$\nabla \cdot [f(\overrightarrow{r})\nabla]\, u(\overrightarrow{r}) + (g(\overrightarrow{r}) - \lambda)\, u(\overrightarrow{r}) = 0, \tag{2-128}$$

Equation 2-128 must be true in a region Ω whose boundary $\partial\Omega$ must be smooth and it must be true that $u(\partial\Omega) = 0$ (Dirichlet problem). If u solves the Eq. 2-128, then for any smooth function ϕ that satisfies the boundary conditions $\phi(\partial\Omega) = 0$, we have

$$\int_\Omega \nabla \cdot [f(\overrightarrow{r})\nabla u(\overrightarrow{r})]\,\phi\, d\Omega + \int_\Omega (g(\overrightarrow{r}) - \lambda)\, u(\overrightarrow{r})\phi\, d\Omega = 0. \tag{2-129}$$

remembering the vectorial property $\nabla \cdot (\overrightarrow{A}v) = \overrightarrow{A} \cdot \nabla v + (\nabla \cdot \overrightarrow{A})v$, where $\overrightarrow{A} = f(\overrightarrow{r})\nabla u(\overrightarrow{r})$ and $v = \phi$, the Eq. 2-129 becomes

$$\int_\Omega f\nabla u \cdot \nabla\phi\, d\Omega + \int_\Omega \nabla \cdot [(f\nabla u)\,\phi]\; d\Omega + + \int_\Omega (g - \lambda)\, u\phi\, d\Omega = 0. \tag{2-130}$$

In the last equation the explicit dependency on the position vector $\overrightarrow{r}$ has been removed. In this point, it is convenient to use the Green's first identity,

$$\int_\Omega \nabla \cdot (a\nabla b)\, d\Omega = \oint_{\partial\Omega} a\nabla b \cdot \widehat{n}\, d(\partial\Omega), \tag{2-131}$$

where $\partial\Omega$ is the boundary of the system and $\widehat{n}$ is the outward pointing unit vector perpendicular on the surface. By using 2-131 in 2-130 we get,

$$\int_\Omega f\nabla u \cdot \nabla\phi\, d\Omega + \oint_{\partial\Omega} f\nabla u \cdot \widehat{n}\,\phi\, d(\partial\Omega) + \int_\Omega (g - \lambda)\, u\phi\, d\Omega = 0, \tag{2-132}$$

In stationary problems, due to the zero flux condition in the boundary of the system, the second term in 2-132 is zero, this is the case of the wave function in the Schrödinger equation. From the above, the final expression of the weak formulation is obtained

$$\int_\Omega f\nabla u \cdot \nabla\phi\, d\Omega + \int_\Omega (g - \lambda)\, u\phi\, d\Omega = 0, \tag{2-133}$$

There are non-trivial proofs in which the uniqueness of the ϕ functions is demonstrated for a single u solution of 2-128. The Fig. **2-5** shows the scheme of the discretization in the FEM, the exact solution corresponds to the blue curve, the violet segments correspond to the approximate solution, the curves in dark blue and red are two functions (v_i and v_{i+1} respectively) of the linear base and

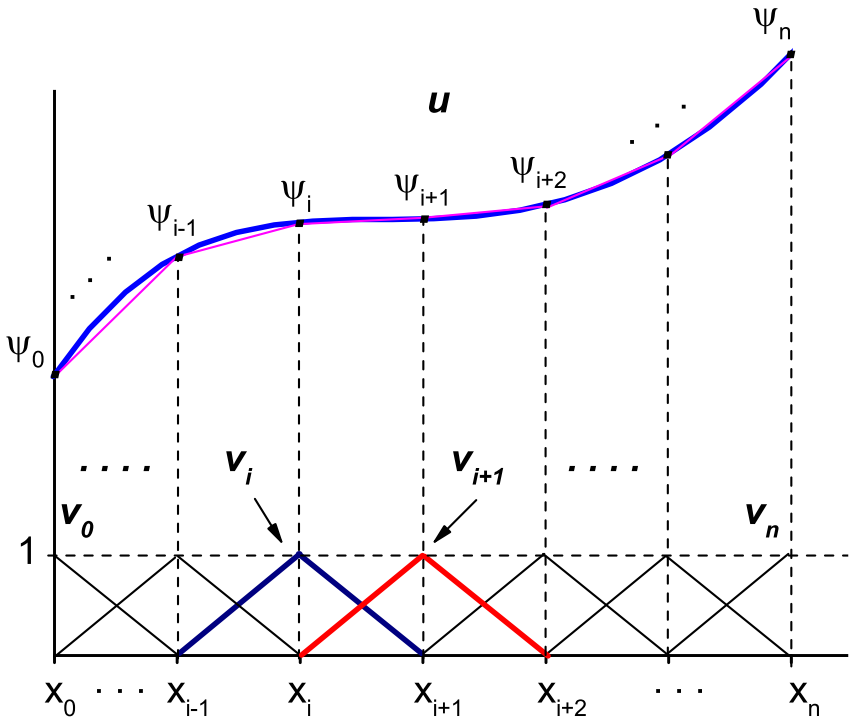

Figure 2-5.: Scheme of the discretization in the FEM, the exact solution corresponds to the blue curve, the violet segments correspond to the approximate solution, the curves in dark blue and red are two functions (v_i and v_{i+1} respectively) of the linear base and ψ_i are the adjustment coefficients between the numerical solution and the exact solution.

ψ_i are the adjustment coefficients between the numerical solution and the exact solution. Each of the ψ_i takes the exact value of the real solution at each node (x_i). In this scheme, the real solution u has been divided into n finite elements of equal length $l = x_{i+1} - x_i$ (in other more complex forms of discretization, the length of each element does not necessarily remain fixed), each element is contained between the vertical dashed lines in figure **2-5**. Within each of the finite elements, the base of linear functions v_i are defined as:

$$v_i = \begin{cases} 0, & x < x_{i-1} \\ \frac{x - x_{i-1}}{x_i - x_{i-1}}, & x_{i-1} \leq x < x_i \\ \frac{x_{i+1} - x}{x_{i+1} - x_i}, & x_i \leq x \leq x_{i+1} \\ 0, & x_{i+1} < x \end{cases} \tag{2-134}$$

two of these functions (v_i and v_{i+1}) are highlighted at the bottom of figure **2-5** in dark blue and red. Note that within each finite element contained between x_i and x_{i+1} there is only contribution of two base functions v_i and v_{i+1}, the other functions base are zero in this region. The real solution to the problem u can be approximated by means of the linear combination $u = \sum_i v_i \psi_i$. Note that at each node x_i the coefficient ψ_i takes the exact value of the function u at that point since the function v_i is equal to 1 at that node. These coefficients ψ_i are obtained by modeling the partial deferential equation in a system of algebraic equations that are generated by discretization. The first step to solve a problem is to take the initial differential equation to its weak form, similar to equation 2-133, later the integrals are solved in each of the finite elements and the complete solution corresponds to the sum of each of the contributions of each element, finally what results is a system of n algebraic equations that correspond to the n nodes in the discretization. In the Galerkin method ref. [21] these base functions v_i correspond to the functions ϕ in the equation 2-133. This method is very precise for the solution of differential equations in systems with complex geometries since it allows the generation of adaptive meshes as well as a refinement or an increase of the nodes in points of difficult solution.

To highlight that in COMSOL Multiphysics software it is possible to enter the

coefficients for a partial differential equation in a general form,

$$e_a \frac{\partial^2 u}{\partial t^2} + d_a \frac{\partial u}{\partial t} + \nabla \cdot (-c \nabla u - \alpha u + \gamma) + \beta \cdot \nabla u + a u = f \tag{2-135}$$

where u is the function to solve and e_a, d_a, c, α, γ, β, a and f they are coefficients that can be arbitrary functions. Through these functions it is possible to introduce effects of magnetic and electric fields, among others, into a problem, noting that the Eq. (2-135) is reduced to the Schrödinger equation.

References

[1] M. Paulsson, *Non Equilibrium Green's Functions for Dummies: Introduction to the One Particle NEGF equations*, Mesoscale and Nanoscale Physics (cond-mat.mes-hall), pp9(2008).

[2] S. Datta, *Electronic transport in mesoscopic systems*, Cambridge University Press, UK (1997).

[3] J. H. Ojeda, L. K. P. Muñoz, J. A. G. Pinzón and J. A. G. Castaño, *1,4-Dithiolbenzene, 1,4-dimethanediolbenzene and 4-thioacetylbiphenyl molecular systems: electronic devices with possible applications in molecular electronics*, RSC Adv. **10**, 32127-32136 (2020).

[4] R. Loudon, *Electronic and Thermal Properties of Biphenyl Molecules*, Superlattices Microstruct. **87**, pp8(2015).

[5] S. Datta, *Quantum transport:atom to transistor*, Cambridge University Press, UK (2005).

[6] D. Ahn and S.-L. Chuang, *Calculation of linear and nonlinear intersubband optical absorptions in a quantum well model with an applied electric field*, IEEE J. Quantum Elect. **23**, 2196 (1987).

[7] R. Loudon, *The Quantum Theory of Light*, Oxford University Press, (2000).

[8] R. Loudon, *Intersubband resonant enhancement of the nonlinear optical properties in asymmetric (CdS/ZnSe)/X-BeTe based quantum wells*, Opt. Mater. **35**, 875-880 (2013).

[9] C. D. Simserides and G. P. Triberis, *A systematic study of electronic states in n-$Al_xGa_{1-x}As$/GaAs/n-$Al_xGa_{1-x}As$ selectively doped double-heterojunction structures*, J. phys. Condens. Matter **5**, 6137-6146 (1993).

[10] G. A. M. Hurkx and W. V. Haeringen, *Self-consistent calculations on $Al_xGa_{1-x}As$ heterojunctions*, J. Phys. C: Solid State Phys. **18**, 5617 (1985).

[11] A. Turkoglu, N. Aghoutane, E. Feddi, M. E. Mora-Ramos and F. Ungan, *Non-resonant intense laser field effect on the nonlinear optical properties associated to the inter- and intra-band transitions in an anharmonic quantum well submitted to electric and magnetic field*, Solid State Commun. **334**, 114390 (2021).

[12] R. L. Restrepo, J. P. González-Pereira, E. Kasapoglu, A. L. Morales and C. A. Duque, *Linear and nonlinear optical properties in the terahertz regime for multiple-step quantum wells under intense laser field: Electric and magnetic field effects*, Opt. Mater. **86**, 590-599 (2018).

[13] W. C. Henneberger, *Perturbation Method for Atoms in Intense Light Beams*, Phys. Rev. Lett. **21**, 838-841 (1968).

[14] K. Burnett, V. C. Reed and P. L. Knight, *Atoms in ultra-intense laser fields*, J. Phys. B - At. Mol. Opt. **26**, 561-598 (1993).

[15] F. M. S. Lima, M. A. Amato, O. A. C. Nunes, A. L. A. Fonseca, B. G. Enders and E. F. da Silva Jr., *Unexpected transition from single to double quantum well potential induced by intense laser fields in a semiconductor quantum well*, J. Appl. Phys. **105**, 123111 (2009).

[16] B. J. Falaye, G.-H. Sun, A. G. Adepoju, M. S. Liman, K. J. Oyewumi and S.-H. Dong, *An electron of helium atom under a high-intensity laser field*, Laser Phys. **27**, 026004 (2017).

[17] M. Gavrila, *Atomic stabilization in superintense laser fields*, J. Phys. B: At. Mol. Opt. Phys. **35**, R147 (2002).

[18] D. L. Logan, *A first course in the finite element method*, Cengage Learning, ISBN 978-0495668251, 2011.

[19] COMSOL *Multiphysics, v. 5.4*; COMSOL AB: Stockholm, Sweden, 2020.

[20] COMSOL *Multiphysics Reference Guide*; COMSOL: Stockholm, Sweden, 2012.

[21] A. Ern and J. L. Guermond, *Theory and practice of finite elements*, Springer, ISBN 0-387-20574-8, 2004.

3. Shallow-donor impurity states with excitonic contribution in GaAs/AlGaAs and CdTe/CdSe truncated conical quantum dots under applied magnetic field

Using the effective mass approximation in a parabolic two-bands model, we study the effects of the geometrical parameters on the electron and hole states in two truncated conical quantum dots: *i*) GaAs-(Ga,Al)As in the presence of a shallow-donor impurity and under an applied magnetic field and *ii*) CdSe-CdTe core-shell type-II quantum dot. For the first system, the impurity position and the applied magnetic field direction have been chosen to preserve the system's azimuthal symmetry. The finite element method obtains the solution of the eigenvalues differential equations for electron or hole with or without impurity with an adaptive discretization of a triangular mesh. The correlation of the electron and hole states is calculated in a first-order perturbative approximation. This study shows that the magnetic field and donor impurities are relevant factors in the optoelectronic properties of conical quantum dots. Additionally, for the CdSe-CdTe quantum dot, where again the axial symmetry is preserved, a switch between direct and indirect exciton is possible to be controlled through geometry.

3.1. Introduction

For decades, the low dimensional systems have been one of the most widely investigated objects in semiconductor physics because of their interesting properties and applications, particularly the quantum confinement effect in these systems, which has opened up a different recipe for designing novel semiconductor materials for optoelectronic devices [1–4]. A great deal of attention of investigators has been attracted to the theoretical analysis of the effect of the quantum confinement on the impurity energies in various nanostructures, such as quantum wells [5–7], quantum-well wires [8], and quantum dots (QDs) [9–11]. In particular, in QDs, which are formed when there is a difference in the energy gap between the materials to be used [12, 13], the charge carriers (electrons and holes) are subjected to three-dimensional confinement, resulting in a discrete energy spectrum for the charge carriers and the system is very sensitive to nano-scale changes in geometry and composition, which generates an important modification in semiconductor properties, such as optical, mechanical, electrical, and thermal. This character is similar to that observed in atoms, but with the advantage that for a QD, the spectrum is adjustable with changes in geometry or by applying external effects such as electric field, magnetic field, and nonresonant intense laser fields. Another effect on which several authors have been interested corresponds to the presence of a shallow donor and acceptor impurities, neutral and charged excitons, which generate changes in the confinement of charge carriers due to attractive or repulsive effects.

In the study of QDs, one of the relevant characteristics is the geometrical shape of the nanostructure. Researches on semiconductor QDs have included different morphologies: pyramidal, spherical, and lens-shaped nanostructures. In the last three decades, different geometries have been intensively studied [12–17]. The sizes and shapes of these quantum systems have been shown to have more predominance in the properties of a semiconductor than its composition [18]. Among these structures, a special interest presents the cylindrical QDs [19–21]. These, depending on their radius and height ratio, can be represented as *i*) 1D-systems, called quantum-well wires, in which the height of the cylinder is much larger than the radius of the structure and *ii*) 2D-systems, called quantum-wells. More recently, the growth and study of QDs with a nanocone type structure [22]

which have fascinating physical properties for the development of new technologies, has also been possible. As a result of these investigations, nowadays, it is well known that morphologies of nanostructures can manifest unique physical properties of the material [23], for example, cone-shaped QDs can be quantum wires, quantum wells, or QDs, as a function of the structure height and solid angle at their top [24, 25].

Nanowires and nanocones have a natural ability to capture light, so their applications in creating optoelectronic devices such as solar cells and photodetectors have a promising future. Currently, quantum wires (nanowires) and cone-shaped QDs (nanocones) are recognized as promising candidates for the next generation of nanoscale devices [26–29]. A strong dependence of light absorption on geometry has been demonstrated for some time by making comparisons of the properties of conical and cylindrical nanowires [30]. The optical and electronic properties of tapered QDs, including the effects of electric and magnetic fields and donor impurities, have also been studied in different works [31, 32].

Analytical solutions of the Schrödinger equation are possible in very limited situations [33], for that, several numerical methods are found in the literature to solve the effective mass differential equations and to model different properties of semiconductor QDs. However, these analytical solutions are used in various works to show the validity of numerical calculations. The different variants of diagonalization, variational calculus, finite differences, and finite elements are among the methods used. The computation time of the numerical calculation can be very long if the codes are not optimized or if there is a need to obtain results for some parameter that is very susceptible to small changes, such as for the magnetic field. The finite element method (FEM) has been used to model QDs since the early 1990s [34], and at present, several studies dealing with electronic structure can be mentioned: optical, structural, impurity, transport, and deformation effects in QDs [35–37]. In [38], research on binding energy and susceptibility for cylindrical and spherical QDs under a different kind of confinement potential was carried out. In recent works, exciting applications have been mentioned concerning QDs. Due to the outstanding optical properties, QDs can be used for cancer cell imaging [39, 40]. A review article on biomedical and drugs administration mediated by QDs is developed in [41]. CdSe and CdTe QDs are candidates for several applications such as memory and

spintronic devices [42].

Type-II QDs come from the combination of two semiconductors where the alignment of the energy gaps gives rise to the confinement of electrons and holes in different regions of space. In this case, while one of the semiconductors behaves as the region of the well for the electron and the barrier for the hole, the situation is reversed in the other semiconductor. Thus, the second semiconductor behaves as the barrier region for the electron and the well region for the hole. In core-shell quantum dots formed for example by the combination of CdTe and CdSe, it is observed that: *i*) the CdTe material is the barrier/well region for the electron/hole and *ii*) the CdSe material is the well/barrier region for the electron/hole. Discussed, for example: biophotonics applications, applications in nanomedicine, pharmacokinetics and biodistribution, in vitro and in vivo toxicity, quantum confinement effects, core/shell architectures, tunability in the biological transparency window, opportunity to introduce tunable plasmonic features, doping to achieve enhanced emission from dopant states, and magnetic doping to introduce magnetic imaging capability.

In this work, we are interested in studying the electron, shallow-donor impurity, and heavy-hole exciton states for two kinds of conical QDs: *i*), shallow-donor impurity states in truncated conical shaped GaAs-(Ga,Al)As QDs, which can be modeled through a Coulomb interaction, in the simple model of a hydrogenic atom and considering the effects of an externally applied magnetic field. The magnetic field and impurity center are considered such as to preserve the axial symmetry of the system; *ii*) CdSe-CdTe core/shell QDs without magnetic field and impurity effects. Once the wavefunctions and energies for electron and hole are available, in the presence or absence of impurity, the correlation between both carriers is calculated using the Coulomb integral together with a first-order perturbative model. We carry out calculations for different donor impurity positions along the symmetry-axis, considering the effects of the magnetic field and the side of the structure (*i*). Finally, the overlap integral is reported, information that is key to understanding the behavior of the binding energies for each configuration (*i* and *ii*). The solution of the differential equations is obtained by applying the FEM. The paper is organized as follows: Section II contains the theoretical framework; Section III is devoted to the results and corresponding discussion; finally, in Section IV are presented the main conclusions.

3.2. Theoretical model

An illustrative scheme of the GaAs-AlGaAs QD under study is shown in Fig. **3-1**. Fig. **3-1**(a) is an axis-symmetric representation of the problem ($\varphi = 0$, with φ the azimuth angle) where the dimensions of the QD bases radii (R_1 and R_2) and the QD height (h) are shown. Two effects on the structure have been taken into account: *i*) a static magnetic field $\vec{B}$, applied in the z-direction and *ii*) the presence of a shallow-donor impurity at different positions along the same z-direction—$(0, z_i)$. In Fig. **3-1**(b) a three-dimensional view of the system obtained from the rotation of Fig. **3-1**(a) around the z-axis is shown. In (c) and (d) are shown the schematic views of the CdTe-CdSe and CdSe-CdTe truncated core-shell QDs without magnetic field and impurity effects. We have two specific cases: in Fig. **3-1**(c) a system of CdTe (core) and CdSe (shell), and in Fig. **3-1**(d), the materials are reversed, i.e., CdSe (core) and CdTe (shell). The ξ-parameter in Fig. **3-1**(c) is the thickness of CdSe, whereas in **3-1**(d) is the thickness of CdTe.

Using the effective mass and parabolic bands approximations, with Dirichlet boundary conditions at the outer edges of the barrier matrix and the Ben Daniel-Duke conditions at the QD and surrounding barrier-matrix interface (see Fig. **3-1**(b)), the Schrödinger equation for an electron (or heavy-hole) confined in the structure under the effect of an applied magnetic field, in the z-direction, and in the presence of a shallow-donor impurity, can be written, in Cartesian coordinates, in the form:

$$\left[\frac{1}{2\,m_j^{*,c}}\left(\widehat{p} - q\,\vec{A}\right)^2 + V_j(x,y,z) + \frac{\kappa\,q^2}{4\,\pi\,\varepsilon_0\,\varepsilon_r\,r}\right]\psi(x,y,z) = E\,\psi(x,y,z)\,, \quad (3\text{-}1)$$

where $r = \sqrt{x^2 + y^2 + (z - z_i)^2}$ is the electron-impurity (hole-impurity) distance, $\widehat{p} = -i\,\hbar\,\vec{\nabla}$, $m_j^{*,c}$ is the electron or heavy-hole effective mass ($j = e, h$ for electron and heavy-hole, respectively, and $c = w/b$ indicates the dot/barrier material), $q = +e, -e$ are the electron and hole charges, respectively, e being the elemental charge, $\kappa = -1$ for the electron, whereas $\kappa = +1$ for heavy-hole, and $\vec{A} = -\frac{B}{2}\,(y\,\widehat{i} - x\,\widehat{j})$ is the vector potential associated to the applied magnetic field, where $\vec{B} = \vec{\nabla} \times \vec{A}$ comes from the symmetric gauge. V_j is the

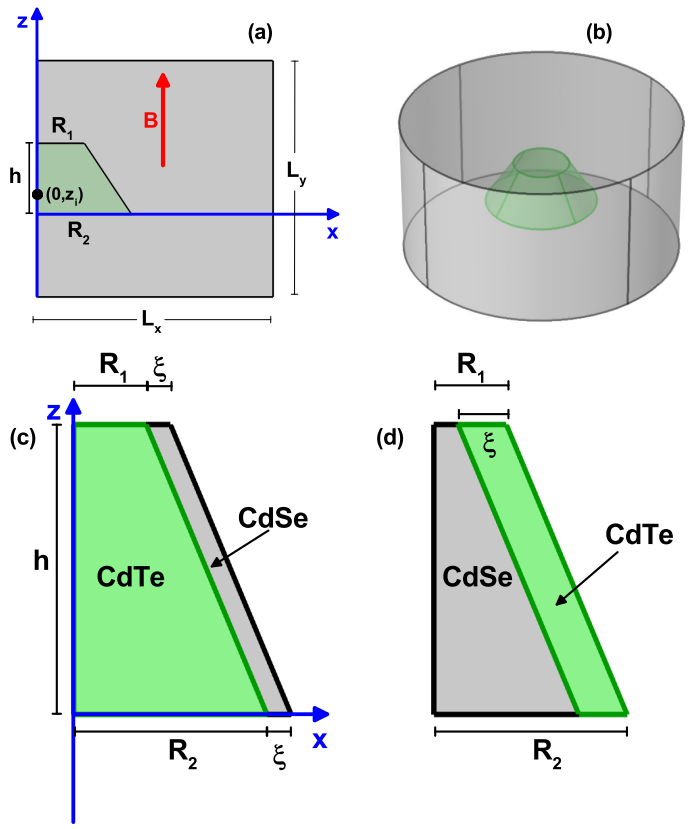

Figure 3-1.: Schematic view of the truncated conical-shaped GaAs-$Al_{0.3}Ga_{0.7}As$ quantum dot, (cone region GaAs, outside the cone AlGaAs). In (a) is depicted the $\varphi = 0$ projection, where the dot dimensions (R_1, R_2, and h), the shallow-donor impurity position $(0, z_i)$, the reference frame, the vertically applied magnetic field, and the dimensions of the large-size square where the open and Dirichlet boundary conditions are applied ($L_x = L_y = 50\,\text{nm}$), are indicated. The position of the cone half-height coincides with the half-height of the large square, and the reference frame coincides with the base of the cone. In (b) is shown the structure obtained by rotating around the z-axis the structure represented in (a). Schematic view of the truncated conical CdTe-CdSe (c) and CdSe-CdTe (d) core-shell quantum dots. The ξ-parameter corresponds to the shell-width of CdSe (c) and CdTe (d). R_1 and R_2 are the bases radii, and h is the QD height. In (c) and (d) the impurity and magnetic field effects have been neglected.

structural potential, which is zero in the dot region and V_j^0 in the barrier material. Additionally, $\varepsilon_0 = 8.85 \times 10^{-12}\,\mathrm{C}^2/(\mathrm{N\,m}^2)$ and ε_r is the static dielectric constant. The image charge effects have been ignored. Tenemos que anotar que en el caso de los core-shell QDs formados de CdTe y CdSe, en el caso de los electrones la región del pozo corresponde a

Expanding the first term in Eq. (3-1) and using the azimuthal symmetry condition of the structure, it is possible to consider in cylindrical coordinates a solution of the type $\psi(x,y,z) = \psi(\rho,\varphi,z) = R(\rho,z)\,e^{i\,l\,\varphi}$. Consequently, the $R(\rho,z)$ function satisfies the differential equation

$$\left[-\frac{\hbar^2}{2\,m_j^c}\nabla^2 + V_j^c(\rho,z) + \frac{\hbar^2\,l^2}{2\,m_j^c\,\rho^2} - \frac{q\,\hbar\,B\,l}{2\,m_j^c} + \frac{q^2\,B^2\,\rho^2}{8\,m_j^c} + \frac{\kappa\,q^2}{4\,\pi\,\varepsilon_0\,\varepsilon_r\,r}\right] R(\rho,z) = E\,R(\rho,z)\,, \tag{3-2}$$

where $l \in \mathbb{Z}$ is the principal quantum number and ∇^2 is the ρ- and z-dependent two-dimensional Laplacian operator.

Once the electron and heavy-hole uncorrelated ground state wavefunctions ($\psi_e^1(\vec{r}_e)$ and $\psi_h^1(\vec{r}_h)$, respectively) are obtained, we can proceed to compute the excitonic contribution from the interaction between the two charges. In a first order perturbative approximation, the Coulomb integral magnitude reads

$$C_{eh} = \frac{q^2}{4\,\pi\,\epsilon_0\,\epsilon_r}\int_{\Omega_h}\int_{\Omega_e}\frac{\left|\psi_e^1(\vec{r}_e)\right|^2\left|\psi_h^1(\vec{r}_h)\right|^2}{|\vec{r}_e - \vec{r}_h|}dV_e\,dV_h\,, \tag{3-3}$$

where $dV_e = \rho_e\,d\rho_e\,dz_e\,d\varphi_e$ and $dV_h = \rho_h\,d\rho_h\,dz_h\,d\varphi_h$ are the volume differentials in cylindrical coordinates for the electron and hole, respectively. In Eq. (3-3), Ω_h and Ω_e indicate the volume of the cylinder represented in Fig. **3-1**(b) for hole and electron, respectively, whose radius and height are L_x and L_y, respectively. Since we are only interested in the magnitude of the Coulomb interaction, in Eq. (3-3), we have omitted the negative sign of the electrostatic energy.

Because of the azimuthal symmetry, it is possible to write the angular part of

Eq. (3-3) analytically. This reduces the integral from 6 to 4 variables:

$$C_{eh} = \frac{q^2}{4\,\pi\,\varepsilon_0\,\varepsilon_r} \int_{S_h}\int_{S_e} \left|\psi_e^1\left(\rho_e\,,z_e\right)\right|^2 \left|\psi_h^1\left(\rho_h\,,z_h\right)\right|^2 \left[\frac{8\pi\,K\left(\frac{r_p}{1+r_p}\right)}{r\,\sqrt{1+r_p}}\right] dV_e^{'}\,dV_h^{'}\,, \tag{3-4}$$

where $r = \sqrt{\left(\rho_e-\rho_h\right)^2+\left(z_e-z_h\right)^2}$, $r_p = \frac{4\rho_e\,\rho_h}{r}$, $K(x)$ is the complete elliptic integral of the first kind, $dV_e^{'} = 2\,\pi\,\rho_e\,d\rho_e\,dz_e$, and $dV_h^{'} = 2\,\pi\,\rho_h\,d\rho_h\,dz_h$. In Eq. (3-4), the expression inside the squared parenthesis comes from the double angular integral of the inverse of electron-hole distance and S_h and S_e correspond to the large rectangle area in Fig. **3-1**(a). Note that in Eq. (3-3) and due to the azimuthal symmetry of the system, the electron and heavy-hole ground state wavefunctions are independent of the φ_e and φ_h coordinates, respectively.
A quantity that allows complementing the exciton analysis is the overlap integral between the electron and heavy-hole ground states, whose calculation is obtained in cylindrical coordinates using the expression

$$I_{eh} = 4\,\pi^2 \left|\int_S \psi_e^1\left(\rho,z\right)\psi_h^1\left(\rho,z\right)\rho\,d\rho\,dz\right|^2\,, \tag{3-5}$$

where in the previous equation, the electron and heavy-hole are located simultaneously at the same place, (ρ, z) of the large rectangle in Fig. **3-1**(a) with area S.
The wavefunctions and corresponding energies associated with Eq. (3-2) have been obtained by implementing the FEM [43–47]. Within the Comsol-Multiphysics licensed software [45–47], a user-controlled mesh was chosen in order to achieve greater control over discretization. Since the quantum states of interest correspond to the location of the charge carrier in the GaAs QD, three refinements have been generated in that region of the system. As a result, the number of evaluation nodes in the entire mesh is 7005. Thanks to the mesh adaptation, there are 11328 triangles in the GaAs QD region and 2513 in the AlGaAs matrix. On the border between the QD and the matrix, there are 217 nodes. Other

general characteristics of the mesh are the maximum and minimum element size of 1.85 nm and 0.00625 nm, respectively. In an 8th generation Intel core i7 processor, the computation time for calculating energies in fixed parameters is approximately 8 s. For the numerical calculation of Eq. (3-4), a Fortran 77 code was used. From the results obtained in Comsol-Multiphysics, the values of the ground state wavefunction were exported in a regular mesh, in terms of the (ρ, z) coordinates, taking as input of these coordinates the same values for electron and hole. Since we have values of the wavefunctions at discrete points of the coordinates, the integral in Eq. (3-4) is converted to a Riemann sum. Due to the azimuthal symmetry of the system, the integration corresponding to the φ-angular coordinates was obtained by using elliptic integrals.

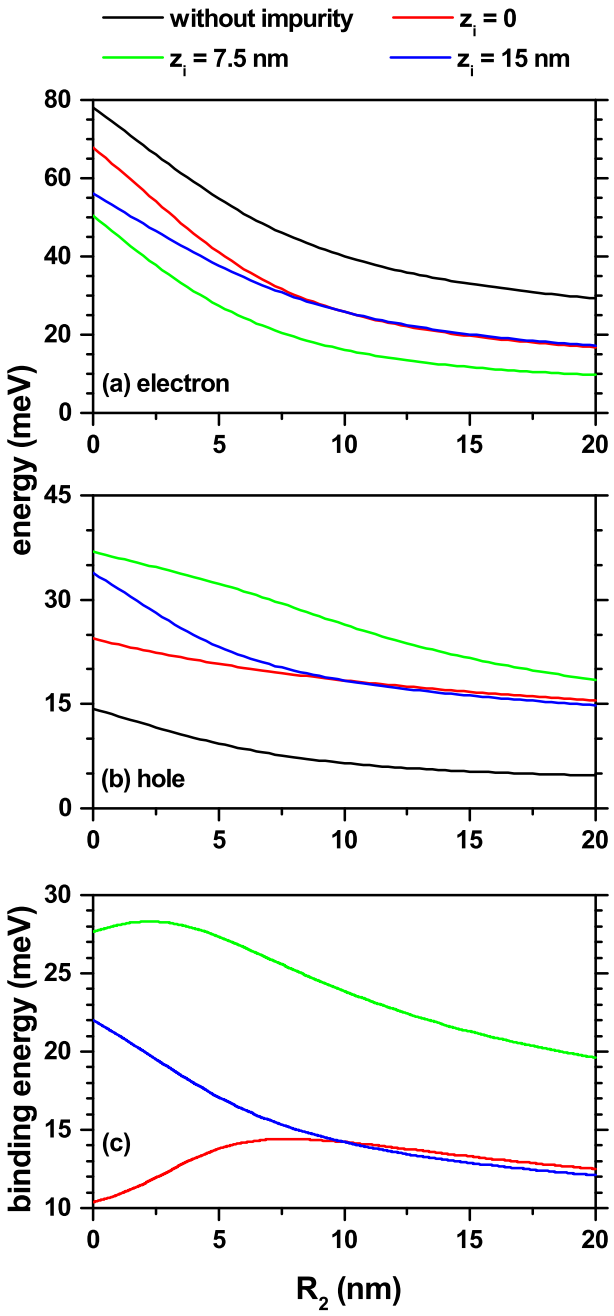

Figure 3-2.: The ground state level for a confined electron/hole (a)/(b) in a truncated conical-shaped GaAs-$Al_{0.3}Ga_{0.7}As$ quantum dot as a function of the R_2-lower structure radius and the corresponding biding energy (c). Calculations are for $R_1 = 10\,\text{nm}$, $h = 15\,\text{nm}$, $B = 0$, with and without impurity effects according to the color code. Three impurity positions were considered: $z_i = 0$, $7.5\,\text{nm}$, and $15\,\text{nm}$.

3.3. Results and discussion

3.3.1. Electron and hole spectra in GaAs-$Al_{0.3}Ga_{0.7}As$ truncated conical quantum dot under donor impurity and static magnetic field effects

In subsections A and B the parameters we will use are: $m_e^{*,w} = 0.067\, m_0$ (where m_0 is the free electron mass), $m_e^{*,b} = 0.092\, m_0$, $m_h^{*,w} = 0.51\, m_0$, $m_h^{*,b} = 0.57\, m_0$, $V_e^0 = 0.262\,\text{eV}$, $V_h^0 = 0.174\,\text{eV}$, and $\varepsilon = 13$ [48, 49].

In this subsection, the impurity and static magnetic field effects on GaAs-$Al_{0.3}Ga_{0.7}As$ truncated conical QD are explored.

In Fig. **3-2**, the electron and heavy-hole energy spectra in a GaAs-$Al_{0.3}Ga_{0.7}As$ truncated conical QD are shown as a function of the lower base radius (R_2), leaving fixed the upper base radius (R_1) and the dot height (h). Three different positions for the donor impurity were considered according to the color code. In order to interpret the results, the ground state level for impurity absence also was plotted. Fig. **3-2**(a) and 2(b) are for the ground state of electron and hole, respectively. Fig. **3-2**(c) is the corresponding binding energy for impurity associated with the electron. This fact allows to have a change in geometry from a conical QD ($R_2 = 0$), through a cylindrical QD ($R_2 = R_1 = 10\,\text{nm}$) and reaching a truncated conical QD, as shown in Fig. **3-1**(b). The results are given with consideration of donor impurity and without applied magnetic field effects. In general, it is observed that by increasing R_2 there is a decrease in the confinement effect for both charge carriers due to the increase in the volume of the structure. This is reflected in a systematic decrease in all energy levels with R_2. The ground state exhibits a higher rate of decrease in energy values in the range $0 < R_2 < 10\,\text{nm}$. This behavior is explained by the fact that for these small R_2 values, the vertex region expels the carriers' wavefunction towards the base of radius R_1. When R_2 increases, the ground state rapidly shifts its maximum probability towards the lower dot region, a condition that occurs until the formation of the cylindrical QD ($R_2 = 10\,\text{nm}$). When the value of R_2 continues to increase, the ground state, which tends to show its maximum probability density at the center of the QD (away from the edges), does not show drastic changes, which results in energy with a low rate of decline.

The most considerable differences between the electron and the hole spectra occur in the magnitudes of their energies, a situation that is typical of the potential barriers associated with each particle and of their corresponding effective masses. A donor impurity is located in three different positions along the z-axis: $z_i = 0$, $z_i = 7.5\,\text{nm}$, and $z_i = 15\,\text{nm}$. Compared with the energy without the impurity, the difference related to the interaction between the two types of carriers and the impurity is remarkable. On the one hand, the electron experiences attraction towards the impurity reflected in a spectrum shift towards lower energies. In contrast, the heavy-hole is modeled with a repulsive interaction with the donor impurity (see the Eq. (3-1)), which causes an energy increase for each impurity position. In Fig. **3-2**(a), the ground state with an impurity at $z_i = 0$, for R_2 values close to zero, is the one with the smallest energy redshift in comparing with the other two positions of the impurity, due to the existence of a competition between the geometrical confinement, which causes the wavefunction to be concentrated in the upper part of the QD, and the attractive effect of the impurity, which is responsible for the impurity shifting towards the lower structure region. Clearly, for the ground state, the Coulomb interaction effect is less significant concerning the geometric effect. It should be noted that the presence of the impurity does not influence the degeneracy associated with azimuthal symmetry.

The ground state binding energy (E_b) for the same three impurity positions is obtained by the difference $E_b = E_1 - E_1^i$, where E_1 is the electron ground state energy in the absence of impurity center ($\kappa = 0$) and E_1^i is the corresponding one but in the presence of the impurity ($\kappa = -1$). For $z_i = 0$, the binding energy is increasing in the range $0 < R_2 < 7\,\text{nm}$. In this R_2-regime, the maximum probability density occurs in the upper part of the QD (that is, near the surface of radius R_1) because the electron tends to be in the region of least confinement, that is, in the region of greater local volume and away from the edges of the cone. With the appearance of the impurity at $z_i = 0$, there is a systematic decrease in the electron-impurity distance as R_2 increases due to the decrease in the repulsive effect associated with the potential barriers present in the apical point. This results in an increase in the Coulomb interaction and consequently in the binding energy. Once the cylindrical shape of the QD is obtained ($R_2 = 10\,\text{nm}$) and R_2 continues to increase from there, it is observed

an effective reduction of the confinement effect due to the systematic increase in the volume of the structure. In this case, the binding energy is mainly associated with the Coulomb interaction, and the geometric confinement associated with the structure is transformed into a perturbative effect that decreases with the increase of R_2. For the case in which the impurity is located in the half-height of the QD, $z_i = 7.5\,\text{nm}$, the binding energy is an increasing function in the range $0 < R_2 < 2.3\,\text{nm}$, which is associated with the fast saturation and weak effect of the potential barriers located at the apical point of the inverted truncated cone ($R_2 < R_1$). When $z_i = 15\,\text{nm}$, the E_b is a monotonically decreasing function of R_2. In this case, the increase of R_2 implies a constant displacement of the probability density maximum from the top of the structure towards the half-height region, or even below it, with a permanent increase of the mean electron-impurity distance. This is reflected in a drop in electrostatic interaction and consequently in binding energy.

In Fig. **3-3**, the energy results are presented as a function of the applied magnetic field for $l = 0$ and $l = 1$, both for the electron, Fig. **3-3**(a), and the heavy-hole, Fig. **3-3**(b), confined into a truncated conical-shaped GaAs-$Al_{0.3}Ga_{0.7}As$ QD. For $\kappa = 0$, the electron ground state maintains its symmetry over the entire range of the calculated magnetic field, which corresponds to an s-like state with $l = 0$. In the case of the heavy-hole, there are multiple crossovers for excited states since one set loses degeneration accompanied by an increase in energy, and the other set of states, which was part of the degeneration in the absence of a magnetic field, goes towards lower energies. This behavior can be observed, for example, for the first excited state in Fig. **3-3**(b) with an impurity at $z_i = 7.5\,\text{nm}$; the first excited state ($l = 1$) goes towards lower energies, and on the contrary, the ground state ($l = 0$) goes towards higher energies.

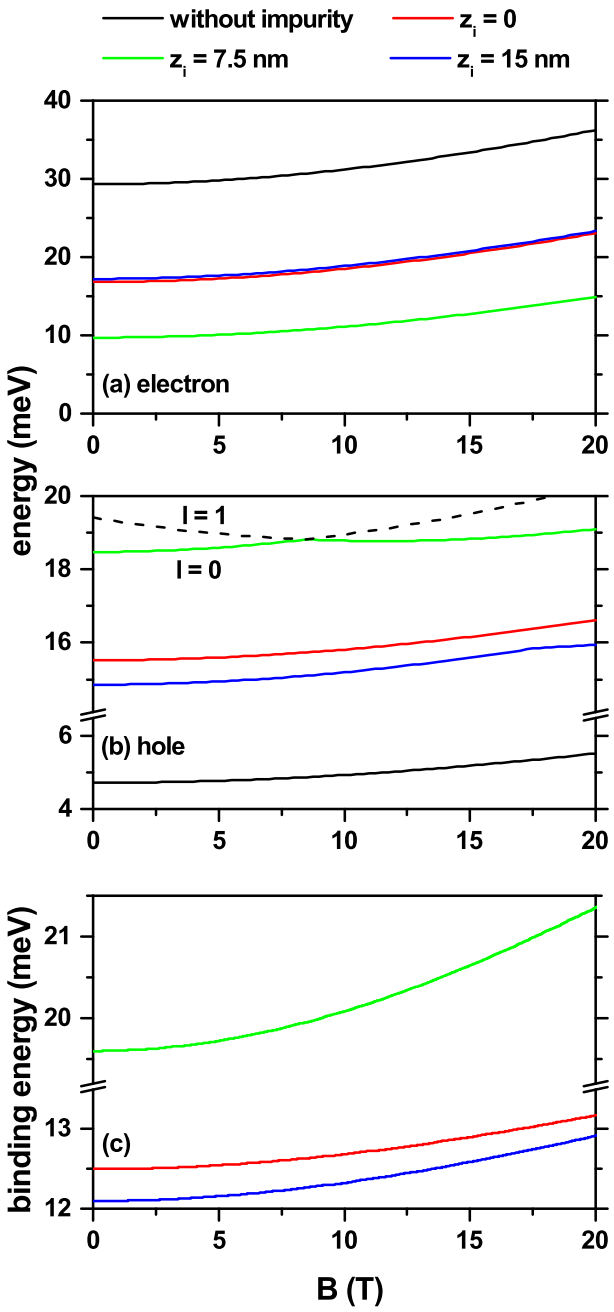

Figure 3-3.: The ground state level for a confined electron/hole (a)/(b) in a truncated conical-shaped GaAs-$Al_{0.3}Ga_{0.7}As$ quantum dot as a function of the vertically applied magnetic field and the corresponding binding energy (c). Calculations are for $R_1 = 10\,\text{nm}$, $R_2 = 20\,\text{nm}$, $h = 15\,\text{nm}$, with and without impurity effects according to the color code. Three impurity positions were considered: $z_i = 0$, $7.5\,\text{nm}$, and $15\,\text{nm}$.

Considering the presence of a donor impurity which is located at three different positions along the z-axis: $z_i = 0$, $z_i = 7.5\,\text{nm}$, and $z_i = 15\,\text{nm}$, the combined effect of the applied magnetic field and the impurity allows for shifting the energy levels and generating a rise in the degeneracy for the states with $l \neq 0$. The uncorrelated electron's ground state has its maximum probability density along the z-axis, which coincides with the impurity position. In this case, the magnetic field generates additional confinement towards the z-axis, thus effectively reducing the electron-impurity distance, thereby enhancing the Coulomb interaction. The greatest effects on the energies of the correlated system occur for the impurity located at the QD's half-height, Fig. **3-3**(c)-green color, since the influence of the Coulomb interaction occurs in all directions of space. For the heavy-hole, the repulsive effect of the donor impurity generates a quantum ring-like behavior, which becomes evident with the ground state's oscillations when the magnetic field is turned on. For example, in Fig. **3-3** the ground state corresponds to $l = 0$ for $B = 0$ while for $B = 15\,\text{T}$ the ground state occurs with $l = +1$. It is evident from that, for impurities in the lower and upper bases of the structure, the heavy-hole ground state continues to present the oscillatory character with the magnetic field. However, the repulsion generated by the potential barriers reduces the manifestation of this effect. In Fig. **3-3**(c), the ground state binding energies for the confined electron are presented as a function of the applied magnetic field for three considered donor impurity positions, $z_i = 0$, $z_i = 7.5\,\text{nm}$, and $z_i = 15$ nm. The results were obtained by subtracting from the ground state energy in black color in Fig. **3-3**(a), the corresponding ground state energies to the three impurity positions. Although the magnetic field decreases the expected value of $\rho = \sqrt{x^2 + y^2}$, that is, it compresses the wavefunction towards the z-axis, when the impurity is located at the upper or lower face of the QD, the variation of the binding energy increases to a low rate. For impurities located at the QD's half-height, $z_i = 7.5\,\text{nm}$, the most significant interaction with the electron is reached. With the increase in the magnetic field, there is a smaller distance between the electron and the impurity, obtaining higher binding energy. In the latter case, as mentioned above, the Coulomb interaction has a quasi-3D symmetrical character, except for the variations that the structure shape induces at the boundaries between the QD and the surrounding material.

Two sets of panels for the electron and heavy-hole ground state wavefunction (WF) are shown in Fig. **3-4**. There are cuts in the first, third and fourth rows for the $y = 0$-plane. A first set corresponds to the electron WFs, Figs. **3-4**(a-d) and the second one, Figs. **3-4**(e-l) for hole WFs. The real and imaginary parts of the heavy-hole WFs correspond to Figs. **3-4**(e-f, i-j) and Figs. **3-4**(g-h, k-l), respectively. The second set of cuts is for the plane $z = 7.5\,\mathrm{nm}$, Figs. **3-4**(c-d, i-l), and the two columns are for two different values of the applied magnetic field. With a ground state of s-like symmetry, the electron is located fundamentally in the QD center and independently of the applied magnetic field's value, but the strength of confinement is stronger with the magnetic field. This distribution of the WF is the result of the attraction towards the impurity center. When the magnetic field is applied, it is evident that the electron has a more significant location towards the axial axis. Note that the s-like symmetry of the electron ground state is maintained with the magnetic field's inclusion, even for the highest value of $B = 20\,\mathrm{T}$ used in this work. The real part of the heavy-hole WF (Figs. **3-4**(e-f, i-j)) shows that the WF has the ring's symmetry in the absence of a magnetic field since the donor impurity generates electrostatic repulsion on the hole. When the magnetic field is included, there are

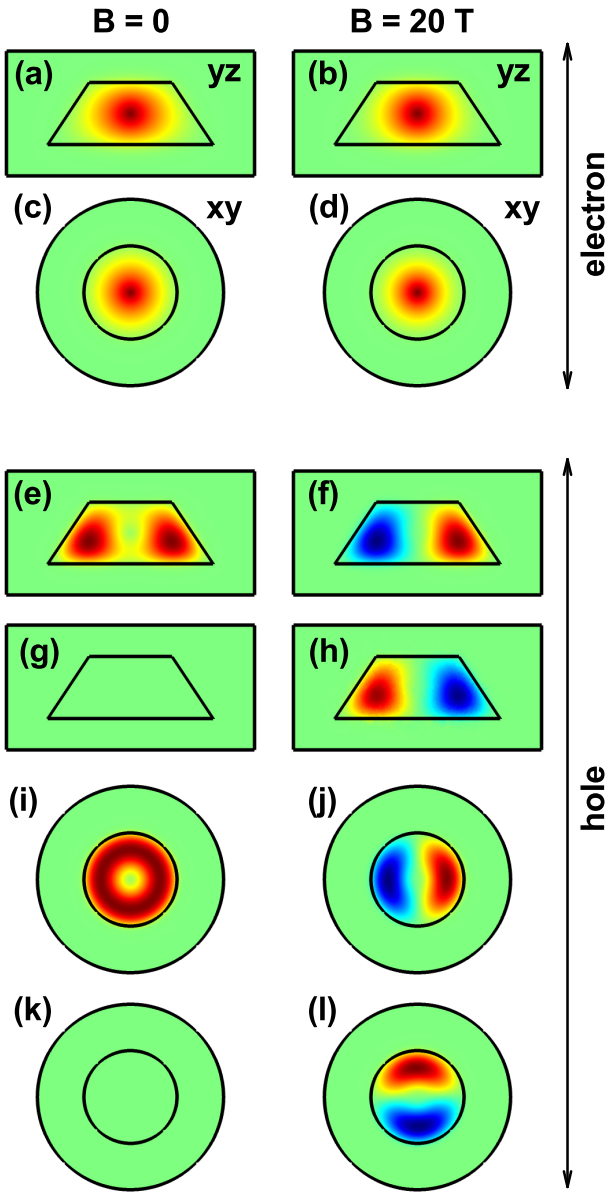

Figure 3-4.: The $x = 0$ (a-b, e-h) and $z = 7.5\,\mathrm{nm}$ (c-d, i-l) projections of the electron and heavy-hole ground state wavefunctions (WF) in a truncated conical-shaped GaAs-$Al_{0.3}Ga_{0.7}As$ quantum dot, for two values of the vertically applied magnetic field (each column corresponds to a fixed value of the magnetic field). The first two rows are for the real part of the electron WF, rows 3 and 5 are for the real part of the hole WF, whereas rows 4 and 6 are for the imaginary part of the hole WF. Calculations are for $R_1 = 10\,\mathrm{nm}$, $R_2 = 20\,\mathrm{nm}$, $h = 15\,\mathrm{nm}$, and with a donor impurity located at $z_i = 7.5\,\mathrm{nm}$.

changes in the symmetry of the heavy-hole ground state (evolving from $l = 0$ for $B = 0$ up to $l = +1$ for $B = 20\,\mathrm{T}$; (see the row 5 in Fig. **3-4**). These results are in agreement with the ground state of Fig. **3-3**(b). For $B = 20\,\mathrm{T}$, there is complementarity between the WF's real and imaginary components (see panels (j) and (k)). This means that the sum of the two components' squares generates a probability density that shows ring-shaped symmetry, as occurs in the absence of a magnetic field, see Fig. **3-4**(i).

3.3.2. Exciton states in GaAs-$Al_{0.3}Ga_{0.7}As$ truncated conical quantum dot under impurity and static magnetic field

This subsection is dedicated to studying the excitonic contribution in GaAs-$Al_{0.3}Ga_{0.7}As$ truncated conical QD considering the effects of shallow-donor impurity and static applied magnetic field.

In Fig. **3-5** are shown the results for the electron-hole pair in a truncated conical-shaped GaAs-$Al_{0.3}Ga_{0.7}As$ QD as a function of the R_2-lower structure radius. In Fig. **3-5**(a) is shown the Coulomb energy calculated by Eq. (3-4). Fig. **3-5**(b) results are for the overlap integral (OI) between the electron and heavy-hole ground states. Finally, the Figs. **3-5**(c-d) correspond to the electron and heavy-hole z-expected value ($\langle z_e \rangle$ and $\langle z_h \rangle$). From Fig. **3-5**(a), it can be inferred that, regardless of the presence or not of the donor impurity, with the increase of R_2 there is a loss of the electron-hole interaction. Note the decreasing character with R_2 of all the curves, which can be explained by an increase in the expected value of the electron-hole distance —$\langle |\vec{r}_e - \vec{r}_h| \rangle$. In the absence of impurity, the electron and hole are located essentially at the same vertical position. As R_2 goes from zero to 20 nm, the maxima of the electron and hole probability densities shift (with decreasing values of $\langle z_e \rangle$ and $\langle z_h \rangle$) from the gravity center of an inverted cone towards the gravity center of a truncated cone with a major/minor radius at the bottom/top base of the QD. This fact explains the quasi-overlap and decreasing behavior of $\langle z_e \rangle$ and $\langle z_h \rangle$ in Figs. **3-5**(b-d). The increase of the OI with $\kappa = 0$ is mainly associated with the increase of the structure's volume. In the case $\kappa \neq 0$, the OI follows the behavior exhibited by the difference between $\langle z_e \rangle$ and $\langle z_h \rangle$. The OI is maximum when

$|\langle z_e\rangle - \langle z_h\rangle| \to 0$ and is minimum when $|\langle z_e\rangle - \langle z_h\rangle|$ is maximum. The previously mentioned change in the structure's geometry also explains the decreasing value of $\langle z_e\rangle$ and $\langle z_h\rangle$ in Figs. **3-5**(c-d). Including the impurity at different positions modifies the behavior of $\langle z_e\rangle$ and $\langle z_h\rangle$. For $z_i = 0$, $|\langle z_e\rangle - \langle z_h\rangle|$ increases in the range $0 < R_2 < 7\,\text{nm}$. With the increase of R_2, the electron moves towards the impurity center; this explains why it goes faster towards lower z_e-values. In contrast, the hole is subjected to two conditions that generate inverse effects; on the one hand, the decrease in confinement associated with the increase R_2 implies a fall in $\langle z_h\rangle$, but the rate of decrease is lower than that of $\langle z_e\rangle$, with a quasi-linear behavior, because on the other hand, the impurity at $z_i = 0$ repels the hole.

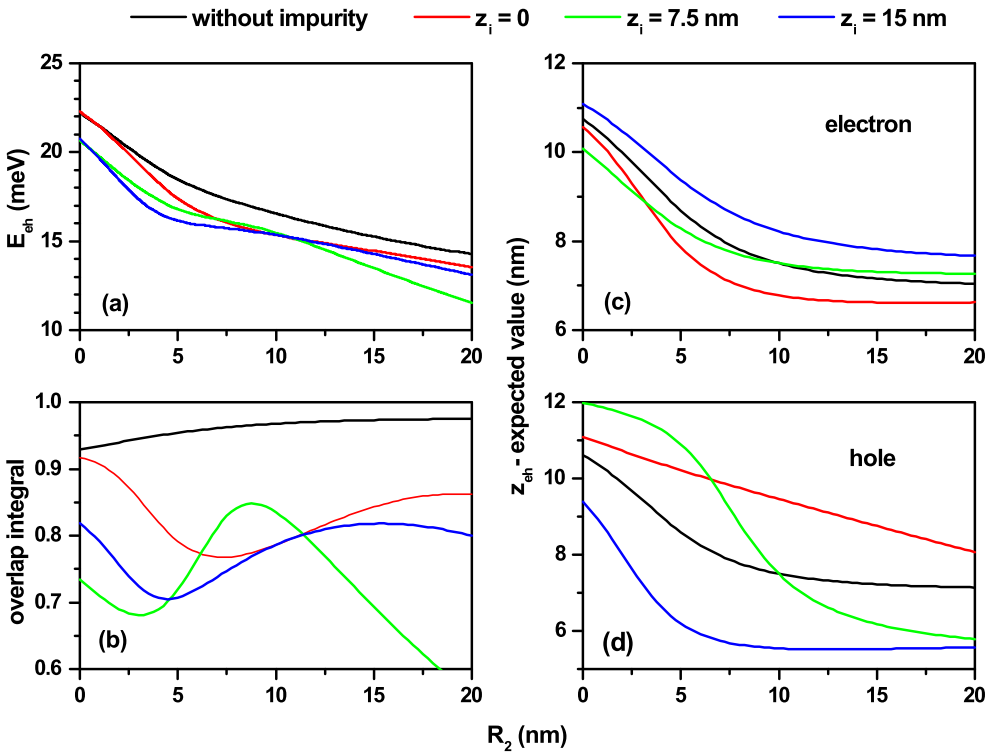

Figure 3-5.: Characterization of the heavy-hole exciton states in a truncated conical-shaped GaAs-$Al_{0.3}Ga_{0.7}As$ quantum dot as a function of the R_2-lower structure radius. (a) Electron-hole Coulomb energy, (b) overlap integral, and (c-d) the z-average position of the carriers; electron (c) and heavy-hole (d). According to the color code, calculations are without and with a shallow-donor impurity, localized at three positions along the z-axis. The results are for $R_1 = 10\,\text{nm}$, $h = 15\,\text{nm}$, and $B = 0$.

In Fig. **3-6**, the same kind of results are reported as in Fig. **3-5**, but for fixed QD dimensions and as a function of the applied magnetic field. In Fig. **3-6**(a), without impurity, the electron-hole Coulomb energy increases. This fact is largely explained by the decrease in the carriers' separation with the increase in the magnetic field, information extracted from Figs. **3-6**(d-f) for $|\langle z_e\rangle - \langle z_h\rangle|$, where the OI systematically increases. Due to the opposite effect that the impurity has on the electron and the hole, that is, attraction and repulsion, respectively, lower Coulomb energies are generally observed compared to the case of no impurity. In Figs. **3-6**(b-c), the Coulomb energies for $z_i = 7.5\,\text{nm}$

and $z_i = 15\,\text{nm}$, respectively, from Fig. **3-6**(a) are plotted. The idea of these plots is to emphasize the confinement behavior of both the electron and the hole when symmetry changes of the ground state WFs occur due to the effect of the applied magnetic field. In Fig. **3-6**(b), for $B < 8.5\,\text{T}$, the electron and hole ground state WFs are obtained for $l = 0$, and in this case, the imaginary part of the WFs for both carriers is zero. The s-type symmetry for the electron and ring symmetry for the hole is clearly identified. For $B > 8.5\,\text{T}$, the ground state of the hole corresponds to $l = 1$, and complementarity between the real and imaginary parts of the WFs appears, but a ring symmetry for the probability density is maintained. In Fig. **3-6**(c), the results are similar to those depicted in Fig. **3-6**(b), but in this case, the transition of the ground state hole WF moves to a higher magnetic field value. The small increase observed in the Coulomb energy for $z_i = 0$ and $z_i = 15\,\text{nm}$, with the magnetic field influence, is because despite having a lower OI with the increasing of the magnetic field, the WFs are located in a smaller volume, which increases the Coulomb integral value. The change in symmetry of the WFs for the ground state of the hole explains the jumps in the curves of the Coulomb integral for $z_i = 7.5\,\text{nm}$ and $z_i = 15\,\text{nm}$ shown in Fig. **3-6**(a) and detailed in Figs. **3-6**(b) and **3-6**(c) with the corresponding electron and hole WFs for two particular values of the applied magnetic field.

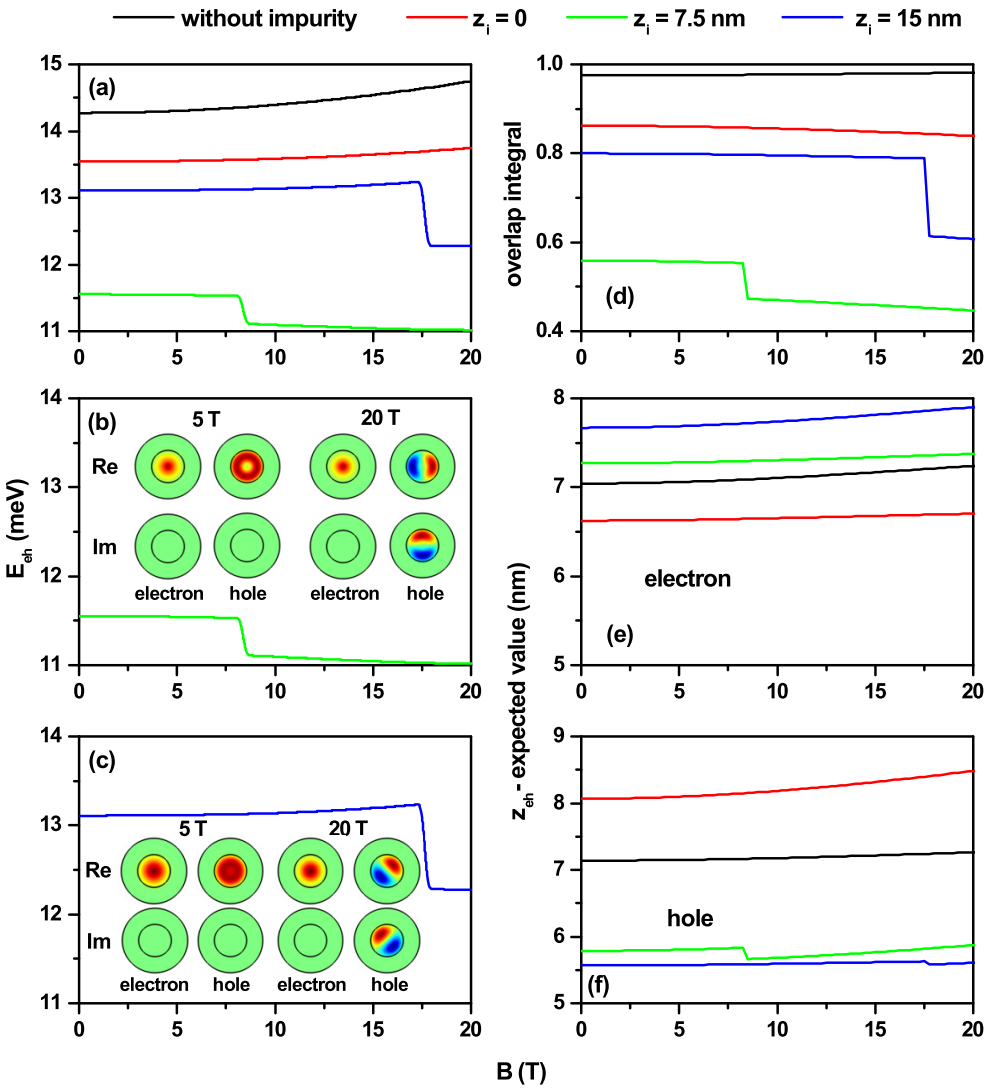

Figure 3-6.: Characterization of the exciton effects in a truncated conical-shaped GaAs-$Al_{0.3}Ga_{0.7}As$ quantum dot as functions of the vertically applied magnetic field. (a) e-h Coulomb energy with $\kappa = 0$ and $\kappa \neq 0$ with three impurity positions, (b) e-h Coulomb energy with the impurity at $z_i = 7.5\,\text{nm}$, (c) e-h Coulomb energy with the impurity at $z_i = 15\,\text{nm}$, (d) overlap integral, (e) z_e-average electron position, and (f) z_h-average hole position. The results are for $R_1 = 10\,\text{nm}$, $R_2 = 20\,\text{nm}$, and $h = 15\,\text{nm}$. Few electron and hole wavefunctions projections (real and imaginary parts) at the $z = 7.5\,\text{nm}$ plane are shown in panels (b) and (c).

In order to have a better perspective on the effects of the impurity position, it has been varied from the lower base to the upper base of the truncated conical-shaped GaAs-$Al_{0.3}Ga_{0.7}As$ QD, always located along the z-axis. This position is controlled by the parameter z_i. The following graphs are shown in Fig. **3-7**: (a) the electron and hole ground state energies, (b) the electron-hole Coulomb energy, (c) the overlap integral, and (d) z the average position of the electron and hole along the z-axis. Calculations are for $R_1 = 10\,\text{nm}$, $R_2 = 20\,\text{nm}$, $h = 15\,\text{nm}$, and $B = 0$. In Fig. **3-7**(a), the reverse effect on the electron and the hole of a donor impurity is clearly seen. The electron has an attractive character, and for the hole, it is a repulsive one. When the impurity is in the first half of the height, that is $z_i \leq 15\,\text{nm}$, the electron is attracted to a region of lower confinement, and the hole is being expelled to the region of higher confinement. In the second half of the height, i.e. for $z_i \geq 15\,\text{nm}$, the opposite effect on each charge carrier occurs. Hence, there is increasing energy for the electron and decreasing energy for the hole. The Coulomb energy in

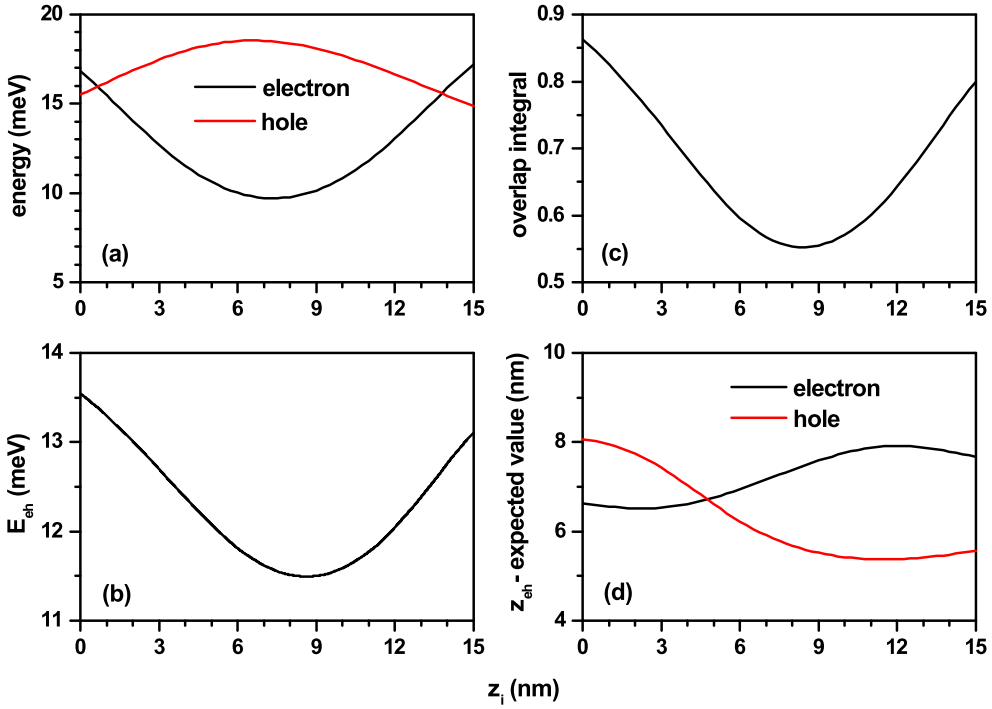

Figure 3-7.: Characterization of the exciton effects in a truncated conical-shaped GaAs-$Al_{0.3}Ga_{0.7}As$ quantum dot as a function of donor impurity position z_i. (a) Ground state for electron and hole, (b) electron-hole Coulomb energy, (c) overlap integral, and (d) z expected value for each carrier. Calculations are for $R_1 = 10\,\text{nm}$, $R_2 = 20\,\text{nm}$, $h = 15\,\text{nm}$, and $B = 0$.

Fig. **3-7**(b) decreases up to $z_i = 8.5\,\text{nm}$ because statistically speaking, the electron and hole are being separated by the donor impurity. From $z_i = 8.5\,\text{nm}$, the competition between the impurity effect and the volume for the electron causes the electron to stay in a region that is in a better overlap with the hole, which is in absolute agreement with the OI in Fig. **3-7**(c). Since the impurity is located on the z-axis, the z-expected value for each of the particles is evidence from how the impurity modifies the positions of the charge carriers. Note that the Coulomb energy for the impurity at $z_i = 0$ is higher than the energy for $z_i = 15\,\text{nm}$, which is justified by the larger z-separation between the two particles at $z_i = 15\,\text{nm}$ (see Fig. **3-7**(d)). Also, note that for $z_i = 4.75\,\text{nm}$ the combined effects of geometry and impurity make the expected z-value the same for electron and hole. At that value of z_i the higher Coulomb energy does not

occur because it must be taken into account that there are geometry effects at different z-planes.

3.3.3. Tuning from direct to indirect exciton in truncated conical CdSe-CdTe core-shell quantum dots

In this section, according with the Figs. **3-1**(c) and **3-1**(d), a core-shell system of CdTe-CdSe and CaSe-CdTe quantum dots is studied, in which a transition between spatially direct and spatially indirect exciton occurs. The parameters we will use in this subsection are: *i*) in CdTe $m_e = 0.096\, m_0$, $m_h = 0.40\, m_0$, and $\varepsilon = 10.2$; *ii*) in CdSe $m_e = 0.120\, m_0$, $m_h = 0.45\, m_0$, and $\varepsilon = 10.2$ [50]. Additionally, $V_e^0 = 0.42\,\text{eV}$ and $V_h^0 = 0.57\,\text{eV}$. [50]
In Fig. **3-8** is presented the characterization of the exciton states related to the case of Fig. **3-1**(c). As stated in the introduction section, the CdTe behaves as the barrier/well region for electrons/holes in this case, and the CdSe corresponds to the well/barrier region for electrons/holes. When $\xi = 0$, the electron and hole are confined in a truncated conical QD with an infinite potential barrier. When $\xi \neq 0$ appears, the potential well for electrons is located in the CdSe region. For small values of ξ ($\xi < 1.5$ nm), the electron remains in the CdTe region due to the strong confinement in the CdSe region. For $\xi > 1.5\,\text{nm}$, the CdSe volume becomes large enough for the electron to penetrate the region where its potential well is located. At that time, both charge carriers are each located in the regions of their own potential wells, i.e., the hole in CdTe and the electron in CdSe, and a spatially indirect excitonic system appears. The sharp drop in electron energy in Fig. **3-8**(a) is associated with the change of confinement region and the subsequent increase in the volume of the shell region. The slight perceptible variations in the hole's energy appear when the finite potential barrier located on the lateral face of the structure becomes present. However, from a specific value of ξ, the hole's energy does not show variations due to the constant volume of the core region as ξ increases. The drop in the Coulomb energy in Fig. **3-8**(c) is explained by the fact that the mean electron-hole distance is increasing with the ξ-parameter. Fig. **3-8**(d) allows identifying the transition from direct to indirect exciton, due to initially the particles are

in the CdTe and as ξ increases, the electron shifts to the CdSe region, with the hole always localized at the CdTe region, reaching an indirect exciton.

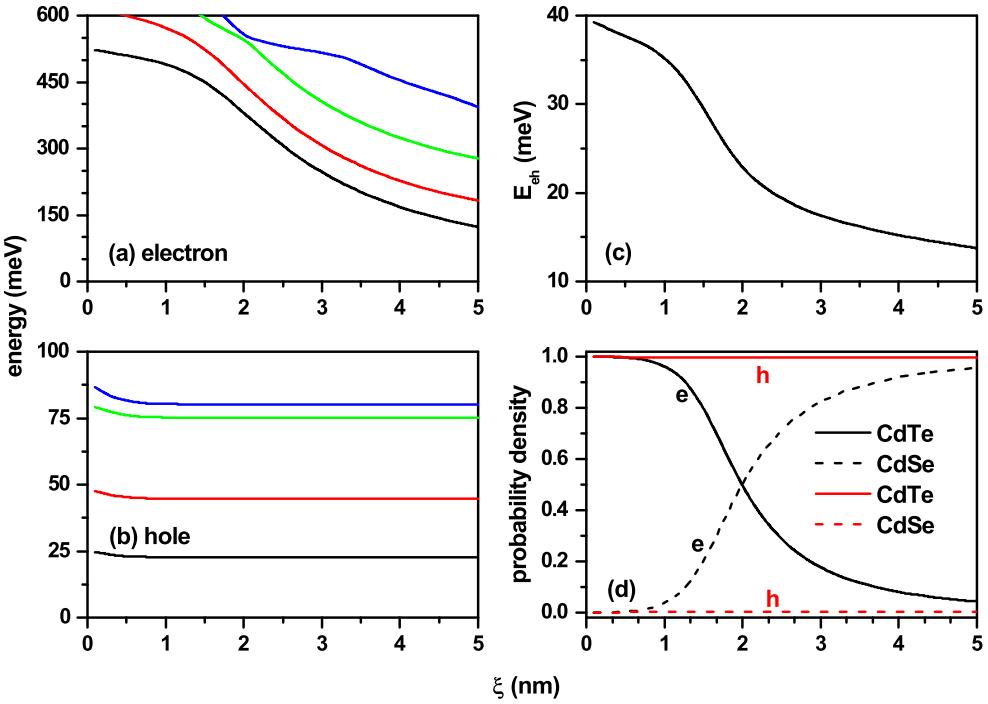

Figure 3-8.: Characterization of the exciton effects in a truncated CdTe-CdSe conical-shaped quantum dot concerning the ξ-parameter. The first fourth energy levels for the electron (a) and hole (b) are shown. In (c) electron-hole Coulomb energy, whereas in (d) are depicted the probability density for both electron and hole in each material CdTe and CdSe. The calculations are for $R_1 = 3\,\text{nm}$, $R_2 = 8\,\text{nm}$, $h = 12\,\text{nm}$, $B = 0$ and impurity absence.

The characterization of the exciton states related to the case of Fig. **3-1**(d) is shown in Fig. **3-9**, where the results are concerning the ξ-parameter. From Fig. **3-1**(d), it can be seen that by increasing the ξ-parameter, the volume of the CdSe region decreases, which corresponds to the potential well for electrons. Consequently, the energy of the electron levels must grow with the ξ-parameter, as shown in Fig. **3-9**(a). When $\xi \to 0$, the hole is confined in the region of its potential barrier, surrounded by an infinite potential, and in this case, the energies of all confined states (E) fulfill the condition $E > V_h^0 = 0.57\,\text{eV}$, as shown in Fig. **3-9**(b) in the regime $\xi < 1.0\,\text{nm}$. When $\xi > 1.0\,\text{nm}$, the volume

of the shell region becomes large enough for the hole to migrate towards the region of its potential well, that is, towards the CdTe region. The volume of the CdTe, shell region, grows progressively with the ξ-parameter, and with it, the confinement on the hole decreases, which is manifested in a fall in all energy levels, a situation shown in Fig. **3-9**(b). We can then conclude that the system presents an evolution from a spatially direct exciton with the hole and the electron both located in the CdSe region towards a spatially indirect exciton for large values of ξ-parameter with the electron in the core region, whose volume decreases, and the hole in the shell region, the volume of which increases. The interpretation presented here is confirmed by the ever-decreasing behavior of the Coulomb integral in Fig. **3-9**(c) and the probability densities in Fig. **3-9**(d).

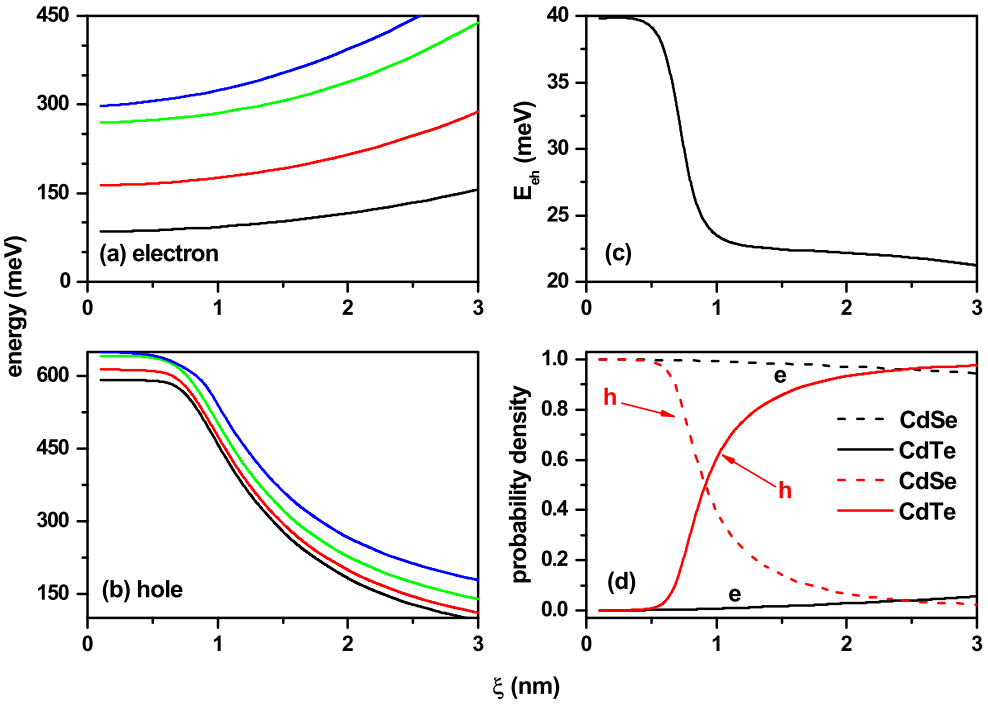

Figure 3-9.: Characterization of the exciton effects in a truncated CdSe-CdTe conical-shaped quantum dot as a function of the ξ-parameter in accordance with Fig. **3-8**(b). The lowest energy levels for the electron (a) and hole (b) are shown. In (c), the results are for the electron-hole Coulomb energy, whereas in (d), the probability density for both electron and hole in each CdSe and CdTe material are presented. The calculations are for $R_1 = 3\,\text{nm}$, $R_2 = 8\,\text{nm}$, $h = 12\,\text{nm}$, $B = 0$, and impurity absence.

3.4. Conclusions

In this paper, we have studied the electron and hole states in GaAs-(Ga,Al)As conical-shaped QDs in the presence of an axially located shallow-donor impurity under the effects of an externally applied magnetic field and CdSe-CdTe core-shell QDs without impurity and magnetic field effects. The impurity position and the magnetic field direction preserve the axial symmetry of the system. Variations of the geometry have been considered, in which case the structures evolve from conical QDs to truncated conical QDs. Calculations have been do-

ne in the effective mass approximation and considering a parabolic two-bands model. The eigenvalues differential equations have been solved via a finite element method with a flexible discretization mesh. The electron-hole correlation was studied with a first-order perturbation approximation. Among the most relevant results of this study we can cite: *i*) the presence of the shallow-donor impurity is responsible for a red/blue shift of the electron/hole energies, *ii*) the binding energy for the electron-impurity system in general decreases with the size of the structure; but with exceptions for specific geometries, the binding energy is an increasing function with the radius of the lower base of the system, *iii*) the applied magnetic field is responsible for the hole-impurity ground state oscillations, *iv*) the binding energy for the electron-impurity system is always an increasing function of the applied magnetic field, and *v*) a control to tune between direct and indirect exciton by changes of thickness of CdSe or CdTe in the core-shell type QD was reached. In the case of the correlation energy between the electron-impurity and hole-impurity states, it is observed that, in general, they decrease with the size of the structure. Considering the presence of applied magnetic fields, they present an essentially constant behavior in specific ranges of the magnetic field with jumps associated with oscillations of the hole-impurity ground state. The localization of the electron and hole states in the presence of impurity and the overlap integral are essential information to adequately interpret the Coulomb correlation between the electron-impurity and hole-impurity states.

References

[1] Lorke, A.; Luyken, R.J. Many-particle ground states and excitations in nanometer-size quantum structures. *Physica B* **1998**, *256-258*, 424–430.

[2] Warburton, R.J.; Schulhauser, C.; Haft, D.; Schäflein, C.; Karrai, K.; Garcia, J.M.; Schoenfeld, W.; Petroff, P.M. Giant permanent dipole moments of excitons in semiconductor nanostructures. *Phys. Rev. B* **2002**, *65*, 113303.

[3] Alén, B.; Martínez-Pastor, J.; Granados, D.; García, J.M. Continuum and discrete excitation spectrum of single quantum rings. *Phys. Rev. B* **2005**, *72*, 155331.

[4] Kuroda, T.; Mano, T.; Ochiai, T.; Sanguinetti, S.; Sakoda, K.; Kido, G.; Koguchi, N. Optical transitions in quantum ring complexes. *Phys. Rev. B* **2005**, *72*, 205301.

[5] Bastard, G. Hydrogenic impurity states in a quantum well: a simple model. *Phys. Rev. B* **1981**, *24*, 4714–4722.

[6] Greene, R.L.; Bajaj, K.K. Effect of magnetic field on the energy levels of a hydrogenic impurity center in GaAs/$Ga_{1-x}Al_xAs$ quantum-well structures. *Phys. Rev. B* **1985**, *31*, 913–918.

[7] Greene, R.L.; Bajaj, K.K. Energy levels of hydrogenic impurity states in GaAs-$Ga_{1-x}Al_xAs$ quantum well structures. *Solid State Commun.* **1983**, *45*, 825–829.

[8] Branis, S.V.; Li, G.; Bajaj, K.K. Hydrogenic impurities in quantum wires in the presence of a magnetic field. *Phys. Rev. B* **1993**, *47*, 1316–1323.

[9] Zhu, J.-L. Exact solutions for hydrogenic donor states in a spherically rectangular quantum well. *Phys. Rev. B* **1989**, *39*, 8780–8783.

[10] Ribeiro, F.J.; Latgé, A. Impurities in a quantum dot: a comparative study. *Phys. Rev. B* **1994**, *50*, 4913–4916.

[11] Szafran, B.; Adamowski, J.; Bednarek, S. Electron–electron correlation in quantum dots. *Physica E* **1999**, *5*, 185–195.

[12] Zhou, W.; Coleman, J.J. Semiconductor quantum dots. *Curr. Opin. Solid St. M.* **2016**, *20*, 352—360.

[13] Gaponenko, S.V.; Demir, H.V. *Applied Nanophotonics*, Cambridge University Press, Cambridge, 2019, p. 433.

[14] Porras-Montenegro, N.; Pérez-Merchancano, S.T.; Latgé, A. Binding energies and density of impurity states in spherical GaAs-(Ga,Al)As quantum dots. *J. Appl. Phys.* **1993**, *74*, 7624–7626.

[15] Le Goff, S.; Stébé, B. Influence of longitudinal and lateral confinements on excitons in cylindrical quantum dots of semiconductors. *Phys. Rev. B* **1993**, *47*, 1383–1391.

[16] Cristea, M.; Niculescu, E.C.; Truşcă, C.R. Optical non-linearities associated to hydrogenic impurities in InAs/GaAs self-assembled quantum dots under applied electric fields. *Philos. Mag.* **2017**, *97*, 3343–3360.

[17] Niculescu, E.C.; Stan, C.; Cristea, M.; Truscă, C. Magnetic-field dependence of the impurity states in a dome-shaped quantum dot. *Chem. Phys.* **2017**, *493*, 32–41.

[18] Medvid, A. Nano-cones formed on a surface of semiconductors by laser radiation: technology, model and properties. *Nanowires Science and Technology*; Intech, Vukovar, 2010, 61—82.

[19] Nedzinskas, R.; Karpus, V.; Čechavičius, B.; Kavaliauskas, J.; Valušis, G. Electron energy spectrum in cylindrical quantum dots and rods: approximation of separation of variables. *Phys. Scripta* **2015**, *90*, 065801.

[20] Sil, N.; Daripa, N.; Kapoor, A.; Dey, S.K. Perturbation method for calculating impurity binding energy in an inhomogeneous cylindrical quantum dot with dielectric mismatch. *Pramana-J. Phys.* **2018**, *90*, 7.

[21] Mal, I.; Samajdar, D.P.; John Peter, A. Theoretical studies on band structure and optical gain of GaInAsN/GaAs/GaAs cylindrical quantum dot. *Superlattice Microst.* **2018**, *119*, 103–113.

[22] Lin, H.-M.; Chen, Y.-L.; Yang, J.; Liu, Y.-C.; Yin, K.-M.; Kai, J-.J.; Chen, F.-R.; Chen, L.-C.; Chen, Y.-F.; Chen, C.-C. Synthesis and characterization of core-shell GaP@GaN and GaN@GaP nanowires. *Nano Lett.* **2003**, *3*, 537–541.

[23] Medvid, A.; Mychko, A.; Strilchyk, O.; Litovchenko, N.; Naseka, Y.; Onufrijevs, P.; Pludonis, A. Exciton quantum confinement effect in nanostructures formed by laser radiation on the surface of CdZnTe ternary compound. *Phys. Status Solidi C* **2009**, *6*, 209–212.

[24] Maher, O.; Témim, K.; Jlassi, B.; Balti, J.; Jaziri, S. Effect of the In (Ga) inter-diffusion on the optical properties in InAs/GaAs annealed quantum dots. *J. Phys. Conf. Ser.* **2010**, *245*, 012066.

[25] Medvid, A.; Onufrijevs, P.; Mychko, A. Properties of nanocones formed on a surface of semiconductors by laser radiation: quantum confinement effect of electrons, phonons, and excitons. *Nanoscale Res. Lett.* **2011**, *6*, 582.

[26] Nadj-Perge, S.; Frolov, S.M.; Bakkers, E.P.A.M.; Kouwenhoven, L.P. Spin-orbit qubit in a semiconductor nanowire. *Nature* **2010**, *468*, 1084–1087.

[27] Tatebayashi, J.; Kako, S.; Ho, J.; Ota, Y.; Iwamoto, S.; Arakawa, Y. Roomtemperature lasing in a single nanowire with quantum dots. *Nat. Photonics* **2015**, *9*, 501–505.

[28] Svensson, J.; Dey, A.W.; Jacobsson, D.; Wernersson, L.-E. III-V nanowire complementary metal-oxide semiconductor transistors monolithically integrated on Si. *Nano Lett.* **2015**, *15*, 7898–7904.

[29] Heedt, S.; Prost, W.; Schubert, J.; Grützmacher, D.; Schäpers, T. Ballistic transport and exchange interaction in InAs nanowire quantum point contacts. *Nano Lett.* **2016**, *16*, 3116–3123.

[30] Diedenhofen, S.L.; Janssen, O.T.A.; Grzela, G.; Bakkers, E.P.A.M.; Gómez Rivas, J. Strong geometrical dependence of the absorption of light in arrays of semiconductor nanowires. *ACS Nano* **2011**, *5*, 2316–2323.

[31] Khordad, R.; Bahramiyan, H. Study of impurity position effect in pyramid and cone like quantum dots. *Eur. Phys. J. Appl. Phys.* **2014**, *67*, 20402.

[32] Hayrapetyan, D.B.; Kazaryan, E.M.; Sarkisyan, H.A. Magneto-absorption in conical quantum dot ensemble: possible applications for QD LED. *Opt. Commun.* **2016**, *371*, 138–143.

[33] Delerue, C.; Lannoo, M. *Nanostructures Theory and Modelling*, Springer, Heidelberg, 2004, p. 304.

[34] Wang, Y.; Wang, J.; Guo, H. Magnetoconductance of a stadium-shaped quantum dot: a finite-element-method approach. *Phys. Rev. B* **1994**, *49*, 1928–1934.

[35] Zhou, W.-M.; Wang, C.-Y.; Chen, Y.-H.; Wang, Z.-G. Finite element analysis of stress and strain distributions in InAs/GaAs quantum dots. *Chinese Phys.* **2006**, *15*, 1315–1319.

[36] Satori H.; Sali, A. The finite element simulation for the shallow impurity in quantum dots. *Physica E* **2013**, *48*, 171–175.

[37] Jurczak, G.; Dłużewski, P. Finite element modelling of threading dislocation effect on polar GaN/AlN quantum dot. *Physica E* **2018**, *95*, 11–15.

[38] Solaimani, M. Binding energy and diamagnetic susceptibility of donor impurities in quantum dots with different geometries and potentials. *Mater. Sci. Eng. B-Adv* **2020**, *262*, 114694.

[39] Khaledian, S.; Nalaini, F.; Mehrbakhsh, M.; Abdoli, M.; Salehi Zahabi, S. Applications of novel quantum dots derived from layered materials in cancer cell imaging. *FlatChem* **2021**, *27*, 100246.

[40] Nxele, S.R.; Nyokong, T. The effects of the composition and structure of quantum dots combined with cobalt phthalocyanine and an aptamer on the electrochemical detection of prostate specific antigen. *Dyes Pigments* **2021**, *192*, 109407.

[41] Gidwani, B.; Sahu, V.; Shukla, S.S.; Pandey, R.; Joshi, V.; Jain, V.K.; Vyas, A. Quantum dots: prospectives, toxicity, advances and applications. *J. Drug Deliv. Sci. Tec.* **2021**, *61*, 102308.

[42] Kumar, P. Semiconductor (CdSe and CdTe)quantum dot: synthesis, properties and applications. *Mater. Today-Proc.* **2021**.

[43] Vinasco, J.A.; Radu, A.; Kasapoglu, E.; Restrepo, R.L.; Morales, A.L.; Feddi, E., Mora-Ramos, M.E.; Duque, C.A. Effects of geometry on the electronic properties of semiconductor elliptical quantum rings. *Sci. Rep.* **2018**, *8*, 13299.

[44] Vinasco, J.A.; Radu, A.; Restrepo, R.L.; Morales, A.L.; Mora-Ramos, M.E.; Duque, C.A. Magnetic field effects on intraband transitions in elliptically polarized laser-dressed quantum rings. *Opt. Mater.* **2019**, *91*, 309–320.

[45] COMSOL Multiphysics, v. 5.4. COMSOL AB, Stockholm, Sweden.

[46] COMSOL Multiphysics Reference Guide, Stockholm, Sweden (May 2012).

[47] COMSOL Multiphysics Users Guide, Stockholm, Sweden (May 2012).

[48] Heyn, C.; Duque, C.A. Donor impurity related optical and electronic properties of cylindrical GaAs-$Al_xGa_{1-x}As$ quantum dots under tilted electric and magnetic fields. *Sci. Rep.* **2020**, *10*, 9155.

[49] Heyn, C.; Radu, A.; Vinasco, J.A.; Laroze, D.; Restrepo, R.L.; Tulupenko, V.; Hieu, N.N.; Phuc, H.V.; Mora-Ramos, M.E.; Ojeda, J.H.; Morales, A.L.; Duque, C.A. Exciton states in conical quantum dots under applied electric and magnetic fields. *Opt. Laser Technol.* **2021**, *139*, 106953.

[50] Suresh, S.; Arunseshan, C. Dielectric Properties of Cadmium Selenide (CdSe) Nanoparticles synthesized by solvothermal method. *Appl. Nanosci.* **2014**, *4*, 179–184.

4. Self-Consistent Schrödinger-Poisson Study of Electronic Properties of GaAs Quantum Well Wires with Various Cross-Sectional Shapes

Quantum wires continue to be a subject of novel applications in the fields of electronics and optoelectronics. In this work, we revisit the problem of determining the electron states in semiconductor quantum wires in a self-consistent way. For that purpose, we numerically solve the 2D system of coupled Schrödinger and Poisson equations within the envelope function and effective mass approximations. The calculation method uses the finite-element approach. Circle, square, triangle and pentagon geometries are considered for the wire cross-sectional shape. The features of self-consistent band profiles and confined electron state spectra are discussed, in the latter case, as functions of the transverse wire size and temperature. Particular attention is paid to elucidate the origin of Friedel-like oscillations in the density of carriers at low temperatures.

4.1. Introduction

Quantum wires (QWs) are low-dimensional semiconductor structures with strong two-dimensional localization of charge carriers, leaving a single spatial direction

for their "free" displacement so that the term quasi-one-dimensional systems became adopted. This feature leads to the quantization of the energy spectrum for the motion along the cross-section of the conduction channel. The beginnings of research on this type of nanosystems date back to the 1980s, with illustrative examples in References [1–17], and has continued until the present, with a significant number of experimental and theoretical reports in the literature. Among the most recent works on QWs, we can mention those appearing in References [18–28].

With time, the concept of QW has included a modification through the term "nanowire", due to the possibility of practical realization of wire-shaped structures with finite length [29]. Among the applications of these low-dimensional semiconductor systems, one finds the case of solar cells, in which a suitable selection of nanowire geometry can have advantages in terms of cell performance and efficiency [30]. On the other hand, in a recent report, Jia and collaborators review the state-of-the-art concerning applications of nanowires to electronics [31]. The authors discuss nanoscale devices and integrated circuits assembled from nanowire building elements, including nanowire thin-film transistors, oriented to the fabrication of high-performance large-area flexible electronics.

The self-consistent (SC) method has been a choice for determining the spectrum of electron and hole states in low-dimensional semiconductor nanostructures when many-body contributions on the energy band profile are taken into account. A typical procedure of this kind is the one described in [32], which uses the finite element method for the SC non-linear problem of coupled Schrödinger and Poisson equations for layered heterostructures with arbitrary doping profiles and layer geometries within a multiband $\vec{k} \cdot \vec{p}$ framework. In the particular case of QW-like systems, it is possible to mention initial works by Laux and co-workers [33, 34]. In the first of these two works, the electron states in narrow gate-induced channels in a one-dimensional Si conduction channel are self-consistently determined solutions. In the second one, the solution of the Schrödinger-Poisson (SP) system of equations allowed to calculate electron states in a split-gate quasi-one-dimensional GaAs/AlGaAs heterostructure. Later on, Luscombe et al. solved the SCSP problem to investigate the electron confinement in laterally confined cylindrical QWs [35]. The Fourier expansion method was the approach selected by Tadić and collaborators to investigate the SC elec-

tronic structure of rectangular free-standing quantum wires [36]. A report by Trellakis and Ravaioli discusses the computational issues in the SC simulation of the electronic features of QWs [37]. The authors discuss the numerical solution for the coupled SP equation system (including exchange and correlation effects) and outline an iteration procedure—based on the predictor-corrector method—for convergence of the outer iteration.

The SC method of 2D finite differences for solving the SP equations for etched mesa GaAs/AlGaAs structures has been reported by Snider et al. in a 1990 paper [38]. This was one of the first studies showing that, for quantum wire behavior to occur, it is necessary to precisely control the width variation of the fabricated wire. The coupled Schrödinger and Poisson equations, within the Hartree approximation, have been solved by Proetto for a GaAs quantum wire with cylindrical symmetry [39]. The charge distribution, potential profile and electronic structure dependence on the wire radius and surface states' concentration were discussed. Kerkhoven et al. have demonstrated the importance of self-consistency for analyzing the electrons confined in quantum wires [40]. By solving the Schrödinger and Poisson equations, they simulated the behavior of the low-temperature electrons behavior in QW-like structures formed by crossing layers of GaAs and AlGaAs. By using an SC screening scheme, Hu and Das Sarma have calculated the elastic mean free path of impurity-scattered carriers in a quantum wire [41]. They discussed the scale over which the electronic conduction in quantum wires is expected to exhibit metallic behavior. By solving the Poisson and Schrödinger equations iteratively for a QW-like split-gate heterojunction, Martorell et al. have studied the accuracy of the commonly used 2D approximation when applied to whole 3D systems [42]. Their work focused on interpreting general trends rather than on some specific system and simplifying assumptions for reducing the computational effort. Aristone and Sanchez-Dehesa have used the SC-SP method to investigate arbitrary profile quantum wires [43]. They discussed the numerical results for QWs of rectangular cross-sections, emphasizing the conditions under which such low-dimensional systems exhibit bi-stability. May et al. have performed an SC two-dimensional calculation of the electronic width of quantum wires formed by local oxidation on GaAlAs heterostructures [44]. They envisioned the key role that was going to be played by the SC simulations in designing novel structures and bet-

ter understanding the electrostatic action of the electronic gates. Chuen et al. have calculated by an SC approach the induced charge density, capacitance, and conductance of a quantum wire [45]. They discussed the dependence of these quantities on the Fermi energy and the frequency of the external voltages.

Sharma and Suryanarayana presented a cyclic and helical symmetry-adapted formulation and large-scale parallel implementation of real-space Kohn-Sham density functional theory for one-dimensional nanostructures, with application to the mechanical and electronic response of carbon nanotubes subject to torsional deformations. They developed a high-order finite-difference parallel implementation capable of performing accurate cyclic and helical symmetry-adapted Kohn-Sham calculations in both the static and dynamic settings. Their findings were in good agreement with experimental observations and measurements. Their numerical tools and formalism were previously applied to the study of band structure and bending properties of large X (X = C, Si, Ge, Sn) nanotubes and Xene sheets [46, 47].

A theoretical study of two-dimensional quantum dots with the shape of a regular polygon where the number of sides has varied from three (triangle) to infinity (circle) has been reported by Popescu and coauthors [48]. They used the finite element method to calculate the energies and probability densities for an electron confined in the quantum system. Among their findings, they report that no matter the shape, any regular polygonal quantum dot with more than four sides and a given area has just the same quantitative optoelectronic properties. Additionally, they found that at the nanoscale, the shape may not be as important as the size is.

Efforts to develop cheap and efficient schemes for the electron states' numerical solution in wire-shaped nanosystems have continued throughout the years. A 3D finite-difference time-domain simulation was recently used to solve the problem in cylindrical QWs [49]. Bearing all this in mind, we are interested in bringing a new vision to the subject by solving the SCSP problem in quantum wires with the help of finite-element approach. We shall explore the influence of the QW cross-section shape by considering the circle, square, triangle, and pentagon geometries. We aim at discussing the features of confined state energies and electron density in the system. We are also widely motivated to extend the work

of Popescu et al. [48] to analyze to what extent the shape of the QW boundary (which is controlled by the number of sides of the regular polygon corresponding to its cross-section) can or not be relevant compared to other characteristics of the system such as the cross-sectional area, the density of donors with which the system is doped, and the temperature. In this work, using the effective mass approximation, we study an electron confined in a GaAs QW of infinite length and infinite confinement potential added to an electrostatic potential at the boundary. These two potentials are associated with QWs surrounded by a vacuum or by a matrix with an energy gap greater than that corresponding to the QW one. We report the energy levels in each of the structures with different cross-sections as a function of the transversal area, the doping donor density, and the temperature. We analyze the oscillations that appear in electron density at low temperatures and discuss the contribution made by each of the confined electron states to such oscillations. The chapter is organized as follows—Section 4.2 presents the theoretical framework of the simulation. In Section 4.3 we show and discuss the results obtained, whilst Section 4.4 is devoted to the conclusions of the work.

4.2. Theoretical Framework

The system of interest corresponds to a GaAs QW with a so-called exposed lateral surface. Under this condition, the model has a core-shell structure, where the core constitutes the wire region and the shell would be the surface of the semiconductor. The electronic properties are studied for this system with four different cross-section geometries. In Figure **4-1** are depicted the four structures considered in this work and are defined the coordinate axis, the surrounding material, and the radius of the cylindrical wire case. The wire length is large enough such that a wire with infinite length along the z-axis is a good approximation. Due to the vacuum surrounding matrix, the confinement potential is zero inside the wire region and infinite elsewhere. Having the system with exposed borders is a characteristic of fundamental importance in the numerical approach since the boundary conditions are established for the potential $V(\Omega)$, where Ω represents, in each case, the boundary. This function V establishes the form of the confinement potential.

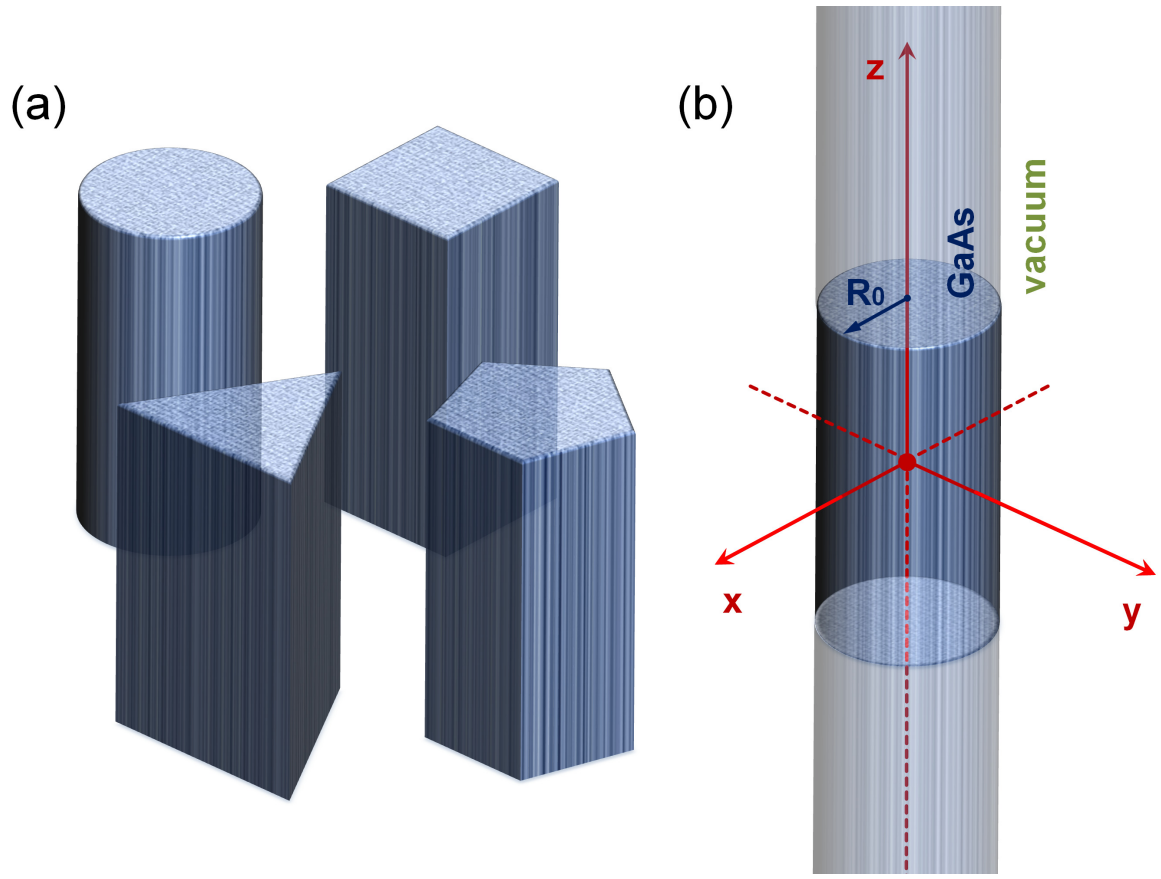

Figure 4-1.: Pictorial view of the GaAs quantum well wire studied in this work. In (**a**) are depicted the four considered structures. In (**b**) are defined the coordinate axis, the R_0-radius for the cylindrical case, and the vacuum surrounding matrix. The wire length is large enough such that a wire with infinite length along the z-axis is a good approximation. Due to the vacuum surrounding matrix, the confinement potential is zero inside the wire region and infinite elsewhere.

In the GaAs quantum wire with the exposed surface, a depletion region is generated at the bottom of the conduction band, which allows the appearance of empty states above the Fermi level; these are surface states that cause a charge transfer from bulk energy states to surface energy states. Consequently, a phenomenon known as "Fermi level Pinning" is present [50]. That is, the Fermi level is kept fixed to a characteristic value within the bandgap of the system, and this value is independent of the density of donors or acceptors. For GaAs,

it is normally used the value on the surface which corresponds to half of the energy bandgap. So, defining the Fermi level as E_F, then the potential at the frontier for each structure will be $V^*(\Omega) - E_F = 0.7$ eV [35].
The Schrödinger-Poisson Equation multiphysics interface, available in the COMSOL Multiphysics version 5.4 [51–53], creates a bidirectional coupling between the electrostatics interface and the Schrödinger Equation interface to model charge carriers in quantum-confined systems. The electric potential from the electrostatics contributes to the potential energy term in the Schrödinger equation. A statistically weighted sum of the probability densities from the energy eigenvalues of the Schrödinger equation contributes to the space charge density in the electrostatics. All spatial dimensions (1D, 1D axial symmetry, 2D, 2D axial symmetry, and 3D) are supported.
In the numerical procedure, it is required to solve coupled SP differential equations in a self-consistent way to obtain the potential profile and electron density for each of the quantum wire systems and the corresponding wave functions and energy eigenvalues [32]. Here, we use the effective mass approximation and choose the finite element method (FEM) to perform the SCSP calculation. It is worth mentioning here that this is the typical SC scheme of working within a single-band or multiband $\vec{k} \cdot \vec{p}$ environment in semiconductor physics. However, there are very recent reports on the adaptation of density functional theory which is, intrinsically, self-consistent to deal with nanowire-type systems or with nanotubes; thus opening a way to a powerful, although more computationally demanding, microscopic calculation tool for this particular kind of systems [46, 47].
Following [54], we select the electron gas density given by the Thomas-Fermi approximation as the starting point for the method. This quantity will enter the Poisson equation to contribute to the system's charge density along with donor concentration N_d (assumed to be fully ionized) within the QW core. We have

$$n(x, y, T) = N_C \, F_{1/2} \left(\frac{E_F - V^*(x, y, T)}{k_B T} \right) , \tag{4-1}$$

where $N_C = (2m^* k_B T / \pi \hbar^2)^{3/2}/4$ is the effective density of states, $V^*(x, y, T)$ is the electronic potential generated by the Fermi level Pinning on the exposed

lateral surface, the level of doping and the lateral dimensions of the system, m^* is the electron effective mass, and $F_{1/2}(x)$ is the Fermi-Dirac integral given by

$$F_{1/2}(\xi) = \frac{1}{\Gamma(3/2)} \int_0^\infty \frac{\beta^{1/2}}{e^{\beta-\xi}+1}\, \mathrm{d}\beta\,. \tag{4-2}$$

In this equation, Γ is the Gamma function and in this case $\xi = (E_F - V^*(x,y,T))/k_BT$, where k_B is the Boltzmann constant and T is the temperature. The potential energy of the electron is given by $V^*(x,y,T) = -e\,\phi(x,y,T)$, where $\phi(x,y,T)$ is the Hartree potential. Then, the associated Poisson equation is:

$$\nabla^2\phi(x,y,T) = -\frac{1}{\varepsilon_0\,\varepsilon_r}\,\rho(x,y,T)\,, \tag{4-3}$$

where $\rho(x,y,T) = e\,[N_d - n(x,y,T)]$ is the charge density, e is the electron charge, and ε_r and ε_0 are the GaAs relative permittivity and vacuum permittivity, respectively. This equation must be solved taking into account the boundary conditions imposed by the Fermi level pinning, which for GaAs takes the form $\phi(\Omega) = -(E_F + 0.7\mathrm{eV})/e$.

The potential, $\phi(x,y,T)$, obtained through Equation (4-1) must contribute to the potential energy term in the Schrödinger equation as $-e\,\phi(x,y,T)$. On the other hand, the electrons are assumed to be totally confined within the volume of the QW and, therefore, it must be satisfied that for the Ψ-electron wave function the condition $\Psi(\Omega) = 0$ must be satisfied. Under these considerations, the Schrödinger equation for the confined electron in the QW reads

$$-\frac{\hbar^2}{2m^*}\nabla^2\Psi(\vec{r}) + (V - e\,\phi(x,y,T))\Psi(\vec{r}) = E\,\Psi(\vec{r}), \tag{4-4}$$

where V is the confinement potential of the structure. Considering the infinite length along the z-axis, the 3D wave function of the system can be written as

$$\Psi(\vec{r}) = e^{ik_z z}\,\psi(x,y)\,. \tag{4-5}$$

By using Equation (4-5) in Equation (4-4), we obtain the following 2D differential equation

$$-\frac{\hbar^2}{2m^*}\nabla^2\psi(x,y) + (V - e\,\phi(x,y,T))\psi(x,y) = E_0\,\psi(x,y)\,, \tag{4-6}$$

where $E = \frac{\hbar^2 k_z^2}{2\,m^*} + E_0$.
As the electrons must be confined to the interior of the quantum wire, therefore, to solve this equation, it is necessary to impose the boundary condition $\psi(\Omega) = 0$. Solving the last equation, we shall find the first set of self-functions ψ_i and self-energies $E_{0,i}$ for the system. With these elements at hand, it is possible to calculate the electron density associated with the occupation of each of these states:

$$\eta(x, y, T) = \sum_{i=1} N_i \, F_{-1/2}\left(\frac{E_F - E_{0,i}}{k_B T}\right) |\psi_i(x, y)|^2 \,, \tag{4-7}$$

where $N_i = g_i \sqrt[3]{4N_C}$, E_F is the Fermi energy and g_i is the degeneracy factor. This equation represents the density of electron gas in a (x, y)-point at a temperature T. It can also be understood as the summation of the probability of finding the electron in the point (x, y) inside the quantum wire in each determined state ψ_i with energy $E_{0,i}$. From the electron density calculated in Equation (4-7), a new profile for the charge density of the system is obtained:

$$\rho_{new}(x, y, T) = e[N_d - \eta(x, y, T)] \,. \tag{4-8}$$

By solving the Poisson Equation (4-3) and using the corresponding charge density profile, a new Hartree potential $\phi_{new}(x, y, T)$ is obtained that will -again- contribute to the potential energy term in the Schrödinger equation. Then, via the solution of Equation (4-6), with this consideration, we obtain a new set of eigenfunctions and eigenvalues for the system $\psi_i^{new}, E_{0,i}^{new}$. This set will be associated with a new electron density profile η_{new} relative to each state of the system's occupation. In this way, the process is repeated iteratively until the absolute value of the difference between potential terms corresponding to two successive self-consistent steps is smaller than a certain tolerance $|U - U_{old}| < 10^{-6}\,\text{eV}$, where $U = V - e\,\phi(x, y, T)$. At this point, the system has reached self-consistency, finally obtaining a set of eigenstates, eigenvalues, a definitive form for the potential profile of the system, and the SC electronic densities.

4.3. Results and Discussion

For all calculations, the following parameters have been set—effective mass of electron in GaAs $m^* = 0.067\, m_0$ (where m_0 is the mass of the free electron) and dielectric constant $\varepsilon_r = 12.9$. All the equations have been solved through the finite element method with the COMSOL-Multiphysics licensed software (5.4, COMSOL AB, Stockholm, Sweden.) [51–53]. The used typical numerical parameters are inner mesh with triangular-shaped elements, 6550 elements, 160 edge elements, 3356 mesh vertices, 40 as the maximum number of iterations of the self-consistent method, and 10^{-6} as the absolute tolerance.

Figure **4-2** shows the plots of the first five QW confined state wave functions in each of the four configurations studied, from top to bottom—circle, square, triangle and pentagon. It should be noted that the cross-sectional area for all considered QWs has been kept the same. The cross-sectional area of all structures are set to be equal to $\pi\, R_0^2$ (the area of the circular QW with R_0 radius). The electron density N_d has been fixed as 3×10^{19} cm^{-3} for all cases. For all considered structures, the ψ_1 and ψ_2 states are doubly degenerated. The states ψ_3 and ψ_4 are degenerate only for circular and pentagon QW. The states' sequence of degeneration in the structures shown is as follows—$(1, 2, 1, 2, 2)$ for the square and triangle and $(1, 2, 2, 1, 2)$ for the circle and pentagon. The color scale in each figure goes from blue, which corresponds to the wave function's negative values, to dark red, which represents positive values of the wave function. The yellow color indicates the points at which the wave function is zero. The first column on the left corresponds to the ground state ψ_0 for each system. There, it is possible to notice the s-type character that this state acquires for all studied configurations, as detailed by the next paragraph. Additionally, it is emphasized that the electrons in the wire with the triangular section are more confined towards the symmetry axis than in the other structures. The first and second excited states, ψ_1 and ψ_2, are presented on the second and third columns from left to the right. Note that these states have a p-type character. Finally, in the rightmost two columns, the third and fourth excited states, ψ_3 and ψ_4, are shown for each configuration. These states show a d-type behavior, as can be noticed from their projections.

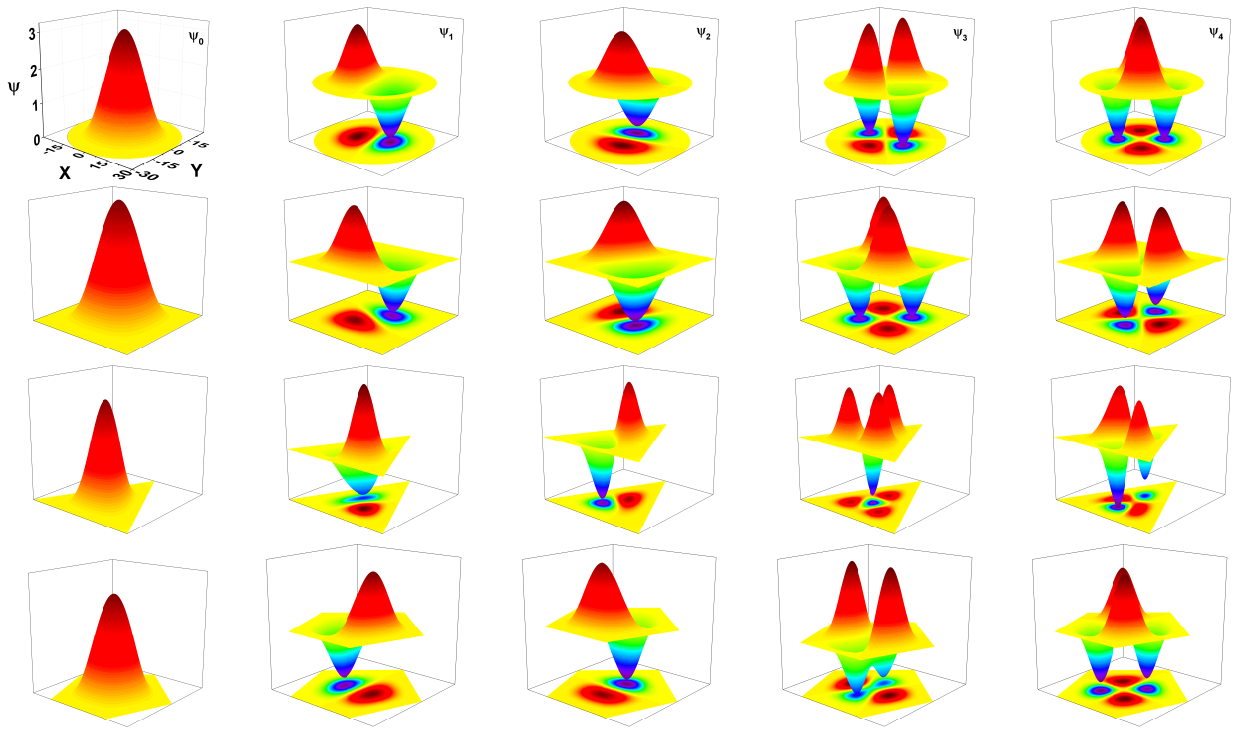

Figure 4-2.: First five wave functions for a confined electron in GaAs quantum wires. The rows from top to bottom are for circle, square, triangle, and pentagon, respectively. The left−hand side column corresponds to the ground state; the next four columns from left to right are for each system's first four excited states. For all figures, the cross−sectional areas are the same.

The xy-cross-sections of the electron wave functions exhibit particular symmetries that we refer to by partial analogy with electronic orbitals in atoms. For all types of wire, the ground level orbital is the s-like orbital, which means a single central extreme (*sharp* orbital) of the wave function in the xy-plane, corresponding to the symmetry center of the wire cross-section. There is only the central lobe (positive amplitude) and no angular nodal surface (zero amplitude) for the s-like orbitals. The second energy level (second and third column) is double degenerate in all types of wire. The two orthogonal wave functions corresponding to this energy have two extremes each (*principal* orbitals), therefore being denoted as p-like orbitals. They both have one lobe of positive amplitude and one lobe of negative amplitude, separated by an angular nodal surface perpendicular to the xy-plane. The angular nodal surfaces of the two

different p-like orbitals are orthogonal.

Figure **4-3** shows the self-consistent confinement potential for each of the structures. In the calculation, the circular QW radius has been taken equal to 50 nm, which fixes the cross-sectional area of all the other systems. Keeping the color code in which red indicates the most significant values shows that the potential becomes higher at the boundary regions, which favors electronic confinement in the core regions within the QW. Electrons feel a similar potential near the symmetry axis of each structure. The change is noticeable mostly near the border of the QW where the potential presents a less smooth behavior.

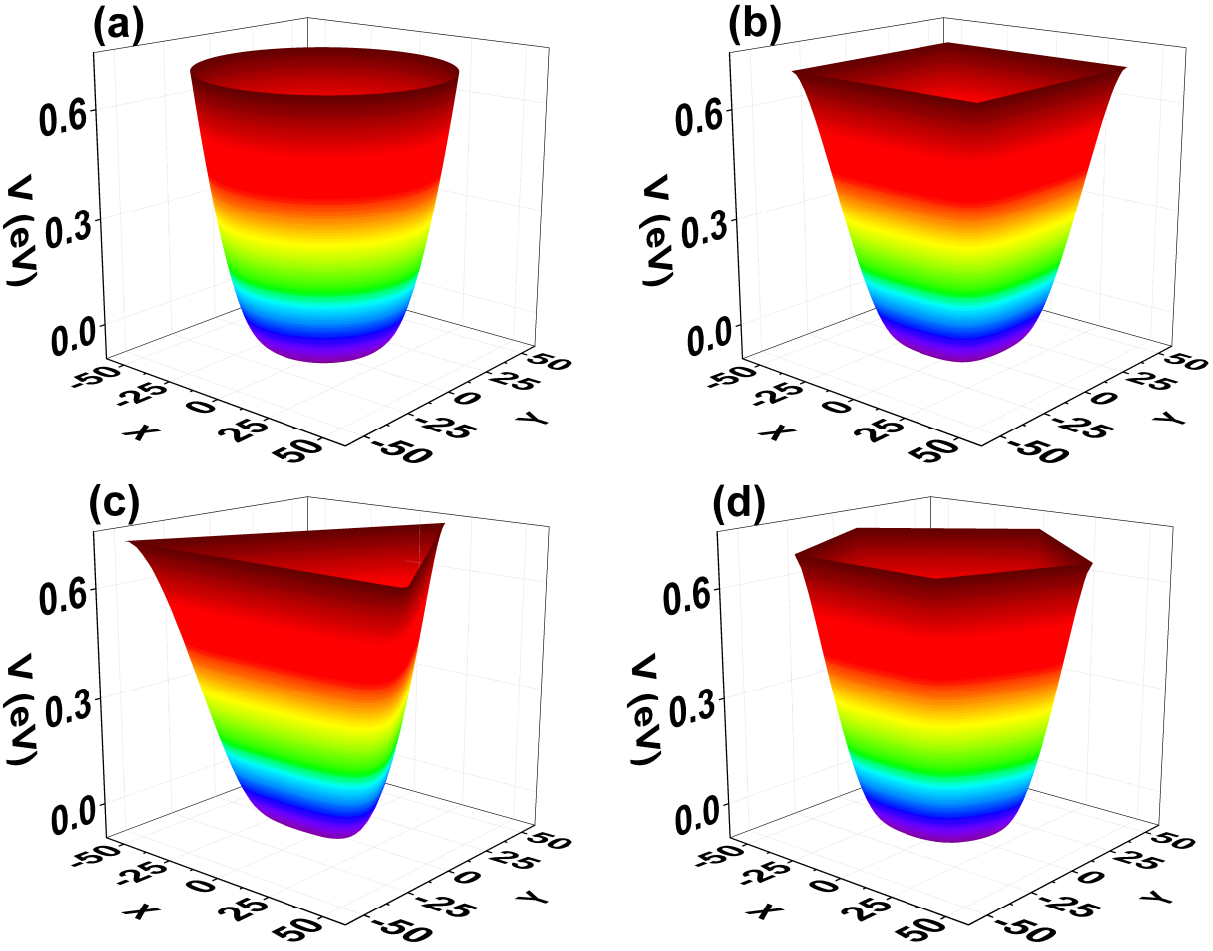

Figure 4-3.: Self−consistent confining potentials for the different GaAs quantum wire geometries investigated: circle (**a**), square (**b**), triangle (**c**), and pentagon (**d**). Calculations are with $N_d = 3 \times 10^{19}$ cm^{-3} and $T = 10$ K.

Figure **4-4** shows the electron density $\eta(x)$ (with $y = 0$) for each structure, normalized to the doping value $N_d = 3 \times 10^{19}$ cm^{-3}. It has been calculated along the arrow indicated in the inset at the bottom of each figure. Accordingly, a higher concentration is evidenced in the core region or near the symmetry axis of each QW. This feature was expected, given that—as seen from Figure **4-3**—the confining potential is low around this zone. The results plotted in Figure **4-4** are for $T = 10\,\mathrm{K}$. In these systems, with exposed borders, at low temperatures, Friedel-like spatial oscillations of the carrier density appear [55]. These can be viewed as irregularities in the density profile, especially around the central zone of the QW. These oscillations could be explained by the presence of subbands associated to surface states and by how the electrons populate each of them. They can be caused by the electronic occupation of the oscillation-related lower states closer to the center of the QW, while the higher occupied states can also contribute to a lesser extent. One may observe that very fast decrease of the electron density occurs in regions close to each system's boundary, while in regions close to $x = 0$ a maximum value is reached. However, $\eta(x)/N_d$ does not reach 1.0 in any system. This is evidence of the charge transfer from inner states (the core) to surface states since the complete system must remain neutral. These states are the ones that contribute to the Fermi level pinning.

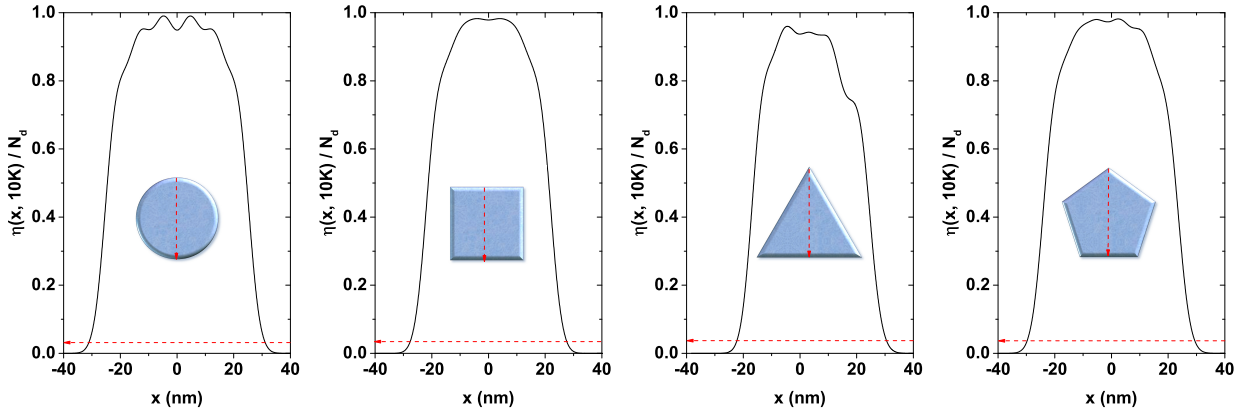

Figure 4-4.: Normalized electron density functions for each investigated GaAs quantum wire structure as a function of the $x-$coordinate (see the red arrow in the inset in each figure) for $T = 10\,\mathrm{K}$ and $N_d = 3 \times 10^{19}$ cm^{-3}. For all figures the cross−sectional area has been set at $A = 2500\,\pi\,\mathrm{nm}^2$.

Figure **4-5** presents the ground state energy variation for the four studied GaAs QWs as a function of R_0. In this figure, the donor density has been taken as $N_d = 2\times10^{18}\,\mathrm{cm}^{-3}$, the temperature is $T = 10\,\mathrm{K}$, and the Fermi level is $E_F = 0$. As long as R_0 increases for all structures, a clear decreasing behavior of the ground state is evidenced [56, 57]. This decrement is more abrupt for the circular system, and it is less so for the triangular one. To explain this fall in energy, we must notice that, due to the increase in R_0, the cross-section area of all the QWs augments leads to a reduction of the electronic confinement, a redshift in the eigenvalues takes place. For $R_0 = 10\,\mathrm{nm}$, the ground state energy is very similar in all structures, taking a value around $0.67\,\mathrm{eV}$. Something alike occurs for $R_0 = 50\,\mathrm{nm}$ where the energy decreases to approximately $-0.075\,\mathrm{eV}$. For intermediate values, a separation between the states corresponding to each structure is clearly noted, this separation being greater for $R_0 = 30\,\mathrm{nm}$. This fact appears in the inset, where the difference between the ground state of the triangular and circular GaAs QWs is shown. It reaches a maximum value of approximately $130\,\mathrm{meV}$. The ground state's behavior for the circular, square, and pentagonal systems is very similar, and the largest differences appear for the triangular system.

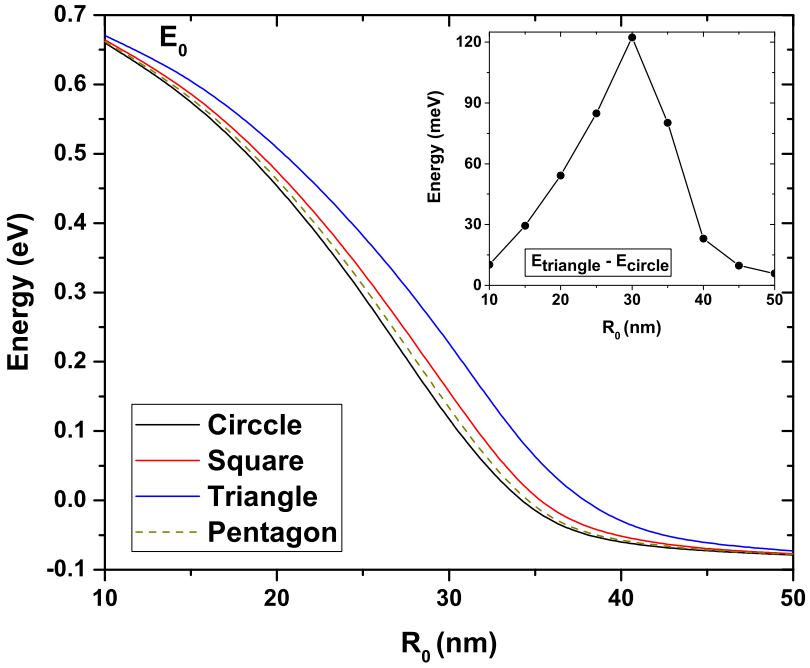

Figure 4-5.: Ground state energy for each GaAs quantum wire structure as a function of the R_0 parameter. The inset shows the energy difference between the triangular and circular wires. Calculations are for $N_d = 2 \times 10^{18}\,\mathrm{cm}^{-3}$, $T = 10\,\mathrm{K}$, and $E_F = 0$.

Figure **4-6** shows the first excited state energy for the four GaAs QWs as a function of the R_0 under the same conditions as for Figure **4-5**. We can see that a clear decreasing trend is evidenced as R_0 increases. The first excited state of the four systems presents an energy of $0.69\,\mathrm{eV}$ at $R_0 = 10\,\mathrm{nm}$ which decreases to $-0.06\,\mathrm{eV}$ when $R_0 = 50\,\mathrm{nm}$. Quantitatively, this first excited is very similar for the circular, square, and pentagonal QWs. The main difference appears with the triangular system, which has higher energy. This behavior is evidenced in the inset where the circular and triangular systems' energy difference is presented. As in Figure **4-5**, a maximum difference is noted for $R_0 = 30\,\mathrm{nm}$.

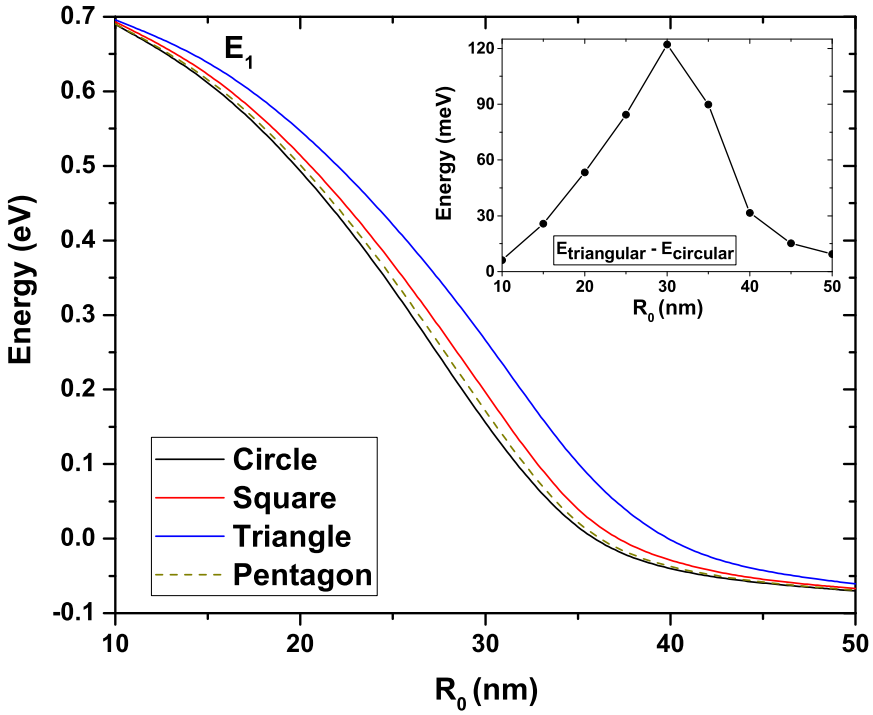

Figure 4-6.: First excited state energy for each GaAs quantum wire structure as a function of R_0. The inset shows the energy difference between the triangular and circular wires. Calculations are for $N_d = 2 \times 10^{18}\,\mathrm{cm}^{-3}$, $T = 10\,\mathrm{K}$, and $E_F = 0$.

In Figure **4-7**, the first two energy states are shown for each of the systems—circular (a), square (b), triangular (c), and pentagonal (d)—plotted as functions of the R_0 parameter. For $R_0 < 25\,\mathrm{nm}$ the systems show an approximately parabolic decrease in energy. Then, for $25\,\mathrm{nm} < R_0 < 35\,\mathrm{nm}$ this decrease displays an approximately linear behavior and for $R_0 > 35\,\mathrm{nm}$ the decrease becomes approximately exponential. There is a degeneracy of order two for all systems concerning the first excited state (this generation is indicated by label 2 in each figure).

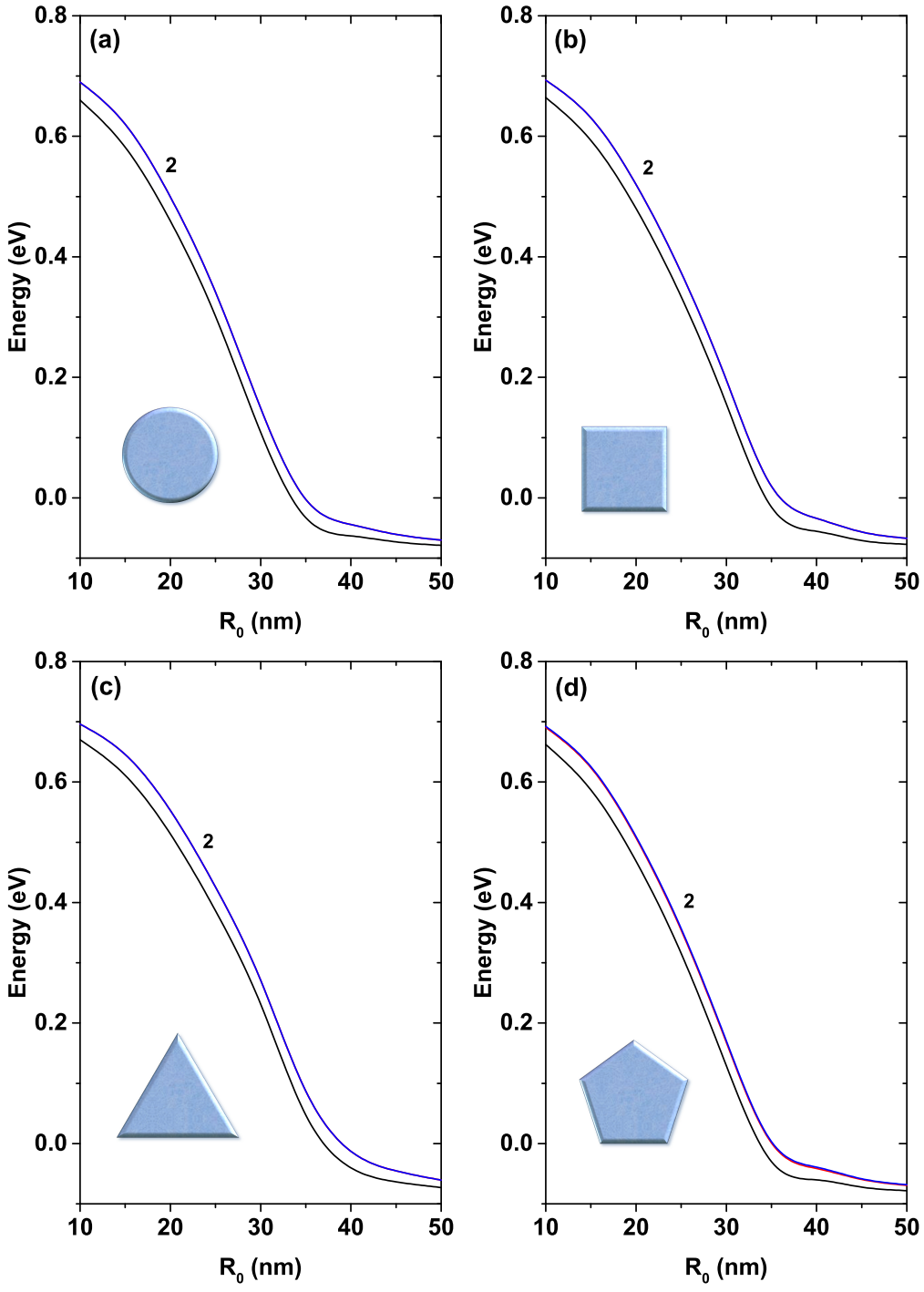

Figure 4-7.: First two energy levels for a confined electron in a GaAs quantum wire as a function of the R_0 parameter. The label 2 indicates that the first excited state is doubly degenerated. Calculations are for $N_d = 2 \times 10^{18}\,\mathrm{cm}^{-3}$, $T = 10\,\mathrm{K}$, and $E_F = 0$.

Figure **4-8** shows the energy difference between the first excited state and the ground state for each of the four GaAs QW structures as a function of the R_0 parameter. In this case, the donor density and temperature have been kept fixed at $N_d = 2\times10^{18}\,\mathrm{cm}^{-3}$ and $T = 10\,\mathrm{K}$, respectively. An increase in the separation between these two states is evidenced as R_0 augments within the range between 10 nm and 17 nm, going from an average value of 28 meV to around 38 meV, for all structures. In this range, it is also noted that the separation between levels in the cases of square and pentagonal geometry presents a very similar behavior. The curves show a linear and parallel tendency. The greatest separation of $E_1 - E_0$ appears from the comparison between the circular and triangular QWs, followed by that involving the pentagonal and triangular wires. Within the range $17\,\mathrm{nm} < R_0 < 30\,\mathrm{nm}$, the separation between the levels does not show significant growth, maintaining an average value of about 38 meV. In this region, the curves show a kind of oscillatory behavior, presenting a close approach between the circular, square and triangular QWs for a value of $R_0 \sim 23.5\,\mathrm{nm}$. Then, for values $R_0 > 30\,\mathrm{nm}$, these energy values keep getting closer until reaching a difference of 8.8 meV approximately at $R_0 = 50\,\mathrm{nm}$ for circular and pentagonal QWs and of 10 meV and 12.3 meV for wires with square and triangular sections, respectively. Note the similar behavior shown by the curves corresponding to the circular and pentagonal QW for values of R_0 greater than 35 nm. This is explained as a consequence of the fact that electrons, for a large QW cross-section, do not feel the edge effects in the system. This fact can be analyzed in conjunction with the results presented in Figure **4-4**, which show that the electron density is practically concentrated at the center of the structure, and the pentagonal profile is closer to the circular one. The opposite occurs with the square and triangular systems, for which the profile electron density is changed in greater extent due to the shape of system boundaries. In the region, $R_0 < 17\,\mathrm{nm}$, a greater separation between the curves occurs again for the circular and triangular QWs. But now, the curves have been inverted, being higher than that of the triangular QW.

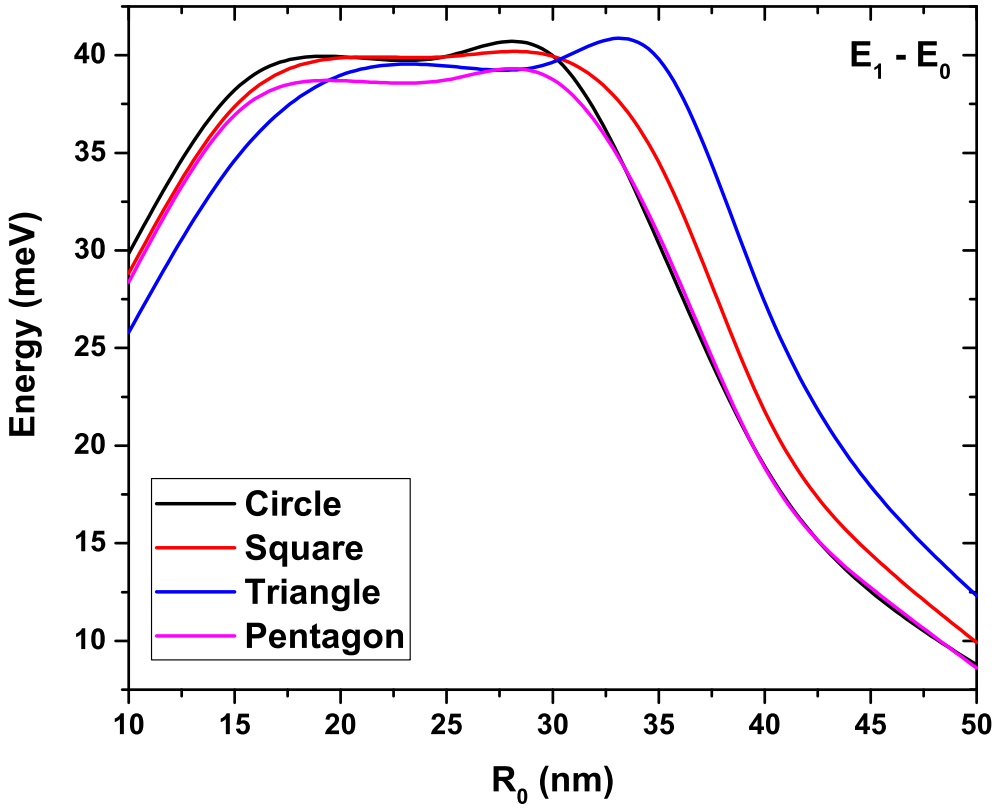

Figure 4-8.: Energy difference between the first excited state and the ground state for each GaAs quantum wire as a function of the R_0 parameter. Calculations are with $N_d = 2 \times 10^{18}\,\mathrm{cm}^{-3}$, $T = 10\,\mathrm{K}$, and $E_F = 0$.

In previous figures, the electronic energies in each system have been plotted as functions of R_0, keeping the doping fixed at $N_d = 2 \times 10^{18}\,\mathrm{cm}^{-3}$ and the temperature at $T = 10\,\mathrm{K}$. Next, the variation of the energies will be studied while allowing variations of the N_d parameter and keeping fixed the dimensions of the QWs and the temperature. At this point, it must be remembered that the system under study is a QW with exposed boundaries. Thus, an immediate consequence is the Fermi level pinning due to the transfer of charge towards surface states. These states' appearance is transcendental since it fixes the surface potential and the Fermi level independently of the donor density in the system. Figure **4-9** shows the ground state energy for each of the GaAs QW systems as a function of the donor density, N_d. The remaining system parameters have been fixed at $R_0 = 30\,\mathrm{nm}$ and $T = 10\,\mathrm{K}$. Note that for $N_d < 5 \times 10^{18}\,\mathrm{cm}^{-3}$,

there is practically no difference in electron energy when comparing results for the four distinct cross-section geometries. This fact can be more clearly noticed by seeing the upper inset, in which the energy difference between the ground state of the triangular and circular QWs is presented. One may observe that the difference between state energies is of the order of 4 meV when $N_d \to 0$. On the other hand, when $N_d = 5 \times 10^{18}\,\mathrm{cm}^{-3}$, this difference reaches a maximum value of 18.7 meV to subsequently show an approximately constant decrease around 7.5 meV. Note the type of linear decrease that occurs for $N_d > 12 \times 10^{18}\,\mathrm{cm}^{-3}$ for all structures. In general, the ground state shows a decrease from 0.69 meV for $N_d = 0$ to approximately -0.5 meV, independently of the QW shape. The lower inset is a magnification of the curves, where the very close behavior for circular, square and pentagonal QW structures is again obvious, with the state of the triangular system presenting a more noticeable separation.

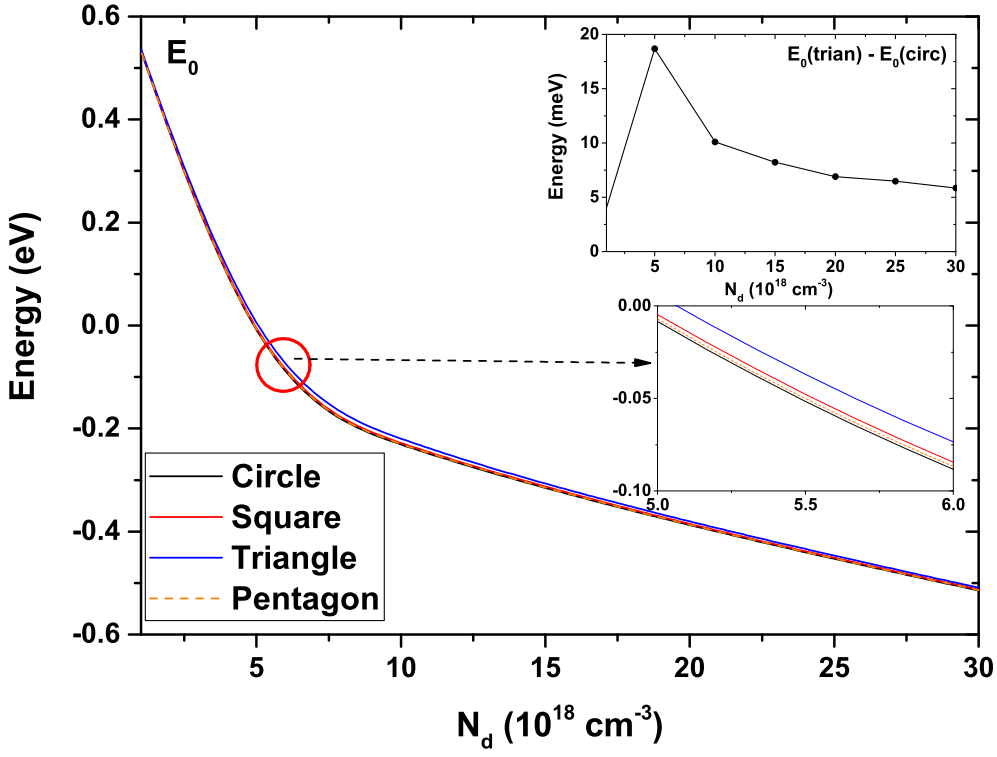

Figure 4-9.: Ground state energy for each GaAs quantum wire structure as a function of the N_d parameter. The inset shows the energy difference between the triangular and circular wires. Calculations are for $R_0 = 30\,\mathrm{nm}$ and $T = 10\,\mathrm{K}$.

Figure **4-10** presents the first two electronic states for each of the GaAs QW systems as a function of the donor density, N_d. The temperature has been kept fixed at $T = 10\,\mathrm{K}$ and the geometric R_0 parameter at $30\,\mathrm{nm}$. For all the structures, a decreasing behavior is observed with the increase in N_d, this decrease being approximately linear for values $N_d > 10^{19}\,\mathrm{cm}^{-3}$. It should be noted that there is a degeneracy of the second degree in the case of the first excited state for all systems. Just to quantify the fall in energy levels, for the circular system it goes from $0.7\,\mathrm{eV}$ for $N_d = 10^{16}\,\mathrm{cm}^{-3}$ to $-0.5\,\mathrm{eV}$ for $N_d = 3 \times 10^{19}\,\mathrm{cm}^{-3}$ in the case of the first excited state.

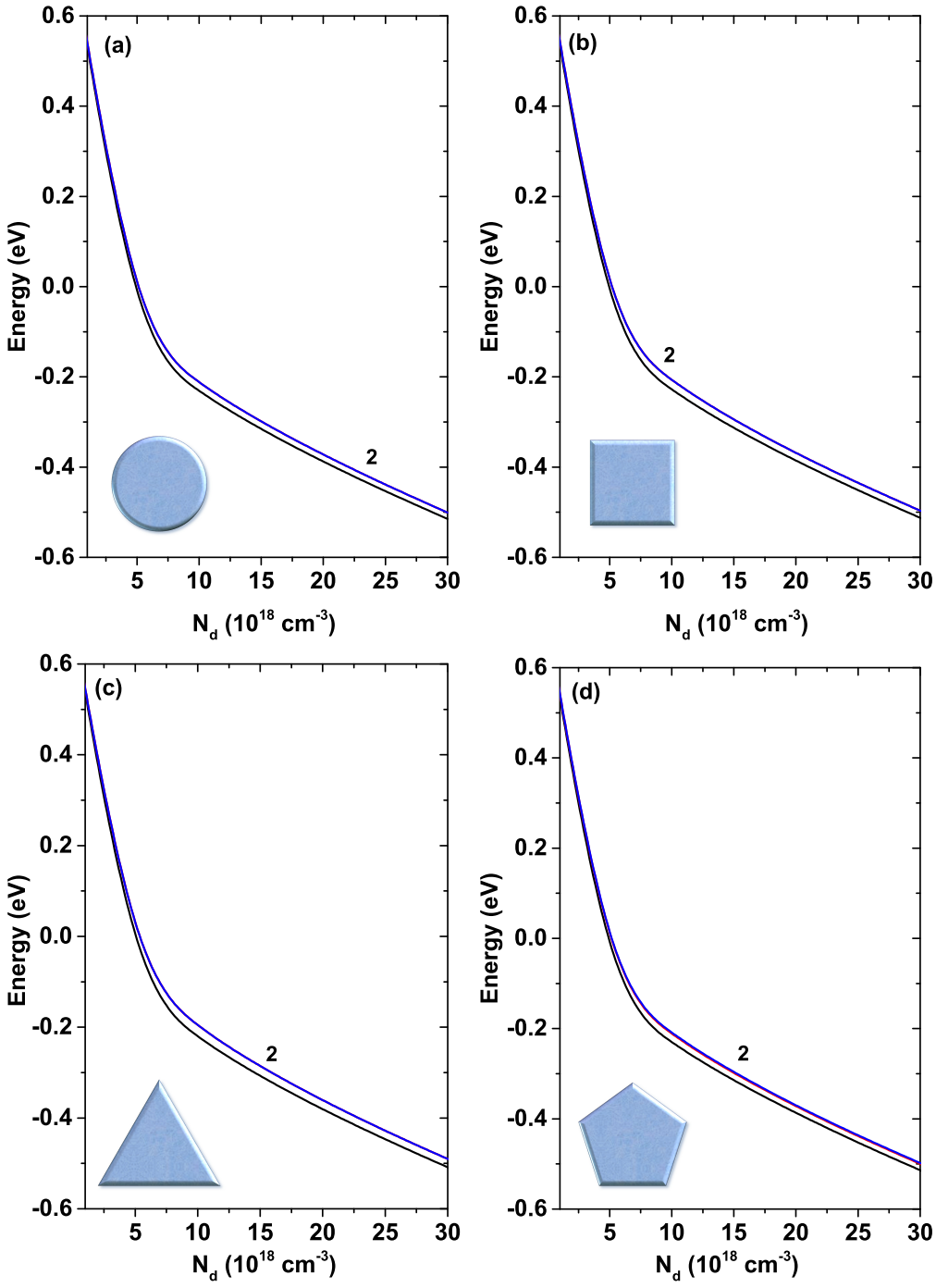

Figure 4-10.: First two states of each GaAs quantum wire system as a function of the N_d parameter. The label 2 in each figure indicates that the first excited state is doubly degenerated. Calculations are for $R_0 = 30\,\text{nm}$ and $T = 10\,\text{K}$.

We are presenting in Figure **4-11** the difference between the first excited sta-

te energy and the ground state energy for all considered GaAs QW systems, depicted as a function of the electron density, N_d. The same parameters as in Figure **4-10** have been kept fixed. A monotonically decreasing behavior is immediately evident for all curves. In the same way it should be noted that the maximum separation between these two levels takes place in the particular case of the QW with triangular cross-section, reaching a maximum value of approximately 32.2 meV at $N_d = 5 \times 10^{18}$ cm^{-3}, and decreasing to 18 meV at $N_d = 3 \times 10^{19}$ cm^{-3}. In order of separation between these two levels, the next structure is the square-shaped QW which goes from 27.2 meV to 15.7 meV in the same range of N_d. Here, a particular behavior is present for circular and pentagonal QWs. Actually, they present exactly the same separation between these two lowest levels for $N_d = 5 \times 10^{18}$ cm^{-3}, taking a value of 24.7 meV. However, as N_d is increased, an appreciable difference is reached between these two kinds of QWs, the circular one taking a slightly higher value. This behavior is maintained with the increase in N_d.

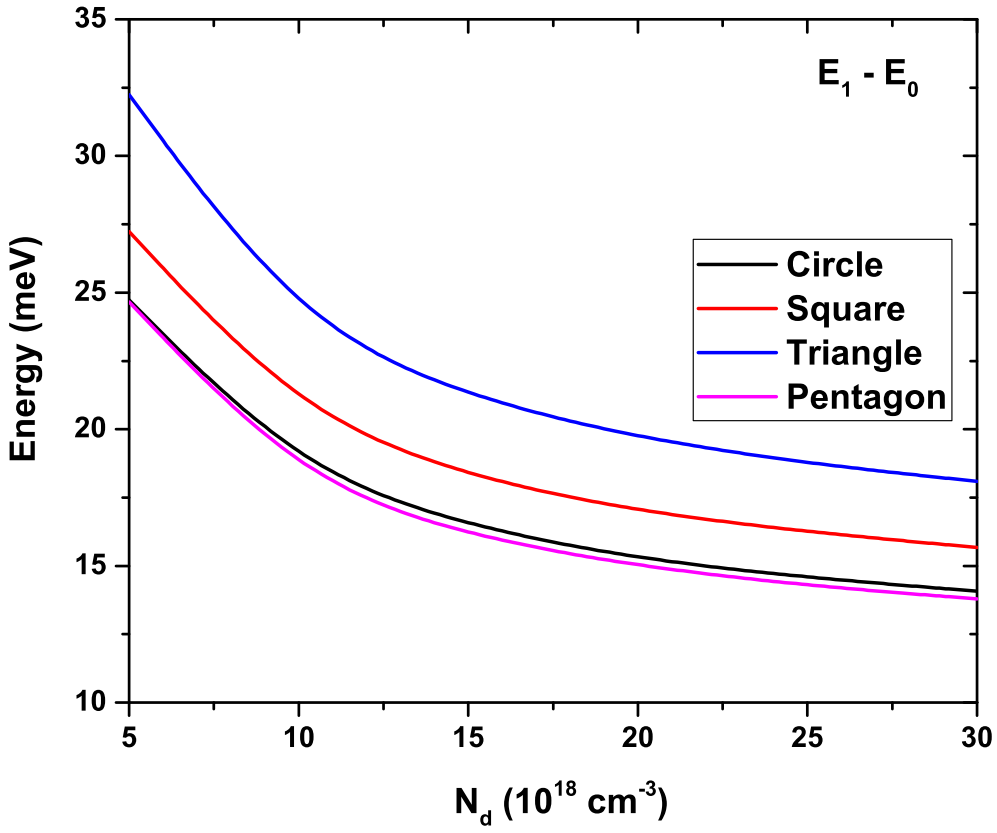

Figure 4-11.: Energy difference between the first excited state and the ground state for each GaAs quantum wire system as a function of the N_d parameter. Calculations are for $R_0 = 30\,\text{nm}$ and $T = 10\,\text{K}$.

The variation of the lowest six energy levels for the four GaAs QW systems as a function of temperature is shown in Figure **4-12**. For this case, R_0 has been fixed at 50 nm and $N_d = 2 \times 10^{18}\,\text{cm}^{-3}$. The number that appears next to some states indicates their degree of degeneracy. Note the similar behavior of the energy degeneracy for the circular and pentagonal QWs (also for the triangular and square QW). This was expected, bearing in mind the results obtained in Figures **4-9** and **4-11**. It should be noted that the highest value of the ground state energy happens for the triangular QW system, taking a minimum value of $-72.9\,\text{meV}$ at $T = 10\,\text{K}$ and a maximum of $-65.3\,\text{meV}$ at $T = 290\,\text{K}$. Note that all states show an increasing trend with rising temperatures. This fact is a consequence of the stronger confinement at high temperatures.

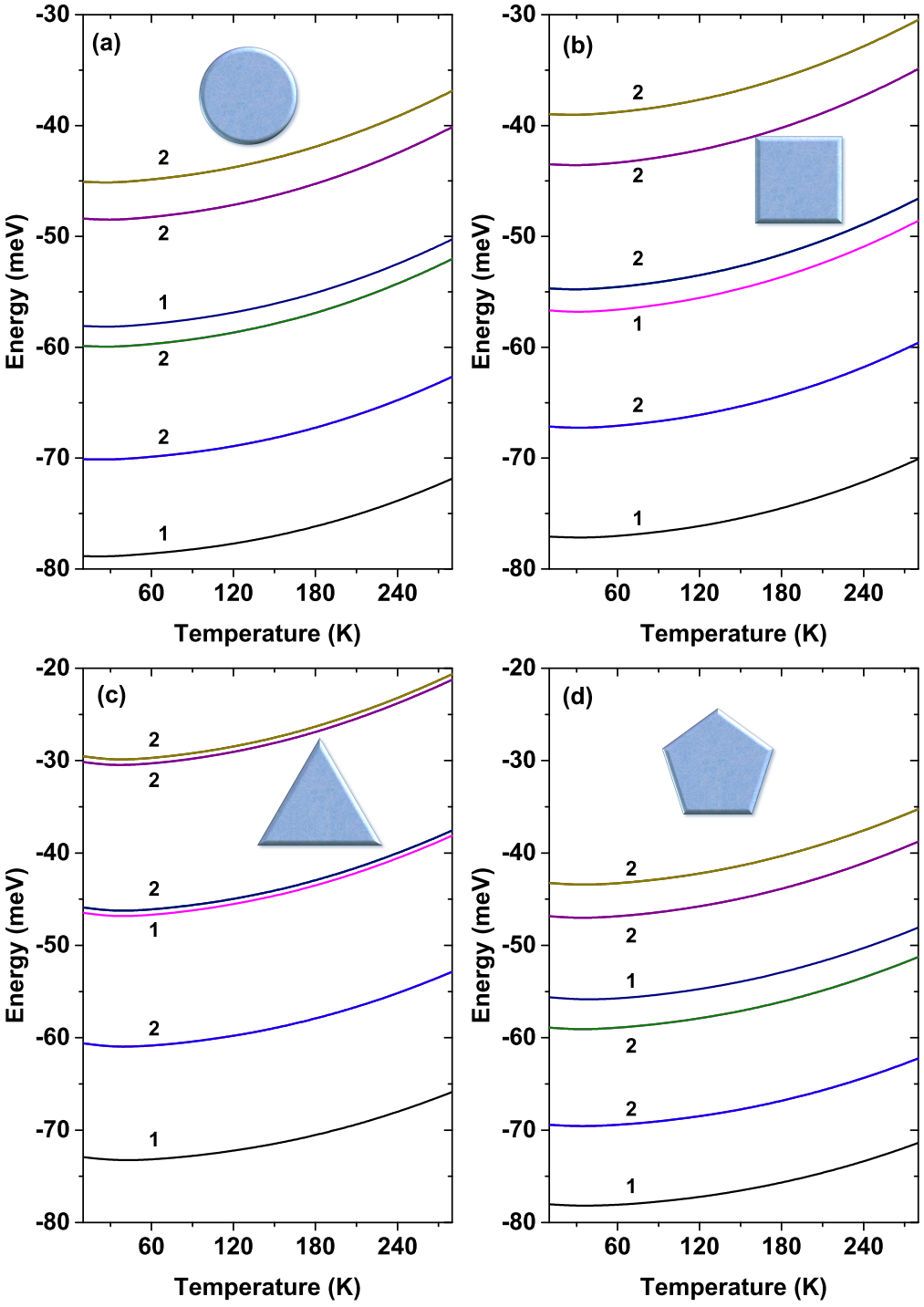

Figure 4-12.: The first six energy levels of each GaAs quantum wire system as a function of temperature. The labels 1 and 2 indicate the degree of degeneracy. Calculations are for $R_0 = 50\,\text{nm}$ and $N_d = 2 \times 10^{18}\,\text{cm}^{-3}$.

Figure **4-13** shows the difference between the first excited state energy and the ground state energy as a function of temperature for the four QW types analyzed. The other parameters have been kept fixed in a similar way as in Figure **4-12**. The highest separation is given for the triangular system, and goes from 12.3 meV at $T = 10\,\mathrm{K}$ to 13.1 meV at $T = 290\,\mathrm{K}$. It is followed by the square QW which, for the same temperature range, goes from 9.9 meV to 10.5 meV. Finally, as in the previous figures, again the most similar behavior is exhibited by the curves of circular and pentagonal system. This was seen in Figure **4-12** with the similar behavior that the first two levels followed in both structures. However, this similarity is not present in the case of higher states. The minimum separation between the levels is given for pentagonal-shaped QW, which, in the same range of temperatures studied, goes from 8.6 meV to 9.2 meV. Note the increasing character of all the curves with temperature.

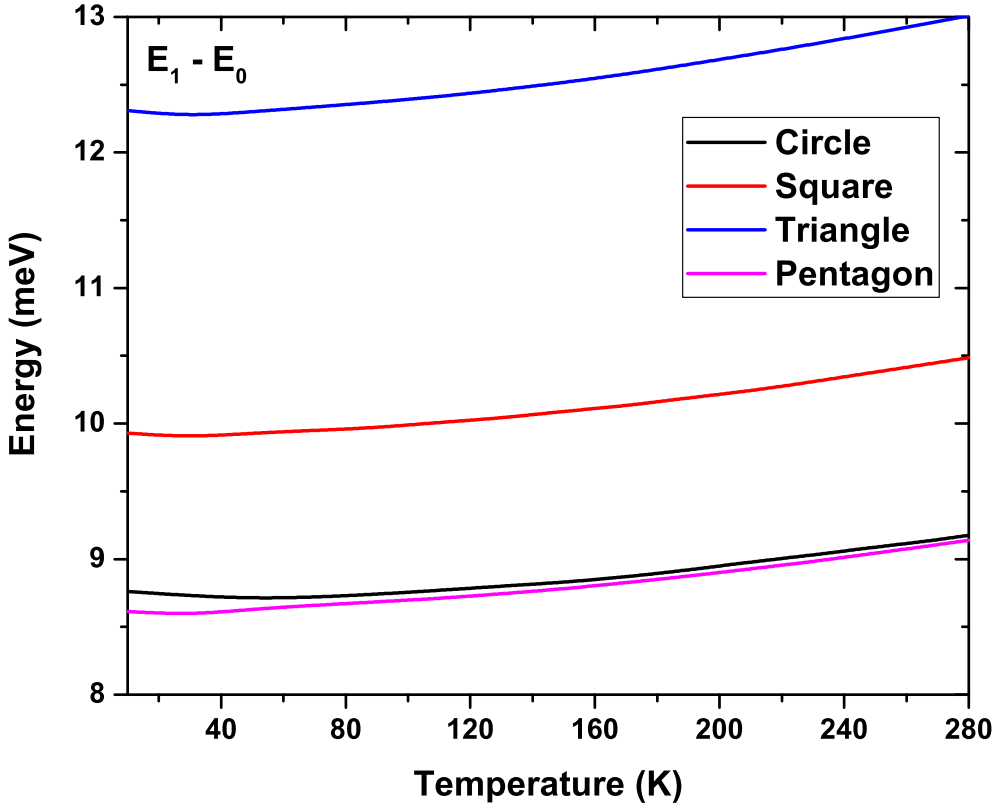

Figure 4-13.: Energy difference between the first excited state energy and the ground state energy for each GaAs quantum wire system as a function of temperature. Calculations are for $R_0 = 50\,\text{nm}$ and $N_d = 2 \times 10^{18}\,\text{cm}^{-3}$.

The results for the electron density profile given by Equation (4-7) are presented in Figure **4-14** for the circular QW at a temperature of $T = 10\,\text{K}$ and $R_0 = 50\,\text{nm}$. Figure **4-14**a shows the total density (black curve). The dashed vertical lines indicate the local maxima that appear as oscillations in points (1), (2), and (3). The contributions coming from the different electron states in these points appear in Table **4-1**. The first number in parentheses corresponds to the azimuthal quantum number (m) and the second to the radial quantum number (l). Note that in the case of the circular quantum wire, and due to its axial symmetry, the $\psi_i(x, y)$ wave function in Equation (4-6) can be written as $\psi_i(x, y) = f_l(\rho)\,\exp(im\phi)$, where $m = 0, \pm1, \pm2, ...$ is the azimuthal quantum number, $l = 1, 2, 3, ...$ is the radial quantum number, and $\rho = \sqrt{x^2 + y^2}$. The percentage that appears next to each state in Table **4-1** corresponds to

the contribution of each of them to the oscillation of the total density profile at points (1), (2), and (3) in Figure **4-14**, where the probability density has been plotted for the states with a contribution greater than 15.0 % for all peaks. As seen from Figure **4-14**a and Table **4-1**, for the oscillation centered at $x = 4.75\,\text{nm}$, denoted by (1) in the figure, the highest contribution is due to the ground state of the system, $\psi_{0,1}$, with 23.0 %, followed by the $\psi_{0,2}$ and $\psi_{1,2}$ states with 19.6 % and 19.2 %, respectively. The last significant contribution is due to the $\psi_{1,3}$ state with 16.0 %. Meanwhile, the other states present a contribution of less than 10.0 % for this first oscillation in the electron density profile. Accordingly, this particular oscillation is due mainly to the contribution of the lower states of the system; note that states with $m > 3$ do not contribute to the appearance of this oscillation. On the other hand, for the oscillation centered at $x = 12.25\,\text{nm}$, denoted as (2) in the figure, the state that contributes the most is $\psi_{1,1}$ with 23.5 %, followed by $\psi_{2,1}$ with 16.3 % and $\psi_{2,2}$ with 12.1 %. The other states present contributions of the order of 10.0 % and less. Note that the lower states $\psi_{0,1}$ and $\psi_{0,2}$, that for the first oscillation contributed 42.6 % to the electron density, for this second oscillation only provide 10.9 %. However, the $\psi_{1,1}$ and $\psi_{2,1}$ states went from 9.7 % in the first oscillation to 39.8 % in the second one. For the third oscillation at $x = 20.5\,\text{nm}$, denoted by (3) in the figure, being more tenuous, a rather equitable contribution is evidenced between the states with the largest m quantum number. This contribution is on average 13.26 %, while the proportion from the lowest states is less than 7.0 %. An important conclusion here is that the oscillation generated in the density profile near the central zone of the circular QW is due to the contribution of the lower states of the system, while the second oscillation is caused by intermediate occupied states and the final one—around 20 nm—occurs due to the highest occupied states. It should be mentioned that the empty spaces in Table **4-1** correspond to states that do not contribute to the electron density at that specific point. For example, the $\psi_{0,3}$ state contributes to the oscillations presented in points (1) and (2), but it does not contribute to the oscillation generated in point (3). The curves plotted in Figure **4-14**b correspond to the electron density for the cylindrical QW, separating the individual contribution of states with different m-quantum number. This quantum number is kept fixed, and the sum in the Equation (4-7) is made over the l-quantum number. It should

be noted that, for $m > 6$, there are no longer occupied states, and therefore they do not contribute to the electron density. Figure **4-14**c, together with the total electron density (black curve), shows the sum over occupied states up to the state $m = i$ (the Σm_i symbol represents the value of summation). Sums up to the states that have $m = 6$—the highest occupied—are shown. Figure **4-14**b,c are evidence that the contribution to the first oscillation's appearance at $x = 4.75\,\text{nm}$ is mainly caused by electrons occupying the states with $m \leq 3$. On the other hand, for the outermost oscillations that are located at $x = 12.25\,\text{nm}$ and $x = 20.5\,\text{nm}$, the oscillations are caused by states with $4 < m < 6$, that correspond to the highest occupied states in the system. All this means that electrons with lower state energies are located close to the center of the structure's symmetry, between $0 < x < 10\,\text{nm}$; while electrons in higher energy states mainly locate at intermediate regions, $10 < x < 35\,\text{nm}$.

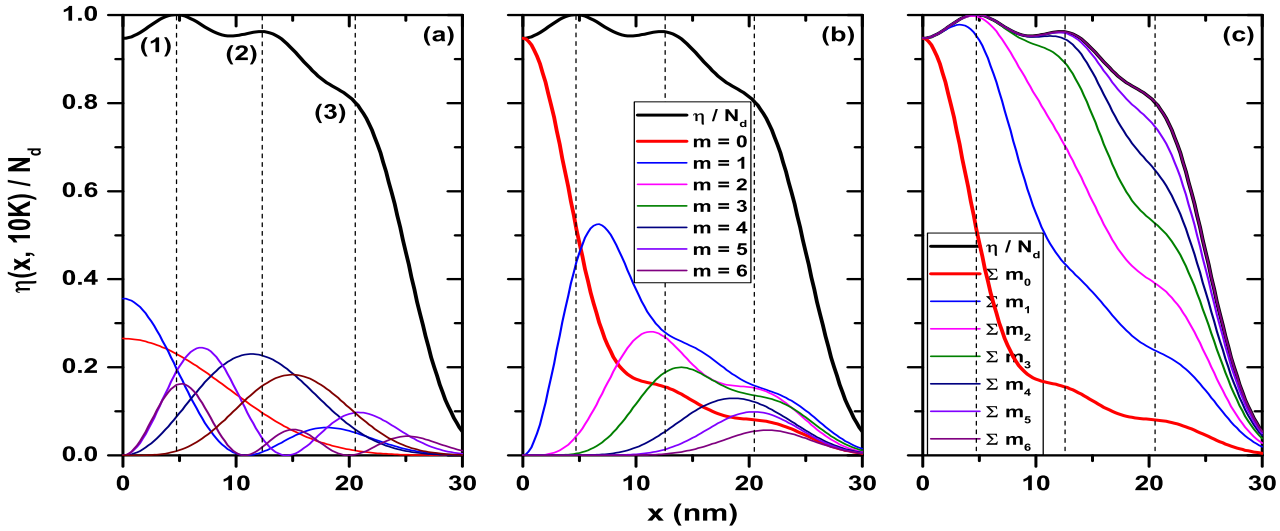

Figure 4-14.: Electron density for circular GaAs quantum wire. In (**a**) the $|\psi_i(x, y = 0)|^2$ states that contribute with the highest percentage to the density profile in points denoted by (1), (2), and (3) to the density profile. In (**b**), the contribution to the electron density for each quantum number m. In (**c**), the sum over the states with equal m. Note that in the case of the circular quantum wire, and due to its axial symmetry, the $\psi_i(x, y)$ wave function in Equation (4-6) can be written as $\psi_i(x, y) = f_l(\rho)\,\exp(im\phi)$, where $m = 0, \pm1, \pm2, ...$ is the azimuthal quantum number, $l = 1, 2, 3, ...$ is the radial quantum number, and $\rho = \sqrt{x^2 + y^2}$. Calculations are for $R_0 = 50\,\text{nm}$, $N_d = 2 \times 10^{18}\,\text{cm}^{-3}$, and $T = 10\,\text{K}$.

Table 4-1.: Contribution in percentage of each of the states to the oscillations at points (1), (2) and (3) in the density profile presented in Figure **4-14**.

(m, l)	$\mathbf{P_1}$ (%)	$\mathbf{P_2}$ (%)	$\mathbf{P_3}$ (%)
(0,1)	23.0	10.2	1.5
(0,2)	19.6	0.7	6.5
(0,3)	8.6	5.5	
(1,1)	8.8	23.5	7.4
(1,2)	19.2	4.3	12.1
(1,3)	16.0	1.8	0.2
(2,1)	0.9	16.3	12.0
(2,2)	3.4	12.1	7.0
(3,1)	0.2	8.4	14.9
(3,2)	0.3	10.6	2.0
(4,1)		3.5	15.0
(4,2)		1.5	
(5,1)		1.3	12.3
(6,1)		0.3	6.9

Finally, Figure **4-15** shows the electron density as a function of the x-position for the structures with square, triangle, and pentagon cross-section geometries. It is equivalent to Figure **4-14**a for the circular system. Each figure shows the plot of the probability density of the states that contribute simultaneously to the two oscillations in all the systems of Figure **4-15**. That is, ψ_0, ψ_2, ψ_5, ψ_{10}, and ψ_{14}, as indicated in Table **4-2**, where the percentage contribution of each one to the electron density at the position determined by the dashed line (points (1) and (2)) is also shown. States above ψ_{15} present a contribution much less than 1.0 % and therefore were not included in Table **4-2**. In these structures, we see again how the lower states provide a higher contribution to the electron density near the symmetry axis of the QW systems. Since these figures have been calculated at low temperature ($T = 10\,\mathrm{K}$), then the electrons will be—to a greater extent—occupying the lowest states of each QW. The opposite case occurs at points far from the symmetry axis of the structure, where we

see a minimum contribution from the lowest states of the system and a higher contribution—in percentage—from the highest occupied states. The $x = 0$ coordinate corresponds to the symmetry axis of each structure. Note the asymmetry in the electron density profile concerning this point for the triangular and pentagonal systems.

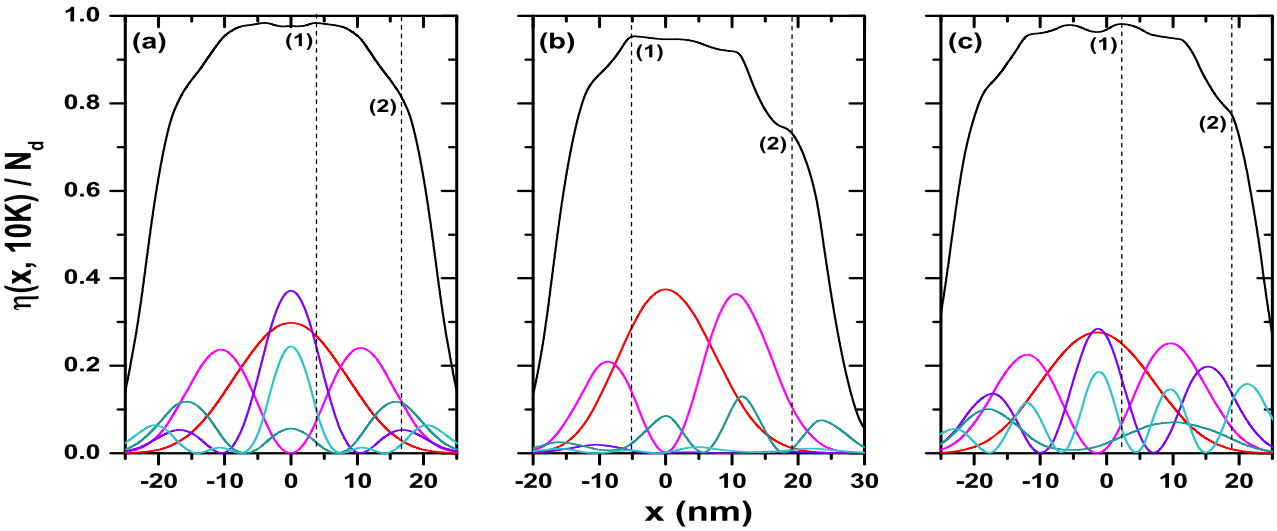

Figure 4-15.: Electron density and $|\psi_i(x, y = 0)|^2$ that contribute with the highest percentage to the density profile in points (1) and (2). Results are for square (**a**), triangle (**b**), and pentagon (**c**) QW. Calculations are for $R_0 = 50\,\mathrm{nm}$, $N_d = 2 \times 10^{18}\,\mathrm{cm}^{-3}$, and $T = 10\,\mathrm{K}$.

Table 4-2.: The first 16 states and their percentage contribution to the electron density profile at points (1) and (2) of Figure **4-15**.

	Square		**Triangle**		**Pentagon**	
ψ_n	$\mathbf{P_1}$ (%)	$\mathbf{P_2}$ (%)	$\mathbf{P_1}$ (%)	$\mathbf{P_2}$ (%)	$\mathbf{P_1}$ (%)	$\mathbf{P_2}$ (%)
ψ_0	27.3	3.4	30.4	1.7	25.5	1.1
ψ_1		0.4	0.1			
ψ_2	7.6	13.8	14.4	14.4	7.2	7.2
ψ_3			14.2	19.5	7.4	3.3
ψ_4	0.7	19.7	10.5	18.0		
ψ_5	24.6	6.6	0.6	0.6	16.9	17.2
ψ_6			8.3	24.4		
ψ_7	2.8	10.8		2.3	2.1	7.0
ψ_8	13.5	16.3				
ψ_9	3.4		2.1	10.2	13.8	24.6
ψ_{10}	2.4	14.1	2.4	1.4	3.9	4.1
ψ_{11}			0.4			
ψ_{12}			9.2	1.6	5.6	6.0
ψ_{13}	1.9	0.8	6.7	4.8		
ψ_{14}	10.2	2.9	0.7	1.1	5.1	15.9
ψ_{15}	1.8	8.3				

4.4. Conclusions

Electronic properties such as wave functions, state energies, potentials and electron densities have been calculated in a self-consistent way, using the finite element method, for GaAs quantum wire systems of different cross-section geometry, taking into account variations in geometric parameters, such as cross-sectional area and non-geometric parameters, such as the donor density and the temperature. It has been shown that the increase in cross-section and/or donor density in all structures generates a lesser degree of confinement by the self-consistent potential and, therefore, a decrease in electronic energies. The opposite case occurs when the temperature is increased, for which there is an in-

crease in the self-consistent potential profile, thus impacting on the increase of energy eigenvalues for all systems. The system that presents the highest values of the confined energy levels is the quantum wire with a triangular cross-section, and the one with the lowest energies is the circular wire. At low temperatures, all structures present irregularities in the electron density profile. These Friedel-like oscillations are due to the degree of occupation of internal and surface states (that arise from having the surface of the quantum wire exposed) by conduction electrons. This new understanding of the quantum wires can be extended without significant changes to the study of finite-length nanowires with the most diverse geometries. Hence, we believe that the results and scheme presented here can be of interest to researchers in the area.

References

[1] Arora, V.K. Quantum size effect in thin-wire transport. *Phys. Rev. B* **1981**, *23*, 5611–5612.

[2] Arora, V.K. Onset of degeneracy in confined systems. *Phys. Rev. B* **1982**, *26*, 2247–2249.

[3] Bryant, G.W. Hydrogenic impurity states in quantum-well wires. *Phys. Rev. B* **1984**, *29*, 6632–6639.

[4] Bryant, G.W. Hydrogenic impurity states in quantum-well wires: Shape effects. *Phys. Rev. B* **1985**, *31*, 7812–7818.

[5] Luryi, S.; Capasso, F. Resonant tunneling of two-dimensional electrons through a quantum wire: A negative transconductance device. *Appl. Phys. Lett.* **1985**, *47*, 1347–1349; Erratum in **1986**, *48*, 1693.

[6] Lai, W.Y.; Sarma, S.D. Ground-state variational wave function for the quasi-one-dimensional semiconductor quantum wire. *Phys. Rev. B* **1986**, *33*, 8874–8877.

[7] Wong, K.B.; Jaros, M.; Hagon, J.P. Confined electron states in GaAs-$Ga_{1-x}Al_xAs$ quantum wires. *Phys. Rev. B* **1987**, *35*, 2463–2466.

[8] Cibert, J.; Petroff, P.M. Carrier confinement potential in quantum-well wires fabricated by implantation-enhanced interdiffusion in the GaAs-$Ga_{1-x}Al_xAs$ system. *Phys. Rev. B* **1987**, *36*, 3243–3246.

[9] Citrin, D.S.; Chang, Y.-C. Valence-subband structures of $GaAs/Al_xGa_{1-x}As$ quantum wires: The effect of split-off bands. *Phys. Rev. B* **1989**, *40*, 5507–5514.

[10] Gold, A.; Ghazali, A. Analytical results for semiconductor quantum-well wire: Plasmons, shallow impurity states, and mobility. *Phys. Rev. B* **1990**, *41*, 7626–7640.

[11] Yamauchi, T.; Arakawa, Y. Tight binding analysis of GaAsAlGaAs quantum wire structures. *Superlattices Microstruct.* **1991**, *10*, 83–87.

[12] Deng, Z.-Y.; Sun, H.; Gu, S.-W. Hydrogenic impurity states in the quantum well wires with lateral surface structures. *Phys. Lett. A* **1992**, *169*, 186–190.

[13] Gréus, C.; Bayer, M.; Forchel, A.; Benner, S.; Haug, H.; Knipp, P.; Reinecke, T.L. Lateral quantization effects in the optical spectra of InGaAs/GaAs quantum wires. *Superlattices Microstruct.* **1994**, *16*, 265–269.

[14] Citrin, D.S. Interband optical properties of quantum wires: Theoryand application. *J. Nonlinear Opt. Phys.* **1995**, *4*, 83–98.

[15] Rossi, F.; Molinari, E.; Rinaldi, R.; Cingolani, R. V-grooved quantum wires as prototypes of 1D-systems: Single particle properties and correlation effects. *Solid State Electron.* **1996**, *40*, 249–255.

[16] Someya, T.; Akiyama, H.; Sakaki, H. Shape analysis of wave functions in T-shaped quantum wires by means of magneto-photoluminescence spectroscopy. *Solid State Commun.* **1998**, *108*, 923–927.

[17] Ogawa, T. GaAs quantum wires. In *Optical Properties of Low-Dimensional Materials*; World Scientific: Singapore, 1998; Volume 303–354, p. 468.

[18] Ridene, S. Mid-infrared emission in $In_xGa_{1-x}As$/GaAs T-shaped quantum wire lasers and its indium composition dependence. *Infrared Phys. Technol.* **2018**, *89*, 218–222.

[19] Zaouali, F.; Bouazra, A.; Said, M. A theoretical evaluation of optical properties of InAs/InP quantum wire with a dome cross-section. *Optik* **2018**, *174*, 513–520.

[20] Antil, S.; Kumar, M.; Lahon, S.; Dahiya, S.; Ohlan, A.; Punia, R.; Maan, A.S. Influence of hydrostatic pressure and spin orbit interaction on optical properties in quantum wire. *Physica B* **2019**, *552*, 202–208.

[21] Giraldo-Tobón, E.; Ospina, W.; Miranda, G.L.; Fulla, M.R. Energy spectrum analysis of a realistic single-electron $Ga_{1-x}Al_xAs/GaAs/Ga_{1-x}Al_xAs$ quantum V-groove in external electric field. *Physica E* **2019**, *114*, 113652.

[22] Van-Tan, L.; Thang, T.V.; Vy, N.D.; Cao, H.T. Spin polarization and temperature dependence of electron effective mass in quantum wires. *Phys. Lett. A* **2019**, *383*, 2110–2113.

[23] Kes, H.; Okan, S.E.; Aktas, S. The excitons in infinite potential centered multilayered coaxial quantum wire and the magnetic field effects on their properties. *Superlattices Microstruct.* **2020**, *139*, 106421.

[24] Hosseinpour, P. Effect of Gaussian impurity parameters on the valence and conduction subbands and thermodynamic quantities in a doped quantum wire. *Solid State Commun.* **2020**, *322*, 114061.

[25] Boström, F.V.; Tsintzis, A.; Hell, M.; Leijnse, M. Band structure and end states in InAs/GaSb core-shell-shell nanowires. *Phys. Rev. B* **2020**, *102*, 195434.

[26] Cunha, S.M.; da Costa, D.R.; Felix, L.C.; Chaves, A.; Junior, J.M.P. Electronic and transport properties of anisotropic semiconductor quantum wires. *Phys. Rev. B* **2020**, *102*, 045427.

[27] Méndez-Camacho, R.; Casta neda-Priego, R.; Cruz-Hernández, E. Many-electron redistribution in n-doped semiconductor nanostructures under external electric field by using a center-of-mass approach. *Phys. Rev. B* **2020**, *102*, 035403.

[28] Woods, B.D.; Sarma, S.D.; Stanescu, T.D. Subband occupation in semiconductor-superconductor nanowires. *Phys. Rev. B* **2020**, *101*, 045405.

[29] Hatami, F.; Bierwagen, O. Growth of low-dimensional semiconductors structures. In *Comprehensive Semiconductor Science and Technology*; Elsevier: Ámsterdam, The Netherlands, 2011; Volume 523–583, p. 3608.

[30] Garnett, E.C.; Brongersma, M.L.; Cui, Y.; McGehee, M.D. Nanowire Solar Cells. *Ann. Rev. Mater. Res.* **2011**, *41*, 269–295.

[31] Jia, C.; Lin, Z.; Huang, Y.; Duan, X. Nanowire electronics: From nanoscale to macroscale. *Chem. Rev.* **2019**, *119*, 9074–9135.

[32] Ram-Mohan, L.R.; Yoo, K.H.; Moussa, J. The Schrödinger–Poisson self-consistency in layered quantum semiconductor structures. *J. Appl. Phys.* **2004**, *95*, 3081–3092.

[33] Laux, S.E.; Stern, F. Electron states in narrow gate-induced channels in Si. *Appl. Phys. Lett.* **1986**, *49*, 91–93.

[34] Laux, S.E.; Frank, D.J.; Stern, F. Quasi-one-dimensional electron states in a split-gate GaAs/AlGaAs heterostructure. *Surf. Sci.* **1988**, *196*, 101–106.

[35] Luscombe, J.H.; Bouchard, A.M. Electron confinement in quantum nanostructures: Self-consistent Poisson-Schrödinger theory. *Phys. Rev. B* **1992**, *46*, 10262–10268.

[36] Tadić, M.; Ikonixcx, Z.; Milanovixcx, V. The self-consistent electronic structure of rectangular free-standing quantum wires: Fourier expansion approach. *Superlattices Microstruct.* **1998**, *23*, 369–379.

[37] Trellakis, A.; Ravaioli, U. Computational issues in the simulation of semiconductor quantum wires. *Comput. Method. Appl. Mech. Eng.* **2000**, *181*, 437–449.

[38] Snider, G.L.; Tan, I.-H.; Hu, E.L. Electron states in mesa-etched one-dimensional quantum well wires. *J. Appl. Phys.* **1990**, *68*, 2849–2853.

[39] Proetto, C.R. Self-consistent electronic structure of a cylindrical quantum wire. *Phys. Rev. B* **1992**, *45*, 11911.

[40] Kerkhoven, T.; Raschke, M.W.; Ravaioli, U. Self-consistent simulation of quantum wires in periodic heterojunction structures. *J. Appl. Phys.* **1993**, *74*, 1199–1204.

[41] Hu, B.Y.; Sarma, S.D. Self-consistent calculation of ionized impurity scattering in semiconductor quantum wires. *Phys. Rev. B* **1993**, *48*, 14388.

[42] Martorell, J.; Wu, H.; Sprung, D.W.L. Systematic trends in self-consistent calculations of linear quantum wires. *Phys. Rev. B* **1994**, *50*, 17298.

[43] Aristone, F.; Sanchez-Dehesa, J. Hysteresis Effects on Quantum Wires: Do They Exist or Not? *J. Korean Phys. Soc.* **2001**, *39*, 497–500.

[44] May, C.P.; Troyer, M.; Ensslin, K. Self-consistent simulation of quantum wires defined by local oxidation of Ga(Al)As heterostructures. *Phys. Rev. B* **2007**, *76*, 235321.

[45] Chuen, J.; Li, D.Y.; Tian, Y.; Shao, L.X. Self-Consistent Calculation on the Time-Dependent Electrons Transport Properties of a Quantum Wire. *J. Nanomater.* **2015**, *2015*, 842937.

[46] Ghosh, S.; Banerjee, A.S.; Suryanarayana, P. Symmetry-adapted real-space density functional theory for cylindrical geometries: Application to large group-IV nanotubes. *Phys. Rev. B* **2019**, *100*, 125143.

[47] Sharma, A.; Suryanarayana, P. Real-space density functional theory adapted to cyclic and helical symmetry: Application to torsional deformation of carbon nanotubes. *Phys. Rev. B* **2021**, *103*, 035101.

[48] Popescu, I.; Hristache, M.; Ciobanu, S.-S.; Barseghyan, M.G.; Vinasco, J.A.; Morales, A.L.; Radu, A.; Duque, C.A. Size or shape-what matters most at the nanoscale? *Comput. Mater. Sci.* **2019**, *165*, 13–22.

[49] Sullivan, D.M.; Mossma, S.; Kuzyk, M.G. Time-domain simulation of three dimensional quantum wires. *PLoS ONE* **2016**, *11*, e0153802.

[50] Zangwill, A. *Physics at Surfaces*; Cambridge University Press: New York, NY, USA, 1988; p. 454.

[51] *COMSOL Multiphysics, v. 5.4*; COMSOL AB: Stockholm, Sweden, 2020.

[52] *COMSOL Multiphysics Reference Guide*; COMSOL: Stockholm, Sweden, May 2012.

[53] *COMSOL Multiphysics Users Guide*; COMSOL: Stockholm, Sweden, May 2012.

[54] Luscombe, J.H.; Luban, M. Lateral confinement in quantum nanostructures: Self-consistent screening potentials. *Appl. Phys. Lett.* **1990**, *57*, 61–63.

[55] Suzuki, T.; Ando, T. Self-consistent results in quantum wires in magnetic fields: Temperature effects. *Physica B* **1996**, *227*, 46–49.

[56] Avazzadeh, Z.; Khordad, R.; Bahramiyan, H.; Mohammadi, S.A. Energy gap renormalization and diamagnetic susceptibility in quantum wires with different cross-sectional shape. *J. Comput. Electron.* **2016**, *15*, 931–938.

[57] Khordad, R.; Sedehi, H.R.R.; Bahramiyan, H. Effects of impurity and cross-sectional shape on entropy of quantum wires. *J. Comput. Electron.* **2018**, *17*, 551–561.

5. Study of Electronic and Transport Properties in Double Barrier Resonant Tunneling Systems

Resonant tunneling devices are still under study today due to their multiple applications in fields such as optoelectronics or logic circuits. In this work, we review an out-of-equilibrium double-barrier resonant tunneling diode system, including the effect of donor density and external potentials in a self-consistent way. The calculation method uses the finite-element approach, as well as the Landauer formalism. Quasi-stationary states, transmission probability, current density, and conductance are discussed considering variations in the donor density and the width of the central well. Finally, a comparison of the simulation with an experimental double barrier system based on InGaAs with AlAs barriers reported in the literature have been obtained.

5.1. Introduction

Resonant tunneling diodes (RTDs) are semiconductor devices that consist of a system of two or more potential barriers that allow the transport of electrons only for certain states known as resonant states. The operating mechanism is fundamentally based on the tunneling effect of quantum mechanics. This type of system is characterized by developing one or more negative differential resistance (NDR) zones that are the fundamental peculiarity of RTDs that enable them for various applications. These devices are experimentally developed in very thin layers which allows an ultra-fast operation speed, enabling

them for applications even in the terahertz range [1–3]. The first investigations in the field of resonant tunneling were carried out around 50 years ago, some of these early developments have been included in the references [4–11]. These studies have progressed continuously, characterizing RTDs both experimentally and theoretically. To mention some of the most recent work in this area, the following references are included [12–21].

Over the years, knowledge about the operation and physics behind this type of semiconductor devices has expanded, thus allowing a numerous applications, among which we can highlight: Wei and Shen's work where a novel universal threshold logic gates (UTLG) based on RTD with simple structure and fixed parameters are proposed, taking advantage of the characteristics of Negative Differential Resistance [22]. Jijun *et al.* analyzed the piezoelectric effects in RTDs based on GaAs/$In_xGa_{1-x}As$/AlAs for potential applications in micromachined mechanical sensors, obtaining as a result that the piezoresistive sensitivity of RTDs can be adjusted through the bias voltage [23]. Due to their particular NDR behavior, these systems are excellent candidates for applications to nanoelectronics, in this sense, Malindretos *et al.* grew a GaAs/AlAs RTD by means of an epitaxy molecular beam, their results are satisfactory and of good precision to fabricate RTDs suitable for application in robust digital logic circuits [24]. Among all the applications of this type of system, it is worth highlighting applications in detector devices that can filter in a varied range of frequencies by simply modifying geometric or material parameters. To mention such a device, Dong *et al.* [25] developed an RTD based on $In_{0.53}Ga_{0.47}As$ for detection in the 1550 nm range, they found that the detector responsivity is nonconstant, it decreases with the increase of the power density of the incident light, this provides the basis for optimizing the performance of the RTD.

Resonant tunneling systems go beyond double-barrier based systems, in 2020 Mehmet Bati studied the effects of an intense laser field on the properties of resonant tunneling in a double-well structure parabolic reverse triple barrier system implementing the method of finite differences combined with the Green function formalism to calculate the transmission functions, obtaining as a conclusion that the increment of the well width causes the incident electron waves to be localized. Consequently, the transmittance decreases, and the resonant peak becomes small or disappear [26].

In this problem, the Landauer approach has been chosen for the calculation of conductance since it is a model that has a fairly broad theoretical development and that has been studied in depth for more than 40 years, in 1981 Langreth D.C. and Abrahams E. gave a rigorous derivation to the conductance formula from the linear response theory (Kubo's formula), giving a generalization to the case of many-scattering-channel and found that only in very special circumstances can the currents in different channels are decoupled in such a way as to give a simple conductance formula [27]. Six years later, S. Eränen and J. Sinkkonen further generalized this formalism, studying the electrical current transport in conductor-insulator-conductor structures, where the charge carriers are assumed to traverse the insulating layer by tunneling. They self-consistently solved the coupled system of Poisson and Boltzmann equations, the latter giving the form of temporary relaxation. An important conclusion of this work is that the tunneling current density comes from the contribution of two effects: the first is the ordinary contribution of the Landauer formula in the linear voltage regime, and the second is a correction term originated by the screening of the electric potential through the insulating layer. The contribution to the current due to this screening term in most systems is negligible compared to the current generated by the effect of resonant tunneling. These results are detailed in reference [28].

Apart from the effect of the charge redistribution caused by the ionized donors and the external electric field applied to the contacts, it is possible to analyze the effect of the electronic spin dependence on the transport properties in magnetic RTD. The three combined effects generate an effective modification in the profile associated with the bottom of the conduction band in the heterostructure that finally causes modifications in the electronic transport properties. In the work of Havu *et al.* [29] it was implemented the self-consistent spin-density-functional theory method within the Wigner formalism with Green functions to analyze the properties of electronic transport in a magnetic resonant tunneling diode obtaining the electronic densities and potentials, studying the computational cost that this requires.

Over the years, work continues to improve numerical techniques to make them more efficient and extend theoretical developments in various physical situations. Taking advantage of the versatility in terms of materials and external

parameters with which it is possible to develop RTDs, our main interest is to develop a methodological approach to address these types of problems by first solving the effect of charge redistribution and electron density in the system out of equilibrium to obtain in this way the profile at the bottom of the self-consistent conduction band. This will act as an input parameter for the potential term in the Schrödinger equation considering open boundary conditions in the effective mass approximation, this equation as well as the Poisson equation are solved by means of the finite element method (FEM) to obtain a set of quasi-stationary states and probabilities of electronic transmission in the system, finally with these transmission functions the Landauer formalism is implemented for the calculation of the density current and conductance. In this study we report the self-consistent potentials, quasi-stationary electronic states, tunneling currents, and conductances for different widths of the central well and different donor densities, then a comparison is made between theoretical results of this procedure with recently reported experimental results. The chapter is organized as follows—Section 5.2 and 5.2.1 presents the theoretical framework of the simulation. In Section 5.3 we show and discuss the results obtained, Section 5.3.1 includes a comparison with experimental results reported in the literature, whilst Section 5.4 is devoted to the conclusions of the work.

5.2. Theoretical model

Our system corresponds to an RTD (Resonant Tunneling Diode), consisting of a GaAs central region (Quantum Well) of length L_w surrounded by two $Al_{0.3}Ga_{0.7}As$ barriers with equal lengths L_b, then two aditional GaAs undoped spacer with lengths L_s, the purpose of these layers is to prevent electronically tunneling scattering effects due to impurities in the contact region. Finally, two outer GaAs doped layers of length L_d. This is the central system that is contacted with two electronic reservoirs or metal contacts on each side as presented in Fig. **5-1**. For this work, we consider a non-rectifying metal-semiconductor junction, which consists of a negligible relative resistance of the contacts compared to the resistance of the central device. In this case, it is considered that mobility effects are due solely to the electronic movement in the conduction

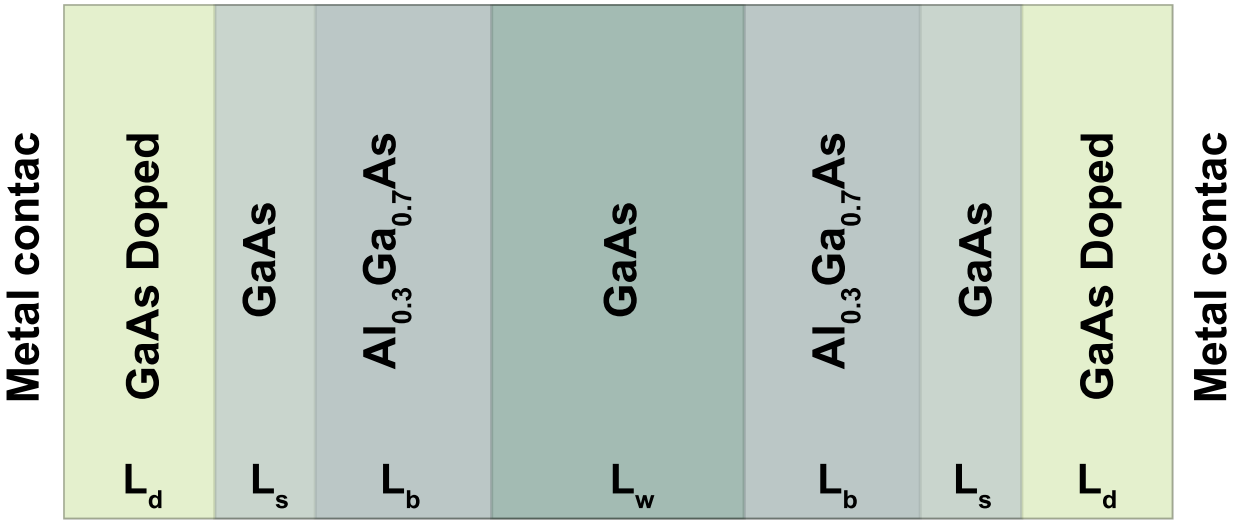

Figure 5-1.: Scheme of the resonant tunneling diode (RTD), with doping n_d in the outer regions, two $Al_{0.3}Ga_{0.7}As$ barriers, a GaAs well and two outer regions of the GaAs undoped with two metal contacts in the external regions.

band.

The system has been solved through the finite element method with the COMSOL-Multiphysics licensed software by (5.4, COMSOL AB, Stockholm, Sweden) [30–32] implementing the semiconductor module ("Semiconductor Module User's GuideÇOMSOL Multiphysics®) [33]. As a starting point, we must consider the effect on the potential due to the donor density and electron density in the system, this can be modeled by means of the Poisson equation,

$$\vec{\nabla} \cdot (\epsilon_0 \epsilon_r \vec{\nabla} V(x)) = -\rho(x), \tag{5-1}$$

in this equation, ϵ_r and ϵ_0 are the relative permittivity and vacuum permittivity respectively, and the charge density $\rho(x)$ has the form

$$\rho(x) = -q_e(n(x) - N_d), \tag{5-2}$$

in this equation N_d is the number of donors which are considered to be fully

ionized, and q_e is the electronic charge. The electronic density has the form

$$n(x) = N_c \gamma_n e^{-\beta\,(E_c - E_F)}, \tag{5-3}$$

in Eq. 5-3, E_c is the bottom of the conduction band which, due to the effect of the redistribution of charges, is not a straight line but is a function that can vary with position, E_F is the quasi-Fermi level (for the system out of equilibrium) associated with the conduction band. The term $Nc = 2(m^*/\,2\pi\beta\hbar^2)^{3/2}$ corresponds to the effective density of states, with m^* the electron effective mass, k_B is the Boltzmann constant, $\hbar$ is the reduced Planck constant, and β is the Boltzmann factor $\beta = 1/k_B T$. In Eq. 5-3, the term γ_n is equal to

$$\gamma_n = F_{1/2}\left(\beta(E_F - E_c)\right) e^{\beta(E_c - E_F)}, \tag{5-4}$$

where $F_{1/2}$ is the Fermi-Dirac integral, k_B is the Boltzmann constant and T the system temperature. In the nondegenerate states limit, the Fermi-Dirac distribution approaches the Maxwell-Boltzmann distribution and $\gamma_n = 1$. The values of the electronic affinity $q_e\,\chi = E_0 - E_c$ (E_0 is the vacuum level) and the band gap $E_g = E_c - E_v$, are input parameters associated with the properties of the materials and necessary to establish the quasi-Fermi level as a reference point during the calculations. The band energies in equations 5-3 and 5-4 are related to the electrostatic potential $V(x)$, as follows [34, 35]:

$$E_c = -\chi - q_e\,V(x). \tag{5-5}$$

The potential obtained in Eq. 5-5 can be replaced in the Schrödinger equation to obtain the eigenfunctions and eigenvalues,

$$-\hbar^2\vec{\nabla}\cdot\left(\frac{\vec{\nabla}\psi_i(\vec{r})}{2m^*}\right) + U(\vec{r})\psi_i(\vec{r}) = E_i\psi_i(\vec{r}), \tag{5-6}$$

$\hbar$ is the reduced Planck constant, $U(\vec{r}) = E_c$ is the profile of the conduction band obtained by solving the system of equations 5-1-5-5 in a self-consistent

way, this includes the potential band offset and the effect of the redistribution of charges due to doping. E_c is depicted in Fig. **5-2** for $L_w = 4\,nm$, $L_b = 3\,nm$, $L_s = 3\,nm$, $L_d = 12\,nm$ and $n_d = 1.2{\times}10^{18}\,cm^{-3}$, the quasi-Fermi level calculated for this configuration is $E_F = 0.026\,eV$ as presented in Fig. **5-2** with the dashed line. ψ_i is the system wave function corresponding to the eigenvalue E_i, the subscript i names the quasi-stationary states generated inside the device central quantum well region. The solutions of equation 5-6 for this system considering open boundary conditions are plane waves,

$$\psi_i(\vec{r}) = A(\vec{r})e^{i\vec{k}_i\cdot\vec{r}} + B(\vec{r})e^{-i\vec{k}_i\cdot\vec{r}}. \tag{5-7}$$

The functions $A(\vec{r})$ and $B(\vec{r})$ indicate that the amplitude of the wave that propagates from left to right and from right to left depends directly on the point in the system at which they are calculated and the full wave function is a superposition of these waves, k_i is the magnitude of the wave vector and is given by $k_i = (2m^*(E_i - E_c)/\hbar^2)^{1/2}$.
Knowing the amplitude of the wave function in all regions, it is possible to calculate the transmission function $T(E)$ through the device by,

$$T(E) = \frac{|A(\vec{r}_f)|^2}{|A(\vec{r}_i)|^2}, \tag{5-8}$$

where $A(\vec{r}_i)$ represents the amplitude of the wave that propagates from left to right evaluated at the emitter (amplitude of the incident wave) and $A(\vec{r}_f)$ is the amplitude of a wave that propagates from left to right but evaluated in the collector (amplitude of the transmitted wave). This function is proportional to the probability of electronic tunneling through the double barrier system.

Current-voltage characteristics of this device can be calculated using the Landauer formula which gives the electronic tunneling current between the contacts,

$$I = \frac{e}{\pi\hbar}\int_{-\infty}^{\infty} T(E)\left[\mathcal{F}_{em}(E,\Phi) - \mathcal{F}_{col}(E,\Phi)\right] dE, \tag{5-9}$$

in this equation e is the electron charge and $\hbar$ is the reduced Plank constant, the terms $\mathcal{F}_{em}(E,\Phi)$ and $\mathcal{F}_{col}(E,\Phi)$ correspond to the Fermi functions evaluated at

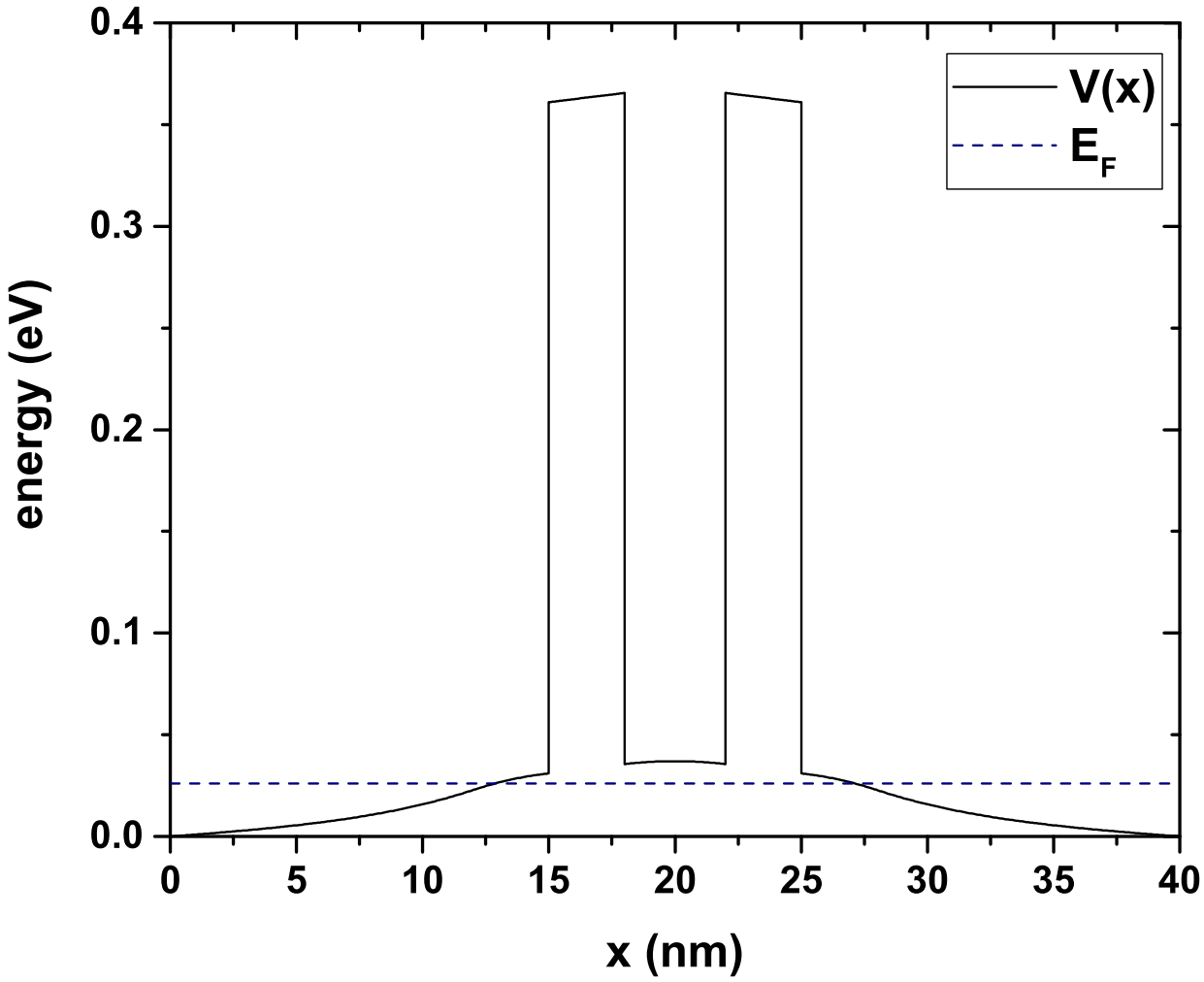

Figure 5-2.: Conduction band profile. The dashed line correspond to the quasi-Fermi Level. The calculations are for $L_w = 4\,\text{nm}$, $L_b = 3\,\text{nm}$, $L_s = 3\,\text{nm}$, $L_d = 12\,\text{nm}$ and $n_d = 1.2 \times 10^{18}\,\text{cm}^{-3}$.

the emitter and collector respectively, given by $\mathcal{F}_{em}(E,\Phi) = (1+e^{(E-E_F)/k_BT})^{-1}$ and $\mathcal{F}_{col}(E,\Phi) = (1+e^{(E-(E_F-\Phi))/k_BT})^{-1}$, where the term Φ is the bias voltage applied between both terminals of the device.
At the zero bias limit (at low temperature) the Fermi functions take the form of Heaviside functions and the Eq. 5-9 reduces to the well known Landauer equation for conductance [36],

$$G = \frac{e^2}{\pi\hbar}\,T(E), \tag{5-10}$$

the term $T(E)$ represents the transmission function between the contacts, that, in this case, correspond to the two terminals of the device (emitter and collector).

5.2.1. A device macroscopically large in the transverse directions

In most of these types of devices, it is reasonable to consider that the structure growth direction is very small compared to the transverse directions of this. Considering this statement, the electronic energy associated with their transverse directions is given by,

$$\varepsilon_{y,z} = \frac{\hbar^2}{2m^*}(k_z^2 + k_y^2). \tag{5-11}$$

With this expression, it is possible to calculate the electronic distribution, depending only on the device growth direction, obtaining,

$$\mathcal{F}(E) = S\,\frac{m^*}{\beta\pi\hbar^2}\,ln\left(1+e^{\beta(E_F-E)}\right), \tag{5-12}$$

where S is the cross-sectional area of the device and $\beta = 1/k_BT$, with k_B the Boltzmann constant and T the device temperature. This expression is proportional to the number of electrons with energy E. With these results, it is

possible to calculate the total current density through the device $J = I/S$, using equation 5-9,

$$J = \frac{em^*}{2\beta\pi^2\hbar^3}\int_0^\infty T(E)\, ln\left(\frac{1+e^{\beta(E_F-E)}}{1+e^{\beta(E_F-E-\Phi)}}\right)dE. \tag{5-13}$$

By means of this equation it is possible to calculate the current-voltage characteristics through the device, considering variations in electronic concentration and temperature.

In this type of systems, the electronic transport process is ballistic, that is, there are no dispersion mechanisms within the device, however, the current does not reach infinite values due to the electron reflection probability is different from zero that acts as a resistance to the passage of charge carriers through the system [37].

In Fig. **5-3** we can see the profile of the conduction band as well as the probability density that corresponds to the only quasi-stationary level within the central region, It is noteworthy that the energy corresponding to this level has an imaginary part as it is expected for this type of confinement in which the electrons do not remain indefinitely inside the well, but they may eventually come out through tunneling through the walls of AlGaAs after a certain half-life that is proportional to the width of the transmission function peak as will be seen later. Since the state presented in this figure corresponds to the quasi-stationary state of the central region (that is, the free electrons have exactly the same energy as the state inside the well), then it corresponds to a state of maximum tunneling probability and therefore the wave function amplitude is not affected after the electrons cross the two barriers. For any other free electron energies in the emitter region, a decrease in the amplitude of the wave function occurs, which implies a decrease in the probability of transmission. The red dashed curve corresponds to the quasi-stationary state with energy E_0 = 0.147 eV, this is precisely the energy for which there must be a maximum electron tunneling incident from the emitter.

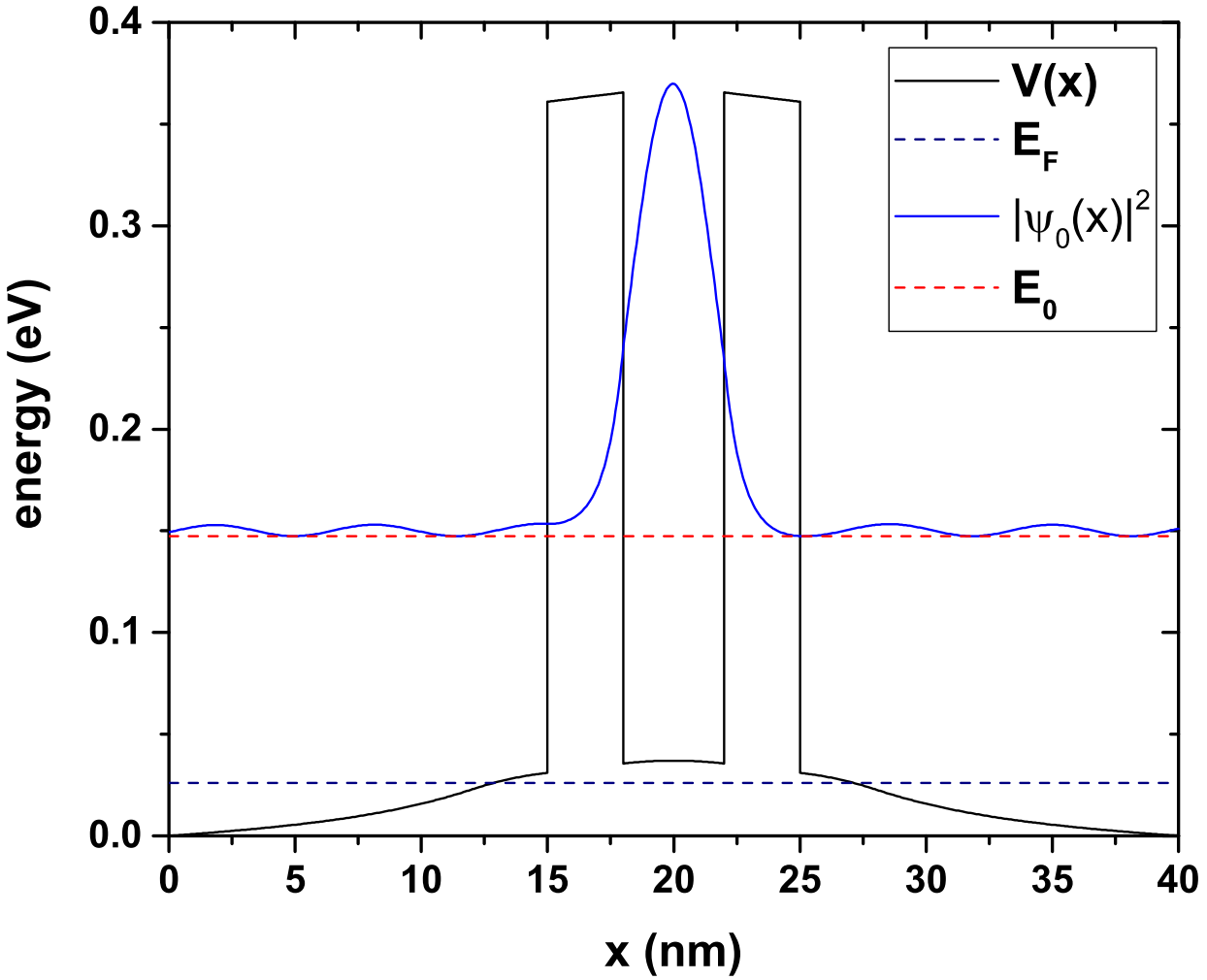

Figure 5-3.: Potential energy for the system in equilibrium (bias voltage 0.0 V), the blue curve corresponds to the probability density of the resonant state and the red dashed curve is the energy for this state E_0. The quasi-Fermi level is also presented with the blue dashed curve. The calculations are for $L_w = 4\,\text{nm}$, $L_b = 3\,\text{nm}$, $L_s = 3\,\text{nm}$, $L_d = 12\,\text{nm}$ and $n_d = 1.2 \times 10^{18}\,\text{cm}^{-3}$.

5.3. Results and discussion

For the transmission calculation except the conductance, the following input parameters have been used [38, 39] at 300 K, for GaAs: electron effective mass $m^* = 0.067\, m_0$ (where m_0 is the mass of the free electron), dielectric constant $\epsilon_r = 12.9$, band gap 1.42 eV, and electronic affinity $\chi = 4.07$ eV. For $Al_{0.3}Ga_{0.7}As$: electron effective mass $m^* = 0.0879\, m_0$, dielectric constant $\epsilon_r = 12.048$, band gap 1.81 eV, and electronic affinity $\chi = 3.74$ eV. For the conductance calculations at 5 K, the following parameters have been used, for GaAs: electron effective mass $m^* = 0.0665\, m_0$, dielectric constant $\epsilon_r = 12.4$, and band gap 1.52 eV. For $Al_{0.3}Ga_{0.7}As$: electron effective mass $m^* = 0.0916\, m_0$, dielectric constant $\epsilon_r = 11.56$, and band gap 1.95 eV. All the equations have been solved through the finite element method considering the following parameters: 538 elements, 538 edge elements, 0.5149 element length radius, 400 as the maximum number of iterations of the self-consistent method, and 10^{-6} as the absolute tolerance. Figure **5-4** shows the self-consistent potential profile and the way in which it changes as well as the resonant state probability density as the potential difference between the emitter and the collector increases. The clear redshift of the resonant level must be highlighted, as well as the decrease in the electronic probability density inside the quantum well, mainly due to the electric field effect. For voltages higher than 0.4 V, the resonant state is very close to the bottom of the conduction band at the emitter and therefore, from this limit, it no longer contributes to the transport properties in the system. From Fig. **5-4**(d), it is possible to notice that, for high voltages, there will no longer exist in the system electronic current due to resonant tunneling, the incident electrons do not have a state inside the well to tunnel and therefore, their probability of passing to the collector must be significantly decreased, this occurs until reaching a certain limit voltage from which the electrons will have two possibilities, perform resonant tunneling with a higher state of the system or perform non-resonant tunneling, this depends on both geometric characteristics and the materials involved in the system.

In Fig. **5-5** we see the transmission probability for different voltage values, as indicated by the arrow, the voltage varies from 0.0 V to 0.6 V, Fig. **5-5**(a) corresponds to a doping $n_d = 1.2{\times}10^{18}\,[1/\mathrm{cm}^3]$, while in **5-5**(b) it is $n_d =$

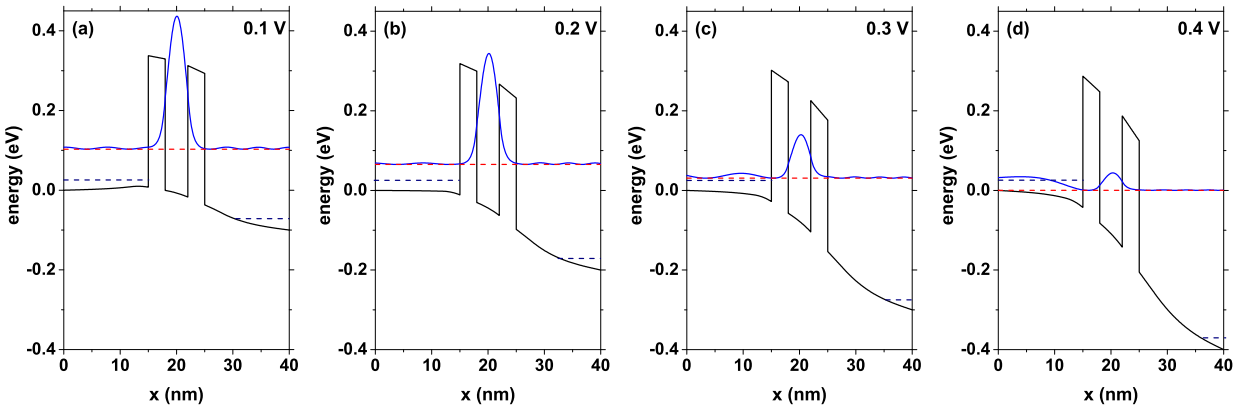

Figure 5-4.: Potential energy change with bias voltage from 0.0 V to 0.4 V, the blue curve correspond to the resonant state probability density and the red curve is the energy for this state E_0. The quasi-Fermi level is also presented by the dark blue dashed line for emitter and collector. The calculations are for $L_w = 4\,\text{nm}$, $L_b = 3\,\text{nm}$, $L_s = 3\,\text{nm}$, $L_d = 12\,\text{nm}$ and $n_d = 1.2 \times 10^{18}\,\text{cm}^{-3}$.

$10\times10^{18}\,[1/\text{cm}^3]$. The red curve is for a 10 nm QW and the black one is 4 nm. As indicated in Fig. **5-5**(b), the quasi-Fermi level at the emitter (shaded region) presents a higher value for the system that has a higher doping, which means that there are a greater number of occupied states in the conduction band that can contribute to current through the device, in Fig **5-5**(a) the quasi-Fermi level at the emitter takes the value of $E_F = 0.026\,\text{eV}$, while in Fig. **5-5**(b) it is of $E_F = 0.081\,\text{eV}$. For zero voltage, the system with $L_w = 4\,\text{nm}$ presents a single resonant level in 0.147 eV, while for $L_w = 10\,\text{nm}$ there are two resonant peaks in 0.083 eV and 0.179 eV respectively, where the one closest to the bottom of the band has a medium amplitude lower than the peak of the highest quasi-steady state, this characteristic in the amplitudes of the peaks is maintained approximately independent of the applied voltage. As the voltage is increased, as mentioned in Fig. **5-4**, there is a redshift of the levels inside the well and at the same time a decrease in the transmission amplitude, this behavior is clearly evidenced in the Fig. **5-5**(a) and **5-5**(b). In Fig. **5-5**(b), where the system presents higher doping, for $L_w = 4\,\text{nm}$ now presents the resonant state for the energy of 0.271 eV, that is, 0.124 eV higher than in the case of lower donor density presented in Fig. **5-5**(a). A fundamental difference with respect to the

system with lower n_d is that now for $L_w = 10$ nm there is only one resonant state inside the well and not two as occurs in the initial case, with an energy of 0.230 eV which, as in Fig. **5-5**(a), presents a much smaller mean amplitude than for the QW of $L_w = 4$ nm.

In Fig. **5-5**, notice how as the voltage increases, the redshift of all the states occurs, for voltages higher than 0.05 V, the system with $L_w = 10$ nm presents a third resonant peak well-defined of greater average width than the previous two, this does not happen for the system with $L_w = 4$ nm. The increase in the average width of each peak is due to the fact that the upper states are "less stable", that is, the lifetime of the electrons in these states is less than in the lower states and this time is proportional to the imaginary part of the energy associated with each of these states and the average width of the resonant peaks. The shaded area indicates the region between the bottom of the conduction band and the quasi-Fermi level at the emitter, as shown in Fig. **5-5**(a), note how the first resonant peak reaches the quasi-Fermi level at the emitter faster for the system with less doping, at approximately 0.1 V for $L_w = 10$ nm and 0.3 V for $L_w = 4$ nm. In the case of higher doping, these values become 0.3 V and 0.45 V for $L_w = 10$ nm and $L_w = 4$ nm respectively. This indicates that the system of Fig. **5-5**(a) will reach a peak in the current faster than the system of Fig. **5-5**(b).

Figure **5-6** shows the transmission probability for 0.0 V red curve and for 0.4 V black curve, Fig. **5-6**(a) is for $n_d = 1.2\times10^{18}$ [1/cm^3], Fig. **5-6**(b) is for $n_d = 10\times10^{18}$ [1/cm^3], from bottom to top results are indicated by increasing the width of the QW. The shaded area indicates the region between the bottom of the conduction band and the quasi-Fermi level at the emitter. As the width of the well increases, a new resonant state with higher energy and higher mean amplitude emerges for both electron densities, this state appears for $L_W \geq 6$ nm in the case of $n_d = 1.2\times10^{18}$ [1/cm^3] and for $L_W \geq 8$ nm in the case of $n_d = 10\times10^{18}$ [1/cm^3] as indicated in the Fig. **5-6**(a) and Fig. **5-6**(b) with the red curve respectively. For larger L_w, the first quasi-stationary state appears closer to the bottom of the conduction band at the emitter (which corresponds to 0.0 energy), which generates the appearance of the first current peak for lower voltages, this effect is more significant in the case of lower donor density. With

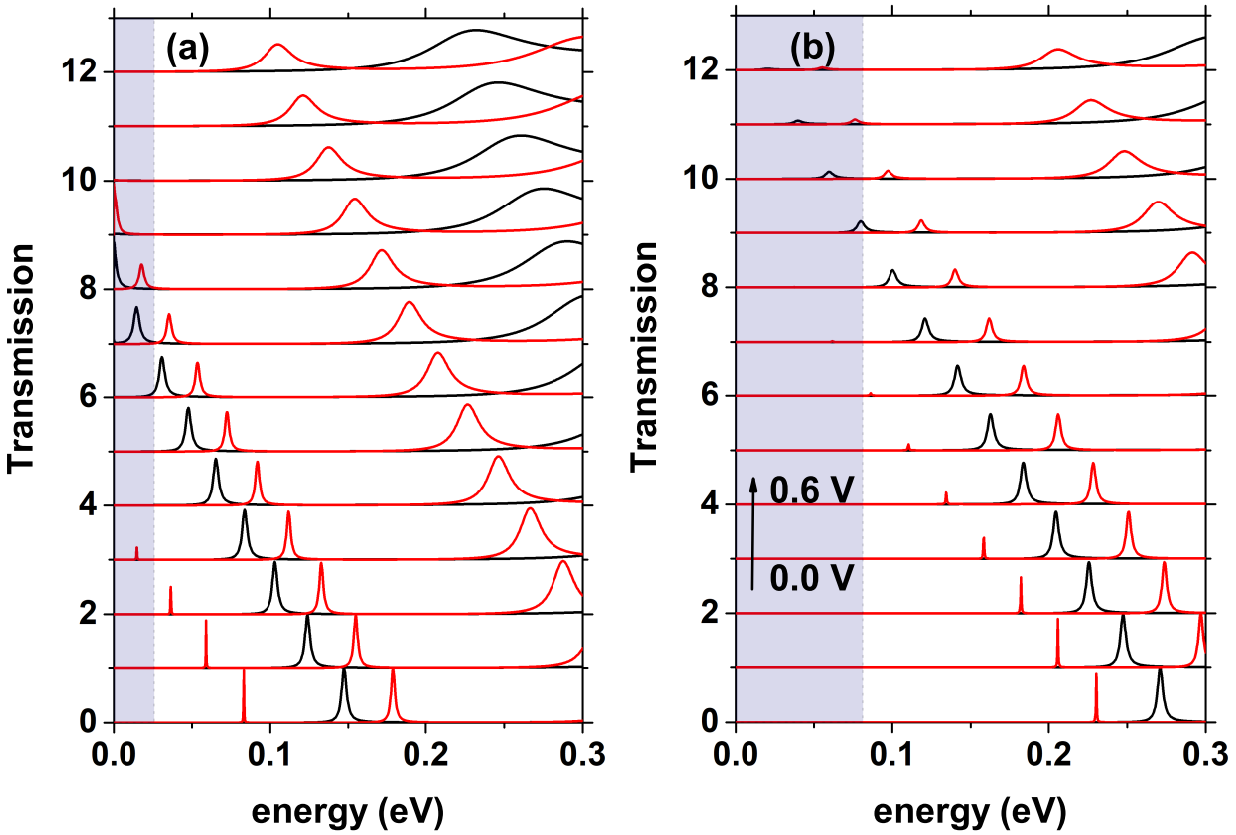

Figure 5-5.: Transmission coefficient for different values of bias voltage, the black curve is for $L_w = 4\,\text{nm}$ and, the red curve is for $L_w = 10\,\text{nm}$. (a) with n_d fixed at $1.2{\times}10^{18}\,[1/\text{cm}^3]$ and (b) with n_d fixed at $10{\times}10^{18}\,[1/\text{cm}^3]$. The shaded area indicates the region between the bottom of the conduction band and the quasi-Fermi level at the emitter. As indicated by the arrow in (b), the voltage for each curve varies from 0.0 V to 0.6 V in steps of 0.05 V.

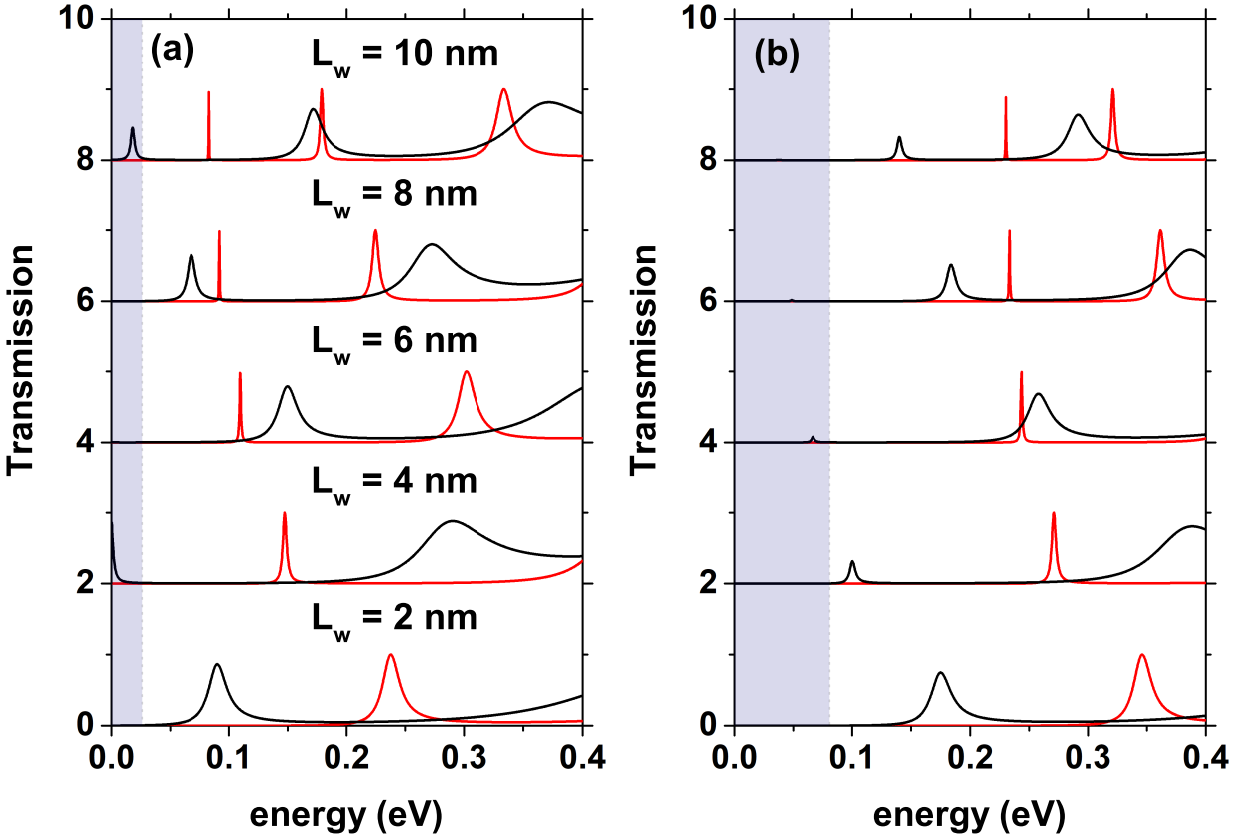

Figure 5-6.: Transmission coefficient for different values of L_w, the red curve is for 0.0 V and the black curve is for 0.4 V. (a) with n_d fixed at $1.2\times10^{18}\,[1/\mathrm{cm}^3]$ and (b) with n_d fixed at $10\times10^{18}\,[1/\mathrm{cm}^3]$. The shaded area indicates the region between the bottom of the conduction band and the quasi-Fermi level at the emitter.

respect to the increase in donor density, there is a slight shift in transmission peaks towards lower energies, which translates into reaching resonance slightly faster than for the lower density. For the 0.4 V voltage, it is possible to see how the peaks have shifted, approaching the bottom of the conduction band and present a decrease in intensity produced by the asymmetry of the potential generated by the effects of the applied electric field.

Figure **5-7** presents the tunneling current density calculated by means of Eq. 5-13 for two different values of L_w, $L_w = 4\,\text{nm}$ black points and $L_w = 10\,\text{nm}$ red points, as a function of the bias voltage. In Fig. **5-7**(a) $n_d = 1.2 \times 10^{18}\,[1/\text{cm}^3]$, in Fig. **5-7**(b) $n_d = 10 \times 10^{18}\,[1/\text{cm}^3]$. An increase in the magnitude of the current peak is evidenced for $L_w = 4\,\text{nm}$ compared to $L_w = 10\,\text{nm}$, this is due to a greater amplitude in the electron transmission probability associated with the only quasi-stationary level for the smaller well compared to the amplitude for the larger system. This is evidenced in Fig. **5-5**(a) comparing the mean amplitudes of the resonant states for both systems, obtaining, as a result, a higher mean amplitude for the system with lower L_W, that is, for $L_W = 4\,\text{nm}$, this behavior holds for both electron densities. Note how there are two peaks associated with the current for the system $L_w = 10\,\text{nm}$ one for 0.15 V and the other for 0.45 V, reaching current density values of the order of $0.042\,[\text{mA}/\mu\text{m}^2]$ and $0.449\,[\text{mA}/\mu\text{m}^2]$ respectively. Note the difference in magnitude of these two current density peaks and it is due to the fact that the first maximum corresponds to the resonant transmission with the lower energy red peak in Fig. **5-5** which, for non-zero voltages, when it reaches values below from the quasi-Fermi level at the emitter, this peak has a very low magnitude compared to that of the second resonant peak. On the other hand, for $L_w = 4\,\text{nm}$ there is only one of greater magnitude for 0.35 V, reaching a current density magnitude of $0.566\,[\text{mA}/\mu\text{m}^2]$, this is due to the fact that the larger system has two quasi-stationary states (states inside the well), while the smallest system presents only one as evidenced in Fig. **5-6**(a) with the red curves. The marked difference concerning the magnitude of the current peaks associated with $L_W = 10\,\text{nm}$ is due to the difference in amplitude of the quasi-stationary states, the amplitude being much smaller for the state of lower energy. It should be noted that for both well lengths, negative differential resistance occurs, that is, a decrease in current density from a certain limit voltage. In Fig. **5-7**(b) which corresponds to a higher donor

density, it is evident that the system with $L_W = 4\,\text{nm}$ reaches the maximum current density faster than the system with $L_W = 10\,\text{nm}$. This is due to the fact that in this system, the quasi stationary state with the lowest energy reaches the bottom of the conduction band at the emitter with a negligible amplitude and average width compared to the second quasi stationary state, this means that in Fig. **5-7**(b), the peak presented at 0.6 V of the red curve corresponding to a current of $0.102\,[\text{mA}/\mu\text{m}^2]$ is due to the resonance generated by the second state inside the well. For the system with $L_W = 4\,\text{nm}$, the resonance with the only quasi steady state is presented for a value of 0.5 V, which corresponds to a current density value of $0.204\,[\text{mA}/\mu\text{m}^2]$. For both values of L_W, with $n_d = 10{\times}10^{18}\,[1/\text{cm}^3]$ negative differential resistance is presented. For voltages higher than 0.6 V and 0.8 V in Figs. **5-7**(a) and **5-7**(b) respectively, there is a monotonous increasing behavior in current density due to the combination of two processes, the first being tunneling not resonant, that is, tunneling through a single potential barriers and the second is a probable transmission of charge carriers in regions above the potential barriers.

The system conductance is proportional to the electronic probability transmission, the constant of proportionality is known in the literature as the conductance quantum and is given by $G_0 = e^2/\pi\hbar^2$. Fig. **5-8**(a) shows the conductance as a function of the incident electron energy for a well width $L_W = 4\,\text{nm}$ for $T = 5\,\text{K}$, this function is calculated by means of Eq. 5-10, each curve corresponds to a different donor density level, the black solid curve is for $n_d = 1.2{\times}10^{18}\,[1/\text{cm}^3]$, and the red dashed curve is for $n_d = 10{\times}10^{18}\,[1/\text{cm}^3]$. For the given value of L_W, the system presents a single resonant state, note that as the donor density increases, a blue shift occurs in the conductance peaks, these quasi-stationary states are ordered from the system with the lowest n_d to the system with the highest n_d, 0.1213 eV, and 0.1299 eV respectively. It should be noted that for both curves the resonant peak average width remains approximately independent of the donor density in the system. The intensity of the resonant peaks must reach the maximum value, that is, a 100 % probability of electronic transmission when the energy of the incident electrons exactly coincides with the energy of the quasi-stationary states inside the well, this result was expected since the system is in equilibrium or equivalently without applied fields. Fig. **5-8**(b) shows the self-consistent potential corresponding to

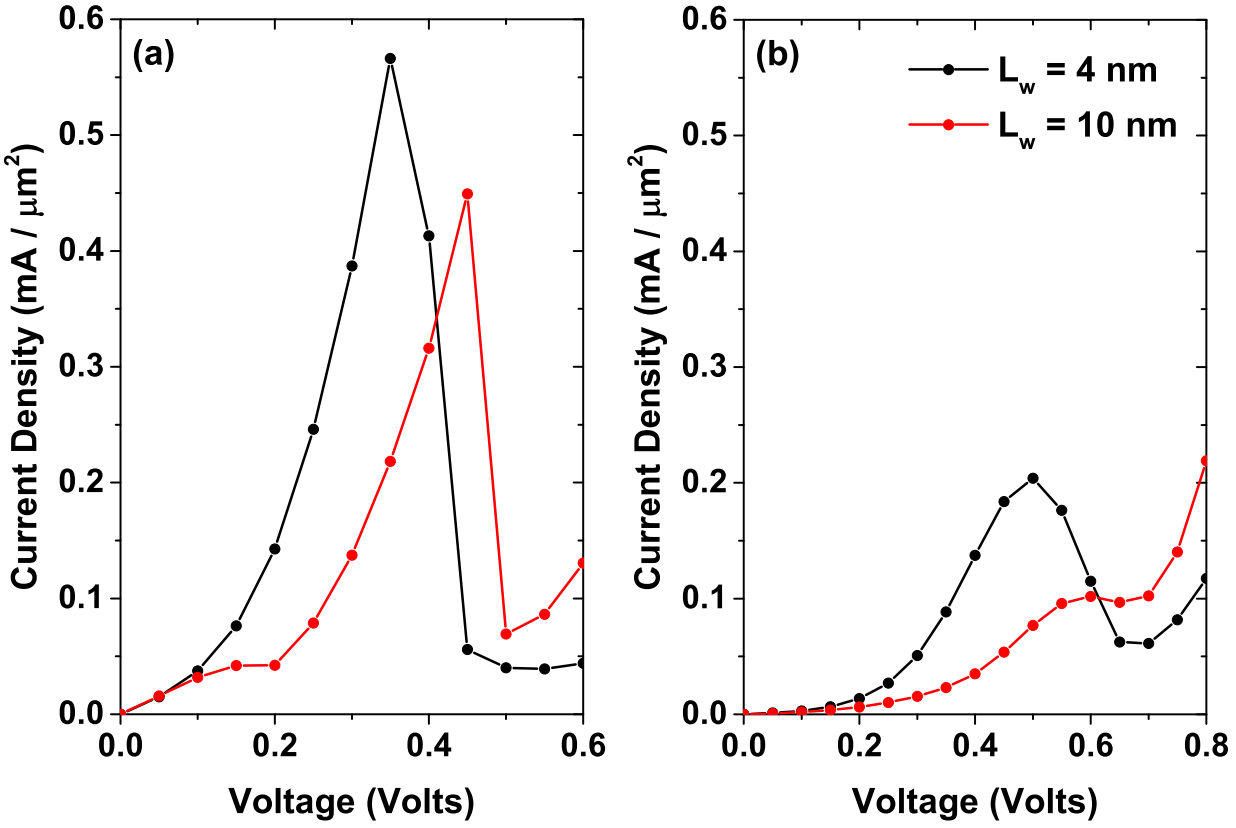

Figure 5-7.: Tunneling current density for two different values of L_W as a function of bias voltage. (a) with $n_d = 1.2{\times}10^{18}\,[1/\mathrm{cm}^3]$ and (b) with $n_d = 10{\times}10^{18}\,[1/\mathrm{cm}^3]$.

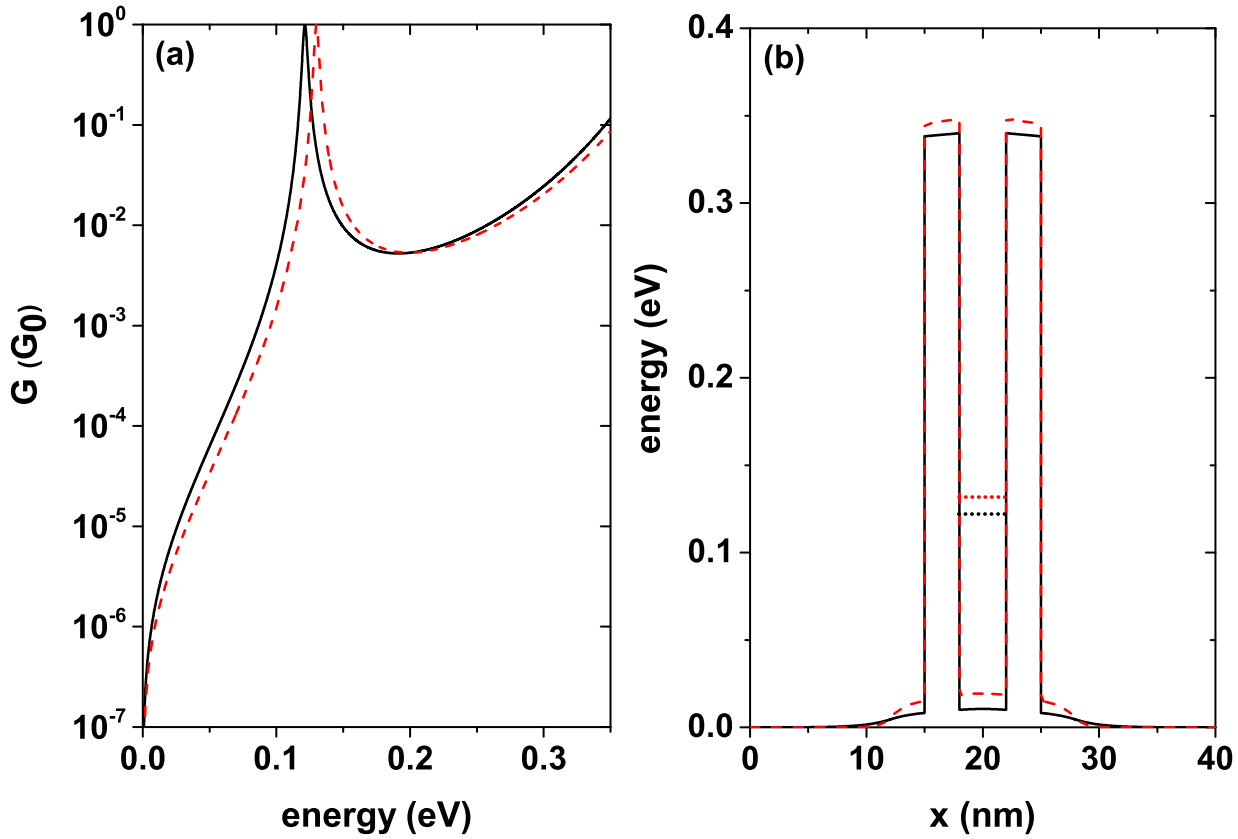

Figure 5-8.: (a) Conductance for $L_W = 4\,\text{nm}$, for two different donor concentrations in units of $G_0 = e^2/\pi\hbar^2$, solid black line $n_d = 1.2{\times}10^{18}[1/\text{cm}^3]$, and dashed red line $n_d = 10{\times}10^{18}[1/\text{cm}^3]$. (b) Corresponding self-consistent potentials. The curves have been calculated at $T = 5\,\text{K}$.

each donor density with which the curves in Fig. **5-8**(a) were calculated, notice how the height of the central region changes with the increase of n_d, taking the quasi-stationary state towards higher energies. This figure also shows the position of the quasi-stationary states inside the well for each n_d. It must be taken into account that the conductance at the calculated temperature, that is, $T = 5\,\text{K}$, differs very little from the conductance at room temperature, which is in agreement with experimental results such as those mentioned in Ref. [40].

Table **5-1** presents in detail the value of the quasi-steady state corresponding to the two donors concentrations calculated, as well as their difference ΔE. The value of the potential in the center of the well and its difference for both confi-

gurations has also been included. As mentioned above, the highest energy state corresponds to the system with the highest donor density. The energy difference between the states corresponding to the two concentrations is 8.6×10^{-3} eV, while the potential difference reaches a value slightly greater than 8.8×10^{-3} eV.

$n_d\,(10^{18}[1/\mathrm{cm}^3])\Rightarrow$	1.2	10	ΔE (10^{-3} eV) $\Downarrow$
V (eV)	0.0105	0.0193	8.8
E_1 (eV)	0.1213	0.1299	8.6

Table 5-1.: Energy associated with the conductance peaks and potential at the center of the well and their differences ΔE for the two calculated concentrations, the data correspond to Fig. 8.

Fig. **5-9**(a) shows the conductance as a function of the energy of the incident electron for a well width $L_W = 10\,\mathrm{nm}$ and $T = 5\,\mathrm{K}$, each curve corresponds to a different donor density level as in Fig. **5-8** for $L_W = 4\,\mathrm{nm}$. The black solid curve is for $n_d = 1.2\times10^{18}\,[1/\mathrm{cm}^3]$, and the red dashed curve is for $n_d = 10\times10^{18}\,[1/\mathrm{cm}^3]$. With the increase in the well width, the number of resonant states in the system increases, this is evident by comparing Fig. **5-8**(a) and **5-9**(a). For this greater width, the same shift behavior of the states towards higher energies occurs as the donor density increases. The two curves present a very sharp peak for the first state inside QW and two more peaks of greater amplitude for an intermediate energy state and for the state closer to the continuum.

$n_d\,(10^{18}[1/\mathrm{cm}^3])\Rightarrow$	1.2	10	ΔE (10^{-3} eV) $\Downarrow$
V (eV)	0.0138	0.0235	9.7
E_1 (eV)	0.0463	0.0558	9.5
E_2 (eV)	0.1432	0.1523	9.1
E_3 (eV)	0.2986	0.3076	9.0

Table 5-2.: Energy associated with the conductance peaks and potential at the center of the well and their differences ΔE for the two calculated concentrations, the data correspond to Fig. **5-9**.

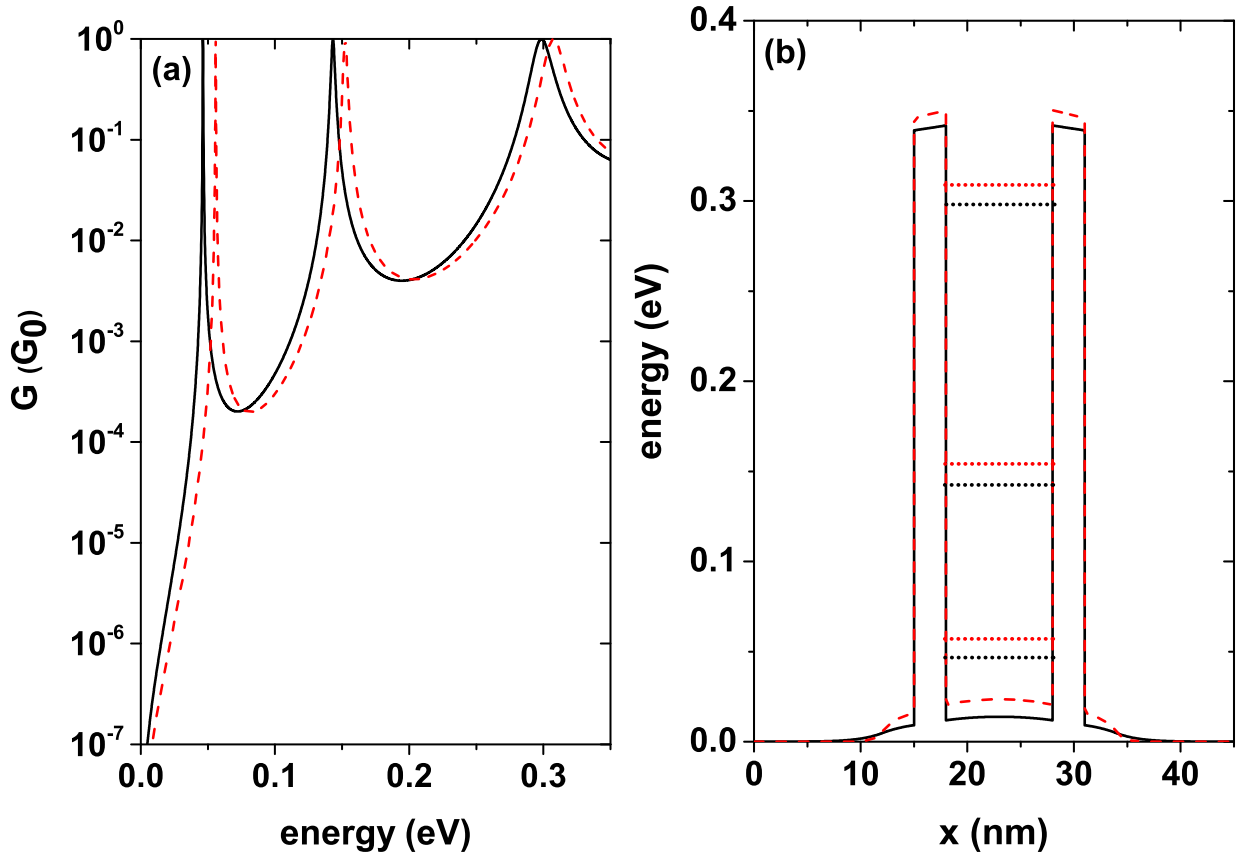

Figure 5-9.: (a) Conductance for $L_W = 10\,\mathrm{nm}$, for two different donor concentrations in units of $G_0 = e^2/\pi\hbar^2$, solid black line $n_d = 1.2{\times}10^{18}[1/\mathrm{cm}^3]$, and dashed red line $n_d = 10{\times}10^{18}[1/\mathrm{cm}^3]$. (b) Corresponding self-consistent potentials. The curves have been calculated at $T = 5\,\mathrm{K}$.

As detailed in table **5-2**, the system with $n_d = 1.2\times10^{18}\,[1/\mathrm{cm}^3]$ presents three peaks in conductance with energies of 0.046 eV, 0.143 eV, and 0.299 eV respectively, in the same way, the system with $n_d = 10\times10^{18}\,[1/\mathrm{cm}^3]$ also presents three peaks with energies of 0.056 eV, 0.152 eV, and 0.308 eV respectively. For both configurations there are three conductance peaks. Table **5-2** also shows the energy difference ΔE between each of the states corresponding to the different configurations, as well as the potential difference in the center of the well. The difference in energy becomes smaller for the highest states, that is, the states closest to the continuum are practically unchanged by the difference in donor concentration. An important conclusion is that the average width of the conductance peaks is independent of the density of donors in the system, what is modified is the position of the peaks, generating a shift towards higher energies. Fig. **5-9**(b) shows the self-consistent potential profile corresponding to each donor density with which the curves in Fig. **5-9**(a) were calculated. For this greater well width, the central region height is modified in a more significant way as compared to the depth of the smaller well width as n_d is increased. This figure also shows the position of each of the states for the two calculated concentrations.

5.3.1. Comparison with experimental data

One way to test the method is through comparison with experimental results, in this section a comparison is made with experimental results obtained by Muttlak *et al.* [41] in 2018, in which the authors presented an experimental study of InGaAs/AlAs resonant tunneling diodes designed to improve the diode characteristics by varying geometric characteristics. The Fig. **5-10** shows a diagram of the simulated device that is made up of 9 layers, of which the DBRTD (Double Barrier Resonant Tunneling Diode) zone, the spacer layers that are on both sides of the DBRTD zone, and zones 1, 2 and 8, 9 which is where donors are added to the system. This arrangement of layers is connected to two electronic reservoirs that are also presented in the figure.

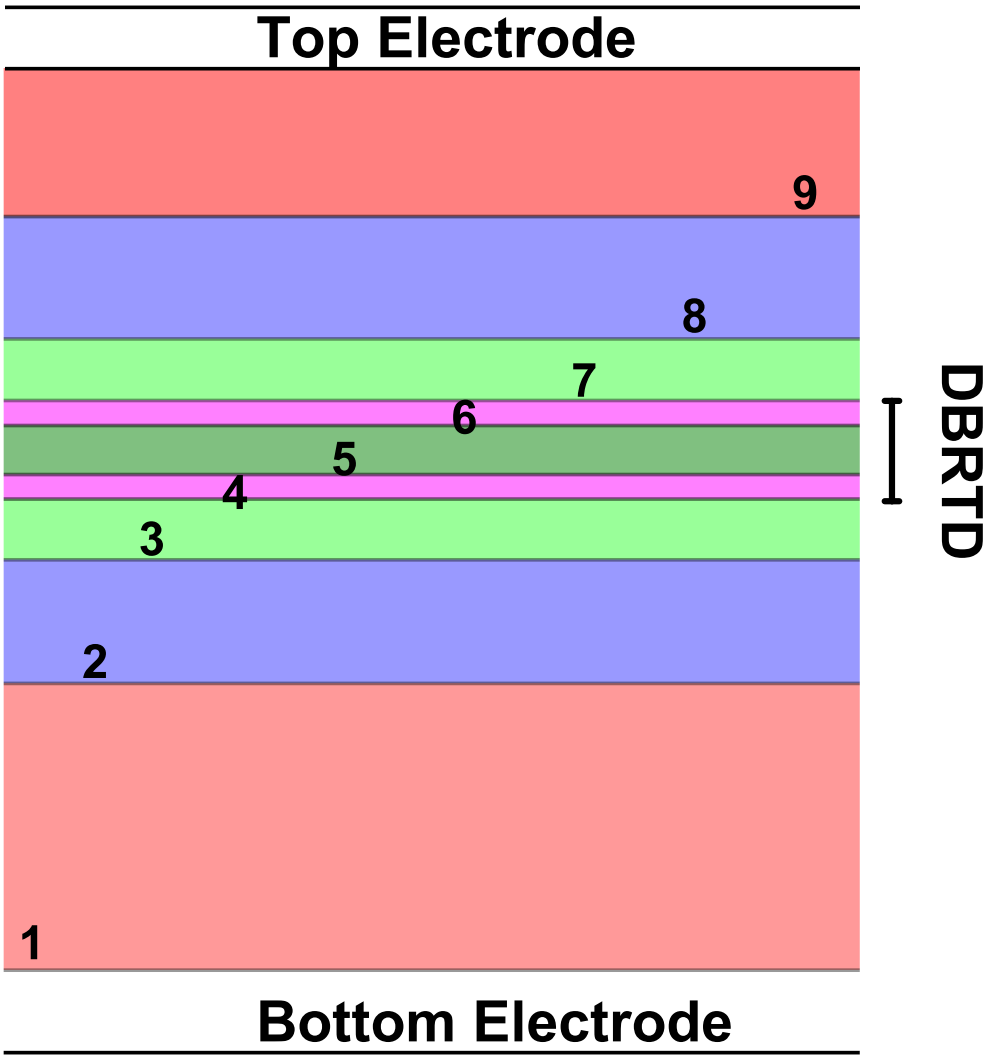

Figure 5-10.: RTD structure composed of 9 layers that are expanded in detail in table **5-3**. The letters DBRTD stand for Double Barrier Resonant Tunneling Diode.

	Parameters by layer		
Layer	Material	Dimensions (nm)	Doping (n^+ cm^{-3})
1	$In_{0.53}Ga_{0.47}As$	400	1×10^{19}
2	$In_{0.53}Ga_{0.47}As$	25	3×10^{18}
3	$In_{0.53}Ga_{0.47}As$	5	
4	AlAs	1.1	
5	$In_{0.8}Ga_{0.2}As$	3.5	
6	AlAs	1.1	
7	$In_{0.53}Ga_{0.47}As$	5	
8	$In_{0.53}Ga_{0.47}As$	25	3×10^{18}
9	$In_{0.53}Ga_{0.47}As$	45	2×10^{19}

Table 5-3.: Parameters corresponding to each of the layers in Fig. **5-10**.

Table **5-3** shows in detail the materials characteristics, as well as the layer dimensions and the donor densities corresponding to those presented in Fig. **5-10**. The outer regions are composed of $In_{0.53}Ga_{0.47}As$ with large dimensions compared to the central region of the device, the DBRTD region is made up of two AlAs barriers with equal widths of 1.1 nm and the QW region is $In_{0.8}Ga_{0.2}As$ with a width of 3.5 nm.

Figure **5-11** shows the self-consistent potential corresponding to the background of the conduction band obtained using the parameters presented in Table **5-3** at a temperature of 300 K that come from an experimental development. The white region in the figure corresponds to the conduction band of the system, the red segment indicates the first quasi-stationary state inside the well that has an energy of 0.67 eV and is near the bottom of the well. Note how the potential that is initially flat is modified considerably due to the electronic redistribution generated by the self-consistent method that takes into account the effect of the density of donors in the outer layers (regions 1,2,8, and 9). Note how the system is asymmetric with respect to the center of the QW due to the asymmetry in the regions outside the DBRTD, these differences are both geometric and with respect to the density of donors in each layer.

Figure **5-12** shows a comparison between the results using our model for the self-consistent calculation of the conduction band bottom profile and later use

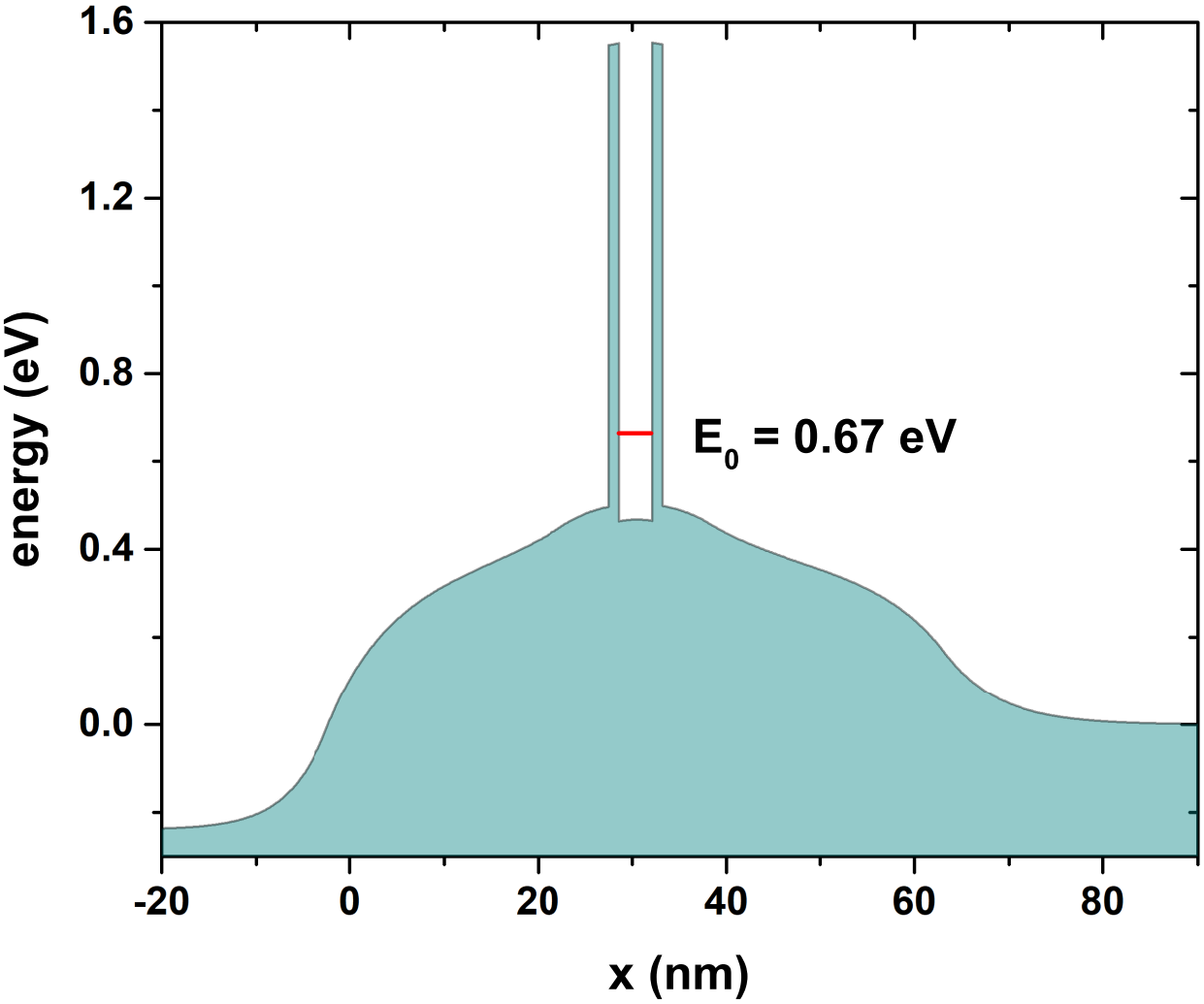

Figure 5-11.: Self-consistent potential corresponding to the conduction band obtained numerically with the experimental parameters detailed in table **5-3**.

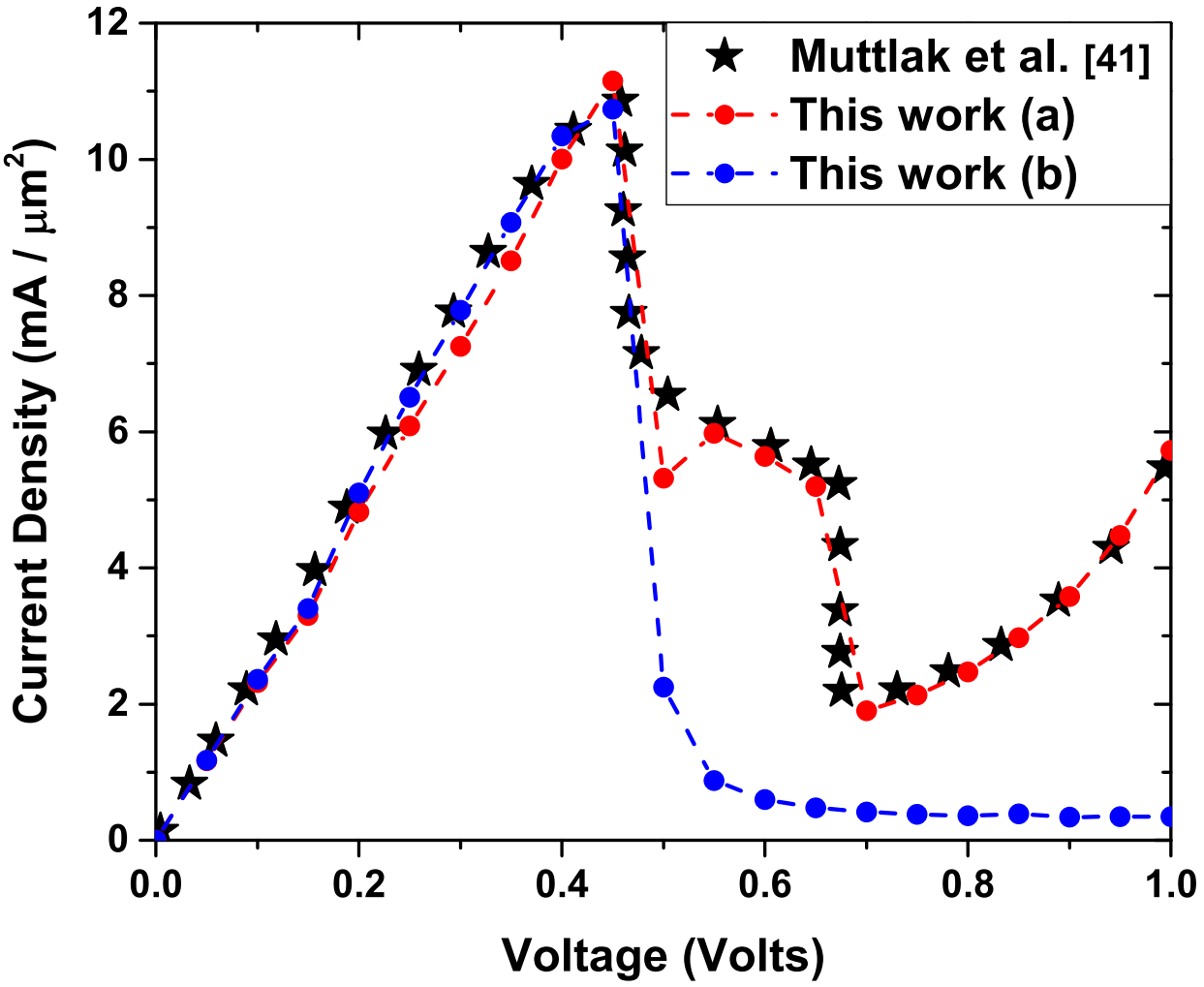

Figure 5-12.: Comparison between simulated results using Eq. 5-13 (red and blue dots) and experimental results [41] (black stars).

it to calculate the transmission by means of the Schrödinger equation in the system and finally by means of Eq. 5-13 which corresponds to a Landauer approach, calculating the current density in the device. The red dots (a) correspond to the current density due to resonant tunneling including the scattering effects simulated as additional resonances in the system, the blue points (b) correspond to the current density obtained only by resonant tunneling, while the black stars are the experimental points. The simulation parameters that correspond to the characteristics of the materials, the dimensions, as well as the donor density are presented in Table **5-3** at a temperature of 300 K, which corresponds to the temperature reported on the experimental level.

In the region between 0 V and 0.46 V there is a very good correspondence of the simulated results with the experimental ones, having a change in the current density between 0 and 10.9 $[\mathrm{mA}/\mu\mathrm{m}^2]$ approximately which corresponds to the maximum value generated by the resonance between the incident electrons and the first quasi-stationary state inside the well shown in Fig. **5-11**. For values greater than 0.46 V, the simulation presents an drop in current density that represents a negative differential resistance. For voltage higher than 0.5 V, the current in the system is mainly due to dispersion effects (this is evident due to the difference between the blue points and the red points in this region), due to possible impurities in the interlayer regions that can eventually contribute to electronic transport in the system. On the other hand, because the experimental temperature is 300 K, it is important to consider dispersion effects due to thermionic emission and electronic absorption of phonons, processes that can provide electrons with enough energy to tunnel through barriers and contribute to current density [42, 43]. These effects are included in the model by adding three additional resonances to the simulated one at positions 1.02 eV, 1.12 eV, and 1.81 eV respectively, these effects correspond to the red dots in Fig. **5-12** that generate a current peak between 0.5 V and 0.7 V and exponential-like behavior for voltages higher than 0.7 V, generated by the third resonance with a state that exceeds the height of the potential barriers of the system as seen in Fig. **5-11**, which corresponds to 1.81 eV, that is, it is a state of the continuum. When only the contribution to the current density due to the resonant tunneling is considered, the blue points are obtained that correspond to a considerable decrease in the current density due to the absence of a second state in resonance inside the well for this maximum voltage.

This model includes the effect generated by the conduction properties of the electrons that can tunnel through the resonance states inside the well, for this to happen, it is necessary that these states are available to be occupied by electrons that come from the emitter, the first peak in current density that is presented in Fig. **5-12** is generated by the resonant transmission between the electrons that are in occupied states in the emitter towards available states in the collector through the first state inside the QW. There is no second state inside the well available for tunneling for the maximum applied voltage, which is 1 V, for this reason, no more zones of negative differential resistance are present

in the system.

	This work		From references	
	E_g (eV)	χ (eV)	E_g (eV)	χ (eV)
AlAs	2.17	3.41	2.16 [44], 2.19 [45]	3.50 [44]
$In_{0.8}Ga_{0.8}As$	0.50	4.50	0.50 [47], [48]	4.73 [47], [48]
$In_{0.53}Ga_{0.47}As$	0.75	4.46	0.74 [46], [48]	4.51 [46], [48]

Table 5-4.: Comparing simulation parameters with reported parameters.

For the results presented in Fig. **5-12**, a variation was made in the input parameters of the numerical method to obtain a convergence and in this way find the optimal parameters that best fit for the experimental description, these parameters were the band gap E_g for each of the materials in each layer and the electron affinity χ in each region. The result of the convergence of these parameters is shown in table **5-4**, where a comparison with results reported in the literature is shown. All the parameters present an error of less than 3 %, which generates certainty with respect to the results presented in Fig. **5-12**.

5.4. Conclusions

The wave functions, quasi-stationary states and self-consistent potentials, among other electronic properties in a double barrier resonant tunneling diode system based on GaAs and InGaAs have been calculated, solving the equations in each step by means of the finite element method. By means of the Schrödinger equation, the probabilities of electronic transmission have been calculated considering variations in geometric parameters such as the width of the central well and non-geometric parameters such as the density of donors in the layers outside the barrier region. Additionally, the system has been converged out of equilibrium to analyze the response of the internal quasi-stationary states to an external potential difference applied to the contacts, obtaining a red shift in all transmission peaks regardless of the donor density used. A way has been found to tune the system, particularly the position or quantity of quasi-stationary states inside the central well, by modifying the bias voltage, modifying the width

of the central well and modifying the density of donors in the system. Once the system was characterized by means of the probability of electronic transmission, the Landauer formalism was used to calculate the density of electric current that circulates through the diode for different well widths and different donor densities. An important conclusion is that the first current peak is obtained for lower voltages in the case of narrower width of the central well. On the other hand, when the donor density is lower, the current peaks reach a higher value for the simulated parameters. For the cases studied, it is possible to show negative differential resistance. The conductance in the double barrier system has been calculated, changing the dimensions of the well and the density of donors, obtaining multiple peaks of conductance for a width of 10 nm and a single peak for a width of 2 nm, the increase in concentration only modifies the position of the peaks, but does not change the shape of the conductance function. Finally, the theoretical procedure has been applied to an experimental system reported in recent literature, this is a non-symmetric system based on InGaAs with AlAs barriers consisting of 9 regions. The current density at room temperature for this system has been compared, obtaining satisfactory results for the calculation of the position of the first resonance in the system and the magnitude of the current density at this point. Likewise, the converged parameters for the experimental comparison do not exceed 3 % error compared to the same parameters reported in the literature. These results indicate that this system could be a good candidate for potential applications in various fields of science or engineering.

References

[1] E. R. Brown, J. R. Söderström, C. D. Parker, L. J. Mahoney, K. M. Molvar, and T. C. McGill, *Oscillations up to 712 GHz in InAs/AlSb resonant-tunneling diodes*, Appl. Phys. Lett. **58**, 2291-2293 (1991).

[2] T. Miyamoto, A. Yamaguchi, and T. Mukai, *Terahertz imaging system with resonant tunneling diodes*, Jpn. J. Appl. Phys. **55**, 032201 (6pp) (2016).

[3] M. Bezhko, S. Suzuki, and M. Asada, *Frequency increase in resonant-tunneling diode cavity-type terahertz oscillator by simulation-based structure optimization*, Jpn. J. Appl. Phys. **59**, 032004 (6pp) (2020).

[4] A. M. Andrews, H. W. Korb, N. Holonyak, C. B. Duke, and G. G. Kleiman, *Tunnel mechanisms and junction characterization in III-V tunnel diodes*, Phys. Rev. B **5**, 2273-2295 (1972).

[5] A. M. Andrews, H. W. Korb, N. Holonyak, C. B. Duke, and G. G. Kleiman, *Photosensitive impurity-assisted tunneling in Au-Ge-doped $Ga_{1-x}Al_xAs$ p-n diodes*, Phys. Rev. B **5**, 4191-4194 (1972).

[6] W. R. Frensley, *Transient response of a tunneling device obtained from the Wigner function*, Phys. Rev. Lett. **57**, 2853-2856 (1986).

[7] V. J. Goldman, D. C. Tsui, and J. E. Cunningham, *Observation of intrinsic bistability in resonant-tunneling structures*, Phys. Rev. Lett. **58**, 1256-1259 (1987).

[8] N. C. Kluksdahl, A. M. Kriman, D. K. Ferry, and C. Ringhofer, *Self-consistent study of the resonant-tunneling diode*, Phys. Rev. B **39**, 7720-7735 (1989).

[9] S. Tarucha, Y. Hirayama, T. Saku, and T. Kimura, *Resonant tunneling through one- and zero-dimensional states constricted by $Al_xGa_{1-x}As/GaAs/Al_xGa_{1-x}As$ heterojunctions and high-resistance regions induced by focused Ga ion-beam implantation*, Phys. Rev. B **41**, 5459-5462 (1990).

[10] H. Yoshimura, J. N. Schulman, and H. Sakaki, *Charge accumulation in a double-barrier resonant-tunneling structure studied by photoluminescence and photoluminescence-excitation spectroscopy*, Phys. Rev. Lett. **64**, 2422-2425 (1990).

[11] M. Rahman and J. H. Davies, *Theory of intrinsic bistability in a resonant tunneling diode*, Semicond. Sci. Tech. **5**, 168-176 (1990).

[12] A. Belkadi, A. Weerakkody, and G. Moddel, *Demonstration of resonant tunneling effects in metal-double-insulator-metal (MI^2M) diodes*, Nat. Commun. **12**, 2925 (6pp) (2021).

[13] H. Qian, S. Li, S.-W. Hsu, C.-F. Chen, F. Tian, A. R. Tao, and Z. Liu, *Highly-efficient electrically-driven localized surface plasmon source enabled by resonant inelastic electron tunneling*, Nat. Commun. **12**, 3111 (7pp) (2021).

[14] S. Ipsita, P. K. Mahapatra, and P. Panchadhyayee, *Optimum device parameters to attain the highest peak to valley current ratio (PVCR) in resonant tunneling diodes (RTD)*, Physica B **611**, 412788 (13pp) (2021).

[15] H. Althib, *Effect of quantum barrier width and quantum resonant tunneling through InGaN/GaN parabolic quantum well-LED structure on LED efficiency*, Results Phys. **22**, 103943 (9pp) (2021).

[16] S. Iwamatsu, Y. Nishida, M. Fujita, and T. Nagatsuma, *Terahertz coherent oscillator integrated with slot-ring antenna using two resonant tunneling diodes*, Appl. Phys. Express **14**, 034001 (4pp) (2021).

[17] A. Shinkawa, M. Wakiya, Y. Maeda, T. Tsukamoto, N. Hirose, A. Kasamatsu, T. Matsui, and Y. Suda, *Hole-tunneling $Si_{0.82}Ge_{0.18}/Si$ asymmetric-double-quantum-well resonant tunneling diode with high resonance current*

and suppressed thermionic emission, Jpn. J. Appl. Phys. **59**, 080903 (4pp) (2020).

[18] I. Ortega-Piwonka, O. Piro, J. Figueiredo, B. Romeira, and J. Javaloyes, *Bursting and excitability in neuromorphic resonant tunneling diodes*, Phys. Rev. Appl. **15**, 034017 (14pp) (2021).

[19] P. Wójcik, J. Adamowski, M. Wołoszyn, and B. J. Spisak, *Intrinsic oscillations of spin current polarization in a paramagnetic resonant tunneling diode*, Phys. Rev. B **86**, 165318 (9pp) (2012).

[20] R. Citro and F. Romeo, *Aharonov-Bohm-Casher ring dot as a flux-tunable resonant tunneling diode*, Phys. Rev. B **77**, 193309 (4pp) (2008).

[21] J. Encomendero, V. Protasenko, F. Rana, D. Jena, and H. G. Xing, *Fighting broken symmetry with doping: toward polar resonant tunneling diodes with symmetric characteristics*, Phys. Rev. Appl. **13**, 034048 (10pp) (2020).

[22] Y. Wei and J. Shen, *Novel universal threshold logic gate based on RTD and its application*, Microelectr. J. **42**, 851-854 (2011).

[23] X. Jijun, W. Jian, Z. Wendong, X. Chenyang, Z. Binzhen, and H. Jie, *Piezoresistive effect in $GaAs/In_xGa_{1-x}As/AlAs$ resonant tunneling diodes for application in micromechanical sensors*, Microelectr. J. **39**, 771-776 (2008).

[24] J. Malindretos, A. Förster, K. M. Indlekofer, M. I. Lepsa, H. Hardtdegen, R. Schmidt, and H. Lüth, *Homogeneity analysis of ion-implanted resonant tunneling diodes for applications in digital logic circuits*, Superlattice Microst. **31**, 315-325 (2002).

[25] Y. Dong, G. Wang, H. Ni, J. Chen, F. Gao, B. Li, K. Pei, and Z. Niu, *Resonant tunneling diode photodetector with nonconstant responsivity*, Opt. Commun. **355**, 274-278 (2015).

[26] M. Bati, *The effects of the intense laser field on the resonant tunneling properties of the symmetric triple inverse parabolic barrier double-well structure*, Physica B **594**, 412314 (9pp) (2020).

[27] D. C. Langreth and E. Abrahams, *Derivation of the Landauer conductance formula*, Phys. Rev. B **24**, 2978-2984 (1981).

[28] S. Eränen and J. Sinkkonen, *Generalization of the Landauer conductance formula*, Phys. Rev. B **35**, 2222-2227 (1987).

[29] P. Havu, N. Tuomisto, R. Väänänen, M. J. Puska, and R. M. Nieminen, *Spin-dependent electron transport through a magnetic resonant tunneling diode*, Phys. Rev. B **71**, 235301 (11pp) (2005).

[30] COMSOL *Multiphysics, v. 5.4*; COMSOL AB: Stockholm, Sweden, 2020.

[31] COMSOL *Multiphysics Reference Guide*; COMSOL: Stockholm, Sweden, 2012.

[32] COMSOL *Multiphysics Users Guide*; COMSOL: Stockholm, Sweden, 2012.

[33] COMSOL *Multiphysics v. 5.2a Semiconductor Module User's Guide;* COMSOL AB: Stockholm, Sweden, 2016.

[34] A.F. Mohiyaddin, F.G. Curtis, M.N. Ericson, and T.S. Humble, *Simulation of Silicon Nanodevices at Cryogenic Temperatures for Quantum Computing*, COMSOL Conference, Boston, (2017).

[35] S.M. Sze and Kwok K. Ng, *Physics of semiconductor devices*, John wiley & sons, ISBN: 9780471143239, 2006.

[36] E.W. Fenton, *Effect of the electron-electron interaction on the Landauer conductance*, Phys. Rev. B **47**, 10135 (1993).

[37] V.V. Mitin, V.A. Kochelap, and M.A. Stroncio, *Introduction to Nanoelectronics, Science, Nanotechnology, Engineering, and Applications*, Cambridge University Press, ISBN: 9780511809095, 2007.

[38] A. F. da Silva, C. Persson, M. C. B. Marcussen, E. Veje, and A. G. de Oliveira, *Band-gap shift in heavily doped n-type* $Al_{0.3}Ga_{0.7}As$ *alloys*, Phys. Rev. B **60**, 2463-2467 (1999).

[39] T.E. Schlesinger, *Gallium Arsenide*, Encyclopedia of Materials: Science and Technology, 3431-3435 (2001).

[40] M. Asada, S. Suzuki, and T. Fukuma, *Measurements of temperature characteristics and estimation of terahertz negative differential conductance in resonant-tunneling-diode oscillators*, AIP Advances **7**, 115226 (2017).

[41] S. G. Muttlak, O. S. Abdulwahid, J. Sexton, M. J. Kelly, and M. Missous, *InGaAs/AlAs resonant tunneling diodes for THz applications: an experimental investigation*, IEEE J. Electron Devi. **6**, 254-262 (2018).

[42] J. P. Sun, G. I. Haddad, P. Mazumder, and J. N. Schulman, *Resonant tunneling diodes: Models and properties*, Proceedings of the IEEE **86**, 641-660 (1998).

[43] F. Chevoir and B. Vinter, *Calculation of incoherent tunneling and valley current in resonant tunneling structures*, Surf. Sci. **229**, 158-160 (1990).

[44] L. J. Brillson, *Appendix d semiconductor properties.* In *An Essential Guide to Electronic Material Surfaces and Interfaces*, John Wiley & Sons, Ltd, Hoboken, 2016, 291-292 p. 298.

[45] E. Trushin, M. Betzinger, S. Blügel, and A. Görling, *Band gaps, ionization potentials, and electron affinities of periodic electron systems via the adiabatic-connection fluctuation-dissipation theorem*, Phys. Rev. B **94**, 075123 (9pp) (2016).

[46] K. N. Zainul Ariffin, Y. Wang, M. R. R. Abdullah, S. G. Muttlak, O. S. Abdulwahid, J. Sexton, K. W. Ian, M. J. Kelly, and M. Missous, *Investigations of asymmetric spacer tunnel layer diodes for high-frequency applications*, IEEE T. Electron Dev. **65**, 64-71 (2018).

[47] A. Chakraborty and D. Singha, *Sensitivity study of staggered heterojunctions based SRG TFET sensor*, Devices for Integrated Circuit (DevIC), 681-684 (2017).

[48] K.H. Goetz, D. Bimberg, H. Jurgensen, J. Selders, A.V. Solomonov, G.F. Glinskii, and M. Razeghi, *Optical and crystallographic properties and impurity incorporation of $Ga_xIn_{1-x}As$ (0.44< x <0.49) grown by liquid phase epitaxy, vapor phase epitaxy, and metal organic chemical vapor deposition*, J. Appl. Phys. **54**, 4543 (1983).

6. Theoretical Study of Electronic and Optical Properties in Doped Quantum Structures with Razavy Confining Potential: Effects of External Fields

We investigate the energy states of confined electrons in doped quantum structures with Razavy-like confining potentials. The theoretical investigation is performed within the effective mass and parabolic band approximations, including the influence of externally applied electric and magnetic fields. First, we analyze the case of a Razavy quantum well and determine its conduction subband spectrum, focusing on the lowest energy levels and their probability densities. These properties have been numerically determined by self-consistently solving the coupled system of Schrödinger, Poisson, and charge neutrality equations. Doping is introduced via an on-center δ-like layer. In order to evaluate the associated total (linear plus nonlinear) optical absorption coefficient (TOAC), we have calculated the corresponding diagonal and off-diagonal electric dipole matrix elements, the main energy separation, and the occupancy ratio which are the main factors governing the variation of this optical response. A detailed discussion is given about the influence of doping concentration as well as electric and magnetic fields, which can produce shifts in the light absorption signal, towards either lower or higher frequencies. As an extension of the self-consistent method to a two-dimensional problem, the energy states of quantum

wire system of circular cross section, with internal doping and Razavy potential have been calculated. The response of eigenvalues, self-consistent potentials and electron densities is studied with the variation of δ-doping layer width and of the donor density. Finally, the origin of Friedel-like oscillations, that arise in the density profile, generated by the occupation of internal and surface electronic states has been explained.

6.1. Introduction

Semiconductor structures based on quantum wells (QWs), quantum-well wires , and quantum dots have acquired a huge importance in the process of designing low-dimensional devices, mostly due to their features of charge carriers confinement. To satisfy the exigence required by new generation of optoelectronic devices, the involved semiconductor structures must be suitably selected upon the basis of their confinement potential geometry, their dimensions, and the possible influence of certain external physical factors. Among these factors, we can cite the insertion of delta doped layers, as well as the application of either nonresonant intense laser field radiation, electric fields, magnetic fields, or a combination of these probe fields. All of them would play a crucial role in tuning the energy spectrum of the confined carrier states [1–10].
As it is well known, the application of an external electric field leads to a tilt of the confining potential and pushes the electron wave functions towards the edge of the structure, producing a significant change in the energy levels and, per consequent, in the transition energies. This, in turn, produces noticeable modifications in the optical absorption response of the system. The application of a magnetic field provides an additional parabolic confinement that causes further spatial spread in the wave functions so that affecting the dipole matrix elements. The influences of both electric and magnetic fields have been theoretically and experimentally studied by many researchers [11–21]. For instance, Dakhlaoui *et al.*, investigated the effects of magnetic and electric fields on the TOAC [22]. They showed that these probes can control the red and blue shifts of the TOAC in double and triple δ-doped GaAs semiconductor heterostructures. Ungan *et al.* reported on the optical responses in hyperbolic-like QWs under external electric and magnetic fields [23]. They demonstrated that the

TOAC and the total relative refractive index change coefficient can be shifted towards the blue or the red by adjusting the applied field intensities. The impacts of external perturbations on the optical and magnetic properties of GaAs/AlGaAs semi-parabolic QW have been widely discussed and commented by Hien *et al.* [24]. They proved that the magneto-optical properties are largely affected by the external fields.

Besides the application of external fields, the $\delta-$doping technique represents an ultimate concept in semiconductor's processing [25–31]. It is proved among the last years that this method is highly practical to adjust the energy levels in order to obtain the desired electronic mobility and optical absorption. For instance, in GaAs-based systems, the most typical n-type $\delta-$doping technique consists of inserting a thin layer containing silicon atoms. Once these atoms are ionized, they supply additional free electrons into the system. In addition, the silicon layer creates a triangular-shaped quantum well which would affect the spatial spread of the wave functions and furnish further confinement to the carriers [32, 33]. Various research works have explored, both experimentally and theoretically, the impact of δ-doping on the behavior of the TOAC in semiconductor quantum nanostructures [34–41]. For instance, Gaggero-Sager *et al.* studied the effects of temperature on the energy levels in a single doped QW [42], whereas Dhafer *et al.* showed the importance of an inserted δ-InGaAs layer in a single $Al_xGa_yIn_{1-x-y}As$ QW. They found that the inserted layer can improve the intensity of the optical gain which is a requirement for fiber-optical communications [43]. J. Osvald studied the effect of a non-central δ-doping layer on the energy levels and electronic density in GaAs QWs [44]. On the other hand, in 1980 M. Razavy used double potential wells in the quantum theory of molecules to describe the motion of a particle in the presence of two force fields [45]. These types of potentials are known today as Razavy potentials [46, 47], and are used as a model to describe the coupling of two molecules or quantum dots [48–51]. Effects of intense laser field and position dependent effective mass in Razavy QWs (Razavy-like quantum wells) were investigated in Ref. [52]. In their works, these authors have shown that the intensity of the TOAC can be largely tuned by varying the ionized impurity concentration in the doping layer.

Another class of heterostructures that can be studied by a similar procedure are

quantum wires (QWRs), which are semiconductor structures in which electrons are confined in the transverse plane and therefore can only move in one dimension. A consequence of the above is that the electronic energy levels present a discrete behavior along the cross section of the structure, while in the free dimension the electrons present a continuous spectrum. QWRs have been the subject of study for more than 40 years, as noticed -for example- from a bunch of early references [53–57]. Due to the remarkable applications of this type of low-dimensional structures in areas as diverse as flexible electronics (when designing thin-film transistors) or high-efficiency solar cells [58], among others; to seek an improvement in the properties of electronic conduction would become a boost to development and characterization of this type of systems. In recent years, results of great interest have been reported along these lines, some of which have appeared in references [59–62].

Motivated by all the cited works, here we aim to investigate the effects of the concentration of an on-center thin doping layer and of externally applied electric and magnetic fields on the TOAC in Razavy-like GaAs quantum structures. We shall study the impact of these parameters on the lowest energy separations, the occupancy ratios, and dipole matrices which are preponderant factors governing the TOAC variation. In the first part we develop the one-dimensional problem of a GaAs δ-doped QW (with z-oriented growth direction) having a Razavy-type confinement potential. For this system, the confined electronic states are calculated, as well as the self-consistent potentials, with a special care taken on determining the Fermi level position, affected by the both temperature and ionized impurity distribution. Subsequently, external electric and magnetic fields are applied in order to analyze the variations in obtained results and finally the optical absorption response is investigated. The second problem dealt with is a two-dimensional system corresponding to a GaAs QWR with circular cross section and exposed borders (the confinement plane has been taken as xy), with an additional δ-type doping and an inner Razavy-like potential. The problem for the electron energy states in this case is also solved in a self-consistent way, taking into account a fundamental difference: In this case the Fermi level is no longer modified by the density of donors because the system has exposed borders. So, a "Fermi Level Pinning" is presented which keeps it fixed. Another fundamental difference with respect to the QW structure is that, in this type of

systems, variations in the electron density profile known as Friedel oscillations can occur at low temperatures. To study this particular phenomenon, electron states in this system has been calculated for $T = 10\,\mathrm{K}$ and not at $300\,\mathrm{K}$ as the first problem. In this second case, the electronic states, self-consistent potential and electron density have been calculated for different widths of the δ-layer, with different concentrations. Self-consistent procedures have been performed by numerically solving the effective mass conduction band equation using the finite element method (FEM). In accordance, this chapter is organized as follows: in sections 6.2 we outline the theoretical equations and the method of resolution for the one-dimensional system quantum well and the quantum wire system with exposed boundaries. The discussion and comments on the obtained results for each system are presented in section 6.3, while the conclusions are given in section 6.4.

6.2. Theoretical framework

6.2.1. Razavy quantum-well (quantum well with Razavy-like potential)

The problem under consideration here consists of a GaAs conduction electron that moves under the influence of an on-center doped Razavy-like QW potential and undergoes the effect of external electric and magnetic fields. The electric field is assumed to be oriented along the z-growth direction and the magnetic field is applied perpendicular to the electric field, and lies within the plane of the layers. In Fig. **6-1** we plot a Razavy-like confining profile, together with a schematic representation of the n-type doped layer. The δ-parameter (2-nm in this work) corresponds to the finite width of the on-center doped layer, which has a two-dimensional N_d concentration of ionized donor atoms. Within the effective mass and parabolic band approximations, the Hamiltonian for a confined electron is given by [1]:

$$H = \frac{1}{2\,m^*}\left[\vec{p} + \frac{e}{c}\,\vec{A}(\vec{r})\right]^2 + V_c(z) + V_H(z) + e\,F\,z\,, \tag{6-1}$$

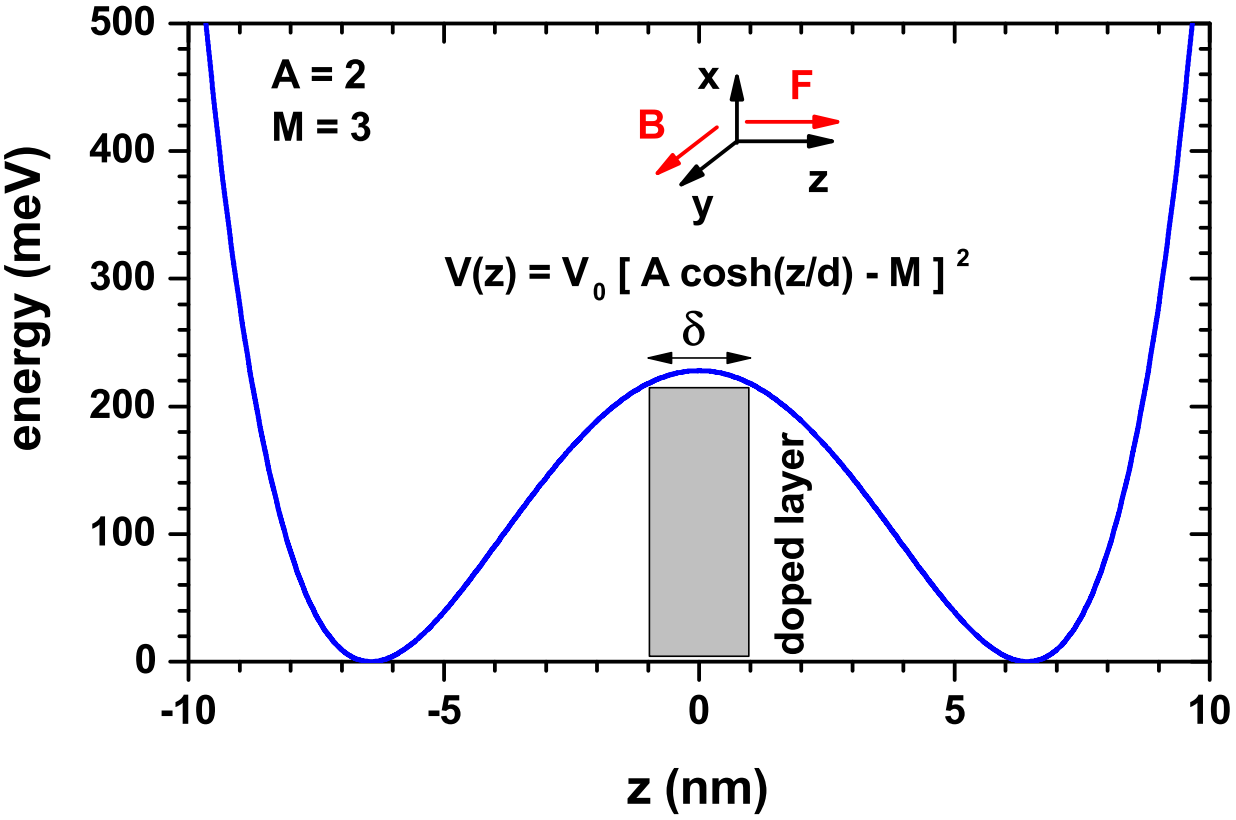

Figure 6-1.: (color online) Schematic representation of doped Razavy quantum well under applied electric and magnetic fields.

where c, e, and m^* denote the speed of light in the vacuum, the absolute value of the elementary charge, and the electron effective mass, respectively. Additionally, $\vec{p}$ represents the momentum operator, and F is the intensity of the applied electric ($\vec{F}$). Within the Landau gauge, the vector potential associated to the applied magnetic field ($\vec{B}$) is given by $\vec{A}(\vec{r}) = B\,z\,\hat{x}$ (B stands for the magnetic field intensity). Furthermore, $V_H(z)$ is the Hartree potential, which represents the additional conduction band reshaping due to the presence of the low-dimensional electron gas that arises from the donor ionization in the δ-layer. Besides, $V_c(z)$ is the Razavy-like confining potential given by [52]:

$$V_c(z) = V_0 \left[A \cosh\left(\frac{z}{D}\right) - M \right]^2 , \tag{6-2}$$

where a set of parameters with $V_0 = 228\,\text{meV}$, $A = 2$, $M = 3$, $D = \frac{L_{eff}}{3}$, and $L_{eff} = 20\,\text{nm}$ (the total width of the QW) has been chosen for the calculation.

The wave function associated to the Hamiltonian in Eq. (6-1) can be written as [63]:

$$\psi\left(\vec{r}\right) = \exp\left(i\,\vec{k_\perp}\cdot\vec{\rho}\right)\Phi'(z)\,, \tag{6-3}$$

where $\vec{k_\perp} = (k_x, k_y)$, $\vec{\rho} = (x, y)$, and $\Phi'(z)$ satisfies the following differential equation [63]:

$$H^0\,\Phi'\left(z\right) = \left(E_z - \frac{\hbar^2\,k_y^2}{2\,m^*}\right)\Phi'\left(z\right)\,. \tag{6-4}$$

where

$$\begin{aligned} H^0 = -\frac{\hbar^2}{2\,m^*}\frac{d^2}{dz^2} \quad & + \frac{e^2\,B^2}{2\,m^*}\left(z + \frac{\hbar\,k_x}{e\,B}\right)^2 \\ & + e\,F\left(z + L_{eff}/2\right) + V_H\left(z\right)\,. \end{aligned} \tag{6-5}$$

The z-component of the Eq. (6-4) can be written in the form [63]:

$$H\,\Phi\left(z\right) = E_z\,\Phi\left(z\right)\,. \tag{6-6}$$

where

$$H = -\frac{\hbar^2}{2\,m^*}\frac{d^2}{dz^2} \quad + \frac{e^2\,B^2}{2\,m^*}z^2 \\ + e\,F\,(z + L_{eff}/2) + V_H\,(z)\ . \tag{6-7}$$

Note that the solutions of Eq. (6-6) correspond to the bottom of the confined conduction subbands, i.e., $(k_x, k_y) = (0, 0)$.
The calculation of the Fermi level (E_F) is based on the charge neutrality condition, such that the total number of electrons must be equal to the total number of ionized donors per unit area (assuming that all the silicon atoms are ionized)

$$n_d = \sum_i \frac{m^*\,k_B\,T}{\pi\,\hbar^2}\,\log\left[1 + \exp\left(\frac{E_F - E_i}{k_B\,T}\right)\right]\ , \tag{6-8}$$

where k_B is the Boltzmann constant and T ($= 300\,\mathrm{K}$ in this work) denotes the absolute temperature.
The Hartree potential $V_H\,(z)$ which describes the electrostatic interaction of electrons and ionized ions results from the solution of the generalized Poisson equation [64]:

$$\frac{d^2V_H\,(z)}{dz^2} = \frac{e^2}{\varepsilon\,\varepsilon_0}\,\left[n_d\,(z) - n\,(z)\right]\ , \tag{6-9}$$

where ε (ε_0) is the GaAs (vacuum) static dielectric constant and n_d is the 3D donor density in the delta layer. Also, in Eq. (6-9)

$$n(z) = \sum_i \frac{m^*\,k_B\,T}{\pi\,\hbar^2}\,\log\left[1 + \exp\left(\frac{E_F - E_i}{k_B\,T}\right)\right]\,\Phi_i^2\,(z)\ , \tag{6-10}$$

The Eqs. (6-6-6-10) are discretized using the finite difference method (FDM) and solved iteratively. Under such a procedure, the Schrödinger and Poisson equations are then changed to matrices of type $A\,x = \lambda\,x$ and $B\,x = \rho$, respectively. Here, λ represents the energy and x is a column wave vector describing the electron wave function. After computing the energy levels and their corresponding wave functions, the linear, third-order nonlinear, and total optical

absorption coefficients for the intersubband transitions between initial and final states $E_i \rightarrow E_f$ can be evaluated from [65–67]:

$$\alpha^1(\omega) = \omega \sqrt{\frac{\mu}{\varepsilon_R}} \times \frac{e^2 \left|M_{if}\right|^2 \widetilde{\sigma}_{if}\, \hbar/\tau_{in}}{\left(\Delta E - \hbar\omega\right)^2 + \left(\hbar/\tau_{in}\right)^2}\,, \tag{6-11}$$

$$\begin{aligned}\alpha^3(\omega, I) = &-2\,\omega \sqrt{\frac{\mu}{\varepsilon_R}} \left(\frac{I}{\varepsilon_0\, n_r\, c}\right) \\ &\times \frac{e^4 \left|M_{if}\right|^4 \widetilde{\sigma}_{if}\ \left(\hbar/\tau_{in}\right)}{\left[\left(\Delta E - \hbar\omega\right)^2 + \left(\hbar/\tau_{in}\right)^2\right]^2} \\ \times &\left(1 - \Omega\, \frac{\left(\Delta E - \hbar\omega\right)^2 - \left(\hbar/\tau_{in}\right)^2 + 2\,\Delta E\left(\Delta E - \hbar\omega\right)}{\left(\Delta E\right)^2 + \left(\hbar/\tau_{in}\right)^2}\right)\end{aligned} \tag{6-12}$$

and

$$\alpha(\omega, I) = \alpha^1(\omega) + \alpha^3(\omega, I)\ . \tag{6-13}$$

In the previous equations $\Omega = \frac{|M_{ff} - M_{ii}|^2}{|2\,M_{if}|^2}$, $\Delta E = E_f - E_i$,

$$M_{if} = \int_{-\infty}^{+\infty} \Phi_f^*(z)\, \Phi_i(z)\, z\, dz \tag{6-14}$$

is the reduced dipole matrix element, and $\widetilde{\sigma}_{if} = \frac{m^*\, k_B\, T}{L_{eff}\, \pi\, \hbar^2}\, \sigma_{if}$, with

$$\sigma_{if} = \ln\left\{\frac{1 + \exp\left[\left(E_F - E_i\right)/k_B T\right]}{1 + \exp\left[\left(E_F - E_f\right)/k_B T\right]}\right\}\ . \tag{6-15}$$

Here, μ represents the free space permeability, $\tau_{in} = 0.14\,\mathrm{ps}$ stands for the intersubband relaxation time, and I is the intensity of incident light. The other physical parameters used in this work are [68, 69]: $m^* = 0.067\, m_0$ (where m_0 is free electron mass), $e = 1.602 \times 10^{-19}\,\mathrm{C}$, $\hbar = 1.056 \times 10^{-34}\,\mathrm{J\,s}$; $n_r = \sqrt{\varepsilon} = 3.2$, $\mu = 4\pi \times 10^{-7}\,\mathrm{H\,m^{-1}}$, $\varepsilon = 12.35$, $\varepsilon_0 = 8.854 \times 10^{-12}\mathrm{C^2\,N^{-1}\,m^{-2}}$, $\varepsilon_R = \varepsilon\,\varepsilon_0$, and $I = 0.5\,\mathrm{MW/cm^2}$.

6.2.2. Razavy quantum-wire

The theory required to study the two-dimensional problem of a QWR with delta-type doping is very similar to that developed for the one-dimensional well system since both problems are solved by means of the self-consistent method. For this reason, and to clarify the procedure without being redundant, some equations have been rewritten in this section, with the aim of presenting generalization to a 2D system.

The structure under consideration corresponds to an infinite QWR of GaAs with circular cross section and exposed borders. That is, the system is not immersed in any substrate but is in contact with vacuum. Additionally, a Razavy potential and a delta-doped layer have been added to shape the confining potential. A consequence of the above is the appearance of both inner and surface states in the system, giving rise to the phenomenon known as "Fermi Level Pinning" [70] in which a charge transfer from bulk states to surface states occurs, thus causing the Fermi level to remain fixed at a value within the band gap, regardless of the donor density in the system. For GaAs, a potential value of 0.7 eV, which corresponds to half the gap is normally used for the surface.

Figure **6-2** shows the schematic representation of the quantum wire, as well as the coordinate system used for numerical calculations. This is a QWR of radius R_0, surrounded by vacuum. Inserted at the center of this cylinder, an inner layer of -fully- ionized donors of radius r_d is included.

Again, the chosen numerical approach to solve this type of problem is the self-consistent method. It consists of a bidirectional coupling between the Poisson and Schrödinger equations. The electric potential that comes from the Poisson equation (including the effect of donor density) must be added to the confining potential term to later be included in the Schrödinger equation. Similarly, a statistically weighted sum of the probability density associated with the electronic occupation of the states of the Schrödinger problem contributes to the space charge density that enters the Poisson equation. This process implies an iteration scheme where the confining potential becomes modified by the redistribution of charges.

As a starting point of the self-consistent method, and following the Luscombe and Luban procedure [71], we shal consider that electrons in the cross section of

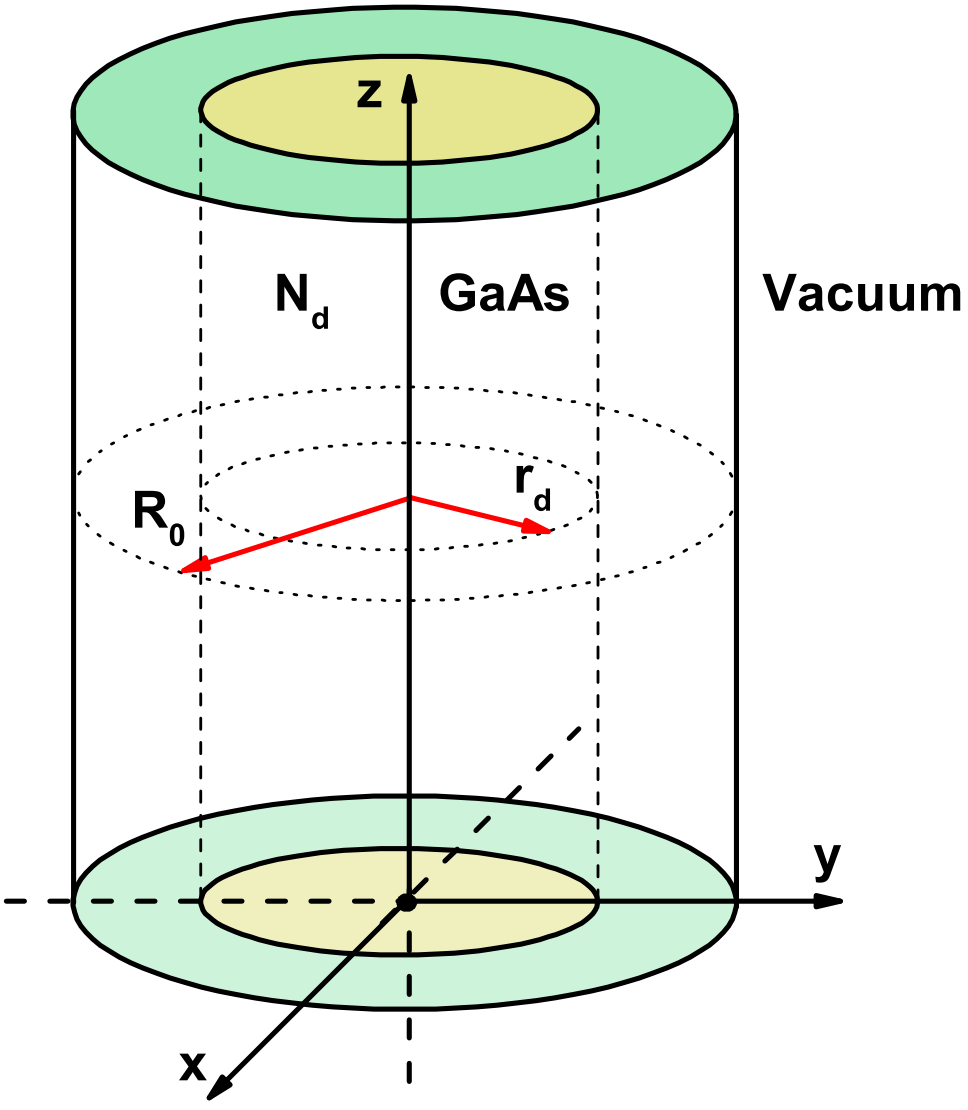

Figure 6-2.: Diagram of the infinite quantum wire of GaAs surrounded by vacuum, with a circular cross section of radius R_0. The coordinate system is centered on the symmetry axis of the wire. An inner doping layer of radius r_d has been included in the system.

the QWR behave as a two-dimensional charge-carrier gas. This indicates that a good approximation for the electron density would be the Thomas-Fermi one (Eq. 6-16). Such electron density must contribute to the charge density in the system and therefore to the Hartree potential that is obtained through the Poisson equation,

$$n(x,y,T) = N_C\, F_{1/2}\left(\beta\left(E_F - \Upsilon(x,y,T)\right)\right) \tag{6-16}$$

where $\beta = 1/k_B T$ is the Boltzmann factor, $N_C = (2m^*/\pi\beta\hbar^2)^{3/2}/4$ is the effective density of states, $\Upsilon(x,y,T)$ is the electronic potential generated by the Fermi level pinning on the exposed lateral surface, the level of doping and the lateral dimensions of the system and is given by $\Upsilon(x,y,T) = -e\,\phi(x,y,T)$, where $\phi(x,y,T)$ is the Hartree potential. Besides, e is the charge of the electron, m^* is the effective mass, and $F_{1/2}(x)$ is the well known Fermi-Dirac integral. With the electron density given by Eq. (6-16) and the density of donors N_d given by N_d for $r \leq r_d$ and 0 for $r > r_d$, it is possible to write the expression for the charge density in the system as,

$$\rho(x,y,T) = e\left(N_d - n(x,y,T)\right) \tag{6-17}$$

where ϵ_r and ϵ_0 are the relative permittivity and vacuum permittivity respectively. Note that, unlike the QW, now the charge density has a two-dimensional dependence, in the same way the donor density for this case is identified as N_d (for the well system it is labeled as n_d). This charge density must enter the two-dimensional Poisson equation (Eq. 6-18) to obtain the Hartree potential,

$$-\epsilon_0\epsilon_r\,\nabla^2\phi(x,y,T) = \rho(x,y,T) \tag{6-18}$$

This equation should be solved taking into account the boundary conditions imposed by the Fermi level pinning, which for GaAs takes the form $\phi(\Omega) = -(E_F + 0.7\text{eV})/e$, where Ω represents the QWR boundary. The potential, $\phi(x,y,T)$, obtained through Eq. (6-18) must contribute to the potential energy

term in the Schrödinger equation,

$$U(x,y,T) = -e\,\phi(x,y,T) + V_c(x,y) \tag{6-19}$$

where $-e\,\phi(x,y,T)$ is the contribution that comes from the Poisson equation and the redistribution of charges due to doping, and $V_c(x,y)$ is the Razavy 2D potential, which has the same form as Eq. (6-2), changing z for $\sqrt{x^2+y^2}$. In this case, $V_0 = 0.228\,\text{eV}$, $A = 2$, $M = 3$, $D = 1.57\,L$, and $L = 20\,\text{nm}$. On the other hand, the electrons are assumed to be totally confined within the volume of the QWR and, therefore, it must be satisfied that $\Psi(\Omega) = 0$ in the Schrödinger equation,

$$-\frac{\hbar^2}{2m^*}\nabla^2\Psi_{ik}(\vec{r}) + U(x,y,T)\,\Psi_{ik}(\vec{r}) = E_{ik}\,\Psi_{ik}(\vec{r}) \tag{6-20}$$

Note that in Eq. (6-20) we have used the approximation of effective mass for electrons in GaAs. In this equation $\Psi(\vec{r})$, the wave function of the system, takes the form,

$$\Psi_{ik}(\vec{r}) = e^{ikz}\,\psi_i(x,y) \tag{6-21}$$

Considering now the Schrödinger equation in the xy plane, with eigenvalue E_i associated with the state $\psi_i(x,y)$, we have to solve the problem

$$-\frac{\hbar^2}{2m^*}\nabla^2\psi_i(x,y) + U(x,y,T)\,\psi_i(x,y) = E_i\,\psi_i(x,y), \tag{6-22}$$

with $\psi_i(\Omega) = 0$. From here, it is possible to find the first set of eigenfunctions and eigenvalues for the system. With this set we can calculate the electron density associated with the occupation of the internal states in the system,

$$\eta(x,y,T) = \xi \sum_{i=1} F_{-1/2}(\beta\,(E_F - E_i))\,|\psi_i(x,y)|^2 \tag{6-23}$$

where $\xi = \sqrt[3]{4N_C}$. This equation represents the density of electron gas at a point (x, y) and temperature T. From the electron density calculated in Eq. (6-24), a new profile for the charge density of the system is obtained:

$$\rho_{new}(x, y, T) = e(N_d - \eta(x, y, T)). \tag{6-24}$$

Replacing this charge density into Poisson's equation (6-18), a new Hartree potential $\phi_{new}(x, y, T)$ is obtained that will -again- contribute to the potential energy term in the Schrödinger equation. Then, a new set of eigenfunctions and eigenvalues for the system ψ_i^{new}, E_i^{new} is obtained. This set will be associated to a new electron density profile η_{new} relative to the occupation of each of each state of the system. In this way, the process is repeated iteratively until the absolute value of the difference between potential terms corresponding to two successive self-consistent steps is smaller than a certain tolerance $|U - U_{old}| < 10^{-6}$ eV. When this condition is met, the system is said to have reached self-consistency. Note that the confining potential and the Razavy potential do not change with the iterative process, only the electrostatic potential changes due to the redistribution of the charge carriers.

Once self-consistency has been reached, the final set of eigenvalues and eigenfunctions as well as the self-consistent potential found are the correct solutions for the quantum wire with exposed boundaries, Razavy potential, and donor density N_d. Figure **6-3** shows the plots of first five QWR confined state wave functions for three different values of r_d; from left to right, each column corresponds to: $r_d = 5\,\text{nm}$, $r_d = 10\,\text{nm}$, and $r_d = 15\,\text{nm}$. Despite varying the inner radius r_d, all the figures maintain the same cross-sectional area since the outer radius $R_0 = 50\,\text{nm}$ remains fixed. The electron density N_d has been fixed as $3 \times 10^{19}\,\text{cm}^{-3}$ for all three cases, and the temperature has also been kept at $T = 10\,K$. The color scale in each figure goes from the blue, which corresponds to negative values of the wave function, to dark red which represents positive values. Yellow indicates the points at which the wave function is zero. With these parameters a degeneracy between ψ_1 and ψ_2 appears for all r_d. Note how for $r_d = 5\,\text{nm}$ -first column plots- the state ψ_3 has the shape of an s-orbital, followed by the state ψ_4 which has a d-type orbital (in analogy with atomic orbitals). For values of $r_d = 10\,\text{nm}$ and $r_d = 15\,\text{nm}$, this s state no longer appears

in ψ_3, it takes the form of a d state. This means that as long as the value of r_d augments, an exchange between states of type s and type d is present for the third excited state.
On the other hand, the first row at the top of Fig. **6-3**, corresponds to the ground state ψ_0 for each system, again in analogy with the atomic orbitals, a clear symmetry equivalent to an s-type state is evidenced. For all system configurations, it is readily apparent that there is a high probability of finding the electrons close to the center of gravity of the structure. Moreover, as r_d increases, the probability at the center of the structure diminishes, at the time that increases along the radial direction. Then, the electrons tend to be distributed along the cross section with the increase of the doping region width. The first and second excited states, ψ_1 and ψ_2, are presented on the second and third rows from top to bottom. Note that these states present a symmetry similar to the p-type orbitals.

6.3. Results and discussion

6.3.1. Results Quantum Well

In Fig. **6-4**, we present our results for the confining potential, energy levels, Fermi level, and probability densities for the lowest four bound electron states in GaAs Razavy-like QWs, considering four different cases of the external electric and magnetic fields, as well as doping concentration. Despite the inclusion of the third excited state, it does not contribute to the electron density since it is above the Fermi level of the system. From Fig. **6-4**(a), where these three parameters are set to zero, it is observed that the central barrier is high enough such that the ground state is almost-degenerate; corresponding to the ground state -with even symmetry- and the first excited state -with energy very close to the ground state one- showing odd symmetry with respect to the $z = 0$ point. The energy difference between the ground state and the second excited state is approximately 150 meV. Notice that the second excited state is located above the central barrier. In Fig. **6-4**(b), where an on-center doping concentration of $n_d = 4.5 \times 10^{19}\,\mathrm{cm}^{-3}$ is considered in the absence of external fields (doping

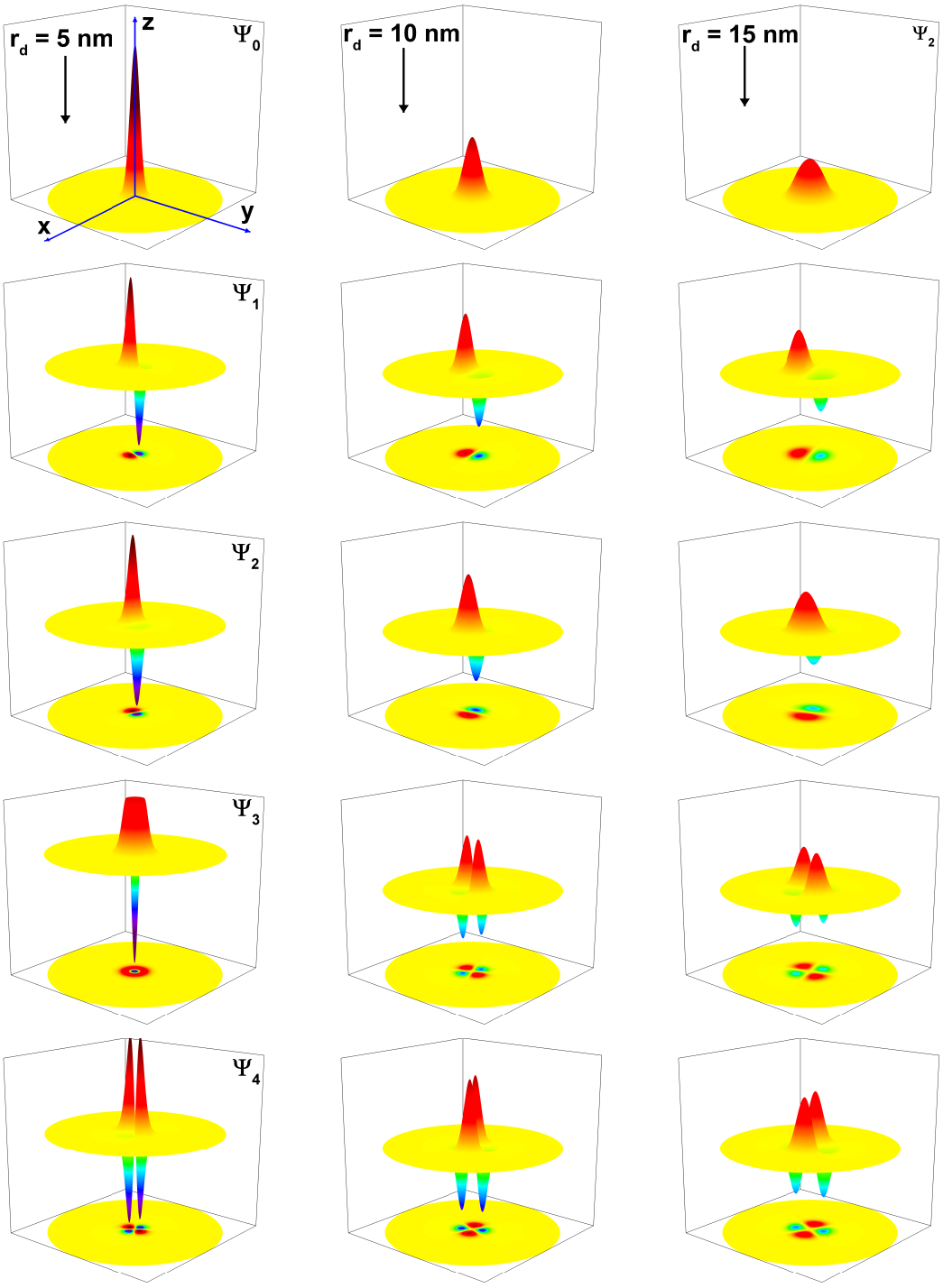

Figure 6-3.: First five wave functions for a confined electron in GaAs quantum wires. The rows from top to bottom are the ground state and first four excited states, columns from left to right correspond to $r_d = 5\,\text{nm}$, $r_d = 10\,\text{nm}$, and $r_d = 15\,\text{nm}$, respectively. For all figures the radius of the quantum wire has been set at $R_0 = 50\,\text{nm}$, $T = 10\,K$, and $N_d = 3 \times 10^{19}\,\text{cm}^{-3}$.

of this order is discussed in Ref. [72]), one may observe the appearance of an additional central potential well. The energy minima of the two side QWs, which in Fig. **6-4**(a) have zero value, now show a slight shift towards lower energies. Besides, the minimum of the central well positions itself at an energy slightly higher than the energy of the two lateral minima.

Under these conditions, the GaAs Razavy-like double quantum well in the presence of central doping is transformed into a triple quantum well with outer barriers that rapidly diverge, generating an infinite confining potential. The presence of the central well in Fig. **6-4**(b) has the function of coupling the two quantum wells initially observed in Fig. **6-4**(a). In this sense, the breakdown of the ground state degeneration is clearly noticed. It is also observed that the first excited state shows a blue shift of 36 meV concerning the ground state. The latter, whose energy is 3 meV less than the maximum of the finite potential barriers, is an even function with its maximum probability density in the central region; the presence of shoulders associated with the irregularity of the potential well bottom is also well apparent. Besides, the first excited state is an odd function whose maximum probability density is located in the region of the two lateral quantum wells. The second excited state is remarkably insensitive to the shape of the potential well. This is concluded by observing that the two lateral maximums in the probability density present magnitudes slightly lower than that shown by the central maximum. On the other hand, in Fig. **6-4**(c), where a delta-like doping volume density of $n_d = 4.5 \times 10^{19}\,\mathrm{cm}^{-3}$ is combined with an applied electric field of 30 kV/cm (developments in high electric fields can be seen in Ref. [73, 74]), it is possibel to see that, by breaking the symmetry of the system, the ground state is pushed towards the left-hand side well structure while, due to orthogonality conditions, the first excited state displaces its maximum towards the right-side of the system. The ground state has a quasi-constant probability density in the region $-5\,\mathrm{nm} < z < 0$. The comparison between the second excited state in Figs. **6-4**(b) and **6-4**(c) shows a slight blue shift due to the field-effect without significant changes in the probability density shape. This effect is associated with the fact that the electric potential is zero at $z = -10\,\mathrm{nm}$. Now, turning to analyzing Fig. **6-4**(d), where a delta-like doping of $n_d = 4.5 \times 10^{19}\,\mathrm{cm}^{-3}$ combines with an applied magnetic field of 30 T (some experimental and theoretical works in high magnetic fields [75–77]),

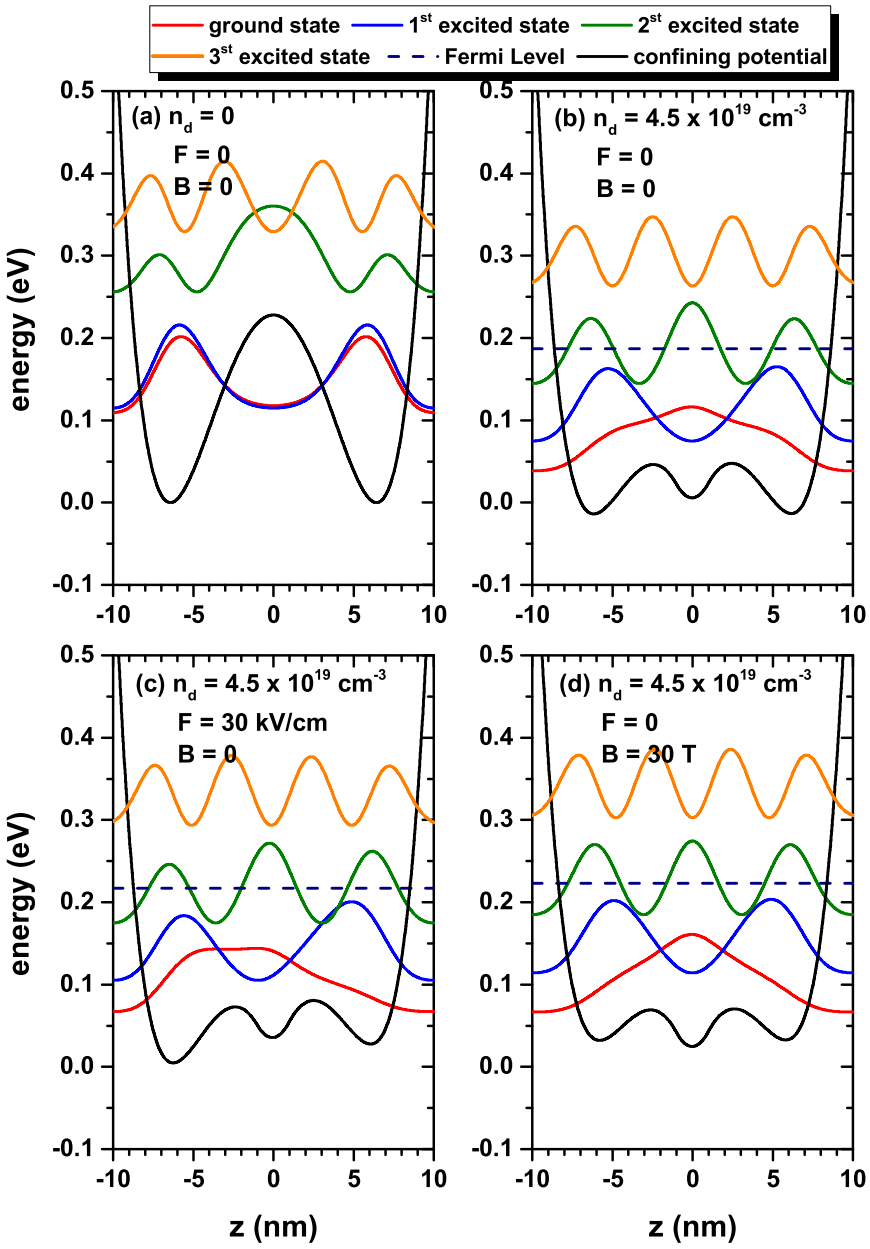

Figure 6-4.: (color online) Confining potentials, energy levels, Fermi level, and probability density for the lowest four bounded electron states in a GaAs Razavy-like quantum wells. Four different cases of the external fields and doping concentration (F, B, n_d) are considered: $(0, 0, 0)$ (a), $(0, 0, 4.5 \times 10^{19}\,\mathrm{cm}^{-3})$ (b), $(30\,\mathrm{kV/cm}, 0, 4.5 \times 10^{19}\,\mathrm{cm}^{-3})$ (c), and $(0, 30\,\mathrm{T}, 4.5 \times 10^{19}\,\mathrm{cm}^{-3})$ (d). In (b-d) the Fermi level is depicted with the horizontal line close to 200 meV.

a parabolic confinement appears associated with the second term in the squared parenthesis of Eq. (6-5). By comparing the confinement potentials in Figs. **6-4**(b) and **6-4**(d), it is observed that, as a first effect, the parabolic potential is responsible for equalizing in energy the bottom of the three quantum wells. In this way, the central maximum of the ground state probability density is reinforced. Additionally, the three confined states show a blue shift related with the reinforcement of carrier space confinement; noting an increase in the separation in energy between the ground state and the first excited state. The probability density of the second excited state now appears with three maxima, all of them with equal amplitude, reflecting a systematic disappearance of the influence of potential well bottom shape. In Figs. **6-4**(b-d), where central doping is present, it is clearly seen that in the three cases there are only three confined levels with energies lower than the Fermi level.

In Fig. **6-5**, we present the results for the variation of the lowest three energy separations ($E_2 - E_1$, $E_3 - E_1$, and $E_3 - E_2$) in a central doped GaAs Razavy-like QW as a function of the applied electric field, without magnetic field effects, Fig. **6-5**(a), and as a function of the applied magnetic field, without electric field effects, Fig. **6-5**(b). The simulations include a fixed delta-like doping concentration, $n_d = 4.5 \times 10^{19}\,\mathrm{cm}^{-3}$. The results in Figs. **6-5**(a) and **6-5**(b) are in complete agreement with those presented in Figs. **6-4**(c) and **6-4**(d), respectively. The electric field -variable in Fig. **6-5**(a)- has the function of tilting the potential well profile, generating a greater localization of the carriers towards the $z < 0$ region. This effect translates into greater confinement of the carriers, thereby increasing the separation between the confined levels and consequently the transition energies. The quasi-parallel behavior of the $E_2 - E_1$ and $E_3 - E_1$ curves justifies the quasi-constant behavior with the electric field of the $E_3 - E_2$ curve which, in the whole range of electric fields considered, only presents a variation of 8 meV; less than 10 %. It is important to note that the wave functions associated to the three states in Fig. **6-5**(a) lose their odd or even symmetry with respect to the $z = 0$ point, which means that all inter-subband transitions are allowed. As commented, the magnetic field -the variable in Fig. **6-5**(b)- is responsible for a parabolic potential whose effect is to increase the localization of all confined states within the region close to $z = 0$. This greater localization of the states translates into an increase in the transition energies with the ap-

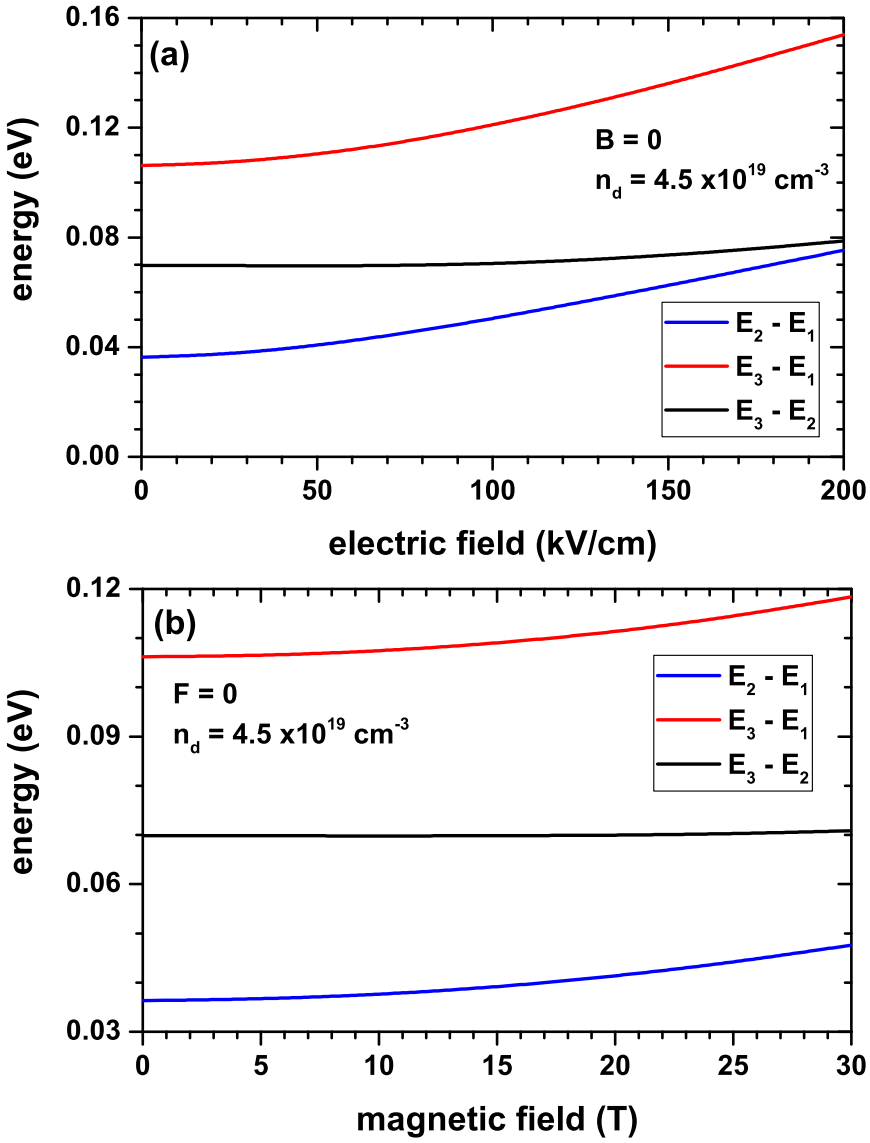

Figure 6-5.: (color online) Variation of the lowest three energy separations in a central doped GaAs Razavy-like quantum well as a function of the applied electric (a) and magnetic (b) field. Calculations are for $n_d = 4.5 \times 10^{19}\,\mathrm{cm}^{-3}$.

plied magnetic field. Due to its greater extension in space, the second excited state (Φ_3) is the one most susceptible to being spatially modified by the effect of the applied magnetic field. The ground state (Φ_1), which has its maximum probability density close to the $z = 0$ region, is essentially insensitive to the effects of the magnetic field. Combining these two aspects, one may understand why, as in Fig. **6-5**(a), the $E_2 - E_1$ and $E_3 - E_1$ transition energies are the most sensitive to the magnetic field, with a growing behavior and parallel to each other. This justifies that in the range of magnetic fields, the $E_3 - E_2$ transition energy is constant. The wave functions associated with the three states considered in the transitions of Fig. **6-5**(b) preserve their even or odd symmetries. The Φ_1 and Φ_3 states are even functions concerning $z = 0$ while the Φ_1 state is an odd function. Consequently, only the $1 \rightarrow 2$ and $2 \rightarrow 3$ transitions are allowed whereas the $1 \rightarrow 3$ transition is forbidden.

In Figs. **6-6** and **6-7** we present the variation of the reduced dipole matrix elements-$|M_{if}|^2$ (a), the occupancy ratio-σ_{if} (b), and the function $F_{if} = \sigma_{if}\,|M_{if}|^2\,(E_f - E_i)$ (c) in a central doped GaAs Razavy-like QW, plotted as functions of the applied electric field, for zero magnetic field; and as functions of the applied magnetic field, for zero electric field, respectively. The results correspond to a delta-like doping with $n_d = 4.5 \times 10^{19}\,\mathrm{cm}^{-3}$. As already said before, since the presence of an electric field removes the even or odd symmetry of the confined states then all the transitions between lowest three confined states are allowed, as shown in Fig. **6-6**(a). therefore all corresponding intersubband $|M_{if}|^2$ elements are nonzero. However, as seen from Fig. **6-7**(a), since the ground and the second excited states are even functions, then $M_{13}^2 = 0$.

Taking into account that both the electric and magnetic fields have the effect of increasing the location of carriers, then the spatial extension where the wave functions spread out decreases. This explains the decreasing tendency of the reduced dipole matrix elements in Figs. **6-6**(a) and **6-7**(a) as functions of the electric and magnetic fields, respectively. An unexpected situation occurs with the term M_{23}^2 in Fig. **6-7**(a). Its growing character with the magnetic field is essentially associated with the increasing spatial overlap of Φ_2 and Φ_3 states. Note that the magnetic field is responsible for the increment (decrement) of the probability density of Φ_3 state in the region where Φ_2 has its two maxima

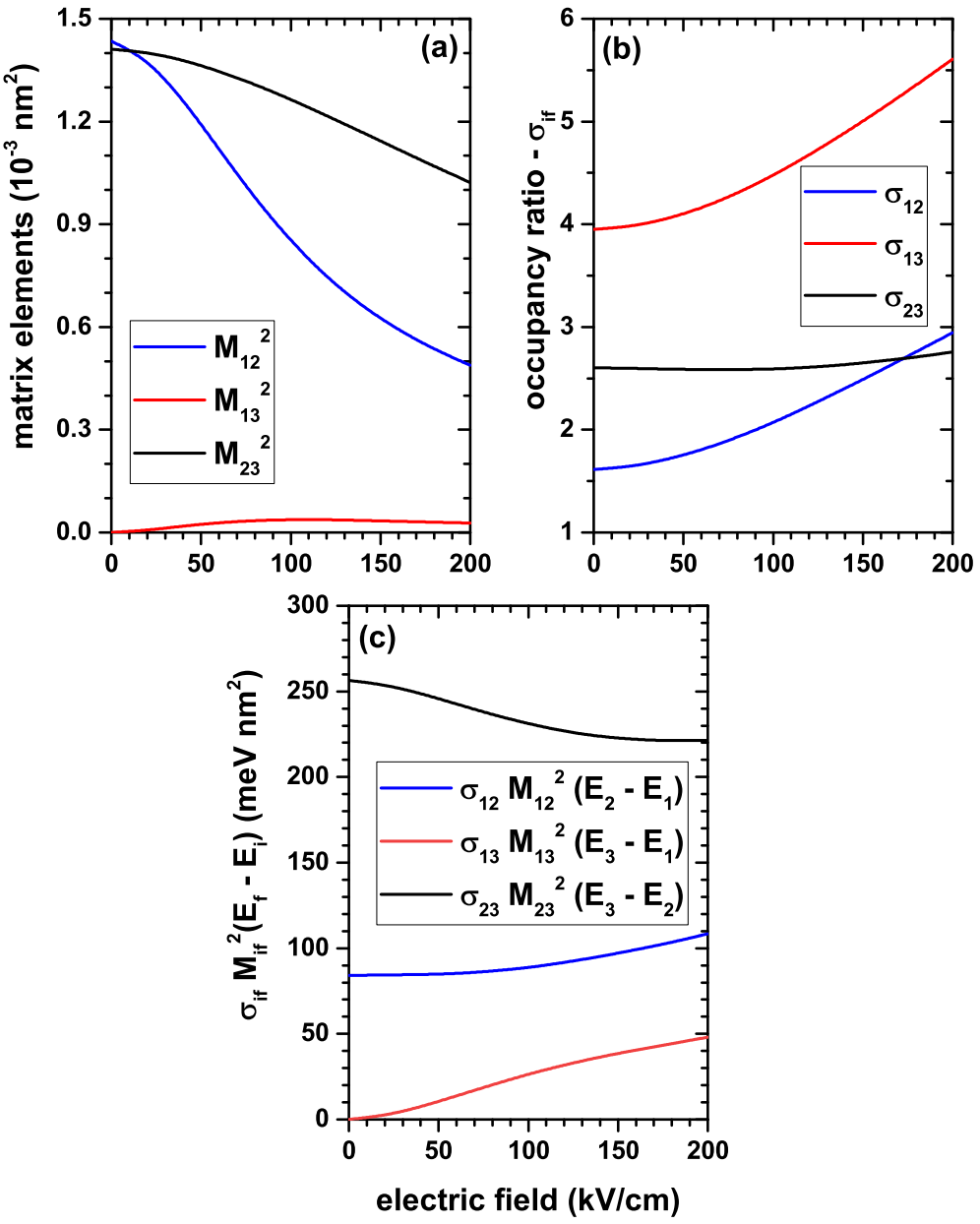

Figure 6-6.: (color online) Variation of the reduced dipole matrix elements-$|M_{if}|^2$ (a), the occupancy ratio-σ_{if} (b), and the function $F_{if} = \sigma_{if}\,|M_{if}|^2\,(E_f - E_i)$ (c) in a central doped GaAs Razavy-like quantum well as a function of the applied electric field, for zero magnetic field. The results are for $n_d = 4.5 \times 10^{19}\,\mathrm{cm}^{-3}$.

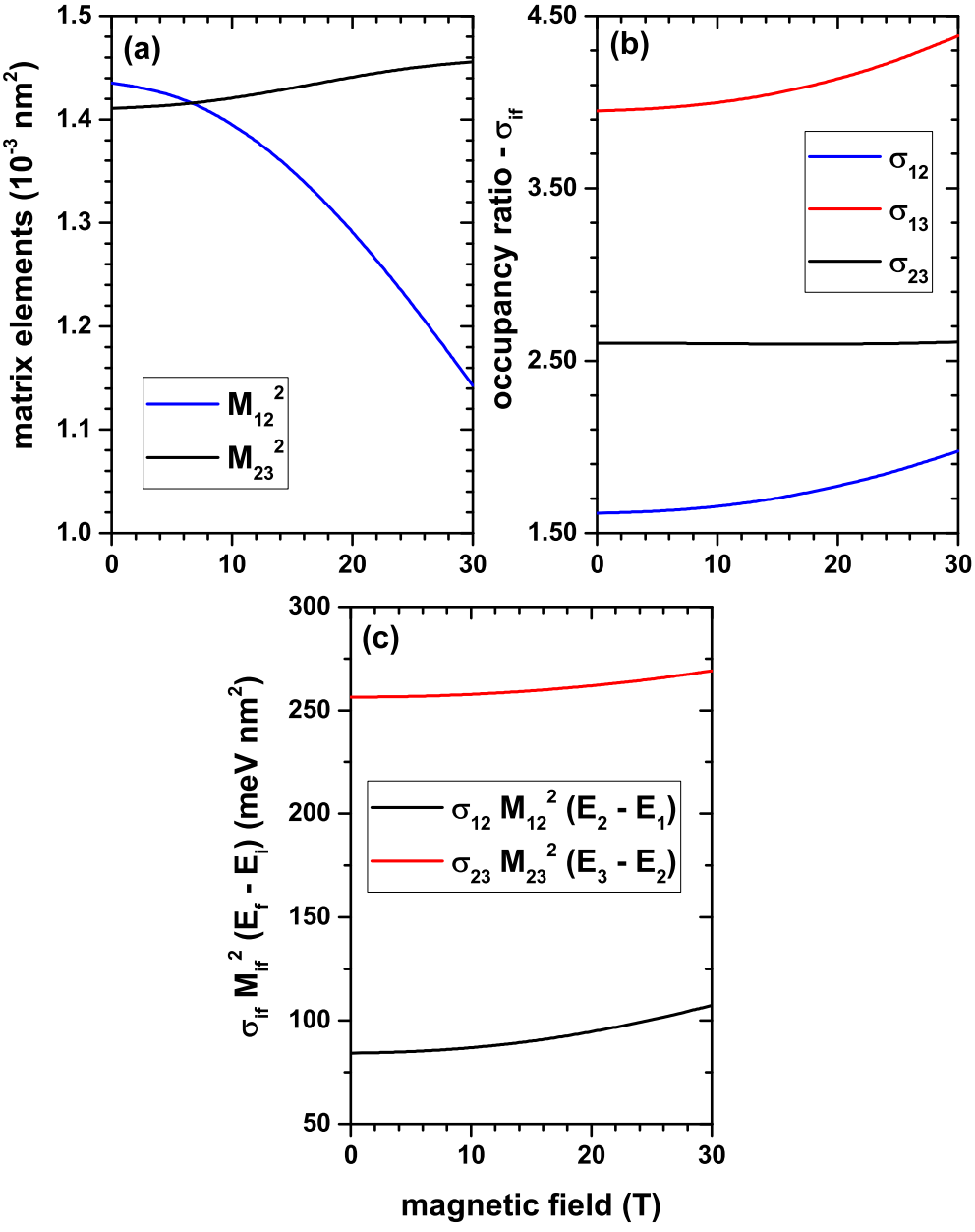

Figure 6-7.: (color online) Variation of the reduced dipole matrix elements-$|M_{if}|^2$ (a), the occupancy ratio-σ_{if} (b), and the function $F_{if} = \sigma_{if}\,|M_{if}|^2\,(E_f - E_i)$ (c) in a central doped GaAs Razavy-like quantum well as a function of the applied magnetic field for zero electric field. The results are for $n_d = 4.5 \times 10^{19}\,\mathrm{cm}^{-3}$.

values (has its minimum value). From Fig. **6-6**(a) it is also possible to observe that the term M_{13}^2 is approximately zero over the entire range of electric fields. Despite the symmetry breaking in the wave functions, the Fig. **6-4**(a) shows that the electric field shifts the only maximum present in the Φ_1 state towards the region where Φ_3 has a minimum. For this reason, the overlap between these two wave functions tends to zero, giving an approximately negligible value of the dipole matrix element. From the increasing behavior of σ_{12} and σ_{13} and approximately constant of σ_{23} in Figs. **6-6**(b) and **6-7**(b), it is concluded that in general the energy separation between the Φ_2 and Φ_3 states is approximately constant with the electric and magnetic fields and that the transition energy between Φ_1 and Φ_2 (or between Φ_1 and Φ_3) is an increasing function of the electric and magnetic fields. As the strength of the two external probe fields augments, an increase in confinement is observed, greater spacing between levels appears; and it is much more difficult to thermally excite the electrons from the ground to excited states. This explains why there is an increase in the occupancy rate with the electric and magnetic field. Figs. **6-6**(c) and **6-7**(c), where we present the function $F_{if} = \sigma_{if} \left|M_{if}\right|^2 (E_f - E_i)$, show quite intricate mixing behavior of the three factors involved, which can be summarized as follows. For the electric field effects in Fig. **6-6**(c), it is observed that: *i*) F_{12} and F_{13} are dominated by the behavior of their corresponding σ_{if} and $E_f - E_i$ parameters and *ii*) F_{23} is dominated by the behavior of M_{23}^2. In the case of Fig. **6-7**(c), the nonzero F_{12} and F_{23} functions increase with the magnetic field and essentially follow the transition energy behavior.

In Fig. **6-8** we present the variation of the total optical absorption coefficient in a central δ-like doped GaAs Razavy-like QW as a function of the z-polarized incident photon energy for three different values of the applied electric field, with $B = 0$ (a) and for three values of the applied magnetic, with $F = 0$ (b) and keeping constant the n_d concentration. According to Eq. (6-11), the magnitude of the first-order correction resonant peak of the optical absorption coefficient is proportional to $F_{if} = \left|M_{if}\right|^2 \sigma_{if} (E_f - E_i)$ which is precisely the quantity reported in Figs. **6-6**(c) and **6-6**(c). The incident radiation intensity chosen in this study is $I = 0.5\,\mathrm{MW/cm^2}$ and, under such assumption, a clear dominance of the linear contribution to the total light absorption is present. Note that the magnitude of the maxima of α_{ij} in all the curves of Fig. **6-8** follow

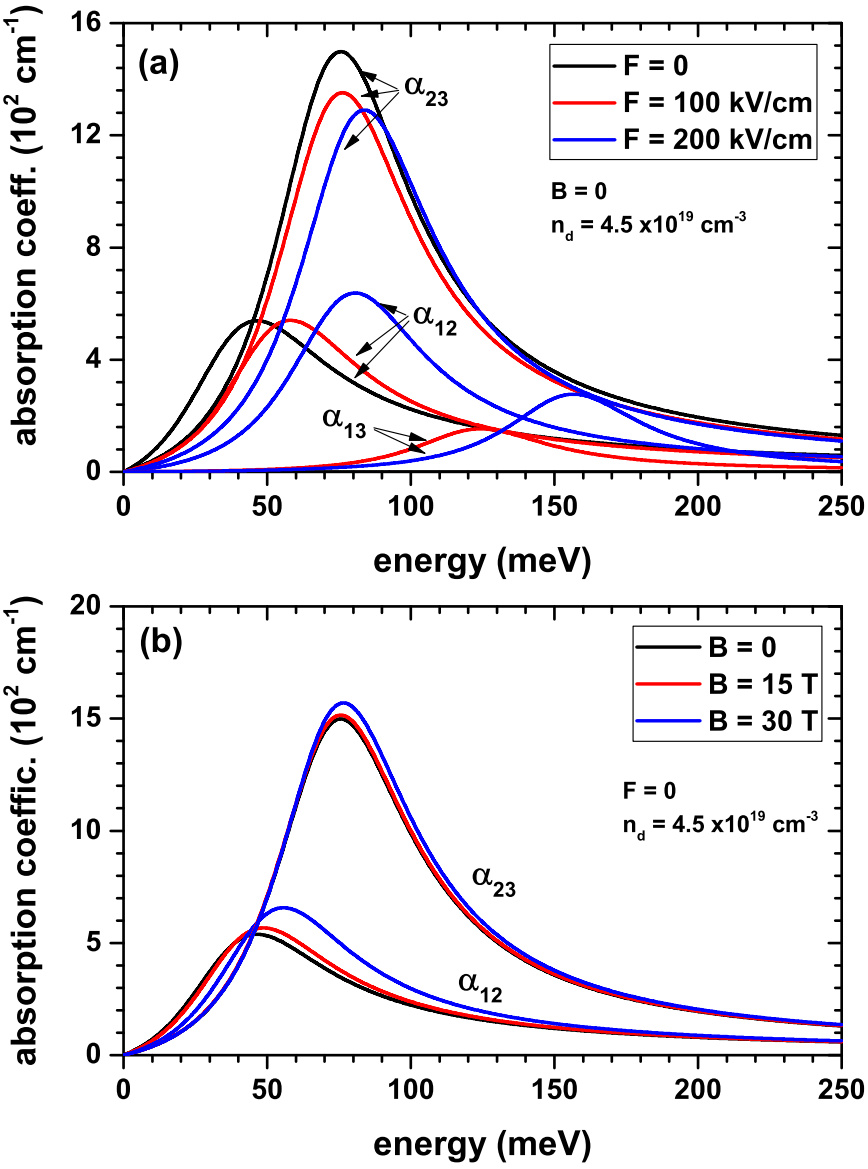

Figure 6-8.: (color online) Variation of the total optical absorption coefficient in a central doped GaAs Razavy-like quantum well as a function of the z-polarized incident photon energy for three different values of the applied electric field, for zero magnetic field (a) and for three values of the applied magnetic, for zero electric field (b). The results are for $n_d = 4.5 \times 10^{19}\,\mathrm{cm}^{-3}$.

the behavior of F_{ij} reported in Figs. **6-6** and **6-7**. For example, in Fig. **6-6**(c), we can see that F_{23} decreases with the electric field, a situation that is identical to the decrease of the resonant peak of α_{23} in the three corresponding curves in Fig. **6-8**(a) as it increases the electric field. The almost constant behavior of the magnitude of the resonant peak of α_{23} in Fig. **6-8**(b) is directly related to the slight variation shown by F_{23} in Fig. **6-7**(c). The absence of the α_{13} coefficient in Fig. **6-8**(b) for all the magnetic fields strengths considered and in Fig. **6-8**(a) for $F = 0$ is since the α_{13} transitions are forbidden between states that have the same even symmetry. As mentioned, in general, the electric and magnetic fields used as external probes in this study are responsible for the increase in carriers' confinement, which finally translates into a greater spacing between adjacent levels and consequently in an increase in the transition energies. This fact is in perfect coherence with the blue shift shown by the resonant peaks of the total absorption coefficient as the electric field increases, as shown in Fig. **6-8**(a), or as the magnetic field increases, as shown in Fig. **6-8**(b).

In Fig. **6-9** we present the variation of the reduced dipole matrix elements (a), the occupancy ratio (b), the transition energies (c), and the F_{if}-function (d) in a central δ-like doped GaAs Razavy-like QW as a function of the doping volume concentration for zero electric and magnetic field. As shown in Fig. **6-4**(b), central doping creates a potential well in the center of the structure, giving rise to a system of three coupled wells in the Razavy-like double quantum well system studied here. When $n_d = 4.5 \times 10^{19}\,\mathrm{cm}^{-3}$, see Fig. **6-4**(b), it is observed that the central well, where doping exists, has its minimum with energy slightly higher than the original two minimums of the Razavy-like double quantum well. As n_d grows from that value, the two potential barriers that separate the wells decrease in their heights until they finally collapse, and the system evolves from three potential wells to a single QW that drags the ground state successively towards lower energies. This effect is responsible for the increasing behavior of the $E_2 - E_1$ and $E_3 - E_1$ transition energies in Fig. **6-9**(c). The central potential well, with increasing n_d, confines within it the Φ_1 and Φ_2 states, with which an increasing behavior appears reinforced by the confinement of the $E_2 - E_1$ transition energy. This fact justifies that the slope with n_d of the $E_2 - E_1$ transition is higher than that exhibited by $E_3 - E_1$, which explains

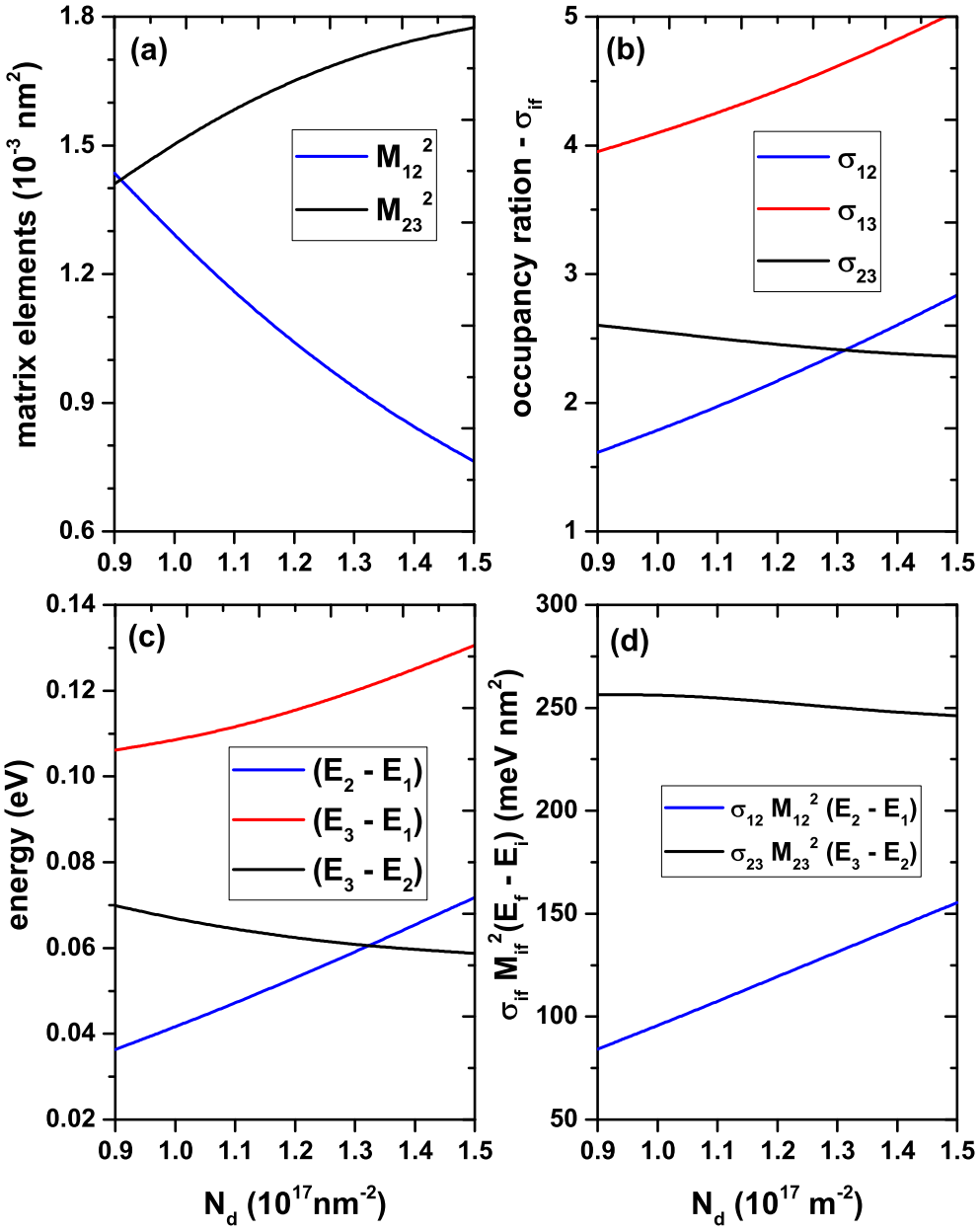

Figure 6-9.: (color online) Variation of the reduced dipole matrix elements-$|M_{if}|^2$ (a), the occupancy ratio-σ_{if} (b), the transition energies-$Ef - E_i$ (c), and the function $F_{if} = \sigma_{if}\,|M_{if}|^2\,(E_f - E_i)$ (d) in a central doped GaAs Razavy-like quantum well as a function of the n_d-doping concentration. The results are for $F = 0$ and $B = 0$.

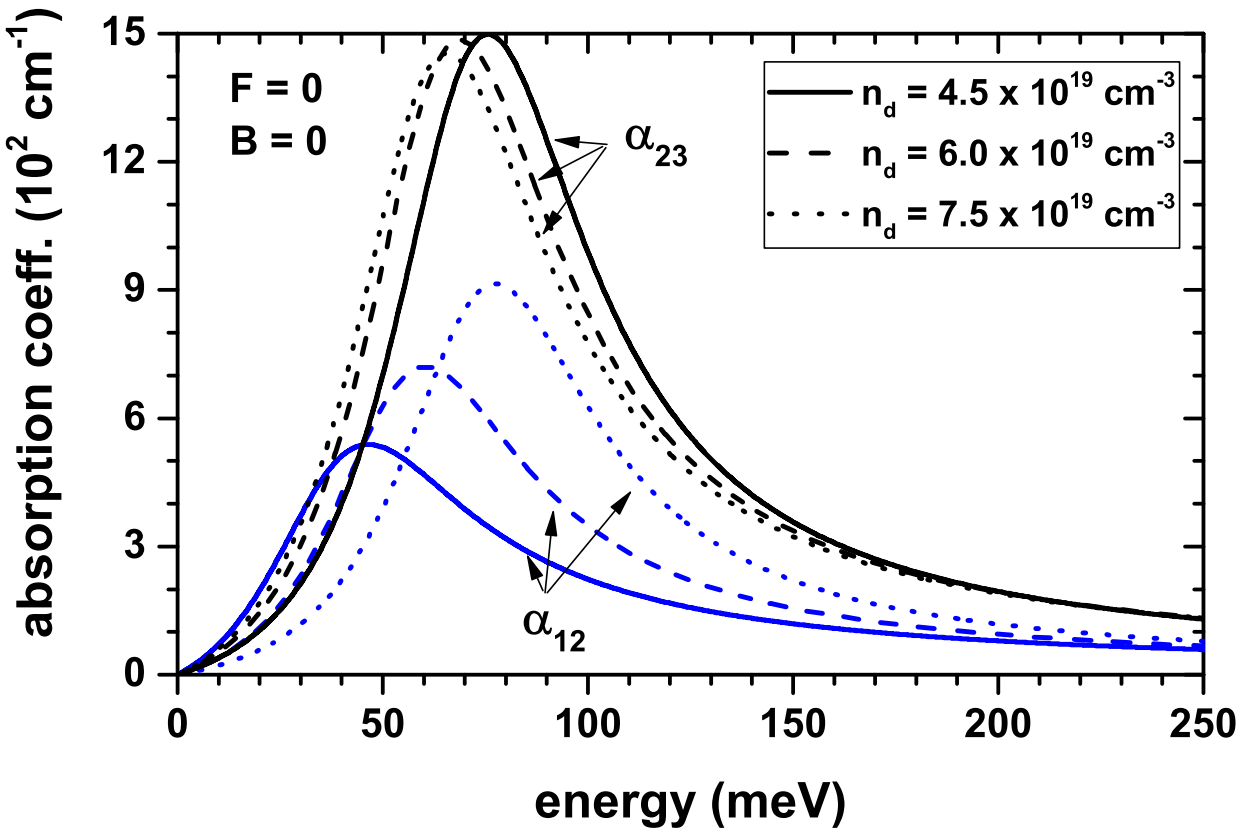

Figure 6-10.: (color online) Variation of the total optical absorption coefficient α_{12} and α_{23} in a central doped GaAs Razavy-like quantum well as a function of the incident photon energy for three different values of the n_d-doping concentration. The results are for $F = 0$ and $B = 0$.

the decreasing character of the $E_3 - E_2$ transition. As the Φ_1 and Φ_2 states are confined in the central well, a greater localization oaround $z = 0$ gives rise to the diminishing character of M_{12}^2 in Fig. **6-9**(a). Due to the increment in the localization of Φ_2 close to $z = 0$ and that the spatial extension of Φ_3 shows negligible changes with the increase of n_d, the augmenting character of M_{23}^2 is justified. The variations of σ_{if} in Fig. **6-9**(b) exactly follow the behavior of $E_f - E_i$ as previously justified. Fig. **6-9**(d) shows unequivocally that in the F_{if} function, the dominant factors are the transition energies and the occupancy ratio.

Figure **6-10** contains our results for the variation of the total optical absorption

coefficient α_{12} and α_{23} in the investigated GaAs Razavy-like QW with on-center delta-like doping, plotted as a function of the incident photon energy for three different values of the n_d-doping concentration in the absence of any external field. The absence of the α_{13} transitions is justified by the symmetric nature of the structure, in which case both the ground state and the second excited state are even functions between which the dipole matrix element is zero. The red/blue shift of α_{12}/α_{23} is explained by the results in Fig. **6-9**(c). Likewise, Fig. **6-9**(d) justifies the variations in the magnitudes of the resonant structures and again makes it possible to argue that the first order correction is the dominant one in the optical absorption coefficient.

6.3.2. Results Quantum Wire

In this subsection, we present the results of calculations for the two-dimensional QWR system with a Razavy potential as described in section 2. As in the previous case, the following parameters have been set: effective mass of electron in GaAs $m^* = 0.067\, m_0$, where m_0 is the mass of the free electron and dielectric constant $\epsilon_r = 12.9$. Coupled differential equations have been solved by means of the finite element method with the following setup: inner mesh with triangular shaped elements, number of elements 6550, edge elements 160, mesh vertices 3356, maximum number of iterations for Self-consistent method 40, absolute tolerance for Self-consistent method 10^{-6}.

Figure **6-11** shows the self-consistently determined confinement potential for three different radii, r_d, for the GaAs QWR: $r_d = 5\,\text{nm}$ (a), $r_d = 10\,\text{nm}$ (b), and $r_d = 15\,\text{nm}$ (c). Calculations are with $R_0 = 50\,\text{nm}$, $T = 10\,K$, and $N_d = 3 \times 10^{19}\,\text{cm}^{-3}$. The red color in each figure indicates larger values for the potential, while the blue color indicates the smaller values for it. For the three cases studied, the self-consistent potential presents a stable equilibrium point at $x = 0$ (center of symmetry of the system), which corresponds to a minimum potential and therefore, the electrons will be practically confined around the central region of the QW, feeling an infinite potential at the system boundary. For $r_d = 5\,\text{nm}$, the potential presents a very sharp peak near the center of the structure generated by the rearrangement of charges. Such a charge distri-

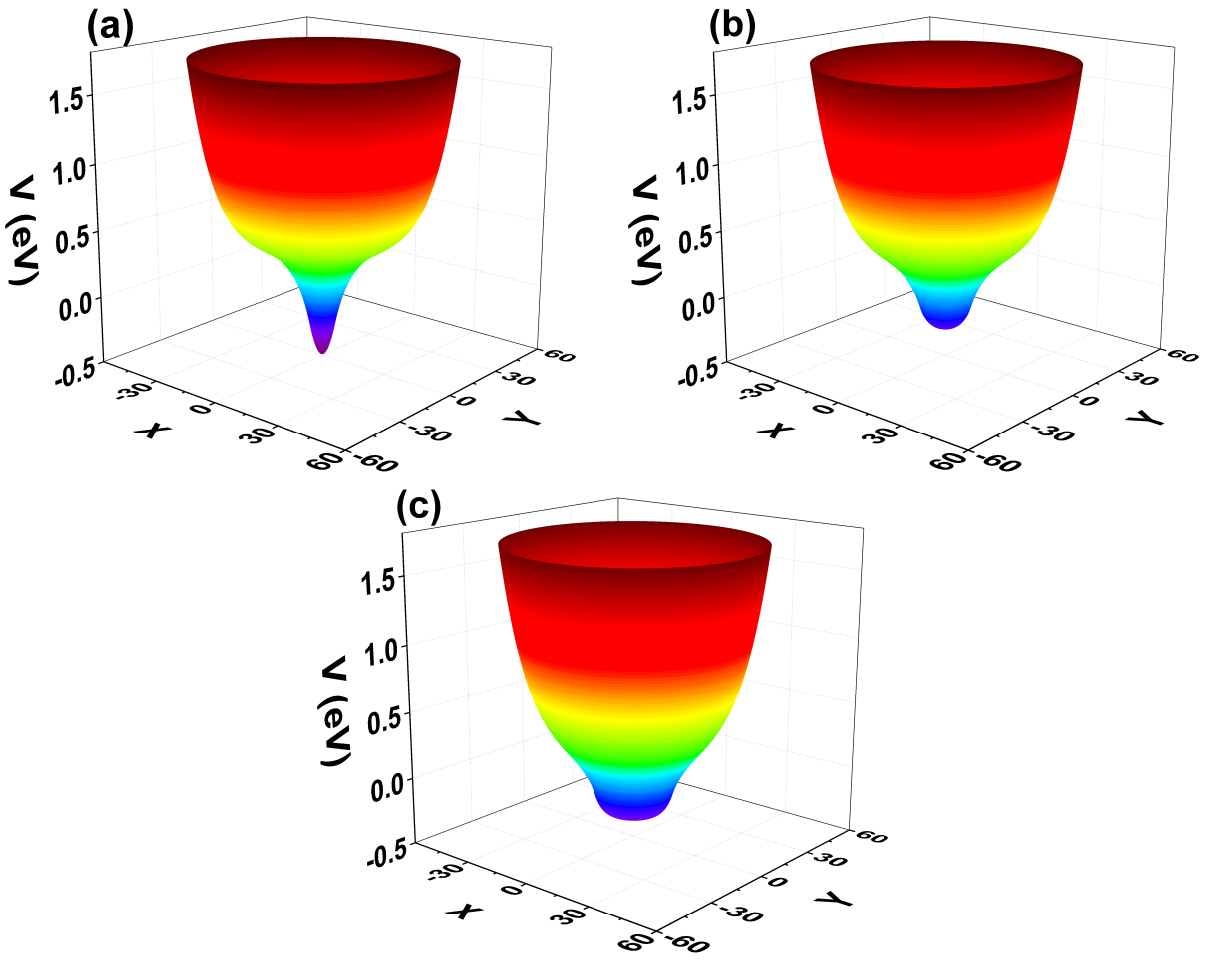

Figure 6-11.: (color online) Variation of the total optical absorption coefficient α_{12} and α_{23} in a central doped GaAs Razavy-like quantum well as a function of the incident photon energy for three different values of the n_d-doping concentration. The results are for $F = 0$ and $B = 0$.

bution practically resembles a delta type doping in the system, given the very small value of r_d compared to the total radius of the wire R_0. For the larger radii of the on-center doping region the sharp peak no longer appears. Instead, the profile shows a flatter bottom around the center of symmetry. However, in all cases, these lower structures correspond to smaller values of the potential energy, compared to the entire cross section of the QW. This indicates that electrons will tend to localize towards the interior this central region.

In the Fig. **6-12**(a) we plot the projection along the x direction of the self-consistent potential for the three values of doping radii r_d considered: 5, 10 and 15 nm. The black curve corresponds to the Razavy potential inside QWR, which is included as a reference. Calculations consider $R_0 = 50\,\text{nm}$, $T = 10\,K$, and $N_d = 3 \times 10^{19}\,\text{cm}^{-3}$. Vertical bars indicate the different doping radii, r_d. The potential reaches a minimum value of -0.49 eV, for $r_d = 5\,\text{nm}$, followed that with $r_d = 15\,\text{nm}$, where the minimum is at -0.32 eV and, finally, when $r_d = 10\,\text{nm}$ the minimum is -0.28 eV. The value of these minima is crucial for the positioning of the electronic states as well as to quantify their contribution to the electron density in the system. In the regions close to the QWR boundary, all potentials converge to a single value of 1.72 eV which corresponds to the sum of the potential due to the Fermi level Pinning in GaAs which is 0.7 eV plus the Razavy potential at the boundary that is equal to 1.02 eV. That is, the potential at the boundary is not modified by the effect of the doped delta layer in the central region of the wire. Note the similarity of the black curve that corresponds to the projection of the Razavy potential on the x-axis with the potential presented in Figure **6-4**(a) (blue curve) for the one-dimensional QW. Figure **6-12**(b) shows the electron density for each configuration of the system. Due to the symmetry of these quantities, they have are plotted only from the center of the structure towards the border. The colors on each curve exactly match to each of the potentials in Fig. **6-12**(a). The electron density that reaches the maximum value is that corresponding to $r_d = 5\,\text{nm}$, which is, precisely, the cylindrical delta-doping region with the smallest radius. In this case, electrons are confined within a circular cross-section that does not exceed 20 nm in diameter, and the behavior of electron density is completely decreasing as we move away from the center of symmetry of the system. For the radii $r_d = 10\,\text{nm}$ and $r_d = 15\,\text{nm}$, the densities decrease in magnitude, having a

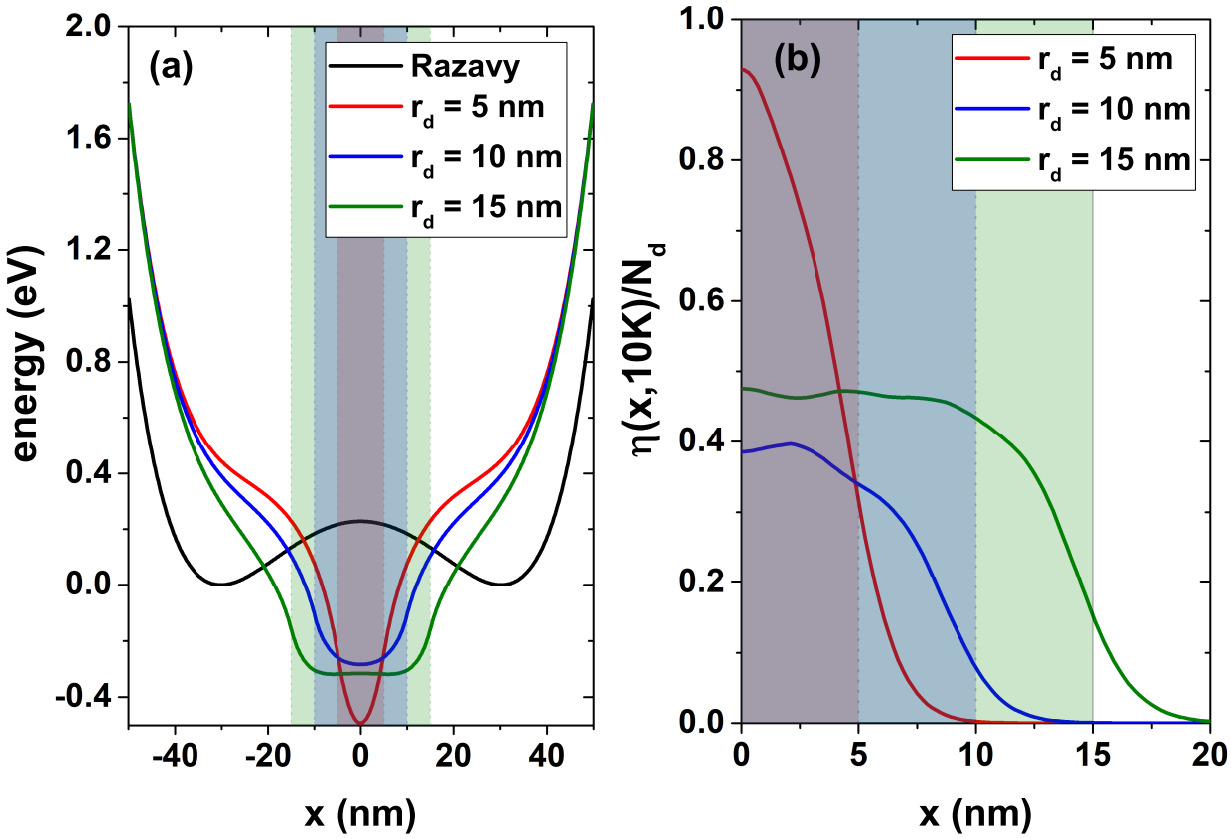

Figure 6-12.: Projection in the x direction of the self-consistent potential for the three doping radio r_d studied, 5, 10 and 15 nm. The black curve corresponds to the Razavy potential inside QW, included as a reference (**a**). Self-consistent electron densities corresponding to each of the potentials presented in (**a**) maintaining the same projection direction in the x direction (**b**). Calculations are with $R_0 = 50\,\text{nm}$, $T = 10\,K$, and $N_d = 3 \times 10^{19}\,\text{cm}^{-3}$.

distribution along the cross section of the wire with diameters not greater than 30 nm and 40 nm respectively. The system that reaches the lowest magnitude in electron density is the system with $r_d = 10\,\text{nm}$, which, as described before, corresponds to the highest potential in the center of the system. It should be noted that density profiles generated for $r_d = 10\,\text{nm}$ and 15 nm are not always totally decreasing, but exhibit the so-called Friedel-like oscillations, which appear as irregularities in the electron density near the center of symmetry of the system.

Figure **6-13** shows the first energy levels for a confined electron in a GaAs QWR as functions of the r_d parameter. The inset shows a zoom for r_d values between 5 nm and 10 nm. Calculations correspond to $R_0 = 50\,\text{nm}$, $T = 10\,K$, and $N_d = 3 \times 10^{19}\,\text{cm}^{-3}$. For all states there is a clear monotonous decreasing behavior. For r_d values smaller than 2.5 nm, the states presented are very close to each other around an average value of 0.72 eV. For r_d values bigger than 2.5 nm, the states present a considerable separation and there are crossovers between some excited states. The inset shows the region $5\,\text{nm} < r_d < 10\,\text{nm}$ in which it is possible to clearly observe some of these crossovers between states, with double or even triple degenerations occurring at specific points. For r_d values greater than 20 nm, the states again tend to be closer together due to the distribution of charges along the cross section of the wire.

The plot in Figure **6-14** shows the lowest energy levels for a confined electron in a GaAs QWR as a function of the N_d parameter. Results presented are for $R_0 = 50\,\text{nm}$, $r_d = 2\,\text{nm}$, and $T = 10\,K$. With this setup, all states present a parallel and approximately linear behavior, existing degeneration of order two for all the states except for the ground one. It should be noted that, unlike Fig. **6-13** in which the r_d is varied, there are no longer any crossovers between the states. Note that the first excited state and the ground state present very close energies, with a separation of approximately 0.7 meV, whilst the other excited states exhibit a more notable separation.

The electron density appears in Fig. **6-15** as a function of the distance from the QWR center (along the x direction), together with the those quantities, $|\psi_i(x, y = 0)|^2$, that contribute with the highest percentage to the density pro-

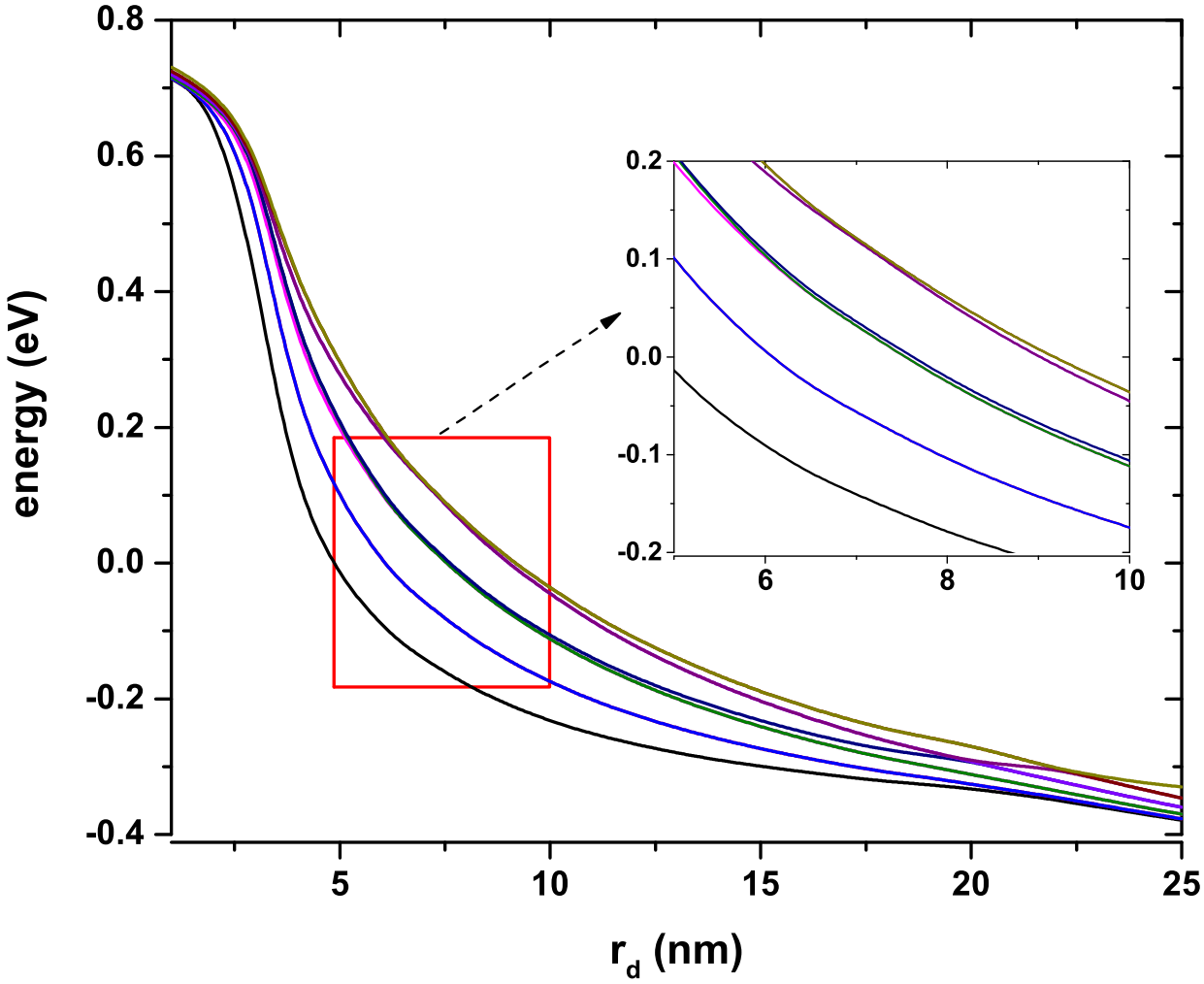

Figure 6-13.: First energy levels for a confined electron in a GaAs quantum wire as a function of the r_d parameter. The inset shows a zoom for r_d values between 5 nm and 10 nm. Calculations are with $R_0 = 50\,\text{nm}$, $T = 10\,K$, and $N_d = 3 \times 10^{19}\,\text{cm}^{-3}$.

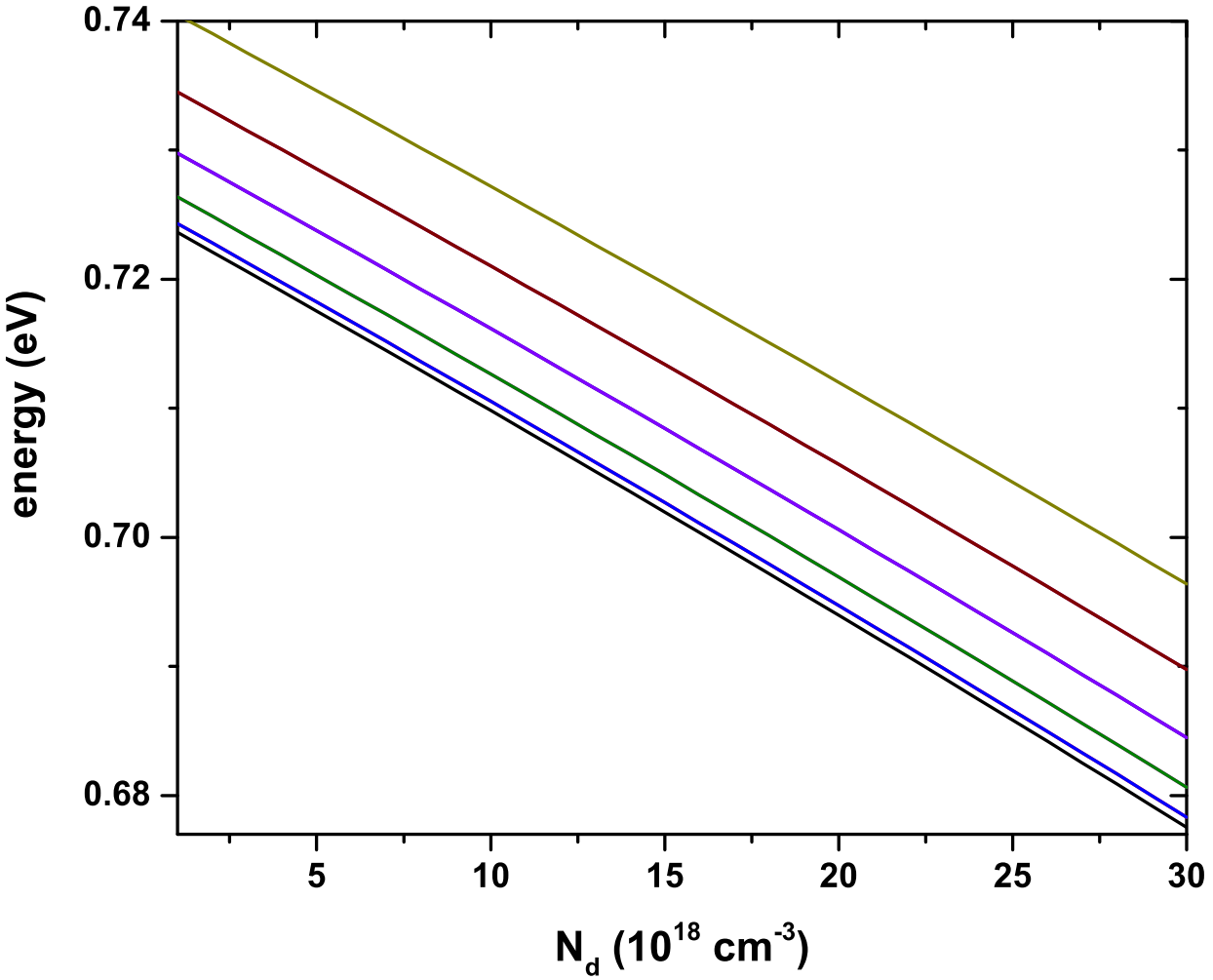

Figure 6-14.: First energy levels for a confined electron in a GaAs quantum wire as a function of the N_d parameter. Calculations are with $R_0 = 50\,\text{nm}$, $r_d = 2\,\text{nm}$, and $T = 10\,K$.

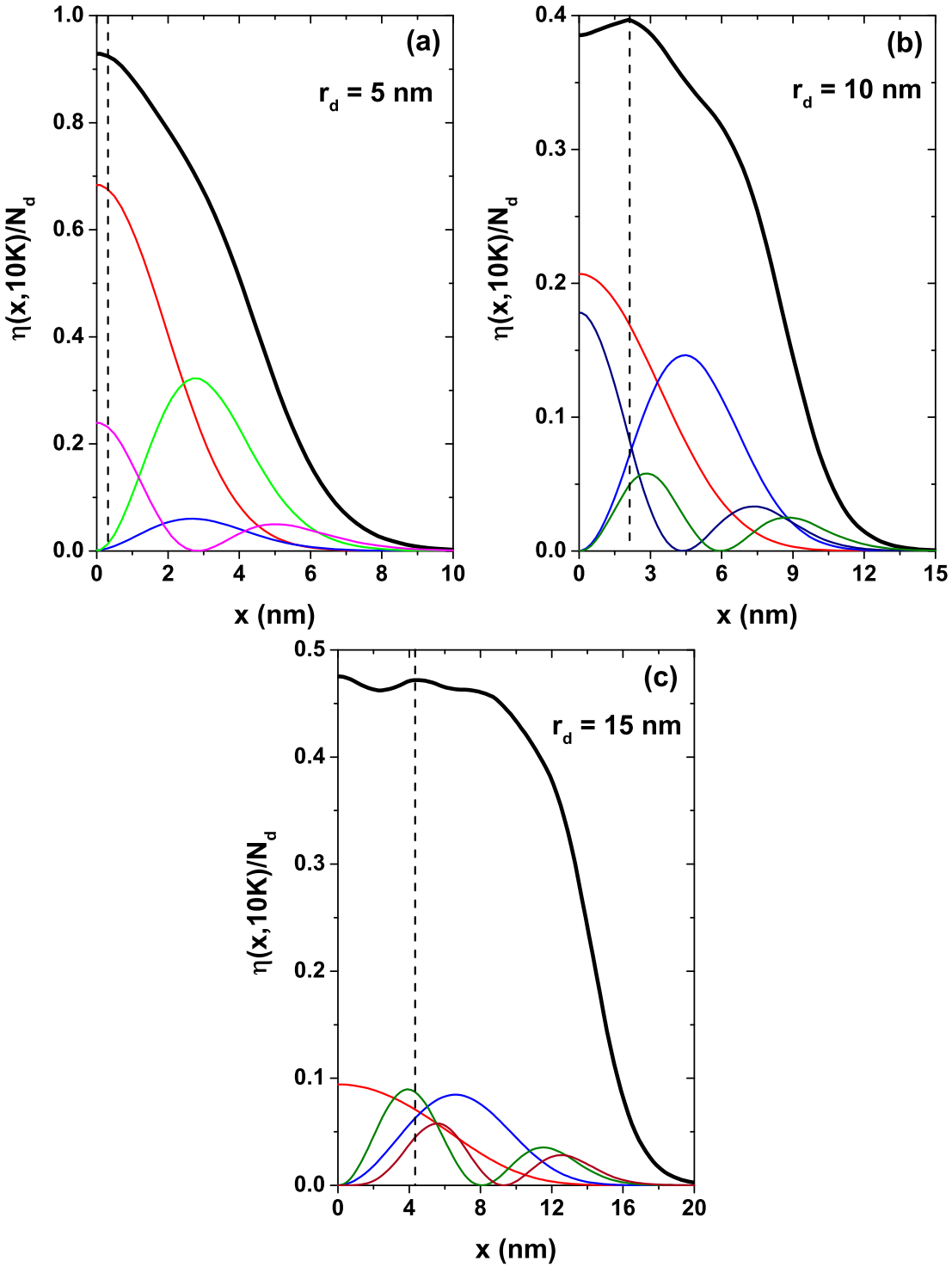

Figure 6-15.: Electron density and $|\psi_i(x, y = 0)|^2$ that contribute with the highest percentage to the density profile at the points marked with the dashed lines. Results are for $r_d = 5\,\text{nm}$ (**a**), $r_d = 10\,\text{nm}$ (**b**), and $r_d = 15\,\text{nm}$ (**c**) QW. Calculations are with $R_0 = 50\,\text{nm}$, $T = 10\,K$, and $N_d = 3 \times 10^{19}\,\text{cm}^{-3}$.

file at the points marked with the dashed lines. Results correspond for $r_d = 5\,\text{nm}$ (a), $r_d = 10\,\text{nm}$ (b), and $r_d = 15\,\text{nm}$ (c) QWR. Calculations were performed with $R_0 = 50\,\text{nm}$, $T = 10\,K$, and $N_d = 3 \times 10^{19}\,\text{cm}^{-3}$.

In Fig. **6-15**(a) the projection of the electron density along the x direction is presented for $r_d = 5\,\text{nm}$ and, for this configuration, there are no oscillations in the density profile. The dashed line corresponds to the point at which the percentage contribution of each of the states of the system to the total electron density has been calculated. This contribution is presented in detail in Table **6-1**. For this first system, the electron density profile is due only to the contribution of four states. the highest contribution is due to the ground state ψ_0 with 73.1 % corresponding to the red curve in Fig. **6-15**(a), followed by state ψ_3 with 25.1 %. No Friedel-like oscillations are present in this case. Fig. **6-15**(b) contains the electron density profile for $r_d = 10\,\text{nm}$ and the states that present a contribution greater than 10 % at the point $x = 2.1\,\text{nm}$ marked with the dashed line. For the total electron density, a contribution of eight states is present as reported in Table **6-1**. Again, the state that has a greater contribution is ψ_0, with 42.8 %, and corresponds to the red curve in the figure. It is followed by the state ψ_5 which is already a higher state with 21.2 % and later the state ψ_1 with 17.8 %. The appearance of this oscillation is mainly due to the occupation of the lowest states in the system (ψ_0 and ψ_1) with a contribution greater than 60 %. Fig. **6-15**(c) presents the electron density profile for $r_d = 15\,\text{nm}$, together with the probability densities of states that present a contribution greater than 9 % to the electron density at the point $x = 4.3\,\text{nm}$ -marked with the dashed line. Comparing with figures (a) and (b), in this case the first oscillation appears further from the center of symmetry of the system. It should be noted that the electron density for this case contains contributions from thirty states, however, none of them exceeds the 19 % contribution to this Friedel-like oscillation as evidenced in Table **6-1**. The state that contributes the most (state with the highest occupancy at this specific point) is one of the higher states, ψ_8, with 18.5 % followed by the ground state, ψ_0, with 15.1 %. The Table **6-1** does not include states with a contribution lower than 1 %. Comparing the three values of r_d and the data collected in Table **6-1**, it is possible to conclude that as the value of r_d augments, the ground state ceases to be the predominant state in terms of occupancy. Instead, a significant contribution from the highest states

in the system will occur.

	Contribution by state (%)		
r_d (nm) $\Rightarrow$	5	10	15
ψ_0	73.1	42.8	15.1
ψ_1	0.5	17.8	13.2
ψ_2	1.3	0.3	1.7
ψ_3	25.1	1.0	1.6
ψ_4		0.9	3.0
ψ_5		21.2	6.0
ψ_8		12.3	18.5
ψ_9		3.7	4.2
ψ_{12}			9.4
ψ_{13}			2.7
ψ_{18}			3.3
ψ_{19}			7.9
ψ_{20}			1.8
ψ_{25}			4.8
ψ_{26}			3.2
ψ_{27}			1.2

Table 6-1.: Contribution in percentage of each of the states to the oscillations in the density profile presented in figure **6-15**.

Finally, in order to have a comparison about the effect of doping geometry on the self-consistent potential in the cylindrical Razavy-like QWR, Fig. **6-16** shows the projection of the self-consistent potential along the x direction considering two different doping zones, the black curves correspond to a central cylinder-shaped doping, as indicated by the dark vertical column, the red curves correspond to a cylindrical ring-shaped doping (the two light red columns in the figure indicate the cross section of the ring in the xz plane, the columns are centered at $x = -30\,\text{nm}$ and $x = 30\,\text{nm}$ respectively). The dashed lines are for $N_d = 1 \times 10^{18}\,\text{cm}^{-3}$ and the solid lines are for $N_d = 5 \times 10^{18}\,\text{cm}^{-3}$. The inset shows the electron density obtained for $N_d = 5 \times 10^{18}\,\text{cm}^{-3}$. Calculations are

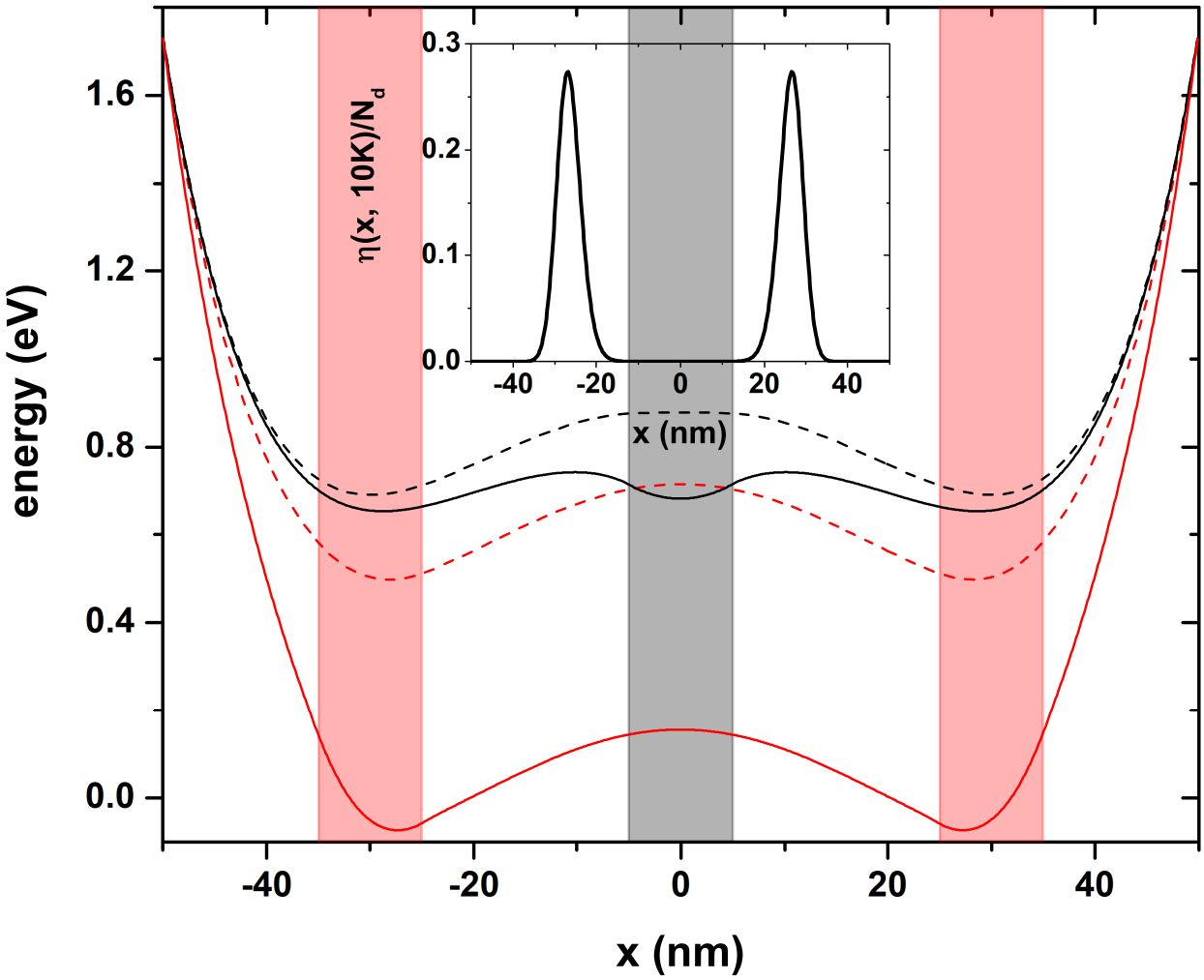

Figure 6-16.: Projection of the self-consistent potential in the x direction considering two different doping zones, the black curves correspond to a central cylinder-shaped doping, as indicated by the dark vertical column, the red curves correspond to a cylindrical ring-shaped doping such as show the two light red columns. The dashed lines are for $N_d = 1 \times 10^{18}\,\mathrm{cm}^{-3}$ and the solid lines are for $N_d = 5 \times 10^{18}\,\mathrm{cm}^{-3}$. The inset shows the electron density obtained for $N_d = 5 \times 10^{18}\,\mathrm{cm}^{-3}$. Calculations are with $R_0 = 50\,\mathrm{nm}$, $r_d = 5\,\mathrm{nm}$, and $T = 10\,K$.

with $R_0 = 50\,\text{nm}$, $r_d = 5\,\text{nm}$, and $T = 10\,K$. When the doping corresponds to the central cylinder, that is, to the black curves, one observes that when the density of donors in the system increases, there is a considerable decrease of the potential in the central zone. This is much more significant when the doping is included in a region with the shape of a cylindrical ring (red curves), where the potential is lowered by an average of 0.5 eV in the regions between -30 nm and 30 nm. It should be noted that in the latter case there is no longer a specific decrease in the central area, that is, the repulsive character is not lost in the center of symmetry. Analyzing the continuous black curve it is possible to realize that, for higher donor densities, the dominant potential in the system will be the potential due to the redistribution of charges, that is, the Hartree potential and the Razavy potential loses significance. Therefore, when the density of donors accumulates in a central cylinder, the self-consistent electron density will be very sensitive to the magnitude of these donors since they can drastically modify the potential profile. The opposite case occurs when the donor density accumulates in a cylindrical ring. There, as the donor density increases, the dominant potential remains the Razavy one, and the Hartree potential only generates a decrease in magnitude of the potential without drastically modifying the shape. The inset in Fig. **6-16** shows the electron density for $N_d = 5 \times 10^{18}\,\text{cm}^{-3}$ for the system with cylindrical ring doping. By comparing this result with the one presented in Fig. **6-12**(b), we see a totally different profile in which the electrons accumulate mostly in the area of doped ring and, despite being at a low temperature, no Friedel-like oscillations are present.

6.4. Conclusions

By using the effective mass and parabolic band approximations, the finite difference method, as well as a self-consistent calculation, we have investigated the features of total optical absorption coefficient of confined electrons in a delta-like doped Razavy-like quantum well under the combined effects of externally applied electric and magnetic field. In the absorption peaks, a clear blue shift is evidenced for all the transitions studied, keeping the donor density fixed, the shift being more significant for changes in the electric field than in the magnetic field, in all cases a change in the magnitude of the optical absorption peaks is

presented. The transition with the greatest resistance to modifications due to external fields is α_{23}. On the other hand, with the increase in donor density, red and blue shifts of the absorption peaks were also reported, as well as a decrease in their magnitude depending on the transition studied. This allows us to tune the system without modifying geometric parameters directly, only applying external fields or increasing the density of donors to obtain the maximum absorption of the material in the positions that are required for a certain application.

On the other hand, the delta-doping effect on electron states has been analyzed in quantum wire systems with exposed borders and circular cross-section subjected to an internal Razavy-like potential at low temperatures. Effects of varying geometric parameters such as the width of delta-doped layer, and not geometric as the density of donors in the system have been studied. In both cases a decrease in the magnitude of all electronic states has been found both with the increase of r_d and N_d. The appearance of irregularities in the electron density profile has been reported for $r_d = 10\,\text{nm}$ and $15\,\text{nm}$, these oscillations are Friedel-like and have been explained by means of the occupation of the electronic states of the system. We hope that this research will stimulate future investigations related to intentional doping in low-dimensional semiconductor heterostructures.

References

[1] R. L. Restrepo, J. P. González-Pereira, E. Kasapoglu, A. L. Morales, and C. A. Duque, *Linear and nonlinear optical properties in the terahertz regime for multiple-step quantum wells under intense laser field: electric and magnetic field effects*, Opt. Mater. **86**, 590–599 (2018).

[2] E. C. Niculescu, *Electromagnetically induced transparency in an asymmetric double quantum well under non-resonant, intense laser fields*, Opt. Mater. **64**, 540–547 (2017).

[3] H. V. Phuc, N. Duy Anh Tuan, and L. Dinh, *Linear and nonlinear magneto-optical absorption in a quantum well modulated by intense laser field*, Superlattice Microst. **100**, 1112–1119 (2016).

[4] J.-F. You, Q. Zhao, Z.-H. Zhang, J.-H. Yuan, K.-X. Guo, and E. Feddi, *The effect of temperature, hydrostatic pressure and magnetic field on the nonlinear optical properties of AlGaAs/GaAs semi-parabolic quantum well*, Int. J. Mod. Phys. B **33**, 1950325 (12pp) (2019).

[5] G. Liu, R. Liu, G. Chen, Z. Zhang, K. Guo, and L. Lu, *Nonlinear optical rectification and electronic structure in asymmetric coupled quantum wires*, Results Phys. **17**, 103027 (6pp) (2020).

[6] G. Liu, K. Guo, L. Xie, Z. Zhang, and L. Lu, *Tunability of linear and nonlinear optical absorption in laterally-coupled $Al_xGa_{1-x}As/GaAs$ quantum wires*, J. Alloy. Compd. **746**, 653–659 (2018).

[7] M. J. Karimi and M. Hosseini, *Electric and magnetic field effects on the optical absorption of elliptical quantum wire*, Superlattice Microst. **111**, 96–102 (2017).

[8] E. Kasapoglu, C. A. Duque, M. E. Mora-Ramos, and I. Sökmen, *The effects of the intense laser field on the nonlinear optical properties of a cylindrical $Ga_{1-x}Al_xAs/GaAs$ quantum dot under applied electric field*, Physica B **474**, 15–20 (2015).

[9] M. G. Barseghyan, H. M. Baghramyan, A. A. Kirakosyan, and D. Laroze, *The transition from double to single quantum dot induced by THz laser field*, Physica E **116**, 113758 (4pp) (2020).

[10] A. Ghosh, A. Bera, and M. Ghosh, *Modulating binding energy and interband emission energy of impurity doped quantum dots in presence of Gaussian white noise*, Curr. Smart Mater. **2**, 56–64 (2017).

[11] I. Karabulut and E. Paspalakis, *The role of permanent dipoles on the intensity-dependent nonlinear optical properties in asymmetric coupled quantum wells under a static electric field*, Physica E **81**, 294–301 (2016).

[12] K. Li, K. Guo, X. Jiang, and M. Hu, *Effect of position-dependent effective mass on nonlinear optical properties in a quantum well*, Optik **132**, 375–381 (2017).

[13] B. T. Diroll, M. Chen, I. Coropceanu, K. R. Williams, D. V. Talapin, P. Guyot-Sionnest, and R. D. Schaller, *Polarized near-infrared intersubband absorptions in CdSe colloidal quantum wells*, Nat. Commun. **10**, 4511 (9pp) (2019).

[14] H. Dakhlaoui and M. Nefzi, *Simultaneous effect of impurities, hydrostatic pressure, and applied potential on the optical absorptions in a GaAs field-effect transistor*, Results Phys. **15**, 102618 (7pp) (2019).

[15] H. Noverola-Gamas, L. M. Gaggero-Sager, and O. Oubram, *Interlayer distance effects on absorption coefficient and refraction index change in p-type double-δ-doped GaAs quantum wells*, Chinese Phys. B **28**, 124207 (5pp) (2019).

[16] Q. Zhao, S. Aqiqi, J.-F. You, M. Kria, K.-X. Guo, E. Feddi, Z.-H. Zhang, and J.-H. Yuan, *Influence of position-dependent effective mass on the non-*

linear optical properties in $Al_xGa_{1-x}As/GaAs$ single and double triangular quantum wells, Physica E **115**, 113707 (7pp) (2020).

[17] Ri. Betancourt-Riera, Re. Betancourt-Riera, L. A. Ferrer-Moreno, and A. D. Sañu-Ginerte, *Electron states and electron Raman scattering in a semiconductor quantum well with step-barriers: electric field effect*, Physica B **575**, 411700 (7pp) (2019).

[18] B. Amiri and A. Belghachi, *First principles investigation of absorption coefficient in quantum well designed for solar cells*, Optik **202**, 163554 (6pp) (2020).

[19] H. Yildirim, *Many-body effects on intersubband transitions in polar ZnO/ZnMgO multiple quantum wells*, Physica B **571**, 26–31 (2019).

[20] Y.-Y. Chen, Y.-N. Li, R.-G. Wan, and H.-W. Yan, *Tunable double-beam optical bistability in an asymmetric double quantum-well system*, Phys. Lett. A **383**, 125921 (7pp) (2019).

[21] S. Panda, T. Das, and B. K. Panda, *Nonlinear optical susceptibilities in $In_xGa_{1-x}N/GaN$ hexagonal single quantum well under applied electric field*, Superlattice Microst. **135**, 106238 (11pp) (2019).

[22] H. Dakhlaoui and M. Nefzi, *Tuning the linear and nonlinear optical properties in double and triple $\delta-$doped GaAs semiconductor: Impact of electric and magnetic fields*, Superlattice Microst. **136**, 106292 (14pp) (2019).

[23] F. Ungan, M. K. Bahar, J. C. Martinez-Orozco, and M. E. Mora-Ramos, *Optical responses in asymmetric hyperbolic-type quantum wells under the effect of external electromagnetic fields*, Photonic. Nanostruct. **41**, 100833 (5pp) (2020).

[24] N. D. Hien, C. A. Duque, E. Feddi, N. V. Hieu, H. D. Trien, L. T. T. Phuong, B. D. Hoi, L. T. Hoa, C. V. Nguyen, N. N. Hiev, and H. V. Phuc, *Magneto-optical effect in GaAs/GaAlAs semi-parabolic quantum well*, Thin Solid Films **682**, 10–17 (2019).

[25] E. F. Schubert, *Delta doping of III–V compound semiconductors: fundamentals and device applications*, J. Vac. Sci. Technol. A **8**, 2980-2996 (1990).

[26] K. Ploog, M. Hauser, and A. Fischer, *Fundamental studies and device application of $\delta-$doping in GaAs Layers and in $Al_xGa_{1-x}As/GaAs$ heterostructures*, Appl. Phys. A **45**, 233-244 (1988).

[27] A. C. Maciel, M. Tatham, J. F. Ryan, J. M. Worlock, R. E. Nahory, J. P. Harbison, and L. T. Forlez, *Raman scattering from electronic excitations in periodically $\delta-$doped GaAs*, Surf. Sci. **228**, 251-254 (1990).

[28] L. Ioriatti, *Thomas-Fermi theory of $\delta-$doped semiconductor structures: Exact analytical results in the high-density limit*, Phys. Rev. B **41**, 8340-8344 (1990).

[29] J. C. Egues, J. C. Barbosa, A. C. Notari, P. Basmaji, L. Ioriatti, E. Ranz, and J. C. Portal, *Electronic transport in periodically $\delta-$doped GaAs layers*, J. Appl. Phys. **70**, 3678-3680 (1991).

[30] M. H. Degani, *Electron energy levels in a $\delta-$doped layer in GaAs*, Phys. Rev. B **44**, 5580-5584 (1991).

[31] M. H. Degani, *Electronic properties of multiple Si δ doping in GaAs*, J. Appl. Phys. **70**, 4362-4365 (1991).

[32] J. Osvald, *Electronic properties of a near surface Si $\delta-$doped GaAs under an applied electric field*, J. Phys. D Appl. Phys. **37**, 2655-2659 (2004).

[33] K.-M. Wong and D. W. E. Allsopp, *Intersubband absorption modulation in coupled double quantum wells by external bias*, Semicond. Sci. Tech. **24**, 045018 (8pp) (2009).

[34] J. Krupski and M. Piętka, *On the accuracy of the Thomas-Fermi-Dirac method applied to sub-band structure calculations in a $\delta-$doped semiconductor*, Solid State Commun. **107**, 141-144 (1998).

[35] E. Ozturk, Y. Ergun, H. Sari, and I. Sokmen, *The self-consistent calculation of Si $\delta-$doped GaAs structures*, Appl. Phys. A **73**, 749-754 (2001).

[36] E. Kasapoglu, F. Ungan, H. Sari, and I. Sökmen, *The hydrostatic pressure and temperature effects on donor impurities in cylindrical quantum wire under the magnetic field*, Physica E **42**, 1623-1626 (2010).

[37] N. Raigoza, A. L. Morales, and C. A. Duque, *Infinite potential barrier and hydrostatic pressure effects on impurity-related optical absorption spectra in GaAs double quantum wells*, Braz. J. Phys. **36**, 350-353 (2006).

[38] M. G. Barseghyan, A. A. Kirakosyan, and C. A. Duque, *Hydrostatic pressure, electric and magnetic field effects on shallow donor impurity states and photoionization cross section in cylindrical GaAs–$Ga_{1-x}Al_x$ As quantum dots*, Phys. Status Solidi B **246**, 626-629 (2009).

[39] I. Rodriguez-Vargas, M. E. Mora-Ramos, and C. A. Duque, *Influence of the hydrostatic pressure onto the electronic and transport properties of n-type double $\delta-$doped GaAs quantum wells*, Microelectr. J. **39**, 438-441 (2008).

[40] P. Nithiananthi and K. Jayakumar, *Pressure study on the semiconductor–metal transition in a quantum well*, Phys. Status Solidi B **246**, 1238-1242 (2009).

[41] R. Khordad, S. Kheiryzadeh Khaneghah, and M. Masoumi, *Effect of pressure on intersubband optical absorption coefficients and refractive index changes in a V-groove quantum wire*, Superlattice Microst. **47**, 538-549 (2010).

[42] L. M. Gaggero-Sager, G. G. Naumis, M. A. Muñoz-Hernandez, and V. Montiel-Palma, *Self-consistent calculation of transport properties in Si $\delta-$doped GaAs quantum wells as a function of the temperature*, Physica B **405**, 4267–4270 (2010).

[43] R. B. Dhafer, H. Saidi, and S. Ridene, *Proposal of InP/AlInGaAs single delta quantum well for fiber-optic communications*, Optik **158**, 164-169 (2018).

[44] J. Osvald, *Self-consistent analysis of Si $\delta-$doped layer placed in a non-central position in GaAs structure*, Physica E **23**, 147-151 (2004).

[45] M. Razavy, *An exactly soluble Schrödinger equation with a bistable potential*, Am. J. Phys. **48**, 285 (1980).

[46] M. Baradaran and H. Panahi, *Exact Solutions of a Class of Double-Well Potentials: Algebraic Bethe Ansatz*, Adv. High Energy Phys. **2017**, 8429863 (2017).

[47] H. Karayer, D. Demirhan, K. G. Atman, *Analytical exact solutions for the Razavy type potential*, Math Meth Appl Sci. **93**, 9185-9194 (2020).

[48] J. Feist, J. Galego, and F. J. García-Vidal, *Polaritonic Chemistry with Organic Molecules*, ACS Photonics **5**, 205–216 (2018).

[49] Y. E. Panfil, D. Shamalia, J. Cui, S. Koley, and U. Banin, *Electronic coupling in colloidal quantum dot molecules; the case of CdSe/CdS core/shell homodimers*, J. Chem. Phys. **151**, 224501 (2019).

[50] Z. Han, G. Czap, C. Xu, Chi-lun Chiang, D. Yuan, R. Wu, and W. Ho, *Probing Intermolecular Coupled Vibrations between Two Molecules*, Phys. Rev. Lett. **118**, 036801 (2017).

[51] X. Li, A. Mandal, and P. Huo, *Cavity frequency-dependent theory for vibrational polariton chemistry*, Nat. Commun. **12**, 1315 (2021).

[52] E. Kasapoglu, H. Sari, I. Sökmen, J. A. Vinasco, D. Laroze, and C. A. Duque, *Effects of intense laser field and position dependent effective mass in Razavy quantum wells and quantum dots*, Physica E **126**, 114461 (12pp) (2021).

[53] V. K. Arora, *Quantum size effect in thin-wire transport.* Phys. Rev. B **23**, 5611-5612 (1981).

[54] G. W. Bryant, *Hydrogenic impurity states in quantum-well wires.* Phys. Rev. B **29**, 6632-6639 (1984).

[55] S. Luryi and F. Capasso *Resonant tunneling of two-dimensional electrons through a quantum wire: A negative transconductance device.* Appl. Phys. Lett. **47**, 1347-1349 (1985); Erratum in **48**, 1693 (1986).

[56] K. B. Wong, M. Jaros, and J. P. Hagon, *Confined electron states in GaAs-$Ga_{1-x}Al_xAs$ quantum wires*. Phys. Rev. B **35**, 2463-2466 (1987).

[57] T. Yamauchi, and Y. Arakawa, *Tight binding analysis of GaAsAlGaAs quantum wire structures*. Superlattices Microstruct. **10**, 83-87 (1991).

[58] E. C. Garnett, M. L. Brongersma, Y. Cui, M. D. McGehee, *Nanowire Solar Cells*. Ann. Rev. Mater. Res. **41**, 269-295 (1991).

[59] F. Zaouali, A. Bouazra, M. Said, *A theoretical evaluation of optical properties of InAs/InP quantum wire with a dome cross-section*. Optik, **174**, 513-520 (2018).

[60] L. Van-Tan, T. V. Thang, N. D. Vy, H. T. Cao, *Spin polarization and temperature dependence of electron effective mass in quantum wires*. Phys. Lett. A, **383**, 2110-2113 (2019).

[61] P. Hosseinpour, *Effect of Gaussian impurity parameters on the valence and conduction subbands and thermodynamic quantities in a doped quantum wire*. Solid State Commun. **322**, 114061 (2020).

[62] B. D. Woods, S. D. Sarma, T. D. Stanescu, *Subband occupation in semiconductor-superconductor nanowires*. Phys. Rev. B **101**, 045405 (2020).

[63] J.-B. Xia and W.-J. Fan, *Electronic structures of superlattices under in-plane magnetic field*, Phys. Rev. B **40**, 8508-8515 (1989).

[64] K. F. Brennan and A. S. Brown, *Theory of Modern Electronic Semiconductor Devices*, John Wiley & Sons, New York, 2002, p. 448.

[65] H. Dakhlaoui, *The effects of doping layer location on the electronic and optical properties of GaN step quantum well*, Superlattice Microst. **97**, 439-447 (2016).

[66] H. B. Dakhlaoui and N. Mouna, *Quantum size and magnesium composition effects on the optical absorption in the $Mg_xZn_{(1-x)}O/ZnO$ quantum well*, Chem. Phys. Lett. **693**, 40-45 (2018).

[67] H. Dakhlaoui and M. Nefzi, *Enhancement of the optical absorption in MgZnO/ZnO quantum well under external electric field*, Optik **157**, 1342-1349 (2018).

[68] M. K. Bahar, K.A. Rodríguez-Magdaleno, J.C. Martínez-Orozco, M. E. Mora-Ramos, and F. Ungan, *Optical properties of a triple AlGaAs/GaAs quantum well purported for quantum cascade laser active region*, Mater. Today Commun. **26**, 101936 (2021).

[69] A. S. Durmuslar, C. A. Billur, A. Turkoglu, and F. Ungan, *Optical properties of a GaAs quantum well with new type of hyperbolic confinement potential: Effect of structure parameters and intense laser field*, Opt. Commun. **499**, 127266 (2021).

[70] A. Zangwill, *Physics at Surfaces*; Cambridge University Press: New York, NY, USA, p. 454 (1988).

[71] J. H. Luscombe, M. Luban, *Lateral confinement in quantum nanostructures: Self-consistent screening potentials*, Appl. Phys. Lett. **57**, 61-63 (1990).

[72] K. Pieniak, M. Chlipala, H. Turski, W. Trzeciakowski, G. Muziol, G. Staszczak, A. Kafar, I. Makarowa, E. Grzanka, S. Grzanka, C. Skierbiszewski, and T. Suski, *Quantum-confined Stark effect and mechanisms of its screening in InGaN/GaN light-emitting diodes with a tunnel junction*, Opt. Express **29**, 1824-1837 (2021).

[73] B.N. Aneeshkumar, *Independent control of valence- and conduction-band states in composite quantum wells*, Phd Thesis Eindhoven University of Technology **29** (2004).

[74] D. Makhlouf, M. Choubani, F. Saidi, and H. Maaref, *Applied electric and magnetic fields effects on the nonlinear optical rectification and the carrier's transition lifetime in InAs/GaAs core/shell quantum dot*, Mater. Chem. Phys. **267**, 124660 (2021).

[75] A. Surrente, M. Baranowski, and P. Plochocka, *Perspective on the physics of twodimensional perovskites in high magnetic field*, Appl. Phys. Lett. **118**, 170501 (2021).

[76] A. Baydin, T. Makihara, N. M. Peraca, and J. Kono, *Time-domain terahertz spectroscopy in high magnetic fields*, Front. Optoelectron. **14**, 110–129 (2021).

[77] A. Arora, *Magneto-optics of layered two-dimensional semiconductors and heterostructures: Progress and prospects*, J. Appl. Phys. **129**, 120902 (2021).

7. Electro-transport properties in GaAs/AlGaAs and InSe/InP finite superlattices under the effect of nonresonant intense laser field and considering geometric modifications

In this work a finite periodic superlattice is studied, analyzing the probability of electronic transmission for two types of semiconductor materials, GaAs/AlGaAs and InSe/InP. The changes in the maxima of the quasistationary states for both materials are discussed, making variations in the number of periods of the superlattice and its shape by means of geometric parameters. The effect of a nonresonant intense laser field has been included on the system to analyze the changes in the electronic transport properties by means of the Landauer formalism. It is found that the highest tunneling current is given for the GaAs-based compared to the InSe-based system and that the intense laser field improves the current-voltage characteristics. Finally, the power of the system is discussed for different bias voltages as a function of the chemical potential.

7.1. Introduction

The study of semiconductor systems has advanced significantly during the last fifty years, particularly in systems based on superlattices (SLs) of GaAs, InSe, among other materials. Modern experimental techniques have allowed us to understand in a much more precise way the behavior of charge carriers within these heterostructures and develop theoretical models with a high degree of precision hand to hand with theoretical models. A significant motivation for the study of heterostructures based on these materials are the novel applications in fields such as the development of field-effect transistors or high electronic mobility, systems in which the effects of impurities, pressures, and applied fields have been analyzed to improve optical absorption; these devices are candidates for the advancement of future technologies in the electronics field [1–5]. Likewise, in this field, there are switching devices capable of working at high-speed [6]. In the optoelectronics field, the development of solar cells that can provide strong absorption in a much wider range of the electromagnetic spectrum stands out, which considerably improves the efficiency of usable energy [7–16]. A typical application of semiconductor systems are detectors, which, depending on the type of material or the geometric arrangement, can be tuned to detect from ultraviolet, infrared, and even up to the terahertz range [17–23]; also in this field, mention should be made to the cascade laser [24]. Finally, various applications such as biosensors to detect some type of cancer cells or zeno-logical applications [25, 26] are worth mentioning. In some of these applications, low dimensional semiconductor devices such as quantum dots, quantum wires or quantum wells are implemented [27, 28].

Some of the first studies of SLs based on semiconductor systems were developed around the 70's in works such as those by Esaki and Chang [29] in which the properties of electronic transport in systems with a periodic structure of GaAs/AlAs were experimentally analyzed. By means of the molecular-beam epitaxy technique, in their work, the evidence of the system oscillatory conductance behavior increasing voltage was found. Later, using the same growth technique for the heterostructures, Dingle *et al.* [30] experimentally demonstrated the formation of a GaAs/AlGaAs SL at low temperatures using optical-absorption measurements on ultra-thin layers. Later in the 90's, Fedirko and

Eremtchenko [31] analyzed the SLs based on GaAs/AlGaAs by means of scanning probe microscopy, finding a pretty good periodic structure.

In more recent years, the SLs of semiconductor materials continue to be studied either to understand excitations in the system or to analyze the response under external fields. In works such as that from Komatsu *et al.* [32], the authors analyzed the intensity of exciton photoluminescence in the presence of an external magnetic field in a GaAs SL. In this type of material, the study of structural properties is of great importance since it is possible to tune electronic properties that lead to the optical response of the system. In 2004, Jeong *et al.* [33] studied these properties in a GaAs/AlGaAs SL layer on InAs quantum dots by means of photoluminescence, photoreflectance spectroscopy, and transmission electron microscopy. Their results showed that the wavelength of the quantum dots was effectively tailored by the high potential barriers. The effect of the interface on the modulation-doped of the SL-type heterostructures can considerably modify the electronic properties in n-doped and p-doped systems. This effect was studied by Bezerra *et al.* [34], finding that the presence of graded interfaces modifies the carrier confinement inside of the GaAs quantum well. When the semiconductor system is subjected to the action of external magnetic fields, it is possible to modify the properties of electronic transport, in particular, the current-voltage curves, or to generate the appearance of Magnetoresistance oscillations [35, 36].

One way to characterize the semiconductor structures is by analyzing the transport properties, whether thermal or electrical, depending on if the system is put in contact with electronic reservoirs at different temperatures or if the system is subjected to a potential difference. These properties can be analyzed by means of the Landauer-Büttiker formalism [37, 38].

In this work, we are interested in studying the electronic transport properties of a finite periodic lattice. We are particularly interested in studying the tunneling current considering geometric variations of the heterostructure for two different combinations of the semiconductor materials, GaAs/AlGaAs and InSe/InP. Using the Landauer formalism, the current due to the tunneling of electrons from the emitter to the collector, generated by a potential difference between the terminals of the device, is calculated. The power due to the diffusion of charge carriers and the effects of a nonresonant intense laser field (ILF)

on the conduction band profile and, therefore, on the conduction current are also studied. The solution of the differential equations and the calculation of the electronic transmission probability have been carried out using the finite element method (FEM). The chapter is organized as follows: Section 7.2 contains the theoretical framework; Section 7.3 is devoted to the results and corresponding discussion; finally, in Section 7.4 are presented the main conclusions.

7.2. Theoretical model

The system under study corresponds to a SL with InSe (GaAs) well regions and InP (AlGaAs) barrier regions. As shown in Fig. **7-1**, each well has a w-width and is made of InSe (GaAs) and the left and right barriers of the first period have b_1 and b_2 lengths, respectively, and are of InP (AlGaAs) material, as shown in Fig. **7-1**(c). The full length of the first period is $a = b_1 + b_2 + w$ and remains fixed for all three figures (see Figs. **7-1**(a-c)). The total length of the barriers inside the first cell is $b = b_1 + b_2$. From the above, it is possible to define the γ-parameter ($\gamma = b/a$) that sets the relationship between the total barrier length and the length of the first SL period. At this point, it is possible to define a factor that can modify the geometry of the complete periodic system, $\beta = b_2/b$, with $0 \leq \beta \leq 0.5$. As we see in Fig. **7-1**, depending on the β-value, the first SL period will have an established form: *i*) for $\beta = 0.0$, the barriers will have the same width as wells; *ii*) for $\beta = 0.2$, the system will be asymmetric regardless of the number of periods, and the well on the right will always be thinner than the one on the left, and finally *iii*) for $\beta = 0.5$, the system will be symmetric for all periods, but the two lateral barriers will always be smaller than the central barriers. Depending on the number of calculated periods and each β-value, Figs. **7-1**(a), **7-1**(b), and **7-1**(c) will be repeated periodically.

From the above, it is possible to write expressions for the barrier and well widths in terms of the γ, β, and a parameters, i.e.,

$$\begin{aligned} b_1 &= \gamma\, a\, (1-\beta)\,, \\ b_2 &= \gamma\, a\, \beta\,, \\ w &= a\,(1-\gamma)\,. \end{aligned} \tag{7-1}$$

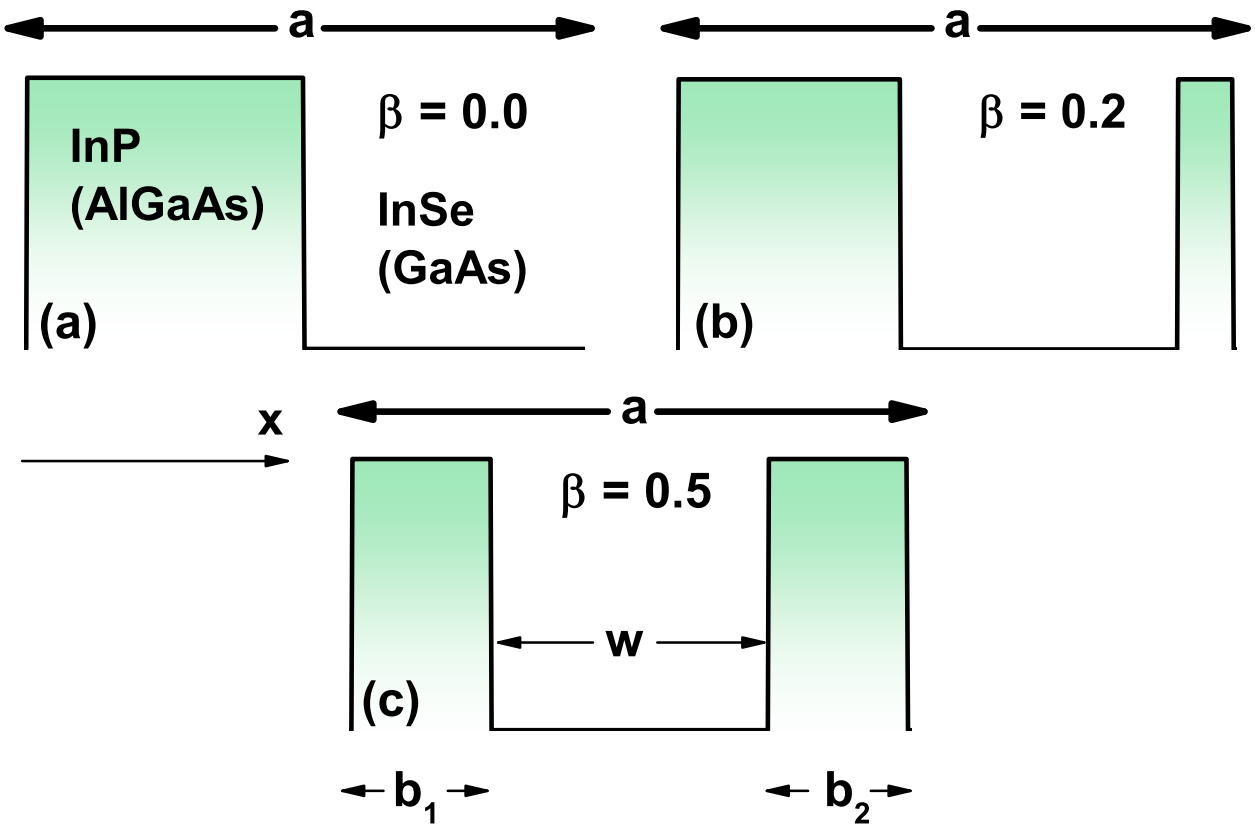

Figure 7-1.: (a-c) Scheme corresponding to a single period of the superlattice for $\beta = 0.0$, $\beta = 0.2$, and $\beta = 0.5$, respectively.

Table **7-1** shows the particular case with $\beta = 0.0$, 0.2, and 0.5,

β	$a\,(\mathrm{nm})$	$w\,(\mathrm{nm})$	$b_1\,(\mathrm{nm})$	$b_2\,(\mathrm{nm})$
0.0	10	5	5	0
0.2	10	5	4	1
0.5	10	5	2.5	2.5

Table 7-1.: Geometric parameters for different values of β.

The shape of each potential can be modified by means of variations in the geometric parameters according to Eq. (7-1) and Table **7-1**, to later be replaced in the time-independent Schrödinger equation to obtain a set of eigenfunctions and eigenvalues ($\psi^{\beta}_{n,i}(\vec{r})$ and $E^{\beta}_{n,i}$),

$$\left[\vec{\nabla}\cdot\left(\frac{-\hbar^2}{2\,m^*(x)}\vec{\nabla}\right)+U^{\beta}_{n}(x)\right]\psi^{\beta}_{n,i}(\vec{r})=E^{\beta}_{n,i}\,\psi^{\beta}_{n,i}(\vec{r})\,, \tag{7-2}$$

where $m^*(x)$ is the x-dependent electron effective mass (note that in this work, we deal with different values of the electron effective mass at the well and barrier regions). $U^{\beta}_{n}(x)$ is the SL-potential (the SL is grown along the x-direction) which depends directly on the n-parameter (number of SL-periods, i.e., the number of times that each panel of Fig. **7-1** is repeated for each β-parameter value). Additionally, $\psi^{\beta}_{n,i}(\vec{r})$ is the electron wavefunction corresponding to the i-th quasi-stationary state and of course it depends on both n and β. Finally, $E^{\beta}_{n,i}$ is the corresponding energy; in general, the eigenvalues have real and imaginary parts since the states are not stationary. Consequently, the electrons have a lifetime inside the wells to later leave these by quantum tunneling effect.
By using the separation of variables method, we can write $\psi^{\beta}_{n,i}(\vec{r})=e^{i\,\vec{k_\perp}\cdot\vec{\rho}}\,\Psi^{\beta}_{n,i}(x)$, where $\vec{k_\perp}$ and $\vec{\rho}$ are the wavevector and electron coordinate along the yz-plane, perpendicular to the growth direction of the heterostructure. With the previous wavefunction inserted in Eq. (7-2), and taking into account that we are dealing with the bottom of all energy subbands (it means $\vec{k_\perp}=0$), we can obtain a 1D-differential equation for the x-coordinate, where by imposing the open boundary conditions, the $\Psi^{\beta}_{n,i}(x)$ function can be written as a linear combination of

plane waves as follows

$$\Psi_{n,i}^{\beta}(x) = A_n^{\beta}(x)\, e^{+i\, k_{n,i}^{\beta}\, x} + B_n^{\beta}(x)\, e^{-i\, k_{n,i}^{\beta}\, x}\,. \tag{7-3}$$

The $A_n^{\beta}(x)$ and $B_n^{\beta}(x)$ functions are the probability amplitudes of the system. The first term on the right-hand side in Eq. (7-3) corresponds to an electron moving from left to right with probability amplitude $A_n^{\beta}(x)$, whereas the second term is an electron moving from right to left (reflected wave) with probability amplitude $B_n^{\beta}(x)$; the complete wave function for any region of the system is a superposition of these plane waves. It is clear that these amplitudes must depend on the x-point, at which they are being calculated, as well as on the (n, β) geometric parameters of the superlattice. $k_{n,i}^{\beta}$ is the magnitude of the wave vector and is given by $k_{n,i}^{\beta} = (2m^*(E_{n,i}^{\beta} - U_n^{\beta}(x))/\hbar^2)^{1/2}$.
The x-dependent differential equation associated with the Eq. (7-2) when the wave function represented by Eq. (7-3) has been considered is solved through the FEM with the COMSOL-Multiphysics licensed software (5.4, COMSOL AB, Stockholm, Sweden) [39–41] by implementing the semiconductor module (Semiconductor Module User's Guide COMSOL Multiphysics®) [42–45]. In this way, the values of the probability amplitudes are found in any region of the system. After that, it is possible to calculate the electron transmission function $T_{n,i}^{\beta}(E)$ through the device as the quotient between the amplitude of the transmitted wave and the amplitude of the incident wave,

$$T_n^{\beta}(E) = \frac{|A_n^{\beta}(x_f)|^2}{|A_n^{\beta}(x_i)|^2}\,, \tag{7-4}$$

where $A_n^{\beta}(x_i)$ represents the amplitude of the wave that propagates from left to right evaluated at the emitter and $A_n^{\beta}(x_f)$ is the amplitude of a wave that propagates from left to right but evaluated in the collector. This function is proportional to the probability of electron tunneling through the system.
Once the transmission probability has been calculated, it is possible to calculate the voltage-current characteristics in the SL using Landauer's theory, which tells us that employing a connection of the system with two electronic reservoirs, it is possible to obtain the electronic tunneling current through the system, given

by

$$I(\Lambda) = I_0 \int_{-\infty}^{\infty} T_n^{\beta}(E,\Lambda)\left[f_L(E,\Lambda) - f_R(E,\Lambda)\right] dE\,, \tag{7-5}$$

where e is the electron charge, $\hbar$ is the reduced Planck constant, and $I_0 = e/\pi\hbar$. The terms $f_L(E,\Lambda)$ and $f_R(E,\Lambda)$ correspond to the Fermi functions evaluated at the emitter and collector, respectively. They are given by $f_L(E,\Lambda) = (1+e^{(E-E_F)/k_BT})^{-1}$ and $f_R(E,\Lambda) = (1+e^{(E-E_F+\Lambda)/k_BT})^{-1}$, where Λ is the bias voltage applied between both terminals of the device. By means of the transmission function, it is also possible to calculate the heat flux and the power in the system, given, respectively, by

$$\Theta_n^{\beta}(l) = \frac{2}{h}\int_{-\infty}^{\infty} T_n^{\beta}(E,\Lambda)(E - E_f(l))(f_L(E,\Lambda) - f_R(E,\Lambda))dE \tag{7-6}$$

and

$$P_n^{\beta} = \Theta_n^{\beta}(L) - \Theta_n^{\beta}(R)\,. \tag{7-7}$$

The term $T_n^{\beta}(E,\Lambda)$ represents the transmission probability for a fixed voltage, $E_f(l)$ is the Fermi energy for $l = L$ ($l = R$), that is, for the emitter (collector). In our study, we consider the effects of a x-polarized nonresonant intense laser field (ILF) applied to the SL structure, which can be modeled as a monochromatic plane wave with angular frequency ϕ. Due to the presence of this nonresonant laser field, a modification occurs in the potential profile that enters Eq. (7-2). So, the transformation $U_n^{\beta}(x) \to \langle V_n^{\beta}(x,\alpha_0)\rangle$ is obtained through the relation

$$\langle V_n^{\beta}(x,\alpha_0)\rangle = \frac{\phi}{2\pi}\int_0^{2\pi/\phi} U_n^{\beta}\left[x + \alpha_0\sin(\phi\, t)\right]\, dt\,. \tag{7-8}$$

The $\langle V_n^{\beta}(x,\alpha_0)\rangle$ potential is known as the laser dressed potential, where the ILF-parameter is defined as $\alpha_0 = (eA_0)/(m^*\phi)$ (here, A_0 is the strength of the laser field). The Eq. (7-8) is obtained by applying an intense, high frequency laser field to an atomic system [46–48].

7.3. Results and discussion

For the calculations the following input parameters have been used at 300 K: $m^* = 0.067\, m_0$ ($m^* = 0.0879\, m_0$) for the GaAs (AlGaAs) electron effective mass (where m_0 is the mass of the free electron) and $U_n^\beta(x) = 0$ ($U_n^\beta(x) = 0.261$ eV) in the GaAs (AlGaAs) material [49, 50]. Additionally, $m^* = 0.023\, m_0$ ($m^* = 0.08\, m_0$) is the InSe (InP) and $U_n^\beta(x) = 0$ ($U_n^\beta(x) = 0.57$ eV) in the InSe (InP) material [51]. Geometric parameters: unit cell length $a = 10$ nm, $\gamma = 0.5$, and angular laser frequency $\phi = 1$ THz. The equations have been solved through the FEM considering the following parameters: 5000 elements, 2 edge elements, 1.0 element length radius, and 5001 mesh vertices.

Fig. **7-2** shows the bottom of the conduction band for a GaAs-$Al_{0.3}Ga_{0.7}As$ lattice (for the InSe-InP system, it would be an equivalent figure, only the value of the band offset changes) varying from 1 to 4 periods and three values of the β-parameters. The dashed lines indicate the potential without ILF effect, whereas the solid curved regions show the potential modified by an ILF-parameter of $\alpha_0 = 1.0$ nm. As we can see, when $\beta = 0$, the number of barriers is equal to the n-parameter, whereas, for $\beta \neq 0$, the number of barriers is equal to $n+1$. Each region shaded with light blue or light red color corresponds to a superlattice period. Note that depending on the n and β values, in the union of two or more periods an overlap of the barrier regions may occur; for example, for $n = 2$ and $\beta = 0.5$, which corresponds to Fig. **7-2**(c2), the union of two periods generates the appearance of a central barrier of 5 nm wide. This being wider than the two lateral barriers that each measure 2.5 nm. Note how applying an ILF to the system can significantly modify the shape of the potential barriers; this variation is more significant for the barriers of smaller width, as can be seen, for example, in Figs. **7-2**(b1,b2,b3,b4) for $\beta = 0.2$; when comparing this effect on the right barrier with the other barriers, a clear decrease in the height of the barrier on the right is seen. This effect is not observed for $\beta = 0$ and $\beta = 0.5$.

Fig. **7-3** shows the energy dependence of the electronic transmission function for the GaAs-$Al_{0.3}Ga_{0.7}As$ well-barrier system presented in Fig. **7-2** for the lower states. Results are for $\alpha_0 = 0$, that is, without ILF effect on the system (upper row), and $\alpha_0 = 1.0$ nm (lower row). The different colors indicate the

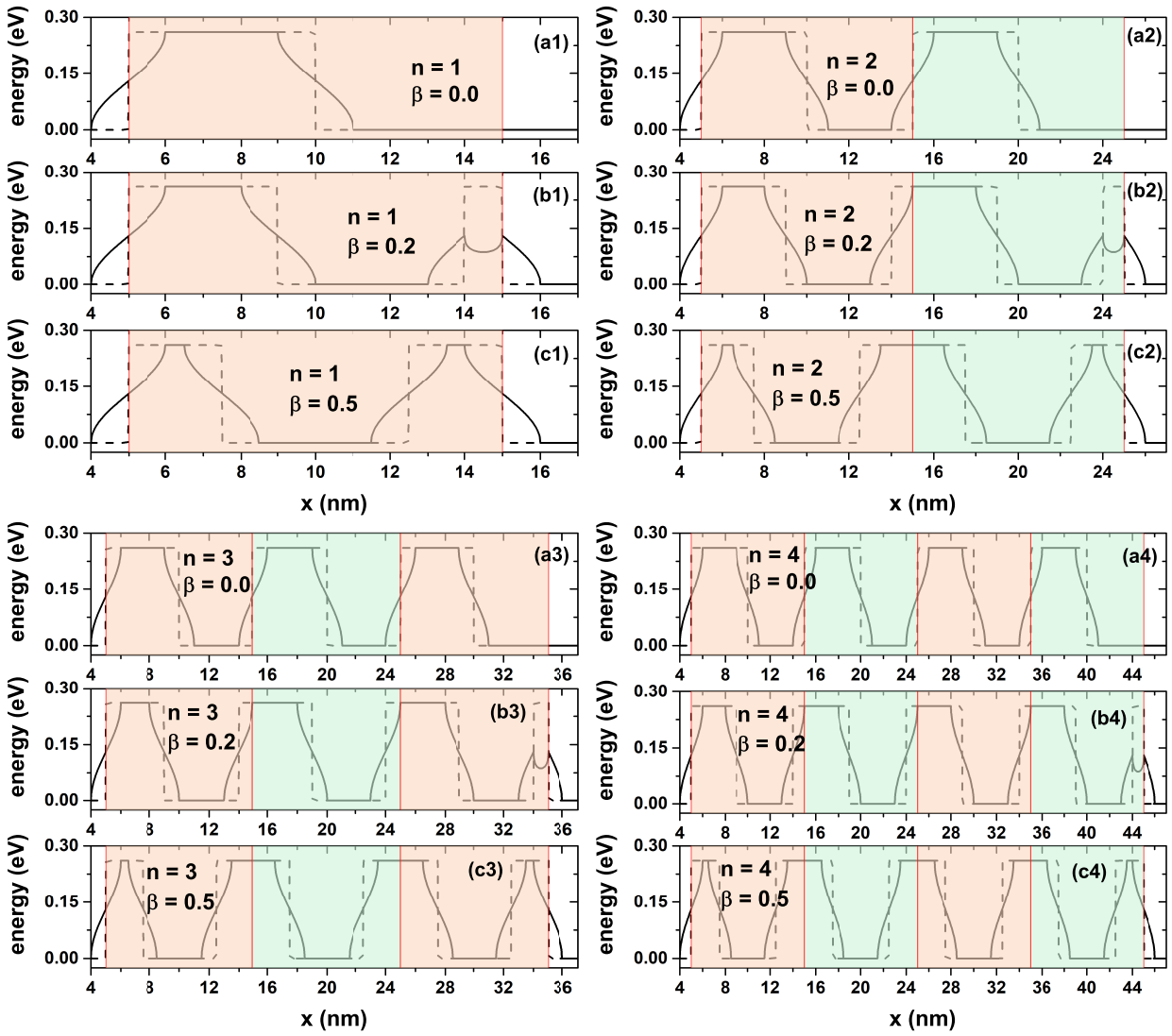

Figure 7-2.: x-dependent potential profile of a GaAs-$Al_{0.3}Ga_{0.7}As$ lattice varying from $n = 1$ to $n = 4$ periods. The shape of the periods is also modified with the $\beta = 0.0$, 0.2, and 0.5 parameters. The dashed lines indicate the potential with $\alpha_0 = 0$, whereas the solid line show the potential modified with $\alpha_0 = 1.0\,\text{nm}$. The different colors shadow regions indicate the superlattice periods for every system.

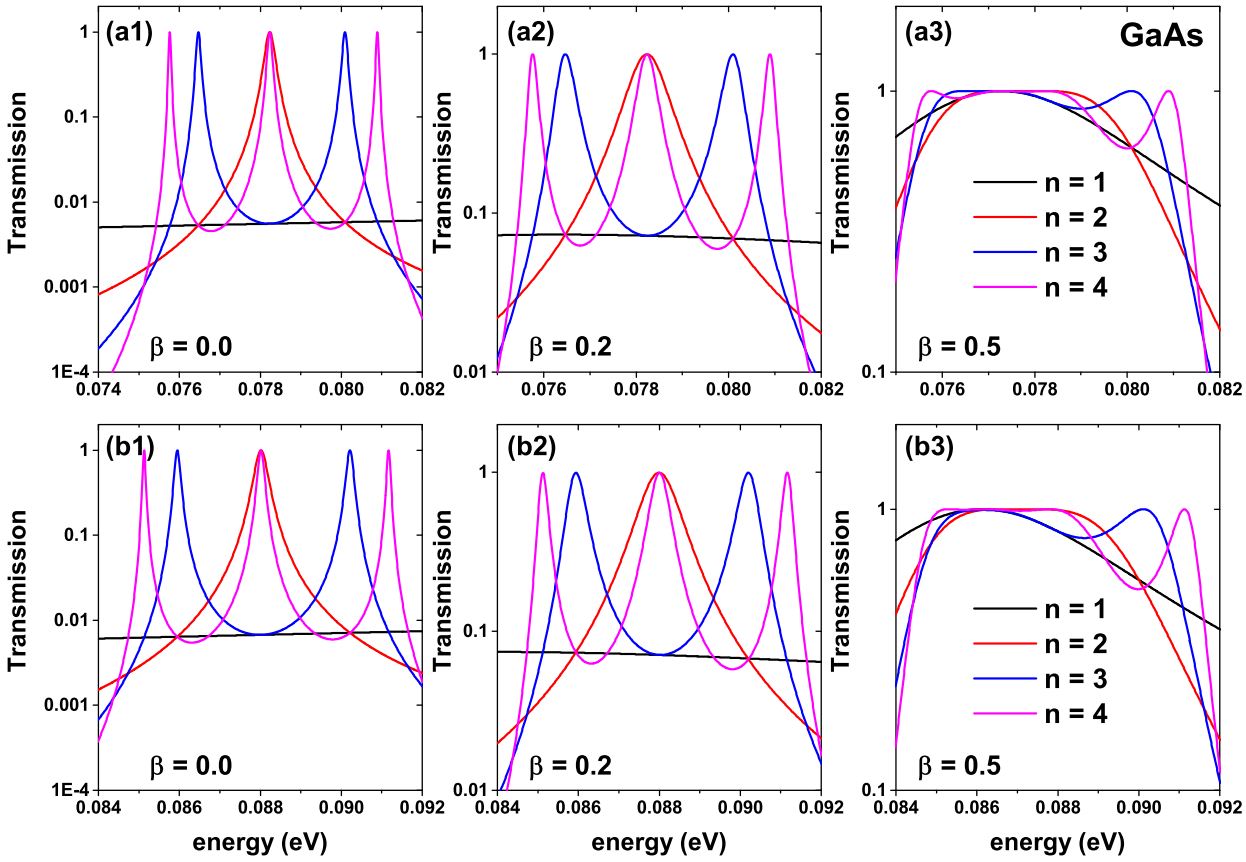

Figure 7-3.: Energy dependence of the electronic transmission probabilities for a GaAs-$Al_{0.3}Ga_{0.7}As$ finite lattice, according to Fig. **7-2**, i.e., varying the n-number of periods and the shape according to the structural β-parameter. Results are without intense laser field effects (upper panels) and with $\alpha_0 = 1\,\mathrm{nm}$ (lower panels).

number of periods calculated as indicated in Fig. **7-3**(a3). Figs. **7-3**(a1) and **7-3**(b1) correspond to $\beta = 0$, Figs. **7-3**(a2) and **7-3**(b2) correspond to $\beta = 0.2$, and finally Figs. **7-3**(a3) and **7-3**(b3) are for $\beta = 0.5$, therefore, each column corresponds to a different structure. As we can see in Fig. **7-3**(a1), the system for $n = 1$ does not present a transmission peak; this is an approximately constant continuous function for this range of energies. This is expected behavior since, for $\beta = 0$, only one potential barrier is present, the transmission is due solely to the tunneling effect. For Fig. **7-3**(a2), with $n = 1$, the system already has two potential barriers (as can be seen in Fig. **7-2**); however, the transmission still does not reach a maximum peak for the depicted energy range. This is because, despite the existence of a resonant state in the central well region, the non-symmetry of the barriers does not allow maximum transmission of 1, furthermore, the right barrier is only 1 nm thick, so the tunneling is almost complete. Already for $\beta = 0.5$ and $n = 1$ in Fig. **7-3**(a3), the system reaches a maximum transmission value that is presented by the effect of resonant tunneling with the state inside the central well. In addition, due to the symmetry of the barriers, for a given energy value, the maximum transmission probability value is reached. For $n = 2$, a well-defined peak is evidenced for the system with and without laser. In this case, the average width of the peak is greater for $\beta = 0.2$ compared to $\beta = 0$. Note that for $\beta = 0.5$, the transmission presents a plateau-type structure, an energy range in which the transmission probability is equal to or very close to 1. For $n = 3$ and $n = 4$, the transmission probability presents 2 and 3 peaks, respectively, for both $\beta = 0$ and $\beta = 0.2$. Finally, for $\beta = 0.5$, the transmission probability functions present flat regions for values close to transmission equal to one. By comparing Figs. **7-3**(a1,a2,a3) with 3(b1,b2,b3), we note that the effect of the ILF on the system does not significantly modify the shape or average width of the electronic transmission peaks. However, there is an evident blue shift in the position of all transmission peaks for all calculated periods and independently of the value of β-parameter. For example, the red peak in Figs. **7-3**(a1) and 3(b1), corresponding to $n = 2$ with $\beta = 0$, goes from 78.2 meV to 88 meV solely due to the laser effect. We have to highlight that the variation in the average width of each transmission peak is of fundamental importance for the response of the electric current through the device.

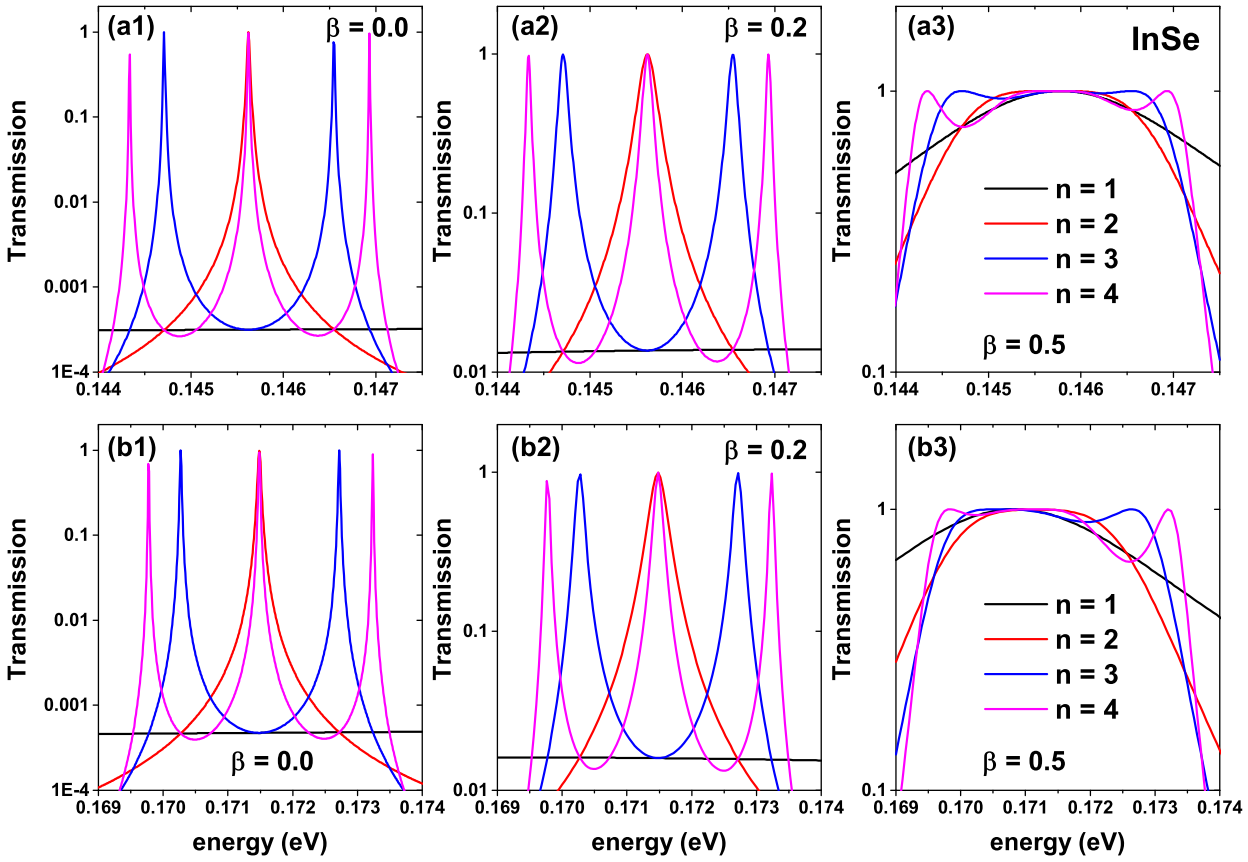

Figure 7-4.: Energy dependence of the electronic transmission probabilities for an InSe-InP finite lattice, according to Fig. **7-2**, i.e., varying the n-number of periods and the shape according to the structural β-parameter. Results are without intense laser field effects (upper panels) and with $\alpha_0 = 1\,\mathrm{nm}$ (lower panels).

Fig. **7-4** shows the electronic transmission function of the well-barrier system presented in Fig. **7-2** for InSe-InP lattice. The upper row is for zero ILF-parameter, whereas the lower row is for $\alpha_0 = 1.0\,\text{nm}$. The different colors indicate the number of calculated periods calculated in a similar way to Fig. **7-3**. The transmission functions present a trend very similar to that of GaAs-$Al_{0.3}Ga_{0.7}As$ well-barrier system, however, for the InSe-InP based system, the average width of each transmission peak for $\beta = 0$ and $\beta = 0.2$ present a small but appreciable decrease concerning the GaAs-$Al_{0.3}Ga_{0.7}As$ system. These differences can change the area under the transmission curve and modify the properties of electronic transport. Due to the different band offsets for both materials, clearly, the position of the maximum probability peaks is not the same. To highlight one, in Fig. **7-3**(a1) for GaAs-$Al_{0.3}Ga_{0.7}As$, the maximum probability for the system with $n = 1$ and $\beta = 0$ is given for 78.2 meV, while in the InSe-InP system with the same parameters the resonant energy value is 145.6 meV. Finally, in Figs **7-4**(b1), 4(b2), and 4(b3) we see how once again the ILF effect generates a shift towards the blue for all transmission maxima. The value of the resonance in the red curve of Fig. **7-4**(b1) appears at 171.5 meV; this indicates that the effect of the ILF on the quasi-stationary states for the InSe-InP based system is more significant than in the GaAs-$Al_{0.3}Ga_{0.7}As$ one. Note that for both materials with and without laser effect, the system with $\beta = 0.5$ (Figs. **7-3**(a3) and **7-3**(b3) and Figs. **7-4**(a3) and **7-4**(b3)) presents approximately flat regions for the transmission profile and a point at which it takes the same value regardless of the number of periods of the device. For example, for the InSe-InP based system, this value is 145.8 meV when the laser is off and 170.9 meV when the laser is on.

To understand why the curves in Figs. **7-3**(a3-b3) and **7-4**(a3-b3) lose their symmetrical appearance and are so different from the other figures in the rest of the panels, in Fig. **7-5**(a) we have calculated the transmission probability for the GaAs-$Al_{0.3}Ga_{0.7}As$ system as a function of the electron energy for $n = 3$ and different values of the β-parameter. In Fig. **7-5**(b,c), the real and imaginary parts of the lattice eigenvalues ($E^{\beta}_{n,i}$), respectively, as a function of the β-parameter have been calculated. In Fig. **7-5**(a) we see that for the lowest values of the β-parameter, the transmission probability presents two clearly defined peaks, such as $\beta = 0.02$ and $\beta = 0.2$ highlighted in red and blue,

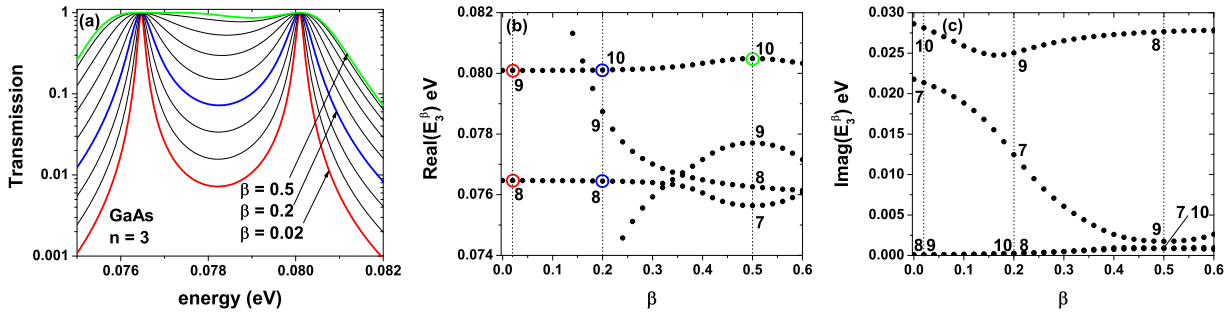

Figure 7-5.: In (a), transmission probability for the GaAs-$Al_{0.3}Ga_{0.7}As$ lattice for $n = 3$ as a function of the electron energy for different values of the β-parameter. In (b-c), lattice eigenvalues real and imaginary parts $E^{\beta}_{n,i}$ respectively as a function of the β-parameter.

respectively. However, as the β-value is increased, the average width of these peaks, corresponding to resonant states within the superlattice, increases. For $\beta = 0.5$ (green curve), which is the highest value, the transmission probability has a peak around 0.08 eV and a region where the transmission probability shows an approximately flat behavior between 0.076 eV and 0.078 eV. When the Schrödinger equation is solved with open boundary conditions, a set of eigenvalues $E^{\beta}_{n,i}$ (where i is the order of the eigenvalue) is obtained for each pair of (n, β) values, these eigenvalues generally have real and imaginary parts. In Fig. **7-5**(b), the real part of the eigenvalues for $n = 3$ is presented as a function of the β parameter in the range $(0.0, 0.6)$. The vertical axis is in the same energy range in which the transmission probability depicted Fig. **7-5**(a) has been calculated. The vertical dotted lines indicate the particular positions of $\beta = 0.02$, $\beta = 0.2$, and $\beta = 0.5$ that correspond to the same values for the red, blue and green curves of Fig. **7-5**(a), respectively. The numbers (labels) indicate the order of the eigenvalue (i-parameter). The red circles in Fig. **7-5**(b) correspond to the value of the two eigenvalues that are presented for $\beta = 0.0$, that is, these values coincide with the two maxima that are shown in the red curve of Fig. **7-5**(a). As we see in Fig. **7-5**(b), for $\beta = 0.2$ in the range of energies presented, the system shows three eigenvalues, however, in Fig. **7-5**(a) the blue curve only shows two resonant peaks corresponding to the eigenvalues 8 and 10 marked by the blue circles, that is, there does not appear a peak associated with the eigenvalue 9 that is around 0.079 eV. The reason for this resonance not appea-

ring can be found by analyzing Fig. **7-5**(c) in which the imaginary part of the eigenvalues is presented. As we see for $\beta = 0.2$, the imaginary part of the eigenvalues 8 and 10 is very low compared to the imaginary part associated with the eigenvalue 9. On the other hand, this imaginary part is inversely proportional to the average life-time of the electrons in each state inside each well. From the above, it is obtained that the life-time of the electrons in state 9 is very low compared to states 8 and 10, which implies a probability density practically zero at the interior of the wells of the superlattice for this state, which disables it for the resonant tunneling process and for this reason that third peak does not appear in the blue curve of Fig. **7-5**(a). Analogous behavior happens for $\beta = 0.5$, in Fig. **7-5**(b) we see that four eigenvalues appear in the range of energies presented; three of them very close between 0.075 eV and 0.078 eV and one more close to 0.08 eV. When we analyze the imaginary part of each of these states by means of Fig. **7-5**(c), it is found that the imaginary part associated with state 8 is very large compared to the other states for this value of β. This implies that there is practically no probability of having electrons inside the wells of the superlattice for this energy value. From the above it is concluded that the green curve in Fig. **7-5**(a) corresponds to the contribution of states 7, 9, and 10, where state 10, highlighted in Fig. **7-5**(b) with a green circle, corresponds at the resonance around 0.08 eV shown in Fig. **7-5**(a). The flat region on the green curve of Fig. **7-5**(a), that is between 0.076 eV and 0.078 eV, is due to the contribution of states 7 and 9 of Fig. **7-5**(b). From the above, we see that the transmission probability of the green curve corresponds to the resonance of the electrons that come from the emitter with states 7, 9, and 10 inside the wells of the superlattice; that is, there is a transmission due to three resonant states, as opposed to the lower values of β for which transmission is due solely to the contribution of two resonant states. This is the main cause of the asymmetry that the green curve has compared to the red and blue curves in Fig. **7-5**(a). This same explanation also applies to the difference marked between Figs. **7-3**(a3, b3) and **7-4**(a3, b3) with respect to those of the other panels.

Fig. **7-6** shows the schematic diagram of the superlattice made up of a system of GaAs (InSe) wells and $Al_{0.3}Ga_{0.7}As$ (InP) barriers. The lower part represents the device connected to two (hot and cold) reservoirs. The top represents the bottom of the conduction band of the system. The width of the wells and the

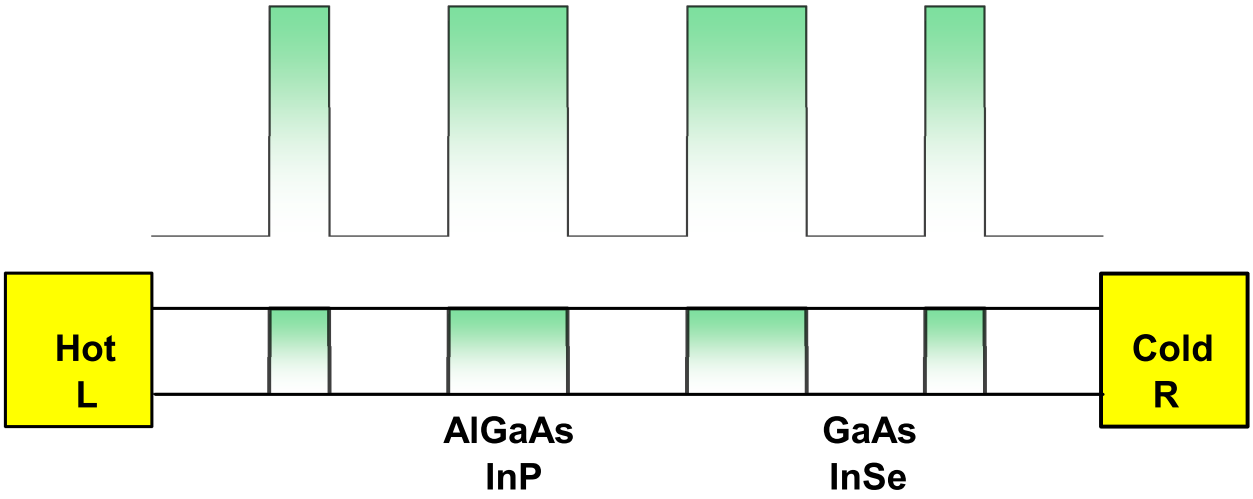

Figure 7-6.: Schematic diagram of the superlattice made up of a system of GaAs (InSe) wells and $Al_{0.3}Ga_{0.7}As$ (InP) barriers. The lower part represents the device connected to hot-left and cold-right reservoirs that also act as emitters and collectors. The top represents the bottom of the conduction band of the system. The width of the wells and the two central barriers have been set at 5 nm, and the barriers at the left and right are set at 2.5 nm (see Fig. **7-2**(c3)).

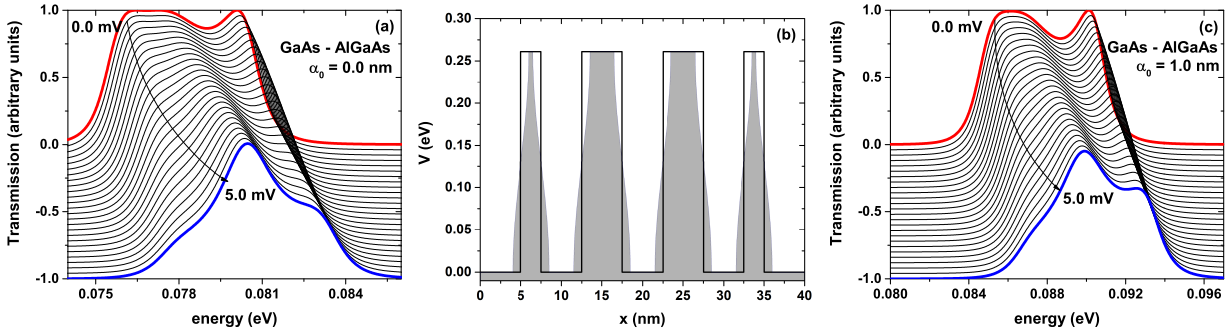

Figure 7-7.: Corresponds to the system shown in Fig. **7-2**(c3). In (a), the transmission probability for the GaAs-$Al_{0.3}Ga_{0.7}As$ lattice without laser effect for different bias voltages concerning the incident electron energy. In (b), the scheme of the potential profile for the barrier-well lattice system, the black curve corresponds to the system without laser effect and the shaded region including an intense laser field parameter strength of $\alpha_0 = 1.0\,\text{nm}$. In (c), the same as in (a), but with intense laser field effect, $\alpha_0 = 1.0\,\text{nm}$. The width of the wells and the two central barriers have been set at 5 nm and the two lateral barriers at 2.5 nm.

two central barriers have been set at 5 nm and the end barriers at 2.5 nm. The system can be brought out of equilibrium through a potential or temperature difference between the electronic reservoirs. This would induce a flow of the charge carriers, which implies an electric or thermal current between the device terminals. An external ILF can be applied to this well-barrier arrangement and analyze how the electronic probability changes; this is represented in Fig. **7-7** and **7-8**.

Fig. **7-7** shows the transmission probability for the GaAs-$Al_{0.3}Ga_{0.7}As$ system without ILF effect for different bias voltages concerning the incident electron energy, Fig. **7-7**(a). Fig. **7-7**(b) shows the scheme of the potential profile for the barrier-well lattice system, see Fig.**7-2**(c3), where the black curve corresponds to $\alpha_0 = 0$ and the shaded region for $\alpha_0 = 1.0\,\text{nm}$. In Fig. **7-7**(c) is depicted the same as in Fig. **7-7**(a), but for $\alpha_0 = 1.0\,\text{nm}$. In Fig. **7-7**(a), we can see how as the bias voltage increases, the flat peak at the left side becomes narrower, that is, more defined, and moves towards higher energies; this can be seen

by comparing the corresponding red curve at zero bias, see Fig. **7-3**(a3) blue curve, with the blue curve corresponding to 5.0 mV. Additionally, it is observed that the peak located at higher energies loses intensity in a systematic way as the bias voltage increases. Summarizing, at zero bias voltage, the transmission probability presents two structures, a flat low-energy structure and a narrow and well-defined high-energy structure, which collapse into a single, much more defined structure with probability 1.0 and localized at 80.5 meV when the bias voltage is 5.0 mV. According to Landauer's theory, the area under each probability curve must be proportional to the electric current due to the flow of electrons through the system for this voltage. For the calculations presented in Fig. **7-7**(a), the profile of the bottom of the conduction band shown in Fig. **7-7**(b) (black curve) has been used. Fig. **7-7**(c) shows the transmission probability for the GaAs-$Al_{0.3}Ga_{0.7}As$ system calculated for the potential profile of Fig. **7-7**(b) (shaded region) including the ILF-effects. As we see in Fig. **7-7**(b), the nonresonant ILF induces a decrease in the width of the well-bottom; this causes the quasi-stationary levels to rise, which corresponds to a blue shift as evidenced in Fig. **7-7**(c). The Fig. **7-7**(c), the zero bias curve corresponds to Fig. **7-3**(b3) blue plot, shows similar behavior to that presented in Fig. **7-7**(a) as the bias voltage is increased in the system, that is, a decrease in the intensity of the extreme peaks and the emergence of a single central peak of maximum probability (one) attached to two external peaks of less intensity. However, clearly, there is a notable difference in the area under each curve compared to the ILF effects as the voltage increases. These differences in transmission probability profiles cause changes in electronic transport properties.

The results depicted in Fig. **7-8** follow the same scheme as Fig. **7-7**, but for the InSe-InP system. In Fig. **7-8**(a), we can see how the system goes from having three peaks all associated with maximum probability 1, red curve for zero bias voltage (see Fig. **7-4**(a3) without laser effect and **7-4**(b3) with intense laser effects) to having a single central peak with probability one and two shoulders of smaller amplitude on each side (blue curve). If we compare Figs. **7-7**(a) and **7-8**(a), we see that for both materials, there is a blue shift in the position of the transmission peaks with the increase in voltage; however, the average width of the peaks is greater in the case of the GaAs-$Al_{0.3}Ga_{0.7}As$ structure than in the InSe-InP one. Analogous behavior occurs when an intense nonresonant

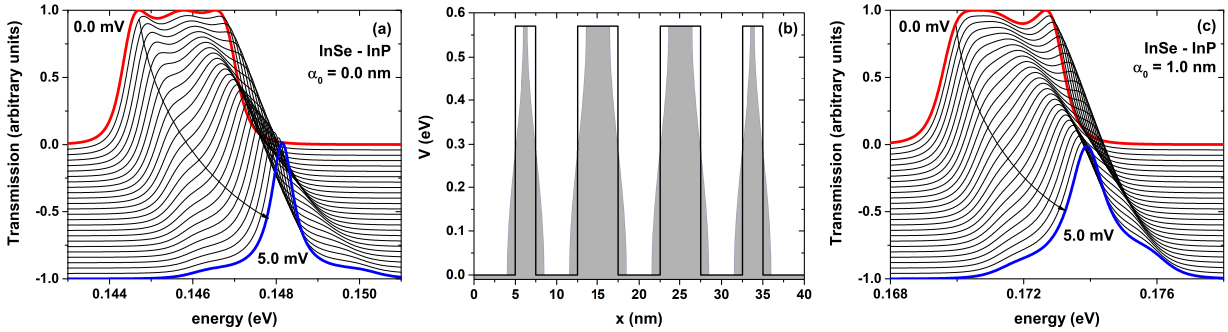

Figure 7-8.: In (a), the transmission probability for the InSe-InP lattice without laser effect for different bias voltages concerning the incident electron energy. In (b), the scheme of the potential profile for the barrier-well lattice system, the black curve corresponds to the system without laser effect and the shaded region including an intense laser field parameter strength of $\alpha_0 = 1.0\,\text{nm}$. In (c), the same as in (a), but with intense laser field effect, $\alpha_0 = 1.0\,\text{nm}$. The width of the wells and the two central barriers have been set at 5 nm and the two lateral barriers at 2.5 nm.

laser is applied to the system; see Figs. **7-7**(c) and **7-8**(c). From Figs. **7-7** and **7-8** it has been found that the transmission profile of the well-barrier lattice system can be modified by applying an external nonresonant laser field and modifying the materials that make up each layer of the system, and of course, applying a bias voltage between the emitter and collector, maintaining fixed geometric parameters. The previous indicates that this system is a good candidate for an electronic device since it is possible to tune the electronic transmission through which physical quantities such as electric current, heat flow, conductance, power, among others, can be modeled.

Fig. **7-9**(a) shows the electronic tunneling current for the well-barrier lattice system as a function of the bias voltage. Analyzing the current for both materials without including laser effects (full symbols), it is found that the system based on GaAs-$Al_{0.3}Ga_{0.7}As$ reaches a value of $5.4\,\text{m}I_0$ for the maximum current peak that occurs at 0.3 mV, and on the other hand, for InSe-InP based material, the maximum current value is $2.9\,\text{m}I_0$ which occurs for the same bias voltage. It should be noted that for both materials, the geometric parameters have re-

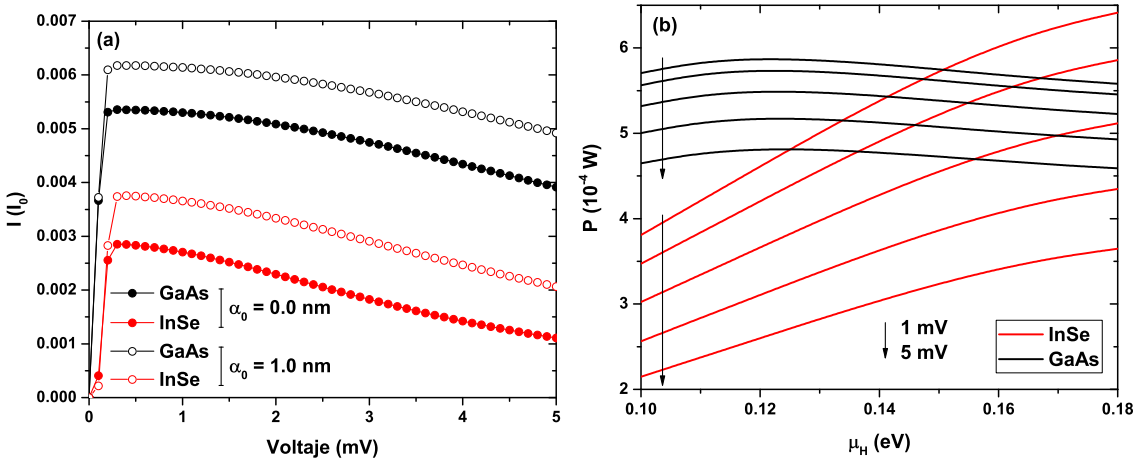

Figure 7-9.: In (a), the electronic tunneling current for the well-barrier lattice system as a function of the bias voltage, in units of $I_0 = 2\,e/h$, for zero ILF-parameter (full symbols) and $\alpha_0 = 1.0\,\text{nm}$ (open symbols). In (b), the power for five different bias voltages concerning the chemical potential of the hot reservoir. The width of the wells and the two central barriers has been set at 5 nm and the two lateral barriers at 2.5 nm (see Fig. **7-2**(c3)). Calculations are for GaAs-$Al_{0.3}Ga_{0.7}As$ and InSe-InP lattices.

mained unchanged. Both materials present an abrupt increase in the current between zero and 0.3 mV to later present a monotonous decreasing behavior, reaching up to 3.9 mI_0 for GaAs-$Al_{0.3}Ga_{0.7}As$ and up to 1.1 mI_0 for InSe-InP. These differences between the currents of both materials are due to the differences in the heights of the potential barriers generated by the different band offsets. The above generates changes in the area under the curve of the probability of electronic transmission, which can be evidenced comparing Figs. **7-7**(a) and **7-8**(a), where we see that the area under the curve is greater for the GaAs-$Al_{0.3}Ga_{0.7}As$ system and according to Landauer's theory, the tunneling current is proportional to such area. With the application of the ILF ($\alpha_0 = 1.0$ nm), as found in previous figures, there is a shift in the quasi-stationary states inside the wells, in the same way, there is a small increase in the area under the curve of electronic transmission for both materials. This fact implies that the tunneling current also shows an increase. For the system based on GaAs-$Al_{0.3}Ga_{0.7}As$, the maximum current peak is now 6.2 mI_0 at 0.3 mV and that of InSe-InP is 3.8 mI_0 at 0.4 mV. The behavior is similar to the system without ILF effects, presenting an abrupt increase for low voltages and a subsequent decrease. Lattices based on GaAs-$Al_{0.3}Ga_{0.7}As$ and InSe-InP reach the values of 4.9 mI_0 and 2.1 mI_0 respectively for 5 mV. This indicates that both by changing the materials and through the application of an external laser field, it is possible to modify the properties of electronic transport, such as the electric current in the wells and barriers system. Fig. **7-9**(b) shows the power for the GaAs-$Al_{0.3}Ga_{0.7}As$ system (black curves) and InSe-InP (red curves) for five different bias voltages concerning the chemical potential of the hot reservoir. The GaAs system shows close to flat power curves, having an increasing slope for low values of the chemical potential, going through a maximum, and the decreasing slowly. The Inse system show almost a lineal behavior starting from low chemical potential values and increasing to larger magnitudes. As the bias voltage is increased, the value of the power in each system decreases. On the other hand, for 1 mV, the power is maximum for the GaAs-$Al_{0.3}Ga_{0.7}As$ system only for $\mu_H < 0.15$ eV, since after this value the power is now maximum in the InSe-InP system. This indicates that for the chemical potential of the hot reservoir at 0.15 eV, both materials present the same power value of 5.8 (10^{-4} W) for a bias voltage of 1 mV, similarly, each crossing of the red curves with the black ones indicates

points in which the power is equivalent for both materials and at different bias voltages.

7.4. Conclusions

A finite superlattice system based on GaAs-$Al_{0.3}Ga_{0.7}As$ and InSe-InP has been studied, analyzing how the probabilities of electronic transmission change for both materials, as well as varying geometric parameters that allow changing the number of periods in the lattice and the well and barrier widths. By applying an external nonresonant intense laser field, it is possible to modify the lattice potential profile, which leads to a blue shift in quasi-stationary states. A four-barriers-three-well arrangement has been taken to analyze the electronic transport properties by means of Landauer's theory for both semiconductor materials, including the laser effects. It has been found that, for the same geometry, the tunneling current is higher for the GaAs-$Al_{0.3}Ga_{0.7}As$ based system than for the InSe-InP based system, in the same way, the point of maximum current is practically unchanged for both materials for the calculated bias voltages. By applying the external laser field, an increase in the tunneling current has been found for both materials but maintaining the same trend of the I-V curves. Finally, the power for the same arrangement has been calculated concerning the chemical potential, finding higher values for the system based on GaAs-$Al_{0.3}Ga_{0.7}As$ for small values of the chemical potential and for high values, the power is more significant in the InSe-InP system. It should be noted that for a set of points, the power for both systems takes the same value. Lastly, it should be noted that depending on the particular application, the power required or the measurable current required of this finite superlattice system, it could be built either based on GaAs-$Al_{0.3}Ga_{0.7}As$ or InSe-InP and improved electronic transport properties employing the application of an external nonresonant intense laser radiation.

References

[1] J. Ajayan, D. Nirmal, P. Mohankumar, D. Kuriyan, A. S. A. Fletcher, L. Arivazhagan, and B. S. Kumar, *GaAs metamorphic high electron mobility transistors for future deep space-biomedical-millitary and communication system applications: a review*, Microelectron. J **92**, 104604(pp18) (2019).

[2] F. Bajelan, A. Y. Goharrizi, R. Faez, and G. Darvish, *Performance improvement of junctionless field effect transistors using p-GaAs/AlGaAs heterostructure*, Superlattices Microstruct. **110**, 305-312 (2017).

[3] H. Dakhlaoui, and M. Nefzi, *Simultaneous effect of impurities, hydrostatic pressure, and applied potential on the optical absorptions in a GaAs field-effect transistor*, Results Phys. **15**, 102618(pp7) (2019).

[4] D. Gregušová, F. Gucmann, R. Kúdela, M. Mičušík, R. Stoklas, L. Valik, J. Greguš, M. Blaho, and P. Kordoš, *Properties of InGaAs/GaAs metal-oxide-semiconductor heterostructure field-effect transistors modified by surface treatment*, Appl. Surf. Sci **395**, 33587(pp21) (2016).

[5] M. G. Mayani, A. Pirhadi, and S. Asadi, *Numerical analysis of high frequency GaAs FET transistor using alternating direction implicit (ADI) finite-difference time-domain method; Distributed modeling approach*, Int. J. Electron. Commun. (AEÜ) **128**, 153514(pp8) (2021).

[6] S. Das, S. Kallatt, N. Abraham, and K. Majumdar, *Gate-tunable trion switch for excitonic device applications*, Phys. Rev. B **101**, 081413(pp7) (2020).

[7] S. Botti, J. A. Flores-Livas, M. Amsler, S. Goedecker, and M. A. L. Marques, *Low-energy silicon allotropes with strong absorption in the visible for photovoltaic applications*, Phys. Rev. B **86**, 121204(pp5) (2012).

[8] A. Segura, A. Chevy, J. P. Guesdon, and J. M. Besson, *Photovoltaic efficiency of InSe solar cells*, Sol. Energy Mater. **2**, 159-165 (1980).

[9] I. -H. Choi, *The preparation of a CuInSe2 solar cell by metal organic chemical vapor deposition*, Thin Solid Films **525**, 137-140 (2012).

[10] C. L. Clement, S. Arvamuthan, and K. S. V. Santhanam, *Stabilization of the polycarbazole protected n-InSe photoanode for photoelectrochemical solar cells*, J. Electroanal. Chem. **248**, 33-231 (1988).

[11] A. Kawaharazuka, K. Onomitsu, J. Nishinaga, and Y. Horikoshi, *Effect of excitons on the absorption in the solar-cell with AlGaAs/GaAs superlattice grown by molecular beam epitaxy*, J. Cryst. Growth **323**, 504-507 (2011).

[12] A. Kawaharazuka, J. Nishinaga, and Y. Horikoshi, *Recombination current in AlGaAs/GaAs superlattice solar-cells grown by molecular beam epitaxy*, J. Cryst. Growth **425**, 326-329 (2015).

[13] F. Petocchi, S. Beck, C. Ederer, and P. Werner, *Hund excitations and the efficiency of Mott solar cells*, Phys. Rev. B **100**, 075147(pp8) (2019).

[14] H. Sasabe, T. Wada, M. Hosoda, H. Ohkawa, M. Hara, A. Yamada, and A. F. Garito, *Photonics and organic nanostructures*, *Nonlinear Optical Properties of Organic Materials III*, 34th Annual International Technical Symposium on Optical and Optoelectronic Applied Science and Engineering, San Diego, CA, United States, Proceedings **1337** (1990).

[15] S. Sinha, D. K. Nandi, P. S. Pawar, S. -H. Kim, and J. H. Hund, *A review on atomic layer deposited buffer layers for Cu(In,Ga)Se2 (CIGS) thin film solar cells: Past, present, and future*, Sol Energy **209**, 515-537 (2020).

[16] Y. Tang, M. Liu, Y. Zhou, C. Ren, X. Zhong, and J. Wang, *First-principles predication of facet-dependent electronic and optical properties in InSe/GaAs heterostructure with potential in solar energy utilization*, J. Alloys Compd. **842**, 155901(pp22) (2020).

[17] M. Antonelli, M. Difraia, S. Carrato, G. Cautero, R. H. Menk, W. H. Jark, T. Ganbold, G. Biasiol, C. Callegari, M. Coreno, A. Desio, and E. Pace, *Fast*

synchrotron and FEL beam monitors based on single-crystal diamond detectors and InGaAs/InAlAs quantum well devices, Nucl. Instrum. Methods. Phys. Res. A **730**, 164-167 (2013).

[18] A. Asgari, E. Ahmadi, and M. Kalafi, *$Al_xGa_{1-x}N/GaN$ multi-quantum-well ultraviolet detector based on p-i-n heterostructures*, Microelectron. J **40**, 104-107 (2009).

[19] Z. Chu, Y. Zhou, J. Zhou, P. Chen, Z. Li, W. Lu, and X. Chen, *Quantum well infrared detectors enhanced by faceted plasmonic cavities*, Infrared Phys. Technol. **116**, 103746(pp7) (2021).

[20] M. Graf, E. Dupont, H. Luo, S. Haffouz, Z. R. Wasilewski, A. J. S. Thorpe, D. Ban, and H. C. Liu, *Terahertz quantum well infrared detectors*, Infrared Phys. Technol. **52**, 289-293 (2009).

[21] M. R. Kitchin, M. J. Shaw, E. Corbin, J. P. Hagon, and M. Jaros, *Optical properties of imperfect strained-layer $InAs/Ga_{1-x}In_xSb/AlSb$ superlattices with infrared applications*, Phys. Rev. B **61**, 8375-8381 (2000).

[22] Y. D. Sharma, Y. C. Jun, J. O. Kim, I. Brener, and S. Krishna, *Polarization-dependent photocurrent enhancement in metamaterial-coupled quantum dots-in-a-well infrared detectors*, Opt. Commun. **312**, 31-34 (2014).

[23] T. Srinivasan, P. Mishra, S. K. Jangir, R. Raman, D. V. S. Rao, D. S. Rawal, and R. Muralidharan, *Molecular Beam Epitaxy growth and characterization of silicon – Doped InAs dot in a well quantum dot infrared photo detector (DWELL-QDIP)*, Infrared Phys. Technol. **70**, 6-11 (2015).

[24] M. K. Bahar, K. A. Rodríguez-Magdaleno, J. C. Martínez-Orozco, M. E. Mora-Ramos, and F. Ungan, *Optical properties of a triple AlGaAs/GaAs quantum well purported for quantum cascade laser active region*, Mater. Today Commun. **26**, 101936(pp7) (2021).

[25] N. C. Clementi, C. D. Cooper, and L. A. Barba, *Computational nanoplasmonics in the quasistatic limit for biosensing applications*, Phys. Rev. E **100**, 063305(pp12) (2019).

[26] L. Schneebeli, T. Feldtmann, M. Kira, S. W. Koch, and N. Peyghambarian, *Zeno-logic applications of semiconductor quantum dots*, Phys. Rev. A **81**, 053852(pp6) (2010).

[27] H. D. Jahromi, and A. Zarifkar, *A physical model for quantum wire infrared photodetectors under illumination condition*, Opt. Commun. **493**, 127043(pp5) (2021).

[28] S. Khaledian, F. Nalaini, M. Mehrbakhsh, M. Abdoli, and S. S. Zahabi, *Applications of novel quantum dots derived from layered materials in cancer cell imaging*, FlatChem **27**, 100246(pp14) (2021).

[29] L. Esaki, and L. L. Chang, *New Transport Phenomenon in a Semiconductor "Superlattice"*, Phys. Rev. Lett. **33**, 495-498 (1974).

[30] R. Dingle, A. C. Gossard, and W. Wiegmann, *Direct Observation of Superlattice Formation in a Semiconductor Heterostructure*, Phys. Rev. Lett. **34**, 1327-1330 (1975).

[31] V. A. Fedirko, and M. D. Eremtchenko, *Scanning probe microscopy of GaAs/AlGaAs superlattices*, Mater. Sci. Eng. **44**, 110-112 (1997).

[32] T. Komatsu, E. Kawahata, T. Karasawa, I. Akai, V. F. Aguekian, M. Nakayama, K. Uchida, and N. Miura, *Dynamical process of excitons under magnetic fields in GaAs/AlGaAs superlattices*, J. Lumin. **66**, 468-472 (1995).

[33] Y. Jeong, H. Choi, Y. Park, S. Hwang, J. -J. Yoon, J. Lee, J. -Y. Leem, and M. Jeon, *Structural and optical properties of GaAs/AlGaAs superlattice layer on InAs quantum dots*, J. Cryst. Growth **273**, 129-135 (2004).

[34] M. G. Bezerra, J. A. K. Freire, V. N. Freire, G. A. Farias, F. M. S. Lima, A. L. A. Fonseca, and O. A. C. Nunes, *Interface effects in modulation-doped GaAs/AlGaAs single quantum wells and superlattices*, Microelectron. J **36**, 359-361 (2005).

[35] L. Smrcka, P. Vaseka, P. Svoboda, N. A. Goncharuk, O. Pacherova, Y. Krupko, Y. Sheikin, and W. Wegscheider, *Magnetoresistance oscillations in*

GaAs/AlGaAs superlattices subject to in-plane magnetic fields, Physica E **34**, 632-635 (2006).

[36] Y. A. Mityagin, V. N. Murzin, and M. P. Telenkov, *Resonant tunneling in weakly coupled GaAs/AlGaAs superlattices in a transverse magnetic field: A probe of electronic distribution function*, Physica E **32**, 297-300 (2006).

[37] R. Landauer, *Electrical Resistance of Disordered One-dimensional Lattices*, Philos. Mag. **21**, 863-867 (1970).

[38] D. C. Langreth and E. Abrahams, *Derivation of the Landauer conductance formula*, Phys. Rev. B **24**, 2978-2984 (1981).

[39] COMSOL *Multiphysics, v. 5.4*; COMSOL AB: Stockholm, Sweden, 2020.

[40] COMSOL *Multiphysics Reference Guide*; COMSOL: Stockholm, Sweden, 2012.

[41] COMSOL *Multiphysics Users Guide*; COMSOL: Stockholm, Sweden, 2012.

[42] COMSOL *Multiphysics v. 5.2a Semiconductor Module User's Guide;* COMSOL AB: Stockholm, Sweden, 2016.

[43] J. A. Gil-Corrales, J. A. Vinasco, A. Radu, R. L. Restrepo, A. L. Morales, M. E. Mora-Ramos, and C. A. Duque, *Self-Consistent Schrödinger-Poisson Study of Electronic Properties of GaAs Quantum Well Wires with Various Cross-Sectional Shapes*, Nanomaterials **11**, 1219(pp23) (2021).

[44] C. Heyn, A. Radu, J.A. Vinasco, D. Laroze, R.L. Restrepo, V. Tulupenko, N. N. Hieu, H. V. Phuc, M.E. Mora-Ramos, J.H. Ojeda, A. L. Morales, C. A. Duque, *Exciton states in conical quantum dots under applied electric and magnetic fields*, Opt Laser Technol **139**, 106953(pp13) (2021).

[45] E. Kasapoglu, H. Sari, I. Sokmen, J.A. Vinasco, D. Laroze, C.A. Duque, *Effects of intense laser field and position dependent effective mass in Razavy quantum wells and quantum dots*, Physica E Low Dimens. Syst. Nanostruct. **126**, 114461(pp12) (2021).

[46] H. Sari, E. Kasapoglu, S. Sakiroglu, I. Sökmen, and C. A. Duque, *Impurity-related optical response in a 2D and 3D quantum dot with Gaussian confinement under intense laser field*, Philosophical Magazine **100**, 619-641 (2020).

[47] M. Gavrila and J. Z. Kamiński, *Free-free transitions in intense high-frequency laser fields*, Phys. Rev. Lett. **52**, 613-616 (1984).

[48] M. Pont, N. R. Walet, M. Gavrila, and C. W. McCurdy, *Dichotomy of the hydrogen atomin superintense, high-frequency laser fields*, Phys. Rev. Lett. **61**, 939-942 (1988).

[49] A. F. da Silva, C. Persson, M. C. B. Marcussen, E. Veje, and A. G. de Oliveira, *Band-gap shift in heavily doped n-type $Al_{0.3}Ga_{0.7}As$ alloys*, Phys. Rev. B **60**, 2463-2467 (1999).

[50] T. E. Schlesinger, *Gallium Arsenide*, Encyclopedia of Materials: Science and Technology, 3431-3435 (2001).

[51] M. F. O'Dwyer, T. E. Humphrey, and H. Linke, *Concept study for a high-efficiency nanowire based thermoelectric*, Nanotechnology **17**, S338-S343 (2006).

8. General conclusions

In this thesis, the electronic states and the transport properties in quantum well, quantum wires and quantum dots have been theoretically investigated considering different materials as GaAs/AlGaAs, InSe/InTe, among others. The results are obtained by using the effective mass approach and numerical finite element method. In the systems addressed, the effect of variations in geometric parameters, the application of external electric and magnetic fields, intense non-resonant laser field, shallow donor impurity, changes in temperature and variations in donor density have been considered.

In the conical quantum dot core-shell based on GaAs-(Ga,Al)As and CdSe-CdTe, the effect of the presence of an axially located shallow-donor impurity was studied, as well as the application of an external magnetic field. The impurity position and the magnetic field direction preserve the axial symmetry of the system. Variations of the geometry have been considered, in which case the structures evolve from conical QDs to truncated conical QDs. The electron-hole correlation was studied with a first-order perturbation approximation.

In this particular work, some of the main results are: the presence of the shallow-donor impurity is responsible for a red/blue shift of the electron/hole energies. The binding energy for the electron-impurity system in general decreases with the size of the structure; but with exceptions for specific geometries. The applied magnetic field is responsible for the hole-impurity ground state oscillations. In the case of the correlation energy between the electron-impurity and hole-impurity states, it is observed that, in general, they decrease with the size of the structure.

For the GaAs quantum wire system, the electronic properties such as wave functions, state energies, potentials and electron densities have been calculated in a self-consistent way, taking into account variations in geometric parameters, such as cross-sectional area and non-geometric parameters, such as the donor

density and the temperature.
In this work it has been shown that the increase in cross-section and/or donor density in all structures generates a lesser degree of confinement by the self-consistent potential and, therefore, a decrease in electronic energies. The opposite case occurs when the temperature is increased, for which there is an increase in the self-consistent potential profile, thus impacting on the increase of energy eigenvalues for all systems. At low temperatures, all structures present irregularities in the electron density profile. These Friedel-like oscillations are due to the degree of occupation of internal and surface states (that arise from having the surface of the quantum wire exposed) by conduction electrons.
Another studied system is a double barrier resonant tunneling diode system based on GaAs and InGaAs in which, the wave functions, quasi-stationary states and self-consistent potentials, among other electronic properties have been calculated. The probabilities of electronic transmission have been calculated considering variations in geometric parameters such as the width of the central well and non-geometric parameters such as the density of donors in the layers outside the barrier region. Additionally, the system has been converged out of equilibrium to analyze the response of the internal quasi-stationary states to an external potential difference applied to the contacts, obtaining a red shift in all transmission peaks regardless of the donor density used. The Landauer formalism was used to calculate the density of electric current that circulates through the diode for different well widths and different donor densities. An important conclusion is that the first current peak is obtained for lower voltages in the case of narrower width of the central well. For the cases studied, it is possible to show negative differential resistance.
The theoretical procedure for this double barrier system, has been applied to an InGaAs/AlAs experimental system reported in recent literature, the current density at room temperature for this system has been compared, obtaining satisfactory results for the calculation of the position of the first resonance in the system and the magnitude of the current density at this point.
In a following work, we have investigated the features of total optical absorption coefficient of confined electrons in a delta-like doped Razavy-like quantum well under the combined effects of externally applied electric and magnetic field.
In the absorption peaks, a clear blue shift is evidenced for all the transitions

studied, keeping the donor density fixed, the shift being more significant for changes in the electric field than in the magnetic field, in all cases a change in the magnitude of the optical absorption peaks is presented. With the increase in donor density, red and blue shifts of the absorption peaks were also reported, as well as a decrease in their magnitude depending on the transition studied. This allows us to tune the system without modifying geometric parameters directly, only applying external fields or increasing the density of donors to obtain the maximum absorption of the material in the positions that are required for a certain application.

On the other hand, the delta-doping effect on electron states has been analyzed in quantum wire systems with exposed borders and circular cross-section subjected to an internal Razavy-like potential at low temperatures. Effects of varying geometric parameters such as the width of delta-doped layer, and not geometric as the density of donors in the system have been studied. The appearance of irregularities in the electron density profile has been reported for certain specific values of the geometric parameters, these oscillations have been explained by means of the occupation of the electronic states of the system.

In the last developed work, a finite superlattice system based on GaAs-$Al_{0.3}Ga_{0.7}As$ and InSe-InP has been studied, analyzing the change of the electronic transmission for both materials, as well as varying geometric parameters that allow changing the number of periods in the lattice and the well and barrier widths. By applying an external nonresonant intense laser field, it is possible to modify the lattice potential profile, which leads to a blue shift in quasi-stationary states.

By using the Landauer formalism, it has been found that, for the same geometry, the tunneling current is higher for the GaAs-$Al_{0.3}Ga_{0.7}As$ based system than for the InSe-InP based system, in the same way, the point of maximum current is practically unchanged for both materials for the calculated bias voltages.

Each of these works can serve as a model to explain the behavior of charge carriers in devices based on low-dimensional systems and under the effect of external fields.

A. COMSOL Example: Self-consistent quantum wire with internal doping

The following is a guide for the implementation of the problem of a quantum wire of circular cross section with internal doping in the COMSOL Multiphysics software to solve the equations by means of the finite element method in a self-consistent way.

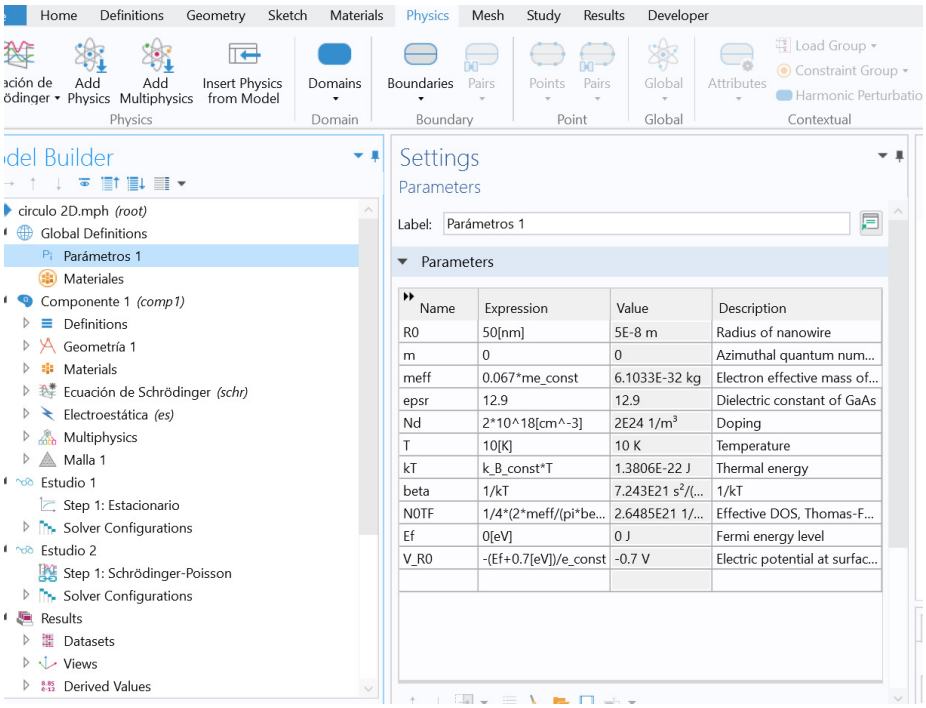

Figure A-1.: Add the corresponding parameters in the system.

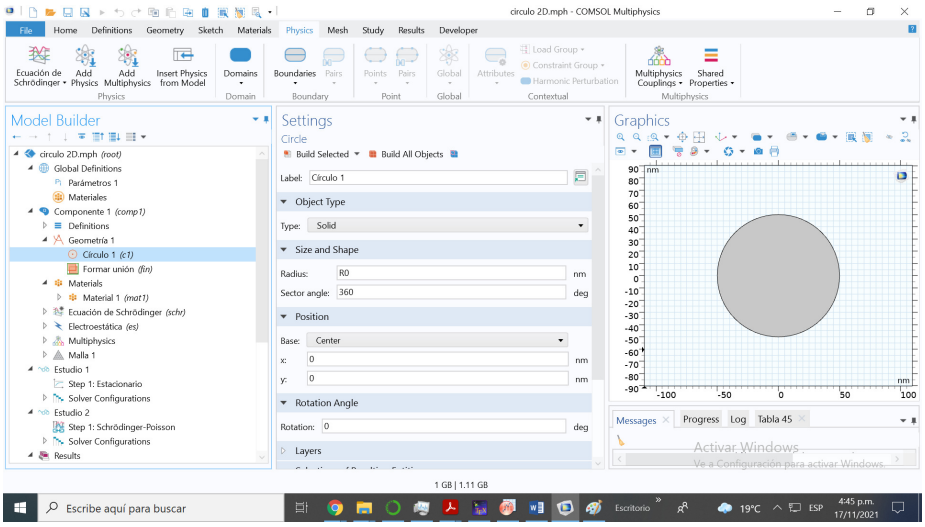

Figure A-2.: In geometry, construct a circumference that will be the cross section of the wire.

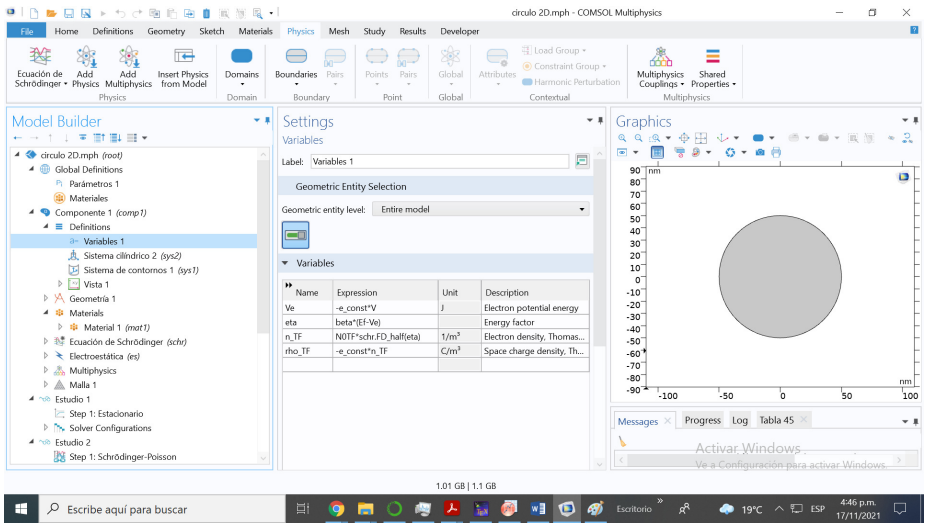

Figure A-3.: In variables, the electronic potential, the charge density, among other functions are defined.

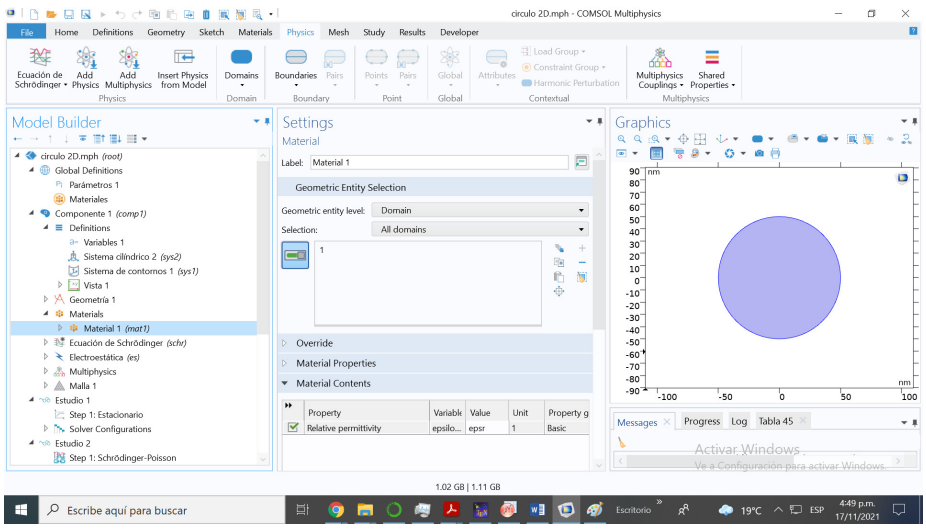

Figure A-4.: In materials, for this case only the relative permittivity is defined.

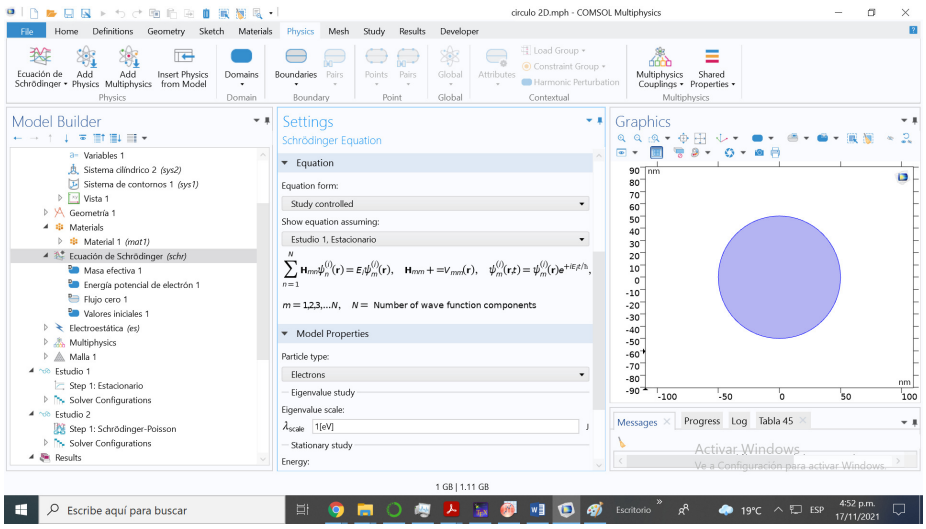

Figure A-5.: In physics, Schrödinger's equation must be added.

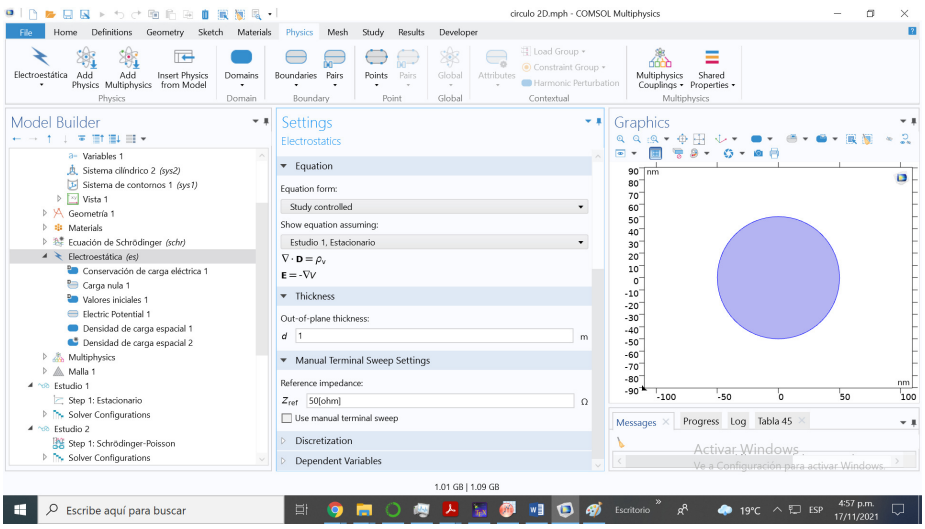

Figure A-6.: In physics, the Poisson equation must be added for electrostatic interaction.

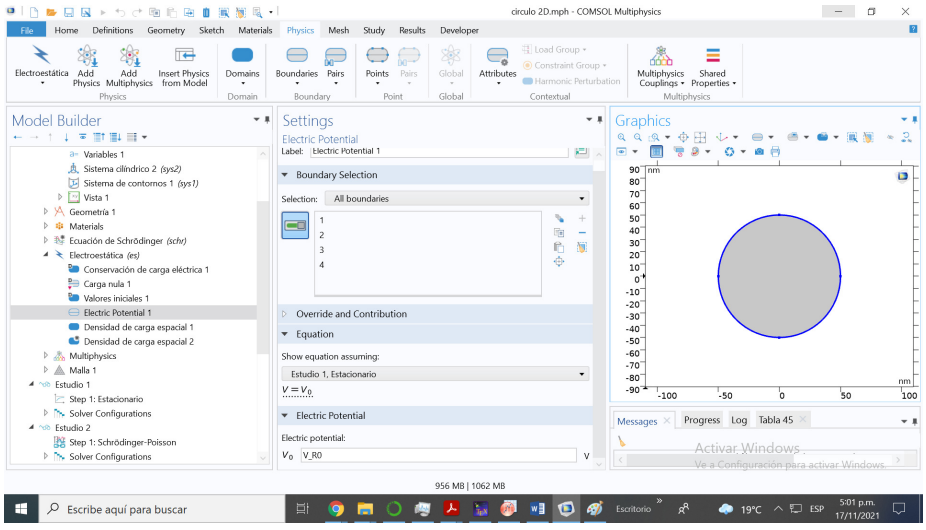

Figure A-7.: The next step is to add the boundary conditions.

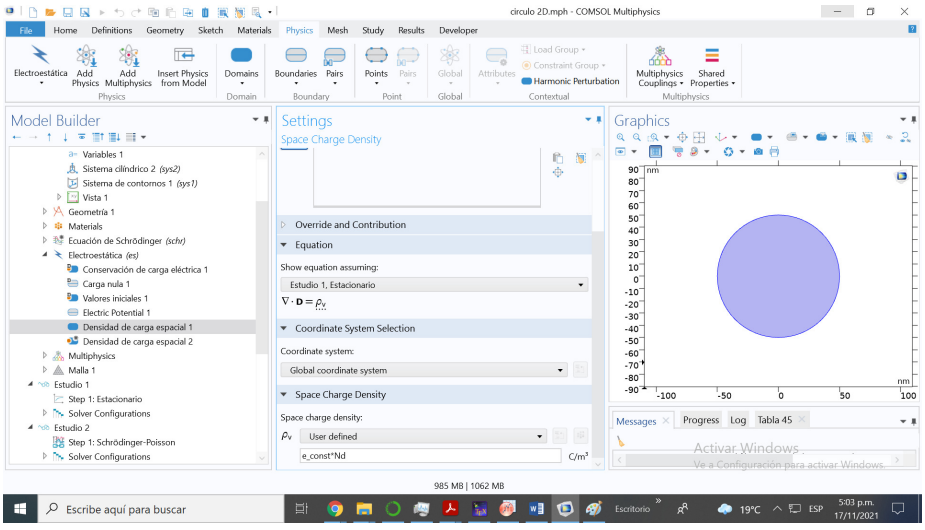

Figure A-8.: Including internal donor density.

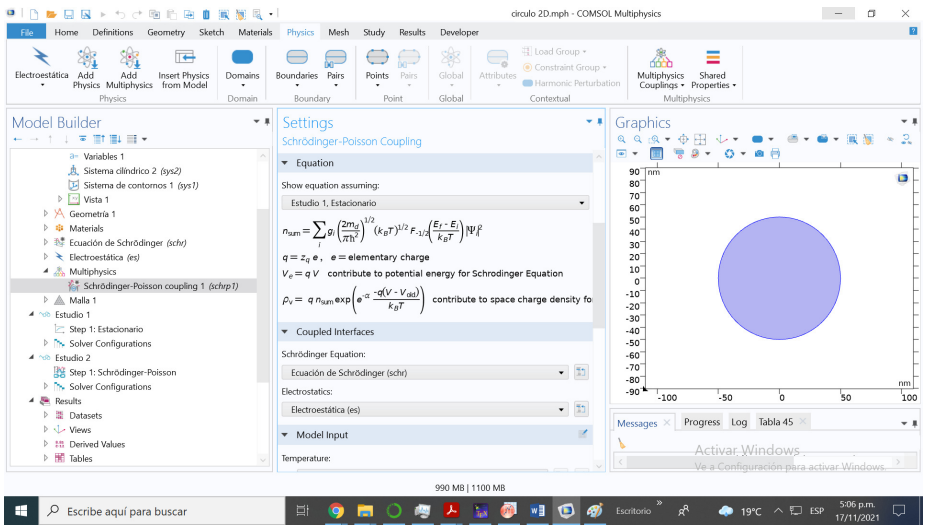

Figure A-9.: In physics, add Multiphysics to solve the Schrödinger and Poisson equations in coupled form.

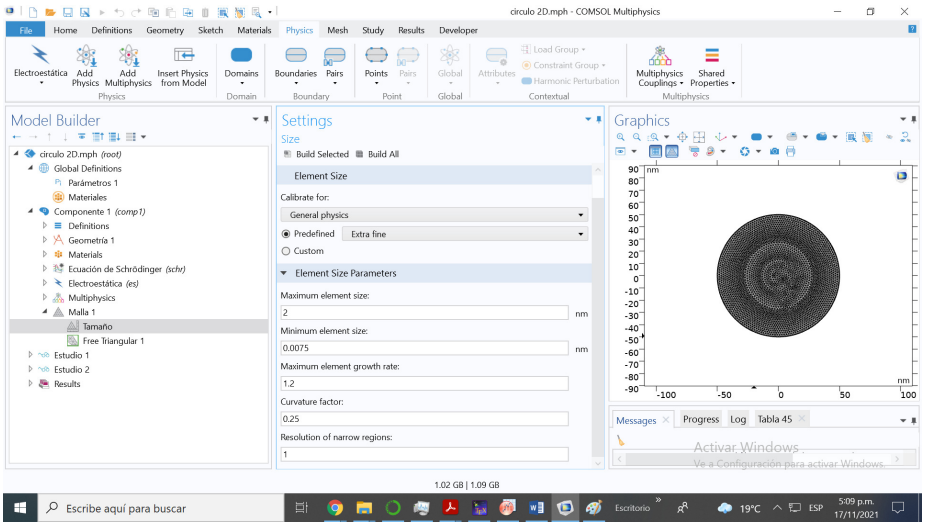

Figure A-10.: Defining the mesh for the finite elements calculation.

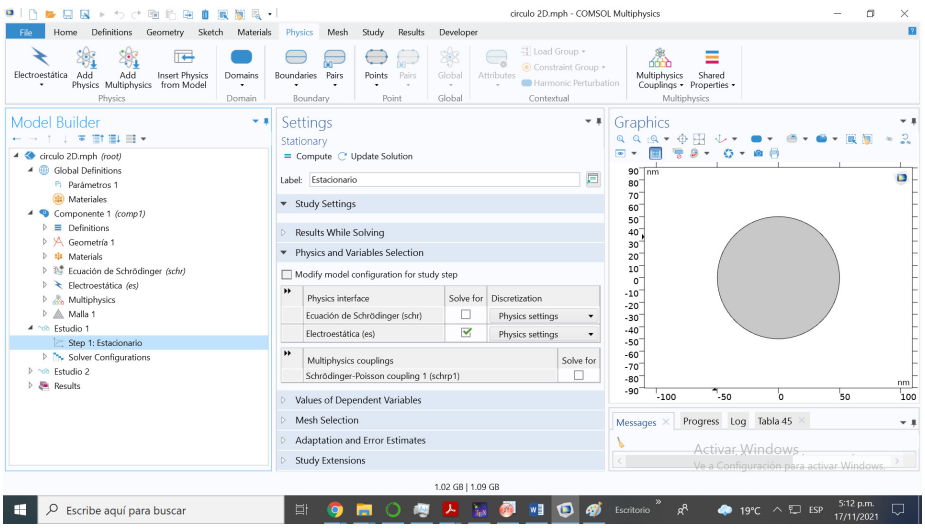

Figure A-11.: In study, select stationary and calculate only the Poisson equation for the initial step in Thomas Fermi approximation.

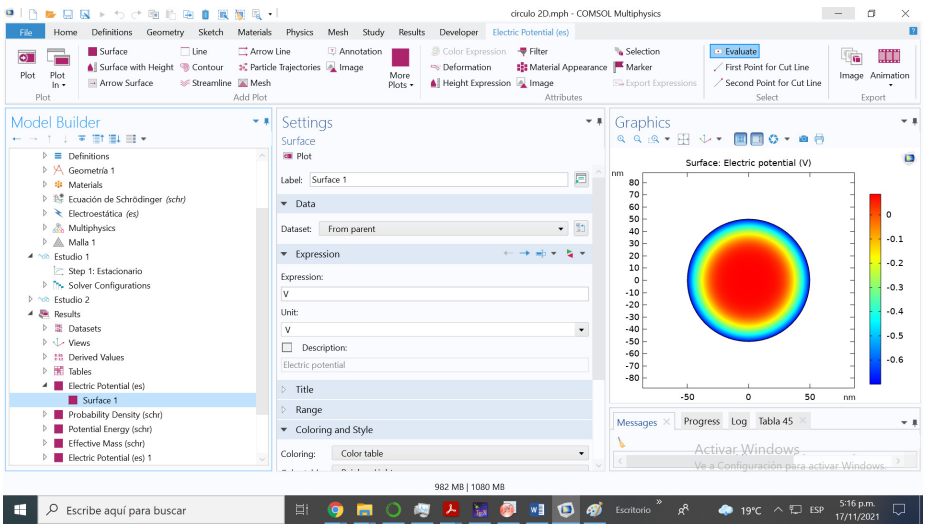

Figure A-12.: In results, it is possible to visualize the initial electrostatic potential.

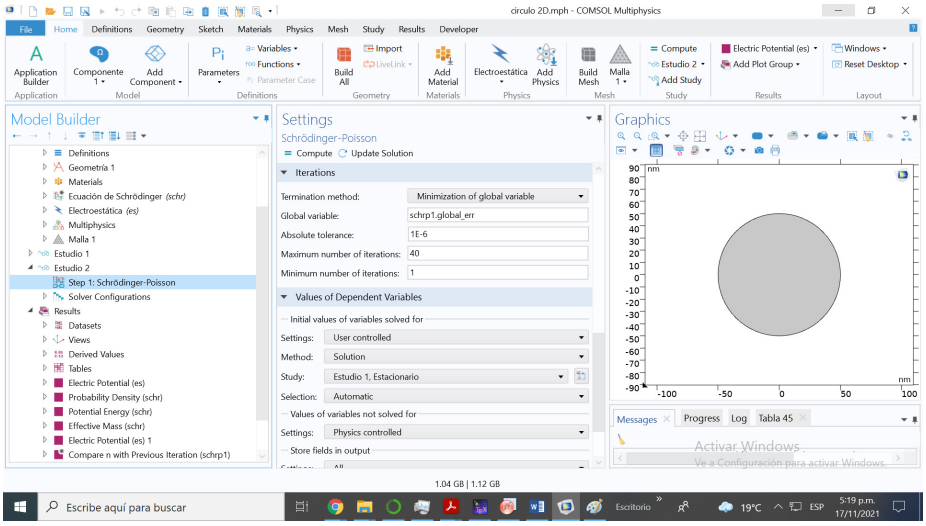

Figure A-13.: In a new study, select Schrödinger-Poisson to solve for self-consistency and consider the potential calculated in the previous step as the starting point for the method. This step also defines the total number of iterations and the tolerance.

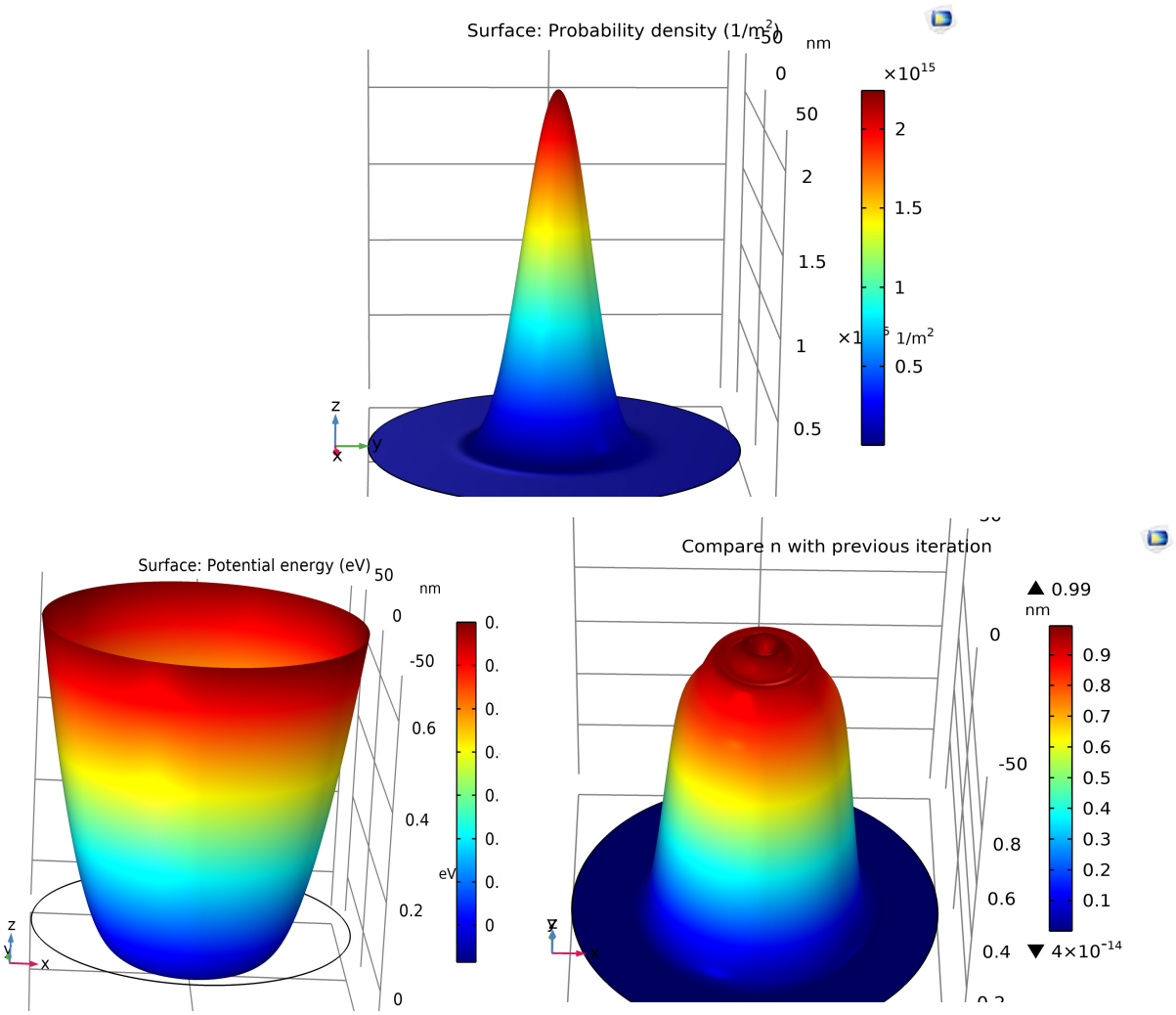

Figure A-14.: Finally, in results, the probability density, the total electron potential and the self-consistent electron density are obtained.

B. Fortran code for a self-consistent doped quantum well

This section includes the code for the self-consistent calculation of the GaAs quantum well with $Al_{0.3}Ga_{0.7}As$ barriers corresponding to the theory presented in section 2.3 of the General theoretical framework. If this code or the previous one developed in COMSOL are required, you can request it at jalexander.gil@udea.edu.co.

```
C       Grupo de Materia Condensada - UdeA
C       Medellin - Colombia - 2021
C*********************************************************************
C       Routines References
C  (C)  Copr. 1986-92 Numerical Recipes Software #0).
C       cleve moler, university of new mexico, argonne national lab.

C*********************************************************************
C                  Dimensional parameters
C*********************************************************************
implicit double precision (a-h,o-z)
parameter(np=70)
parameter(nd=5000)
C*********************************************************************
C             Definition of vectors and
C             the matrices that will be used in the code
```

```
C*********************************************************************
dimension zz(nd+1),roo(nd+1),v(nd+1),voff(nd+1),v_salida(nd+1)
dimension de(np),ve(np,np),punt(nd+1)
dimension AAA(nd+1,200),BBB(nd+1,200)
dimension vxc(nd+1)
C*********************************************************************
C                  Common parameters for the entire code
C*********************************************************************
character*16 filename1,filename2
common/coeficientes/ve
common/energias/de
common/parameters/xL,ee,hbar,xme,Pi,ef
common/x_infinito/x_infinito
common/v_salida/v_salida
common/AAA/AAA
common/iter/iter
DATA PI/3.141592653589793D0/
C*********************************************************************
C                Defining file for writing eigenvalues
C*********************************************************************
open(4,FILE='energias.dat',STATUS='UNKNOWN')
C*********************************************************************
C                Defining parameters for the code
C*********************************************************************
xnd      = 1.0d24      ! Donor density in [1 / m ^ 3]
xna      = 5.0d20      ! Acceptor density in [1 / m ^ 3]
xL0      = 50.0d-10    ! Well length in [m]
step_xL  = 10.0d-10    ! Step size for xL0 in [m]
itermax  = 40          ! Maximum number of iterations
n_pozos  = 1           ! Total number of wells calculated
C*********************************************************************
C                    Varying the width to be solved
C*********************************************************************
do 11000 itt=1,n_pozos
```

```
xL  = xL0 + dfloat(itt-1)*step_xL
ds  = 100.0d-10
C*****************************************************************
C                Defining the boundaries of the system (the Bulk)
C                and some constants
C*****************************************************************
x_infinito = 1000.0d-10   ! Infinite for the system [m]
x1 = -x_infinito/2.0d0    ! Left border (-Bulk) [m]
x6 = +x_infinito/2.0d0    ! Right border (+ Bulk) [m]
ee    = 1.6d-19           ! Electronic charge [C]
hbar  = 1.05d-34          ! Reduced Plank constant [J * s]
xme   = 0.067*9.1d-31     ! GaAs reduced mass [kg]
const = xme/(Pi*hbar**2)
eps0  = 8.8542d-12        ! permittivity of vacuum [C^2/N/m^2]
eprs  = 12.244d0          ! relative permittivity
C*****************************************************************
C                 Starting the arrays with 0
C*****************************************************************
do 500 ip1=1,200
do 501 ip2=1,nd+1
AAA(ip2,ip1)=0.0d0
BBB(ip2,ip1)=0.0d0
501 continue
500 continue
C*****************************************************************
C         Point lattice construction and initial entry potential
C*****************************************************************
ancho_infinito =  x_infinito/1.0d-10
xme_1  = 0.067d0                        ! Effective electrons mass
a0=eprs*0.529177d0/xme_1                ! Effective Bohr radius
ry=13.6058d0*xme_1/(eprs**2)*1000.0d0   ! Effective Rydberg

X1a = (-x_infinito/2.0d0)
X6a = (+x_infinito/2.0d0)
```

```
do 7001 i=0,nd
punt(i+1)=x1a+(x6a-x1a)/dfloat(nd)*dfloat(i)
7001 continue
do 507 nq=1,nd+1
call f_boffset(nd+1,punt,voff)
507 continue
C*****************************************************************
C           Starting the Self-Consistent process
C*****************************************************************
dLx = xL/(1.0d-10)/2.0d0
do 10000 iter=1,itermax
C     ***************************************************************
do 503 nq=1,nd+1
if(iter.eq.1)then
AAA(nq,iter)=voff(nq)/ee*1.0d3/ry
else
AAA(nq,iter)=0.95d0*AAA(nq,iter-1)+0.05d0*BBB(nq,iter-1)
endif
503 continue
do 7041 i=0,nd/2
AAA(nd-i+2,iter)=AAA(i,iter)
7041 continue
C*****************************************************************
C           Calculating Autofunctions and Eigenvalues
C*****************************************************************
call diagonalizacion(dLx)
C     When running diagonalization, wave functions (expansion coefficien
C     and eigenvalues ??are obtained. And those results come out in effe
C     That is, the energies in effective rydbergs and the wave functions
C     root of effective Bohr radius

C*****************************************************************
C     Screen writing of eigenvalues and number of iterations
C*****************************************************************
```

```
write(*,*)itt,iter,de(np-0)*ry,de(np-1)*ry,de(np-2)*ry
C*********************************************************************
C     Integrating the electron density to obtain the N_s
C*********************************************************************
C     Calculation of N_s which is used to obtain Dd
paso  = (x6-x1)/dfloat(nd)
suma=0.0d0
z = x1
200  continue
suma=suma+xnx(z,0,np)
z=z+paso
if(z.le.x6)go to 200
xns = suma*paso
C*********************************************************************
C     With the calculated N_s, the Dd is obtained, which is proportional to
C     the depletion region
C*********************************************************************
dd = (xns+ 2.0d0*(xL/2.0d0 + ds)*xna)/(2.0d0*(xnd - xna))
C*********************************************************************
C     Defining each of the regions to solve
C*********************************************************************
x2 = -(xL/2.0d0 + dd + ds)
x3 = -(xL/2.0d0 + ds)
x4 = +(xL/2.0d0 + ds)
x5 = +(xL/2.0d0 + dd + ds)
C*********************************************************************
C                 charge density calculation
C*********************************************************************
do 1001 ij=0,nd
zz(ij+1) = x1+(x6-x1)/dfloat(nd)*dfloat(ij)
roo(ij)=ro(x1,x2,x3,x4,x5,x6,xnd,xna,0,np,zz(ij+1))*ee/(eps0*eprs)
z=z+(x6-x1)/dfloat(nd)
1001 continue
C*********************************************************************
```

```
C     Calculating the exit potential including exchange-correlation
C*********************************************************************
call v0(nd,zz,roo,v,voff,vxc)
do 504 nq=1,nd+1
BBB(nq,iter)=v(nq)/ee*1.0d3/ry+voff(nq)/ee*1.0d3/ry
%                                +vxc(nq)/ee*1.0d3/ry
504 continue
10000 continue
C*********************************************************************
C     Writing energies and Dd after self-consistency
C*********************************************************************
write(4,*)xL,(de(np-i)*ry,i=0,10),dd
C*********************************************************************
C      Writing wave functions after self-consistency
C*********************************************************************
z=x1
201  continue
zp=z/(1.0d-10)/a0
call FONDAL(ve,np,zp,np-0,f0)
call FONDAL(ve,np,zp,np-1,f1)
call FONDAL(ve,np,zp,np-2,f2)
call FONDAL(ve,np,zp,np-3,f3)
call FONDAL(ve,np,zp,np-4,f4)
call FONDAL(ve,np,zp,np-5,f5)
C     In the next step the wave functions are output in 1 / meter root
C      and are written in external files called f_ondas ##. dat
write (filename1,11)itt
11  format('f_ondas',i3,'.dat')
open(50,file=filename1,status='unknown')
write(50,*)zp
% ,50.0d0*(f0)+de(np-0)*ry
% ,50.0d0*(f1)+de(np-1)*ry
% ,50.0d0*(f2)+de(np-2)*ry
% ,50.0d0*(f3)+de(np-3)*ry
```

```
% ,50.0d0*(f4)+de(np-4)*ry
% ,50.0d0*(f5)+de(np-5)*ry
C     In the same files the electron densities are written
C     Adding were below the Fermi level
% ,xnx(z,0,0),xnx(z,1,1),xnx(z,2,2),xnx(z,0,2)

z=z+xL/dfloat(nd)
if(z.le.x6)go to 201
C*********************************************************************
C     Writing the potential after self-consistency
C*********************************************************************
write (filename2,12)itt
12  format('potencial',i3,'.dat')
open(51,file=filename2,status='unknown')
do 505 nq=1,nd+1
write(51,*)punt(nq)/1.0d-10/a0,punt(nq)/1.0d-10,AAA(nq,itermax)*ry
505 continue
C     *****************************************************************
11000 continue
write(*,*)'Press any key and Enter to finish'
read(*,*)aaaaa
stop
end
C*********************************************************************
C*********************************************************************
C                         End of main program
C*********************************************************************
C*********************************************************************

C*********************************************************************
C                          Building charge density
C*********************************************************************
function ro(x1,x2,x3,x4,x5,x6,xnd,xna,ni,nf,z)
implicit double precision (a-h,o-z)
```

```
common/parameters/xL,ee,hbar,xme,Pi,ef

f1= -ee*xnx(z,ni,nf)
f2= +ee*(xnd - xna - xnx(z,ni,nf))
f3= -ee*(xna + xnx(z,ni,nf))

if(z.ge.x1.and.z.le.x2)ro=f1
if(z.gt.x2.and.z.le.x3)ro=f2
if(z.gt.x3.and.z.le.x4)ro=f3
if(z.gt.x4.and.z.le.x5)ro=f2
if(z.gt.x5.and.z.le.x6)ro=f1

return
end
C*********************************************************************
C                        Constructing the electron density
C*********************************************************************
function xnx(z,ni,nf)
implicit double precision (a-h,o-z)
parameter(np=70)
dimension de(np),ve(np,np)
common/parameters/xL,ee,hbar,xme,Pi,ef
common/coeficientes/ve
common/energias/de
common/units/ry,a0

zp=z/(1.0d-10)/a0
const = xme/(Pi*hbar**2)

suma = 0.0d0
do 1 i=ni,nf
call FONDAL(ve,np,zp,np-i,fi)
en = de(np-i)*ry/(1.0d3)*1.6d-19
if(en.ge.0.0d0)go to 1
```

```
f  = fi/dsqrt(a0*1.0d-10)
suma = suma - en*f**2
1    continue
xnx = const*suma

return
end
C*********************************************************************
C                        Calculating the Hartree Potential
C*********************************************************************
Subroutine v0(nd,x,f,v,voff,vxc)
implicit double precision (a-h,o-z)
dimension x(nd+1),f(nd+1),v(nd+1),voff(nd+1),vxc(nd+1)

a = x(1)
b = x(nd+1)

alfa = 0.0d0
beta = 0.0d0

call double_integral(nd+1,a,b,alfa,beta,x,f,v)
call f_boffset(nd+1,x,voff)
call f_vxc(nd+1,x,vxc)

return
end
C*********************************************************************
C            Double integral to solve the Poisson equation
C*********************************************************************
subroutine double_integral(nd,a,b,alfa,beta,x,f,v)
implicit double precision (a-h,o-z)
dimension x(nd),f(nd),g(nd),h(nd),w1(nd),w2(nd),v(nd)

dx = (b-a)/dfloat(nd-1)
```

```
do 3 i=1,nd
suma = 0.0d0
do 2 j=1,i
suma=suma+f(j)
2   continue
g(i) = suma*dx
3   continue

do 4 i=1,nd
suma = 0.0d0
do 5 j=1,i
suma=suma+g(j)
5   continue
h(i) = suma*dx
4   continue

do 6 i=1,nd
w1(i) = alfa + h(i)
w2(i) = x(i) - a
6   continue

do 7 i=1,nd
v(i) = w1(i) + (beta-w1(nd))/w2(nd)*w2(i)
7   continue

return
end
C*********************************************************************
C                    Building Band-Offset Potential
C*********************************************************************
subroutine f_boffset(nd,x,voff)
implicit double precision (a-h,o-z)
dimension x(nd),voff(nd)
```

```
common/parameters/xL,ee,hbar,xme,Pi,ef

v1 = +0.096d0*ee
v2 = -0.204d0*ee

do 1 i=1,nd
z=x(i)
if(dabs(z).le.xL/2.0d0)then
voff(i)=v2
else
voff(i)=v1
endif
1    continue

return
end
C*********************************************************************
C             Building the exchange potential - Correlation
C*********************************************************************
subroutine f_vxc(nd,x,vxc)
implicit double precision (a-h,o-z)
parameter(np=70)
dimension x(nd),vxc(nd)
common/parameters/xL,ee,hbar,xme,Pi,ef

eps0  = 8.8542d-12
eprs  = 12.244d0

do 1 i=1,nd
z=x(i)
vxc(i)=-0.0783d0*ee**2/(eps0*eprs)*(xnx(z,0,np))**(1.0d0/3.0d0)
1    continue

return
```

```
end

C*********************************************************************
C           Routines for calculating eigenvalues ??and eigenfunctions
C*********************************************************************
Subroutine diagonalizacion(dLx)

implicit double precision (a-h,o-z)
parameter(np=70)
parameter(nd=5000)

dimension de(np),ve(np,np)
dimension puntos(nd+1)
common/longitudes/X1,X6
common/VALORES/PI
common/length/dd, ds, dL
common/XLENGTH/XLENGTH
common/coeficientes/ve
common/energias/de
common/units/ry,a0
common/puntos/puntos
common/x_infinito/x_infinito

DATA PI/3.141592653589793D0/

ancho_infinito =  x_infinito/1.0d-10
xme  = 0.067d0
eprs  = 12.244d0
a0=eprs*0.529177d0/xme
ry=13.6058d0*xme/(eprs**2)*1000.0d0
dL = dLx/a0

X1 = (-ancho_infinito/2.0d0)/a0
X6 = (+ancho_infinito/2.0d0)/a0
```

```
do 7000 i=0,nd
puntos(i+1)=x1+(x6-x1)/dfloat(nd)*dfloat(i)
7000 continue

XLENGTH = ancho_infinito/a0
C     fe0 calculates the self-energies of the well
e0 = fe0(x)
return
END
C     ****************************************************************
C                      Writing the potential as a matrix
C     ****************************************************************
REAL*8 FUNCTION potencial(j,x)
IMPLICIT double precision (A-H,O-Z)

parameter(nd=5000)

dimension v_salida(nd+1),AAA(nd+1,200)

common/units/ry,a0
common/length/dd, ds, dL
common/parameters/xL,ee,hbar,xme,Pi,ef
common/v_salida/v_salida
common/iter/iter
common/contadores/xmm,xnn
common/AAA/AAA

potencial =  AAA(j,iter)

RETURN
END
C     ****************************************************************
C                      Calculate the wave functions
```

```
C     ****************************************************************
SUBROUTINE FONDAL(v,np,z,nestado,summa)
implicit double precision(a-h,o-z)
dimension v(np,np)

COMMON/VALORES/PI
common/XLENGTH/XLENGTH

summa=0.0d0
do 2000 m=1,np
im =  dfloat(m)
fun = dsqrt(2.0d0/XLENGTH)*dsin(im*PI*z/XLENGTH+im*PI/2.0d0)
summa = summa+v(m,nestado)*fun
2000  continue
RETURN
END
C     ****************************************************************
C                      Calculation of eigenvalues
C     ****************************************************************
function fe0(x)
implicit double precision (a-h,o-z)
parameter(np=70)
dimension de(np),ve(np,np)

common/coeficientes/ve
common/energias/de
CALL ESTADO(de,ve)
fe0 = de(np)
return
end
C     ************************************************
C     ************************************************
SUBROUTINE ESTADO(d,v)
implicit double precision(a-h,o-z)
```

```
parameter(np=70)

DATA ITMAX,EPS1,EPS2,EPS3/50,1.E-10,1.E-10,1.E-5/
dimension a(np,np),d(np),v(np,np)
DIMENSION XHH(np,np),XPP(np,np),XWW(np,np),fv1(np),fv2(np)
C     XHH: FULL HAMILTONIAN
C     XPP: KINETIC ENERGY
C     XWW: POTENTIAL WELL
COMMON/VALORES/PI
common/XLENGTH/XLENGTH

C     MAKE ALL THE ENTRIES OF THE MATRICES EQUAL TO ZERO

DO 1 im=1,np
DO 2 in=1,np
XHH(im,in)=0.0D0
XPP(im,in)=0.0D0
XWW(im,in)=0.0D0
v(im,in)=0.0d0
2   CONTINUE
fv1(im)=0.0d0
fv2(im)=0.0d0
d(im)=0.0d0
1 CONTINUE

C     CONSTRUCTION OF THE ELEMENTS OF KINETIC ENERGY
CONST1 = (PI/XLENGTH)**2
DO 3 im=1,np
DO 4 in=1,np
xm = dfloat(im)
xn = dfloat(in)
IF(in.eq.im)XPP(im,in)=CONST1*xn**2
IF(in.ne.im)XPP(im,in)=0.0D0
4 CONTINUE
```

```
3 CONTINUE

DO 7 im=1,np
DO 8 in=1,np
xm = dfloat(im)
xn = dfloat(in)
CALL fein(xm,xn,XLENGTH,vpoz)
XWW(im,in) = vpoz
8 CONTINUE
7 CONTINUE

C     CONSTRUCTION OF THE TOTAL HAMILTONIAN

DO 100 im=1,np
DO 200 in=1,np
XHH(im,in)=XPP(im,in)+XWW(im,in)
200 CONTINUE
100 CONTINUE

C     This routine calculates eigenvalues and eigenvectors of a
C     symmetric square matrix. The eigenvectors are normalized to unity.
call rs(np,np,xhh,d,1,v,fv1,fv2,ierr)
C     This routine orders the eigenvalues ??given by jacobi in decreasing
C     order.In that same order, then it returns the corresponding eigenve
call eigsrt(d,v,np,np)
return
end
C     ************************************************
C     ************************************************
SUBROUTINE fein(xm,xn,XLENGTH,vpoz)
implicit double precision (a-h,o-z)
parameter(nd=5000)
```

```
common/contadores/xmm,xnn
common/longitudes/X1,X6
common/VALORES/PI
common/puntos/puntos

DIMENSION  A11(1), B11(1)
dimension puntos(nd+1)

xmm = xm
xnn = xn

z=puntos(1)
fn = dsqrt(2.0d0/XLENGTH)*dsin(xnn*PI*z/XLENGTH+xnn*PI/2.0d0)
fm = dsqrt(2.0d0/XLENGTH)*dsin(xmm*PI*z/XLENGTH+xmm*PI/2.0d0)
V_i = fn*fm*potencial(1,z)

z=puntos(nd+1)
fn = dsqrt(2.0d0/XLENGTH)*dsin(xnn*PI*z/XLENGTH+xnn*PI/2.0d0)
fm = dsqrt(2.0d0/XLENGTH)*dsin(xmm*PI*z/XLENGTH+xmm*PI/2.0d0)
V_f = fn*fm*potencial(nd+1,z)

suma_i = 0.0d0
do 100 i=2,nd,2
z=puntos(i)
fn = dsqrt(2.0d0/XLENGTH)*dsin(xnn*PI*z/XLENGTH+xnn*PI/2.0d0)
fm = dsqrt(2.0d0/XLENGTH)*dsin(xmm*PI*z/XLENGTH+xmm*PI/2.0d0)
suma_i = suma_i+fn*fm*potencial(i,z)
100  continue

suma_p = 0.0d0
do 101 i=3,nd-1,2
z=puntos(i)
fn = dsqrt(2.0d0/XLENGTH)*dsin(xnn*PI*z/XLENGTH+xnn*PI/2.0d0)
fm = dsqrt(2.0d0/XLENGTH)*dsin(xmm*PI*z/XLENGTH+xmm*PI/2.0d0)
```

```
suma_p = suma_p+fn*fm*potencial(i,z)
101  continue

vpoz=(x6-x1)/dfloat(nd)/3.0d0
%      *(V_i + V_f + 2.0d0*suma_p + 4.0d0*suma_i)

return
end
C     ************************************************
C     ************************************************
C     ************************************************
SUBROUTINE jacobi(a,n,np,d,v,nrot)
IMPLICIT double precision(a-h,o-z)

PARAMETER (NMAX=500)

DIMENSION a(np,np),d(np),v(np,np)
DIMENSION b(NMAX),z(NMAX)


do 12 ip=1,n
do 11 iq=1,n
v(ip,iq)=0.0d0
11      continue
v(ip,ip)=1.0d0
12    continue
do 13 ip=1,n
b(ip)=a(ip,ip)
d(ip)=b(ip)
z(ip)=0.0d0
13    continue
nrot=0
do 24 i=1,50
sm=0.0d0
```

```
do 15 ip=1,n-1
do 14 iq=ip+1,n
sm=sm+dabs(a(ip,iq))
14        continue
15      continue
if(sm.eq.0.0d0)return
if(i.lt.4)then
tresh=0.2d0*sm/n**2
else
tresh=0.0d0
endif
do 22 ip=1,n-1
do 21 iq=ip+1,n
g=100.0d0*dabs(a(ip,iq))
if((i.gt.4).and.(dabs(d(ip))+
*g.eq.dabs(d(ip))).and.(dabs(d(iq))+g.eq.dabs(d(iq))))then
a(ip,iq)=0.0d0
else if(dabs(a(ip,iq)).gt.tresh)then
h=d(iq)-d(ip)
if(dabs(h)+g.eq.dabs(h))then
t=a(ip,iq)/h
else
theta=0.5d0*h/a(ip,iq)
t=1.0d0/(dabs(theta)+dsqrt(1.0d0+theta**2))
if(theta.lt.0.0d0)t=-t
endif
c=1.0d0/dsqrt(1+t**2)
s=t*c
tau=s/(1.0d0+c)
h=t*a(ip,iq)
z(ip)=z(ip)-h
z(iq)=z(iq)+h
d(ip)=d(ip)-h
d(iq)=d(iq)+h
```

```
a(ip,iq)=0.0d0
do 16 j=1,ip-1
g=a(j,ip)
h=a(j,iq)
a(j,ip)=g-s*(h+g*tau)
a(j,iq)=h+s*(g-h*tau)
16            continue
do 17 j=ip+1,iq-1
g=a(ip,j)
h=a(j,iq)
a(ip,j)=g-s*(h+g*tau)
a(j,iq)=h+s*(g-h*tau)
17            continue
do 18 j=iq+1,n
g=a(ip,j)
h=a(iq,j)
a(ip,j)=g-s*(h+g*tau)
a(iq,j)=h+s*(g-h*tau)
18            continue
do 19 j=1,n
g=v(j,ip)
h=v(j,iq)
v(j,ip)=g-s*(h+g*tau)
v(j,iq)=h+s*(g-h*tau)
19            continue
nrot=nrot+1
endif
21        continue
22      continue
do 23 ip=1,n
b(ip)=b(ip)+z(ip)
d(ip)=b(ip)
z(ip)=0.0d0
23      continue
```

```
24    continue
C      pause 'too many iterations in jacobi'
return
END
C  (C) Copr. 1986-92 Numerical Recipes Software #0).
C     **************************************************
C     **************************************************
SUBROUTINE eigsrt(d,v,n,np)
IMPLICIT double precision(a-h,o-z)

DIMENSION d(np),v(np,np)

do 13 i=1,n-1
k=i
p=d(i)
do 11 j=i+1,n
if(d(j).ge.p)then
k=j
p=d(j)
endif
11      continue
if(k.ne.i)then
d(k)=d(i)
d(i)=p
do 12 j=1,n
p=v(j,i)
v(j,i)=v(j,k)
v(j,k)=p
12        continue
endif
13    continue
return
END
C  (C) Copr. 1986-92 Numerical Recipes Software #0).
```

```
subroutine rs(nm,n,a,w,matz,z,fv1,fv2,ierr)

integer n,nm,ierr,matz
double precision a(nm,n),w(n),z(nm,n),fv1(n),fv2(n)
if (n .le. nm) go to 10
ierr = 10 * n
go to 50

10 if (matz .ne. 0) go to 20

call  tred1(nm,n,a,w,fv1,fv2)
*  tqlrat encounters catastrophic underflow on the Vax
*     call  tqlrat(n,w,fv2,ierr)
call  tql1(n,w,fv1,ierr)
go to 50
c     .......... find both eigenvalues and eigenvectors ..........
20 call  tred2(nm,n,a,w,fv1,z)
call  tql2(nm,n,w,fv1,z,ierr)
50 return
end
subroutine tql1(n,d,e,ierr)

integer i,j,l,m,n,ii,l1,l2,mml,ierr
double precision d(n),e(n)
double precision c,c2,c3,dl1,el1,f,g,h,p,r,s,s2,tst1,tst2,pythag

ierr = 0
if (n .eq. 1) go to 1001

do 100 i = 2, n
100 e(i-1) = e(i)

f = 0.0d0
```

```
tst1 = 0.0d0
e(n) = 0.0d0

do 290 l = 1, n
j = 0
h = dabs(d(l)) + dabs(e(l))
if (tst1 .lt. h) tst1 = h

do 110 m = l, n
tst2 = tst1 + dabs(e(m))
if (tst2 .eq. tst1) go to 120

110    continue

120    if (m .eq. l) go to 210
130    if (j .eq. 30) go to 1000
j = j + 1

l1 = l + 1
l2 = l1 + 1
g = d(l)
p = (d(l1) - g) / (2.0d0 * e(l))
r = pythag(p,1.0d0)
d(l) = e(l) / (p + dsign(r,p))
d(l1) = e(l) * (p + dsign(r,p))
dl1 = d(l1)
h = g - d(l)
if (l2 .gt. n) go to 145

do 140 i = l2, n
140    d(i) = d(i) - h

145    f = f + h
```

```
p = d(m)
c = 1.0d0
c2 = c
el1 = e(l1)
s = 0.0d0
mml = m - l

do 200 ii = 1, mml
c3 = c2
c2 = c
s2 = s
i = m - ii
g = c * e(i)
h = c * p
r = pythag(p,e(i))
e(i+1) = s * r
s = e(i) / r
c = p / r
p = c * d(i) - s * g
d(i+1) = h + s * (c * g + s * d(i))
200    continue
c
p = -s * s2 * c3 * el1 * e(l) / dl1
e(l) = s * p
d(l) = c * p
tst2 = tst1 + dabs(e(l))
if (tst2 .gt. tst1) go to 130
210    p = d(l) + f
c     .......... order eigenvalues ..........
if (l .eq. 1) go to 250
c     .......... for i=l step -1 until 2 do -- ..........
do 230 ii = 2, l
i = l + 2 - ii
if (p .ge. d(i-1)) go to 270
```

```
d(i) = d(i-1)
230    continue
c
250    i = 1
270    d(i) = p
290 continue
c
go to 1001

1000 ierr = l
1001 return
end
subroutine tql2(nm,n,d,e,z,ierr)

integer i,j,k,l,m,n,ii,l1,l2,nm,mml,ierr
double precision d(n),e(n),z(nm,n)
double precision c,c2,c3,dl1,el1,f,g,h,p,r,s,s2,tst1,tst2,pythag

ierr = 0
if (n .eq. 1) go to 1001
c
do 100 i = 2, n
100 e(i-1) = e(i)
c
f = 0.0d0
tst1 = 0.0d0
e(n) = 0.0d0
c
do 240 l = 1, n
j = 0
h = dabs(d(l)) + dabs(e(l))
if (tst1 .lt. h) tst1 = h
c     ..... look for small sub-diagonal element .....
do 110 m = l, n
```

```
tst2 = tst1 + dabs(e(m))
if (tst2 .eq. tst1) go to 120
c     .......... e(n) is always zero, so there is no exit
c                through the bottom of the loop ..........
110    continue
c
120    if (m .eq. l) go to 220
130    if (j .eq. 30) go to 1000
j = j + 1
c     .......... form shift ..........
l1 = l + 1
l2 = l1 + 1
g = d(l)
p = (d(l1) - g) / (2.0d0 * e(l))
r = pythag(p,1.0d0)
d(l) = e(l) / (p + dsign(r,p))
d(l1) = e(l) * (p + dsign(r,p))
dl1 = d(l1)
h = g - d(l)
if (l2 .gt. n) go to 145
c
do 140 i = l2, n
140    d(i) = d(i) - h
c
145    f = f + h
c     .......... ql transformation ..........
p = d(m)
c = 1.0d0
c2 = c
el1 = e(l1)
s = 0.0d0
mml = m - l
c     .......... for i=m-1 step -1 until l do -- ..........
do 200 ii = 1, mml
```

```
c3 = c2
c2 = c
s2 = s
i = m - ii
g = c * e(i)
h = c * p
r = pythag(p,e(i))
e(i+1) = s * r
s = e(i) / r
c = p / r
p = c * d(i) - s * g
d(i+1) = h + s * (c * g + s * d(i))
c     ..... form vector .....
do 180 k = 1, n
h = z(k,i+1)
z(k,i+1) = s * z(k,i) + c * h
z(k,i) = c * z(k,i) - s * h
180       continue
c
200    continue
c
p = -s * s2 * c3 * el1 * e(l) / dl1
e(l) = s * p
d(l) = c * p
tst2 = tst1 + dabs(e(l))
if (tst2 .gt. tst1) go to 130
220    d(l) = d(l) + f
240 continue
c     ..... order eigenvalues and eigenvectors .....
do 300 ii = 2, n
i = ii - 1
k = i
p = d(i)
c
```

```
do 260 j = ii, n
if (d(j) .ge. p) go to 260
k = j
p = d(j)
260    continue
c
if (k .eq. i) go to 300
d(k) = d(i)
d(i) = p
c
do 280 j = 1, n
p = z(j,i)
z(j,i) = z(j,k)
z(j,k) = p
280    continue
c
300 continue
c
go to 1001
c     .......... set error -- no convergence to an
c                eigenvalue after 30 iterations ..........
1000 ierr = l
1001 return
end

SUBROUTINE TQLRAT(N,D,E2,IERR)
C
INTEGER I,J,L,M,N,II,L1,MML,IERR
DOUBLE PRECISION D(N),E2(N)
DOUBLE PRECISION B,C,F,G,H,P,R,S,T,EPSLON,PYTHAG

IERR = 0
IF (N .EQ. 1) GO TO 1001
C
```

```
      DO 100 I = 2, N
      100 E2(I-1) = E2(I)
      C
      F = 0.0D0
      T = 0.0D0
      E2(N) = 0.0D0
      C
      DO 290 L = 1, N
      J = 0
      H = DABS(D(L)) + DSQRT(E2(L))
      IF (T .GT. H) GO TO 105
      T = H
      B = EPSLON(T)
      C = B * B
      if (c .ne. 0.0d0) go to 105
      C        Spliting tolerance underflowed.  Look for larger value.
      do 102 i = l, n
      h = dabs(d(i)) + dsqrt(e2(i))
      if (h .gt. t) t = h
      102    continue
      b = epslon(t)
      c = b * b
      C     .......... LOOK FOR SMALL SQUARED SUB-DIAGONAL ELEMENT ..........
      105    DO 110 M = L, N
      IF (E2(M) .LE. C) GO TO 120
      C     .......... E2(N) IS ALWAYS ZERO, SO THERE IS NO EXIT
      C                THROUGH THE BOTTOM OF THE LOOP ..........

      110    CONTINUE
      C
      120    IF (M .EQ. L) GO TO 210
      130    IF (J .EQ. 30) GO TO 1000
      J = J + 1
      C     .......... FORM SHIFT ..........
```

```
L1 = L + 1
S = DSQRT(E2(L))
G = D(L)
P = (D(L1) - G) / (2.0D0 * S)
R = PYTHAG(P,1.0D0)
D(L) = S / (P + DSIGN(R,P))
H = G - D(L)
C
DO 140 I = L1, N
140    D(I) = D(I) - H
C
F = F + H
C     .......... RATIONAL QL TRANSFORMATION ..........
G = D(M)
IF (G .EQ. 0.0D0) G = B
H = G
S = 0.0D0
MML = M - L
C     .......... FOR I=M-1 STEP -1 UNTIL L DO -- ..........
DO 200 II = 1, MML
I = M - II
P = G * H
R = P + E2(I)
E2(I+1) = S * R
S = E2(I) / R
D(I+1) = H + S * (H + D(I))
G = D(I) - E2(I) / G
C           Avoid division by zero on next pass
if (g .eq. 0.0d0) g = epslon(d(i))
h = g * (p / r)
200    CONTINUE
C
E2(L) = S * G
D(L) = H
```

```
C     ..... GUARD AGAINST UNDERFLOW IN CONVERGENCE TEST .....
IF (H .EQ. 0.0D0) GO TO 210
IF (DABS(E2(L)) .LE. DABS(C/H)) GO TO 210
E2(L) = H * E2(L)
IF (E2(L) .NE. 0.0D0) GO TO 130
210    P = D(L) + F
C     ..... ORDER EIGENVALUES .....
IF (L .EQ. 1) GO TO 250
C     ..... FOR I=L STEP -1 UNTIL 2 DO -- .....
DO 230 II = 2, L
I = L + 2 - II
IF (P .GE. D(I-1)) GO TO 270
D(I) = D(I-1)
230    CONTINUE
C
250    I = 1
270    D(I) = P
290 CONTINUE
C
GO TO 1001
C     ..... SET ERROR -- NO CONVERGENCE TO AN
C                    EIGENVALUE AFTER 30 ITERATIONS .....
1000 IERR = L
1001 RETURN
END
subroutine tred1(nm,n,a,d,e,e2)
c
integer i,j,k,l,n,ii,nm,jp1
double precision a(nm,n),d(n),e(n),e2(n)
double precision f,g,h,scale

do 100 i = 1, n
d(i) = a(n,i)
a(n,i) = a(i,i)
```

```
100 continue
c     ......... for i=n step -1 until 1 do -- .........
do 300 ii = 1, n
i = n + 1 - ii
l = i - 1
h = 0.0d0
scale = 0.0d0
if (l .lt. 1) go to 130
c     ......... scale row (algol tol then not needed) .........
do 120 k = 1, l
120    scale = scale + dabs(d(k))
c
if (scale .ne. 0.0d0) go to 140
c
do 125 j = 1, l
d(j) = a(l,j)
a(l,j) = a(i,j)
a(i,j) = 0.0d0
125    continue
c
130    e(i) = 0.0d0
e2(i) = 0.0d0
go to 300
c
140    do 150 k = 1, l
d(k) = d(k) / scale
h = h + d(k) * d(k)
150    continue
c
e2(i) = scale * scale * h
f = d(l)
g = -dsign(dsqrt(h),f)
e(i) = scale * g
h = h - f * g
```

```
d(l) = f - g
if (l .eq. 1) go to 285
c     .......... form a*u ..........
do 170 j = 1, l
170    e(j) = 0.0d0
c
do 240 j = 1, l
f = d(j)
g = e(j) + a(j,j) * f
jp1 = j + 1
if (l .lt. jp1) go to 220
c
do 200 k = jp1, l
g = g + a(k,j) * d(k)
e(k) = e(k) + a(k,j) * f
200       continue
c
220       e(j) = g
240    continue
c     .......... form p ..........
f = 0.0d0
c
do 245 j = 1, l
e(j) = e(j) / h
f = f + e(j) * d(j)
245    continue
c
h = f / (h + h)
c     .......... form q ..........
do 250 j = 1, l
250    e(j) = e(j) - h * d(j)
c     .......... form reduced a ..........
do 280 j = 1, l
f = d(j)
```

```
g = e(j)
c
do 260 k = j, l
260       a(k,j) = a(k,j) - f * e(k) - g * d(k)
c
280    continue
c
285    do 290 j = 1, l
f = d(j)
d(j) = a(l,j)
a(l,j) = a(i,j)
a(i,j) = f * scale
290    continue
c
300 continue
c
return
end
subroutine tred2(nm,n,a,d,e,z)
c
integer i,j,k,l,n,ii,nm,jp1
double precision a(nm,n),d(n),e(n),z(nm,n)
double precision f,g,h,hh,scale

do 100 i = 1, n
c
do 80 j = i, n
80    z(j,i) = a(j,i)
c
d(i) = a(n,i)
100 continue
c
if (n .eq. 1) go to 510
c     .......... for i=n step -1 until 2 do -- ..........
```

```
do 300 ii = 2, n
i = n + 2 - ii
l = i - 1
h = 0.0d0
scale = 0.0d0
if (l .lt. 2) go to 130
c     .......... scale row (algol tol then not needed) ..........
do 120 k = 1, l
120    scale = scale + dabs(d(k))
c
if (scale .ne. 0.0d0) go to 140
130    e(i) = d(l)
c
do 135 j = 1, l
d(j) = z(l,j)
z(i,j) = 0.0d0
z(j,i) = 0.0d0
135    continue
c
go to 290
c
140    do 150 k = 1, l
d(k) = d(k) / scale
h = h + d(k) * d(k)
150    continue
c
f = d(l)
g = -dsign(dsqrt(h),f)
e(i) = scale * g
h = h - f * g
d(l) = f - g

c     .......... form a*u ..........
do 170 j = 1, l
```

```
170    e(j) = 0.0d0
c
do 240 j = 1, l
f = d(j)
z(j,i) = f
g = e(j) + z(j,j) * f
jp1 = j + 1
if (l .lt. jp1) go to 220
c
do 200 k = jp1, l
g = g + z(k,j) * d(k)
e(k) = e(k) + z(k,j) * f
200       continue
c
220       e(j) = g
240    continue
c     .......... form p ..........
f = 0.0d0
c
do 245 j = 1, l
e(j) = e(j) / h
f = f + e(j) * d(j)
245    continue
c
hh = f / (h + h)
c     .......... form q ..........
do 250 j = 1, l
250    e(j) = e(j) - hh * d(j)
c     .......... form reduced a ..........
do 280 j = 1, l
f = d(j)
g = e(j)
c
do 260 k = j, l
```

```
260       z(k,j) = z(k,j) - f * e(k) - g * d(k)
c
d(j) = z(l,j)
z(i,j) = 0.0d0
280    continue
c
290    d(i) = h
300 continue
c     ......... accumulation of transformation matrices .........
do 500 i = 2, n
l = i - 1
z(n,l) = z(l,l)
z(l,l) = 1.0d0
h = d(i)
if (h .eq. 0.0d0) go to 380
c
do 330 k = 1, l
330    d(k) = z(k,i) / h
c
do 360 j = 1, l
g = 0.0d0
c
do 340 k = 1, l
340       g = g + z(k,i) * z(k,j)
c
do 360 k = 1, l
z(k,j) = z(k,j) - g * d(k)
360    continue
c
380    do 400 k = 1, l
400    z(k,i) = 0.0d0
c
500 continue
c
```

```
510 do 520 i = 1, n
d(i) = z(n,i)
z(n,i) = 0.0d0
520 continue
c
z(n,n) = 1.0d0
e(1) = 0.0d0
return
end
double precision function pythag(a,b)
double precision a,b
c
c     finds dsqrt(a**2+b**2) without overflow or destructive underflow
c
double precision p,r,s,t,u
p = dmax1(dabs(a),dabs(b))
if (p .eq. 0.0d0) go to 20
r = (dmin1(dabs(a),dabs(b))/p)**2
10 continue
t = 4.0d0 + r
if (t .eq. 4.0d0) go to 20
s = r/t
u = 1.0d0 + 2.0d0*s
p = u*p
r = (s/u)**2 * r
go to 10
20 pythag = p
return
end
double precision function epslon (x)
double precision x
c
c     estimate unit roundoff in quantities of size x.
c
```

```
double precision a,b,c,eps

a = 4.0d0/3.0d0
10 b = a - 1.0d0
c = b + b + b
eps = dabs(c-1.0d0)
if (eps .eq. 0.0d0) go to 10
epslon = eps*dabs(x)
return
end
subroutine dpodi(a,lda,n,det,job)
integer lda,n,job
double precision a(lda,1)
double precision det(2)

double precision t
double precision s
integer i,j,jm1,k,kp1
c
c     compute determinant
c
if (job/10 .eq. 0) go to 70
det(1) = 1.0d0
det(2) = 0.0d0
s = 10.0d0
do 50 i = 1, n
det(1) = a(i,i)**2*det(1)
c        ...exit
if (det(1) .eq. 0.0d0) go to 60
10       if (det(1) .ge. 1.0d0) go to 20
det(1) = s*det(1)
det(2) = det(2) - 1.0d0
go to 10
20       continue
```

```
30       if (det(1) .lt. s) go to 40
det(1) = det(1)/s
det(2) = det(2) + 1.0d0
go to 30
40       continue
50    continue
60    continue
70 continue
c
c     compute inverse(r)
c
if (mod(job,10) .eq. 0) go to 140
do 100 k = 1, n
a(k,k) = 1.0d0/a(k,k)
t = -a(k,k)
call dscal(k-1,t,a(1,k),1)
kp1 = k + 1
if (n .lt. kp1) go to 90
do 80 j = kp1, n
t = a(k,j)
a(k,j) = 0.0d0
call daxpy(k,t,a(1,k),1,a(1,j),1)
80       continue
90       continue
100    continue
c
c        form  inverse(r) * trans(inverse(r))
c
do 130 j = 1, n
jm1 = j - 1
if (jm1 .lt. 1) go to 120
do 110 k = 1, jm1
t = a(k,j)
call daxpy(k,t,a(1,j),1,a(1,k),1)
```

```
110       continue
120       continue
t = a(j,j)
call dscal(j,t,a(1,j),1)
130    continue
140 continue
return
end
c
subroutine dpoco(a,lda,n,rcond,z,info)
integer lda,n,info
double precision a(lda,1),z(1)
double precision rcond

double precision ddot,ek,t,wk,wkm
double precision anorm,s,dasum,sm,ynorm
integer i,j,jm1,k,kb,kp1
c
c
c     find norm of a using only upper half
c
do 30 j = 1, n
z(j) = dasum(j,a(1,j),1)
jm1 = j - 1
if (jm1 .lt. 1) go to 20
do 10 i = 1, jm1
z(i) = z(i) + dabs(a(i,j))
10    continue
20    continue
30 continue
anorm = 0.0d0
do 40 j = 1, n
anorm = dmax1(anorm,z(j))
40 continue
```

```
c
c     factor
c
call dpofa(a,lda,n,info)
if (info .ne. 0) go to 180
c
c        solve trans(r)*w = e
c
ek = 1.0d0
do 50 j = 1, n
z(j) = 0.0d0
50    continue
do 110 k = 1, n
if (z(k) .ne. 0.0d0) ek = dsign(ek,-z(k))
if (dabs(ek-z(k)) .le. a(k,k)) go to 60
s = a(k,k)/dabs(ek-z(k))
call dscal(n,s,z,1)
ek = s*ek
60       continue
wk = ek - z(k)
wkm = -ek - z(k)
s = dabs(wk)
sm = dabs(wkm)
wk = wk/a(k,k)
wkm = wkm/a(k,k)
kp1 = k + 1
if (kp1 .gt. n) go to 100
do 70 j = kp1, n
sm = sm + dabs(z(j)+wkm*a(k,j))
z(j) = z(j) + wk*a(k,j)
s = s + dabs(z(j))
70          continue
if (s .ge. sm) go to 90
t = wkm - wk
```

```
wk = wkm
do 80 j = kp1, n
z(j) = z(j) + t*a(k,j)
80              continue
90           continue
100       continue
z(k) = wk
110    continue
s = 1.0d0/dasum(n,z,1)
call dscal(n,s,z,1)
c
c         solve r*y = w
c
do 130 kb = 1, n
k = n + 1 - kb
if (dabs(z(k)) .le. a(k,k)) go to 120
s = a(k,k)/dabs(z(k))
call dscal(n,s,z,1)
120       continue
z(k) = z(k)/a(k,k)
t = -z(k)
call daxpy(k-1,t,a(1,k),1,z(1),1)
130    continue
s = 1.0d0/dasum(n,z,1)
call dscal(n,s,z,1)
c
ynorm = 1.0d0
c
c         solve trans(r)*v = y
c
do 150 k = 1, n
z(k) = z(k) - ddot(k-1,a(1,k),1,z(1),1)
if (dabs(z(k)) .le. a(k,k)) go to 140
s = a(k,k)/dabs(z(k))
```

```
call dscal(n,s,z,1)
ynorm = s*ynorm
140       continue
z(k) = z(k)/a(k,k)
150    continue
s = 1.0d0/dasum(n,z,1)
call dscal(n,s,z,1)
ynorm = s*ynorm
c
c        solve r*z = v
c
do 170 kb = 1, n
k = n + 1 - kb
if (dabs(z(k)) .le. a(k,k)) go to 160
s = a(k,k)/dabs(z(k))
call dscal(n,s,z,1)
ynorm = s*ynorm
160       continue
z(k) = z(k)/a(k,k)
t = -z(k)
call daxpy(k-1,t,a(1,k),1,z(1),1)
170    continue
c        make znorm = 1.0
s = 1.0d0/dasum(n,z,1)
call dscal(n,s,z,1)
ynorm = s*ynorm
c
if (anorm .ne. 0.0d0) rcond = ynorm/anorm
if (anorm .eq. 0.0d0) rcond = 0.0d0
180 continue
return
end
c
subroutine dpofa(a,lda,n,info)
```

```
integer lda,n,info
double precision a(lda,1)

double precision ddot,t
double precision s
integer j,jm1,k
c     begin block with ...exits to 40
c
c
do 30 j = 1, n
info = j
s = 0.0d0
jm1 = j - 1
if (jm1 .lt. 1) go to 20
do 10 k = 1, jm1
t = a(k,j) - ddot(k-1,a(1,k),1,a(1,j),1)
t = t/a(k,k)
a(k,j) = t
s = s + t*t
10       continue
20       continue
s = a(j,j) - s
c     ......exit
if (s .le. 0.0d0) go to 40
a(j,j) = dsqrt(s)
30    continue
info = 0
40 continue
return
end
c
double precision function dasum(n,dx,incx)
c
c
```

```
double precision dx(*),dtemp
integer i,incx,m,mp1,n,nincx
c
dasum = 0.0d0
dtemp = 0.0d0
if( n.le.0 .or. incx.le.0 )return
if(incx.eq.1)go to 20
c
c        code for increment not equal to 1
c
nincx = n*incx
do 10 i = 1,nincx,incx
dtemp = dtemp + dabs(dx(i))
10 continue
dasum = dtemp
return
c
c        code for increment equal to 1
c        clean-up loop
c
20 m = mod(n,6)
if( m .eq. 0 ) go to 40
do 30 i = 1,m
dtemp = dtemp + dabs(dx(i))
30 continue
if( n .lt. 6 ) go to 60
40 mp1 = m + 1
do 50 i = mp1,n,6
dtemp = dtemp + dabs(dx(i)) + dabs(dx(i + 1)) + dabs(dx(i + 2))
*  + dabs(dx(i + 3)) + dabs(dx(i + 4)) + dabs(dx(i + 5))
50 continue
60 dasum = dtemp
return
end
```

```
c
subroutine daxpy(n,da,dx,incx,dy,incy)
c
c
double precision dx(*),dy(*),da
integer i,incx,incy,ix,iy,m,mp1,n
c
if(n.le.0)return
if (da .eq. 0.0d0) return
if(incx.eq.1.and.incy.eq.1)go to 20
c
c
ix = 1
iy = 1
if(incx.lt.0)ix = (-n+1)*incx + 1
if(incy.lt.0)iy = (-n+1)*incy + 1
do 10 i = 1,n
dy(iy) = dy(iy) + da*dx(ix)
ix = ix + incx
iy = iy + incy
10 continue
return

20 m = mod(n,4)
if( m .eq. 0 ) go to 40
do 30 i = 1,m
dy(i) = dy(i) + da*dx(i)
30 continue
if( n .lt. 4 ) return
40 mp1 = m + 1
do 50 i = mp1,n,4
dy(i) = dy(i) + da*dx(i)
dy(i + 1) = dy(i + 1) + da*dx(i + 1)
dy(i + 2) = dy(i + 2) + da*dx(i + 2)
```

```
dy(i + 3) = dy(i + 3) + da*dx(i + 3)
50 continue
return
end
c
double precision function ddot(n,dx,incx,dy,incy)

double precision dx(*),dy(*),dtemp
integer i,incx,incy,ix,iy,m,mp1,n
c
ddot = 0.0d0
dtemp = 0.0d0
if(n.le.0)return
if(incx.eq.1.and.incy.eq.1)go to 20

ix = 1
iy = 1
if(incx.lt.0)ix = (-n+1)*incx + 1
if(incy.lt.0)iy = (-n+1)*incy + 1
do 10 i = 1,n
dtemp = dtemp + dx(ix)*dy(iy)
ix = ix + incx
iy = iy + incy
10 continue
ddot = dtemp
return

20 m = mod(n,5)
if( m .eq. 0 ) go to 40
do 30 i = 1,m
dtemp = dtemp + dx(i)*dy(i)
30 continue
if( n .lt. 5 ) go to 60
40 mp1 = m + 1
```

```
do 50 i = mp1,n,5
dtemp = dtemp + dx(i)*dy(i) + dx(i + 1)*dy(i + 1) +
*   dx(i + 2)*dy(i + 2) + dx(i + 3)*dy(i + 3) + dx(i + 4)*dy(i + 4)
50 continue
60 ddot = dtemp
return
end

subroutine  dscal(n,da,dx,incx)

double precision da,dx(*)
integer i,incx,m,mp1,n,nincx
c
if( n.le.0 .or. incx.le.0 )return
if(incx.eq.1)go to 20

nincx = n*incx
do 10 i = 1,nincx,incx
dx(i) = da*dx(i)
10 continue
return

20 m = mod(n,5)
if( m .eq. 0 ) go to 40
do 30 i = 1,m
dx(i) = da*dx(i)
30 continue
if( n .lt. 5 ) return
40 mp1 = m + 1
do 50 i = mp1,n,5
dx(i) = da*dx(i)
dx(i + 1) = da*dx(i + 1)
dx(i + 2) = da*dx(i + 2)
dx(i + 3) = da*dx(i + 3)
```

```
dx(i + 4) = da*dx(i + 4)
50 continue
return
end
```

References

[1] COMSOL Multiphysics, v. 5.2a. COMSOL AB, Stockholm, Sweden.